Sulfur behavior and redox conditions in Etnean hydrous basalts inferred from melt inclusions and experimental glasses

Mimma Emanuela Gennaro

Università degli Studi di Palermo

ÉCOLE DOCTORALE « ENERGIE, MATERIAUX, SCIENCES DE LA TERRE ET DE L'UNIVERS »

Institut des Sciences de la Terre d'Orléans / Université de Palerme

THÈSE EN COTUTELLE INTERNATIONALE présentée par :

Mimma Emanuela GENNARO

soutenue le : 22 Février 2017
pour obtenir le grade de :
Docteur de l'université d'Orléans
et de l'Université de Palerme
Discipline : Sciences de la Terre et de l'Univers

Sulfur behavior and redox conditions in Etnean hydrous basalts inferred from melt inclusions and experimental glasses

THÈSE dirigée par :

Caroline MARTEL	CDR, CNRS-ISTO
Silvio ROTOLO	Professeur, Université de Palerme

Co-tutor:

Andrea RIZZO	Chercheur, INGV-Palerme

RAPPORTEURS:

Rosa Anna CORSARO	Chercheur, INGV-Catania
Joan MARTI	Professeur, ICTJA - CSIS

JURY :

Caroline MARTEL	CDR, CNRS-ISTO
Silvio ROTOLO	Professeur, Université de Palerme
Giada IACONO MARZIANO	CDR, CNRS-ISTO
Vincenzo STAGNO	Chercheur, Université de Rome « La Sapienza »
Domenico COSENTINO	Professeur, Université de Roma Tre
Annachiara BARTOLINI	Professeur, NMNH

Index

ABSTRACT

Sulfur is an important volatile component of magmas that presents different oxidation states, depending on the redox conditions and on the phase of occurence: in silicate melts it is typically dissolved as S^{6+} and/or S^{2-}, in the gas phase it occurs principally as SO_2 (S^{4+}) and H_2S (S^{2-}).

Here, we adopt Mount Etna as a case study to investigate sulfur behavior in hydrous basaltic magmas during magma differentiation and degassing. Mount Etna is a complex magmatic system characterized by a certain variability in terms of both eruptive style and composition of erupted products, and in which magmatic redox conditions are poorly constrained.

In order to improve knowledge about sulfur behavior and redox conditions in Etnean magmas, this research integrates the study of natural olivine-hosted melt inclusions with an experimental study on S solubility in hydrous alkali basalts at magmatic conditions.
We have investigated major element compositions, volatile contents, and Fe speciation of olivine-hosted melt inclusions from 6 eruptions of the last 15 ky. Samples were selected from FS eruption, which is the most primitive (picritic composition, Fo_{91}), Mt. Spagnolo (the oldest) and more recent eruptions (2002/2003, 2006, 2008/2009, and 2013).

Experimental glasses were synthesized in the range of pressure (200 MPa), temperature (1200 °C), and oxygen fugacity conditions (ΔNNO = +0.2 to +1.7) relevant to the Etnean system.

Experimental results suggest the important control of fO_2 on the S abundance in Etnean hydrous magma. The highest S content (6454 ppm) was achieved at fO_2 = NNO+1.7, while at lower fO_2 (ΔNNO = +0.2 to +0.9) and at the sulfide saturation the maximum sulfur content was 2400 ppm. S content and Fe speciation of the experimental glasses are useful to interpret melt inclusions data.

The melt inclusions were entrapped at different depths inside the magmatic system (up to ~ 18 km, below crater level, corresponding to a pressure of almost 500 MPa) as defined by H_2O-CO_2 contents. They delineate a continuous differentiation trend from the FS picrite toward the degassed 2013 basalt, marked by fractional crystallization. Sulfur content in Etnean melt is extremely variable and reaches 4150 ppm in the most primitive melt inclusions of Mt. Spagnolo (Fo_{87}).

XANES $Fe^{3+}/\Sigma Fe$ spectra in some glass inclusions, resulted in the generally decreasing of $Fe^{3+}/\Sigma Fe$ ratios from the most primitive (FS) to the most recent (2013) melts. MELTS software confirms that the $Fe^{3+}/\Sigma Fe$ decrease is due principally to the melt differentiation process, enhanced to the S degassing at fO_2 < NNO+1. Indeed, the magmas of Mt. Spagnolo and of the recent eruptions may be produced by differentiation from the oxidized, parental FS magma, accompanied occasionally by mixing processes.

Magma reduction, in turn, induces the decrease of the sulfur solubility in the hydrous Etnean basalt, as well as of the sulfide saturation, and may constitute a possible enhancer of S exsolution, triggering the important S degassing observed in the last decades in Mt. Etna.

Keywords: sulfur, silicate melt inclusions, experiments, XANES $Fe^{3+}/\Sigma Fe$ ratio, oxygen fugacity

RÉSUMÉ

Le soufre est un composant volatil important des magmas qui présente différents états d'oxydation en fonction des conditions d'oxydoréduction et de la phase dans laquelle il se trouve : dans le liquide silicaté, il est typiquement dissous comme S^{6+} et/ou S^{2-}, dans la phase gazeuse il se trouve principalement comme SO_2 (S^{4+}) et H_2S (S^{2-}).

Dans cette thèse, nous utilisons l'Etna comme cas d'étude pour examiner le comportement du soufre dans les magmas basaltiques hydratés pendant la différenciation et le dégazage. L'Etna est un système magmatique complexe caractérisé par une variabilité continue dans le style éruptif et dans la composition des produits eruptés, et pour lequel les conditions d'oxydoréduction sont faiblement contraintes.

Afin d'améliorer la connaissance sur le comportement du soufre et les conditions d'oxydoréduction des magmas de l'Etna, cette recherche combine l'étude des inclusions vitreuses avec une étude expérimentale en conditions magmatiques sur la solubilité du S dans les basaltes alcalins hydratés.

Nous avons étudié la composition en éléments majeurs, les teneurs en volatiles et la spéciation du Fe dans les inclusions vitreuses piégées dans les olivines de 6 éruptions issues des derniers 15 ka: l'éruption FS, la plus primitive (produit de composition picritique, Fo_{91}), Mt. Spagnolo, la plus ancienne, et des éruptions plus récentes (2002/2003, 2006, 2008/2009 et 2013).

Les verres expérimentaux ont été synthétisés dans les domaines de pression (200 MPa), de température (1200 ° C) et de fugacité d'oxygène (ΔNNO = +0.2 à +1.7) pertinents pour le système de l'Etna.

Les résultats expérimentaux suggèrent l'important contrôle de la fO_2 sur la teneur en S dans les magmas hydratés de l'Etna. La teneur en S maximale (6454 ppm) dans les verres expérimentaux a été atteinte à fO_2 = NNO + 1.7, tandis qu'à fO_2 inférieure (ΔNNO = +0.2 à +0.9) et en saturation en sulfure, la teneur en soufre maximale était de 2400 ppm. Le contenu du S et la spéciation de Fe des verres expérimentaux sont utiles pour interpréter les données des inclusions vitreuses.

Les inclusions vitreuses ont été piégées à différentes profondeurs à l'intérieur du système magmatique (jusqu'à ~ 18 km, au-dessous du niveau des cratères, correspondant à une pression d'environ 500 MPa) définie par les teneurs en H_2O-CO_2. Elles décrivent une tendance continue de différenciation, marqué par une cristallisation fractionnée, à partir de la composition picritique FS vers le basalte dégazé de 2013. Le contenu en soufre dans le liquide de l'Etna est extrêmement variable et atteint les 4150 ppm dans les inclusions vitreuses les plus primitives de l'éruption de Mt. Spagnolo (Fo_{87}).

Les spectres XANES $Fe^{3+}/\Sigma Fe$ des certaines inclusions vitreuses, donnent des rapports $Fe^{3+}/\Sigma Fe$ généralement décroissants à partir du liquide le plus primitif (FS) jusq'au plus évolué (2013). Les simulations effectué par le logiciel MELTS confirme que la diminution des rapports $Fe^{3+}/\Sigma Fe$ est principalement due au processus de différenciation magmatique, renforcé par le dégazage du S à fO_2 < NNO + 1. En effet, les magmas de Mt. Spagnolo et des éruptions récentes peuvent être produits par différenciation du magma parent FS (oxydé), parfois potentiellement accompagné par des processus de mélange.

La réduction du magma provoque à son tour la diminution de la solubilité du soufre dans les basaltes hydratés de l'Etna, ainsi que la saturation en sulfure, et peut constituer un éventuel activateur de l'exsolution du soufre, à l'origine de l'important dégazage du S observé au cours des dernières décennies à l'Etna.

Mots-clés : soufre, inclusion vitreuses silicatiques, expériences, XANES $Fe^{3+}/\Sigma Fe$ ratio, fugacité d'oxygène

1. Introduction

Volatile components play a key role in the volcanic system, influencing the dynamics of ascent, the evolution and the degassing of magmas (e.g. Wallace and Edmonds, 2011). The most abundant magmatic volatiles are water and carbon dioxide, followed by sulfur species and halogens (mainly Cl, F). Worldwide volcanoes emit great amounts of these volatiles and the knowledge of their behavior has many implications for understanding eruptive activity, geodynamic cycles of volatiles, formation of magmatic-hydrothermal ore deposits, as well as for the computation of the magma budget and therefore for volcano monitoring. Among these volatiles components, sulfur species have gained interest in the last years. Sulfur plays, indeed, an important role in many geological contests because it affects the partitioning of metals between sulfide phases, vapor, and silicate melt in magmas during crustal storage. When emitted into the atmosphere, sulfur has an important impact on the atmospheric chemistry (e.g., Wallace and Edmonds, 2011). Indeed, sulfur released during explosive volcanic eruptions, mainly as SO_2 and H_2S (Oppenheimer, 2003), forms sulfate aerosols, causing atmospheric cooling that may persist for months/years (for example, during the 1991 eruption of Mt. Pinatubo; Guo et al. 2004, and references therein). Furthermore, sulfur seems to induce the oxidation of the mantle wedge above the subduction zones (e.g., Wallace and Edmonds, 2011; Kelley and Cottrell, 2012), in which an oxidized subducted plate provides the materials (Fe^{3+} or SO_4^{2-}) that drive oxidation of the mantle wedge.

Recently, sophisticated techniques are been developed for measuring SO_2 and H_2S emitted by volcanoes (e.g., Oppenheimer et al., 2011); most of them were tested at Mount Etna, which is one of the most constantly active volcanoes worldwide.

The behavior of sulfur dissolved in the silicate melts is more complicated to evaluate, as sulfur solubility depends on a multiplicity of parameters: melt composition, pressure, temperature, composition of volatile phase, and redox conditions. Several experimental studies have determined the solubility of sulfur in hydrous silicic melts (e.g., Carroll and Rutherford, 1985; 1987; Luhr, 1990; Carroll and Webster, 1994; Botcharnikov et al., 2004; Clemente et al., 2004; Webster and Botcharnikov, 2011). Conversely, the sulfur solubility in hydrous basaltic melt remains less investigated (e.g., Luhr, 1990; Liu et al., 2007; Moune et al., 2009; Beermann et al., 2011; Lesne et al., 2015).

The principal difficulty to constrain S behavior in a hydrous basaltic melt and to understand sulfur partitioning between the fluid phase and the silicate melt (and the sulfides and/or sulfate phases) is its different oxidation state, strictly linked to the redox conditions of the system. Indeed, sulfur dissolves in the melt primarily as sulfide (S^{2-}) in reduced condition, and sulfate (S^{6+}) in more oxidized condition (Fincham and Richardson, 1954). Experimental determination of the S content in silicate melts clearly shows that the solubility of sulfur in magmas is strictly dependent on the oxygen fugacity (fO_2), inasmuch magmas can dissolve more S when S^{6+} is the dominant species (Carroll and Rutherford, 1985, 1987; Luhr, 1990; Jugo et al., 2005). Estimates of S speciation in natural and experimental samples show that the transition from sulfide to sulfate dominated systems occurs over a narrow fO_2 interval

(roughly from fayalite-magnetite-quartz (FMQ) to FMQ + 2 (Wallace and Carmichael, 1994; Jugo et al., 2005). This fO_2 range is significant because it overlaps with the fO_2 conditions prevalent during magma generation in arc settings (Parkinson and Arculus, 1999) and with those prevalent in back-arc, island arc, and oceanic-island magmas at the time of eruption (Ballhaus, 1993).

In addition, the isotopic fractionation of S between melt and gas phases strongly depends on the speciation of sulfur in both phases, and is related to the oxygen fugacity (fO_2) of the magma, besides temperature, and water fugacity (fH_2O). Consequently, sulfur can experience wide isotopic fractionation during volcanic degassing as the partitioning changes with the magmatic conditions (e.g., Marini et al., 2011; Liotta et al., 2012).

We chose Mount Etna (Italy) as a case study to investigate sulfur behavior in hydrous alkali-basaltic magmas, and its relation with the redox conditions, because (i) magma differentiation and degassing at Mount Etna were already explored by numerous studies and (ii) Mount Etna presents high SO_2 flux in atmosphere, which testifies the degassing of high amount of magma and intense dynamics at depth.

Mt. Etna is a strato-volcano, imposing on the boundary of the colliding African and European plates and close the Aeolian subduction area (e.g., Branca et al., 2011). It begins as a submarine volcano evolving toward an effusive/explosive aerial volcano. Etna's activity of the last years mostly consists of paroxysmal activity at the summit craters (lava fountains and associated lava flows) as well as effusive activity from eruptive fissures opened on the upper flanks of the volcano. Mt Etna is also marked by two caldera collapse events (the last one during the 122 A.D. eruption) and some rarely sub-plinian eruption, as the well-known FS (*"fall stratified"*) eruption, that erupted a picritic basalt (Coltelli et al., 2005).

Magmatic activity is accompanied at Mt. Etna by huge emissions of H_2O, CO_2 and SO_2, with an estimated average total flux of ~ 21000 t day^{-1} during the 2005-2006 eruptive period (Aiuppa et al., 2008). A prominent characteristic of Mt. Etna is the persistent gases emission, also during not-eruptive period, mainly of SO_2 [~3563 t/d (Salerno et al., 2009)]. Mt. Etna crater gases have been largely characterized for their chemical composition (e.g., Martelli et al., 2008; Paonita et al., 2012), their fluxes (e.g., Aiuppa et al., 2007, 2008), and their C (e.g., Martelli et al., 2008; Paonita et al., 2012; Rizzo et al., 2014), S (e.g., Liotta et al., 2012), and Cl isotopic ratio (Rizzo et al., 2013).

In addition, more recently, several studies have been focusing on the elemental abundances of volatiles (H_2O, CO_2, S, Cl and F) in Etnean magmas through the study of melt inclusions (e.g., Métrich and Clocchiatti, 1996; Métrich et al., 2004; Spilliaert et al., 2006a; Kamenetsky et al., 2007; Collins et al., 2009). These studies allowed the evaluation of the degassing pressures permitting to understand the pre-eruptive magma dynamics, and to define degassing models.

Nevertheless, the high SO_2 flows measured in the Etnean area are not entirely constrained either in terms of S origin or in terms of S behavior during magma ascent and differentiation.

Another point left somehow poorly constrained, or contrasting, regards the redox conditions of the Mt. Etna magma. Several studies suggest an oxygen fugacity varying from the Ni-NiO (NNO) oxygen buffer to NNO+1.8, on the basis of phase-equilibria experiments (e.g., Trigila et al., 1990; Armienti et al., 1994; Métrich and Rutherford 1998), Cr-spinel and Fe-Ti oxides compositions (Kamenetsky and Clocchiatti, 1996; Kahl et al., 2011), or S speciation (Métrich and Clocchiatti, 1996; Métrich et al., 2009).

This PhD research relies on the study of natural olivine-hosted melt inclusions, coupled with an experimental investigation of S solubility in Etnean hydrous alkali basalts, in order to improve the knowledge of the S behavior and the redox conditions of Etnean magmas during differentiation and degassing.

Melt inclusions are small volumes of silicate melt, entrapped in minerals during their formation at different depths inside the magmatic system. Once the inclusions are formed, they become a closed system, isolated by the hosting crystal that prevents the enclosed melt from degassing (e.g., Schiano, 2003). Consequently, they may retain high concentrations of volatile elements, which yield estimates of the gas saturation pressure, and in turn, of the minimum depth of entrapment (e.g., Schiano, 2003). Melt inclusions in olivine crystals represent an important tool to provide information on the magma in its more primitive conditions, and during the ascent in the volcanic system; information that is generally not provided by the erupted products. Therefore, melt inclusions are very useful to retrieve the chemical composition of the parental magma and its volatile content before degassing.

Melt inclusions are distinguished between primary and secondary (e.g., Schiano, 2003). The primary inclusions are cogenetic with their host phase and have a spherical and regular shape (often reminiscent of the host crystal). Conversely, the secondary melt inclusions form after the host crystal and are located in healed fractures, developing in the just formed crystal. Their shape is generally ellipsoidal, elongated or amoeboid.

During cooling, the difference in the thermal expansion coefficients between the host phase and the enclosed melt leads to the formation of a shrinkage bubble. Subsequent overgrowth of the host phase on the inclusion walls and nucleation of additional minerals (daughter minerals) may modify the composition of the residual melt inside the inclusion and induce degassing (e.g., Frezzotti, 2001). Consequently, at room temperature, silicate melt inclusions generally contain quenched glass, gas bubbles and ‘‘daughter’’ minerals (e.g., Frezzotti, 2001; Schiano, 2003). For these reasons, melt inclusions should be accurately selected, preferring bubble and crystals-free inclusions.

For this study, olivine hosted melt inclusions were accurately selected from products belonging to six of the most characteristic Etnean eruptions of the last 15000 years, from the oldest and most primitives (Mt. Spagnolo and FS eruptions) up to the recent paroxysm event of April 2013. These eruptions are differently localized in the time and space, in order to highlight eventual temporal and spatial variations in the geochemistry of Etnean magma.

The petrological study of these natural glasses, associated to the bibliography research, allowed us to define the starting material (Mt. Spagnolo composition), the volatile content and the magmatic conditions (P, T, fO_2) to adopt in the experimental study. The experiments were carried out a constant temperature and pressure (1200 °C and 200 MPa) at volatile saturation, varying the oxygen fugacity in the range in which the transition from sulfide to sulfate occurs in silicate melts (e.g., Jugo, 2009, and references therein).

Both natural and experimental glasses were characterized for their S isotope composition ($\delta^{34}S$ ‰) and used for acquiring XANES $Fe^{3+}/\sum Fe$ spectra.

2. Geological setting and magmatism of Mt. Etna

Mt. Etna is the most active volcano in Europe, with a diameter of 40 km as its base and a height of 3350 m, covers an area of 1260 km^2. Because of its particular location, its volcanic history, its explosive activity and persistent degassing, Mt. Etna represents an ideal natural laboratory.

2.1. Geodynamic and structural context

Mount Etna is a Quaternary, composite stratovolcano located on the eastern coast of Sicily (Italy). This area is characterized by the convergence of European and African tectonic plates, with the related subduction of the Ionian oceanic crust, currently still active in the northern Aeolian archipelago (fig. 2.1a).

Mt. Etna lies on the external boundary of the Appennine-Maghrebian chain, overlapping the undeformed African continental margin (Bousquet and Lanzafame, 2004). It is bordered by the Sicilian-Maghrebian Chain northward and westward, the Hyblean Foreland southward, and the oceanic Ionian Basin eastward.

Beneath Mt. Etna, the Moho lies at a depth of about 18-22 km (Nicolich et al., 2000).

Structural and seismic data suggest that the principal regional deformation in the Etnean area is represented by an N-S compression, (Cocina et al., 1997, 1998; Lanzafame et al., 1997), with a roughly E-W extension or right-lateral transtension on the eastern part of the volcanic complex (Torelli et al., 1998; Azzaro, 1999).

The principal tectonic structures at Mt. Etna (fig. 2.1b, Patané et al., 2011; and reference therein) are in the east and south-east sector of the volcano, where frequent shallow (depth < 7 km) seismic activity is associated to a normal faulting system called "Timpe fault". This system is related to the principal lithospheric structure in the eastward Sicily region: the Malta escarpment (NNW-SSE). Another active fault in the Etnean area is the "Pernicana fault" in the north flank (E-W direction, normal dip and strike-slip). This system develops eastward from the "NE rift" (from 1850 m above sea level) to the coastline, over a distance of about 20 km (Patané et al., 2011). It is exactly along this 20 km long fault (the so called "NE Rift") that during the 2002/03 the most explosive and lasting eruption of the last 15 years took place (Acocella et al., 2003; Neri et al., 2004).

The south flank of the volcano is characterized by the "South Rift", consisting of several eruptive fissures, and the Mascalucia-Trecastagni fault system (NNW-SSE striking).

The western flank of Mt. Etna is considered the most stable sector of the volcano, only the Ragalna fault (dip-slip motion) occurs in the southwestern part of the volcano. Conversely, the eastern flank is affected by an ESE slip as revealed by ground fractures and seismicity (< 4 km bsl) during the 2002/2003 eruptive period (Acocella et al., 2003; and references therein).

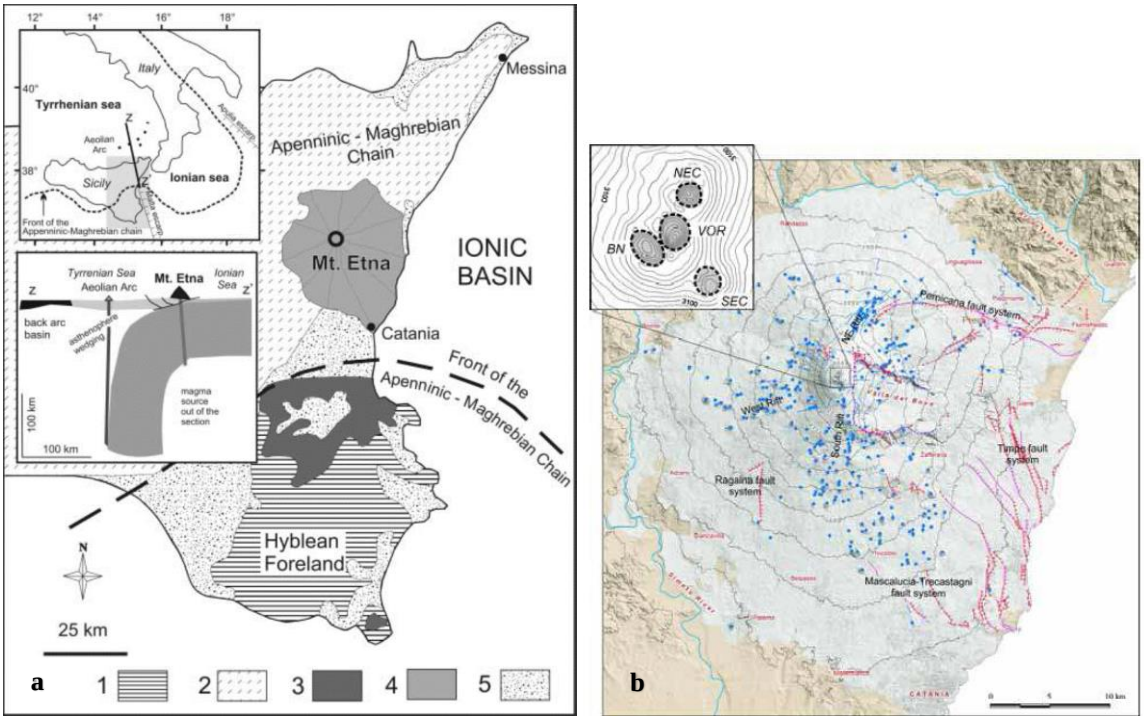

Fig. 2.1 - a) Sketch map of Eastern Sicily (Corsaro and Pompilio, 2004b; and reference therein) showing the geological and structural setting in the Etnean area: (1) Mesozoic-Cenozoic carbonatic sequence of the Hyblean foreland; (2) crystalline and Mesozoic–Cenozoic sedimentary units of the Apenninic-Maghrebian chain; (3) Upper Cretaceous-Pleistocene tholeiitic and alkaline volcanics; (4) Mt. Etna volcanics; (5) Plio-Quaternary marine and continental sediments. The thick dashed curve marks the limit of the Apenninic-Maghrebian Chain front. The top-left inserts show the geodynamic setting of Mt. Etna and the asthenospheric window beneath Mt. Etna as proposed in Doglioni et al., (2001).
b) Structural map of Mt. Etna, with the principal fault systems. In the small picture, the localization of the summit craters (NEC = North-East Crater, SEC = South-East Crater, BN = Bocca Nuova, VOR = Voragine).

2.2. Origin of Etna and magmatism

The origin of magmatic activity in the Etna area is still debated. Although observed in a setting dominated by the convergence between the African and European plates, Mt. Etna cannot be considered a subduction-related volcano, given the composition of its different magma-types (Schiano et al., 2001). Among the different hypothesis proposed with time, can be mentioned a hot spot origin (Tanguy et al., 1997; Clocchiatti et al., 1998), an asymmetric rifting process (Continisio et al., 1997). Other authors instead (Rittmann, 1973; Lanzafame et al., 1997; McGuire et al., 1997) propose that the magmatic activity in the Etnean area is favored by the intersection of major lithospheric faults as the NNW-SSE trending Tindari-Letojanni-Malta and the NNE-SSW Messina-Giardini line.

Furthermore, Gvirtzman and Nur (1999) suggest that the decompression and melting of the mantle beneath Mt. Etna is due to the "suction" of asthenospheric material from under the neighboring African plate, generated by the backward migration in the mantle of the descending slab. Similarly, Doglioni et al. (2001) proposed the existence of a lithospheric

'window' created by the differential rollback of the subduction sectors among the Ionian oceanic domain and the Sicilian continental crust, resulting in mantle decompression and partial melting along a vertical window in the slab (small picture in fig. 2.1). Schiano et al. (2001) suggest that Mt. Etna reflects the juxtaposition of the Ionian slab (southward migrating) on the mantle plume beneath eastern Sicily.

Volcanic activity in the Etnean area began around 500 ky ago, through submarine eruptions. Since its origin, Mount Etna activity is characterized by dominant effusive activity punctuated by highly explosive eruptions. The chemical composition of the erupted magmas changed gradually from sub-alkaline to alkaline affinity.

As described in Branca et al., (2004a, 2004b, 2008, and 2011) the evolution of Etnean volcanism can be divided into four phases (fig. 2.2a):

I. ***"Basal Tholeiitic Supersynthem"*** (500-320 ky BP). The first Etnean activity was localized on the Gela-Catania foredeep basin. The products of this first period consist of shallow subvolcanic bodies, pillow lavas (around Acicastello village and Acitrezza) and hyaloclastic breccias with a tholeiitic affinity [fig. 2.2b; (Tanguy et al., 1997, Corsaro and Cristofolini, 1997, 2000)]. The oldest subaerial lava flows (330 ky BP) are exposed in proximity of the Simeto river (e.g., Corsaro and Pompilio, 2004a), forming a lava plateau between Adrano and Paternò towns, which extends for more than 25 km. The tholeiitic magmatism of this period is considered being the consequence of the northward migration of the magmatic source of the Hyblean volcanism (Corsaro and Pompilio, 2004a; Correale et al., 2014).

II. ***"Timpe Supersynthem"*** (220-110 ky BP). About 200 ky ago the volcanic activity was located mainly along the Ionian coast, where the continuously fissure-type eruptions built a shield volcano with a diameter of about 15 km. The volcanic products are well exposed along the Ionic coast and the Timpe fault system, and mark the important chemical transition from sub-alkaline (tholeiitic) to Na-alkaline.

III. ***"Valle del Bove Supersynthem"*** (110-65 ky BP). In this period, the volcanic activity shifted westward, and recorded another important variation: the eruptions became essentially central-type, both explosive and effusive, and led to the building of the several volcanic edifices: Rocche [until to 102 ky BP, (De Beni et al., 2011)], Tarderia [until to 106 ky BP, (De Beni et al., 2011)], Trifoglietto (2600 m height). The activity of Trifoglietto ended 100 ky ago (De Beni et al., 2011) with a plinian eruption. Afterward, minor eruptive centers formed on its flanks (Monte Cerasa, Giannicola, Salifizio and Cuvigghiuni; fig. 2.2b).

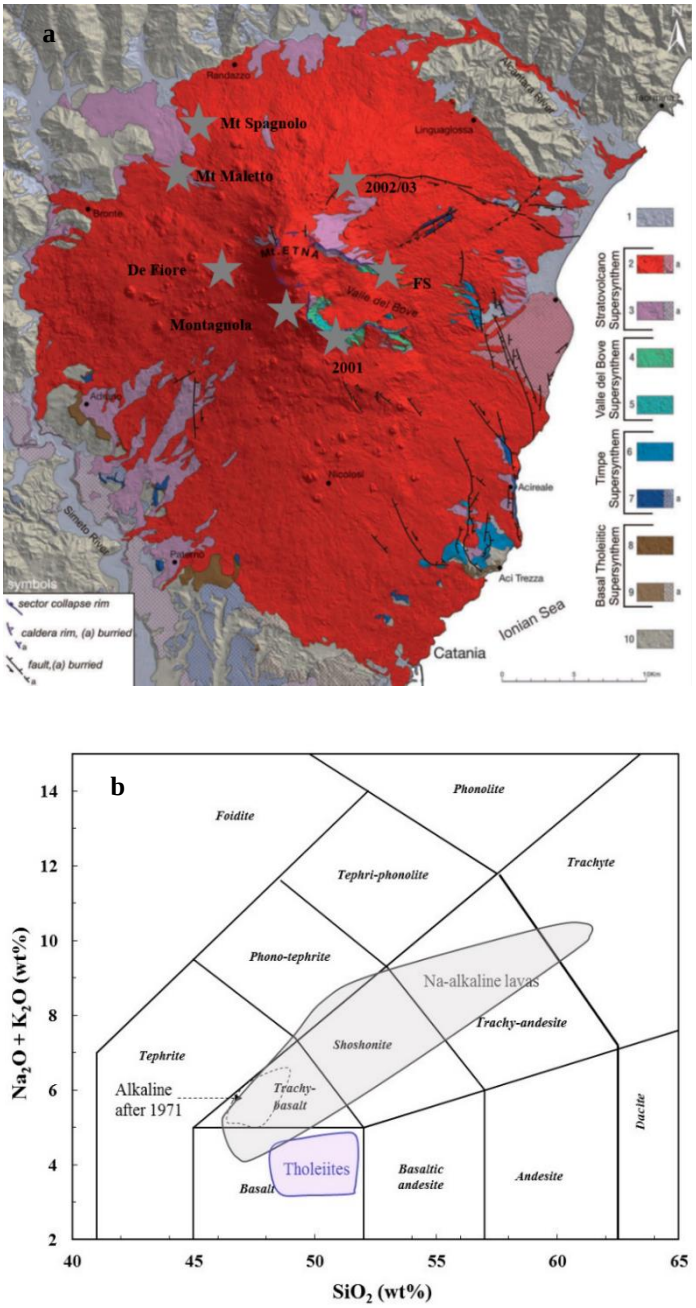

Fig. 2.2 - a) Scheme of the synthems recognized in the stratigraphy of Mt. Etna, from Branca et al. (2011). The stars indicate the eccentric eruptions (see text).
b) Total alkali vs. silica (TAS) diagram (Le Maitre, 2002) showing the composition of the lavas emitted from Etna from its origin, from Correale et al. (2014).

IV. ***"Stratovolcano Supersynthem"*** (last 65 ky). In this stage another westward shift of the volcanic activity occurred, with the building of the stratovolcano that represents the main structure of the actual edifice. This period can be further divided into two sub-periods: the Ellittico volcano [57-15 ky BP, (De Beni et al., 2011)] and the current Mongibello volcano (< 15 ky), both characterized by effusive and explosive

eruptions. The Ellittico volcano ended its activity with four Plinian eruptions, the last of which formed the Biancavilla-Montalto ignimbrite [(De Rita et al, 1991; Coltelli et al., 2000)] and was followed by the collapse of the Ellittico caldera (diameter > 4 km). Afterward, numerous flank eruptions produced lava flows and few highly explosive eruptions (sub-plinian to plinian) that filled the small caldera and built the Mongibello edifice. Mongibello activity is mainly effusive, but is also punctuated by few highly explosive eruptions, as the well-known FS [*"fall stratified"*, ~4 ky BP, (Coltelli et al. 1998)], that produced the most primitive products of Etna series, or the 122 BP eruption. The latter is the most powerful eruption of historical times that formed the caldera *"Cratere del Piano"* (Coltelli et al., 1998, 2005) and produced an important volume of ash and lapilli, causing heavy damages in the town of Catania. During the Mongibello phase [around 6 ky BP (Calvari et al., 2004)] the huge gravitative collapse of the eastern flank of the Mongibello edifice also occurred creating the current depression of *"Valle del Bove"*, which exposes a large portion of the internal structure of Mongibello and Ellittico volcanos.

*"**Historical activity**"*

Since 1911 the Etna morphology has changed, with the building of the *"North East Crater"* (NEC, 3350 m), the *"Voragine"* (1945) and *"Bocca Nuova"* (1968) craters in the summit area (fig. 2.1b). In 1971 the *"South East Crater"* (SEC) formed, where the most explosive activities of the last years occurred. In 2013, this crater was completely overshadowed by a new cone, namely the *"New South-East Crater"* (NSEC), during several paroxysmal events that lasted from 2011 to 2013 (Behncke et al., 2014).

At Mt. Etna, volcanic activity can take place both at the summit ("central eruptions"), and along fractures opened on the flanks of the volcano ("flank eruptions"). These latter eruptions are very frequent, as attested by the presence of 338 monogenic cones of varying age on the volcano slopes (Armienti et al., 2004), preferentially concentrated along the main volcano-tectonic structures of the region (fig. 2.1b). Normally, these flank eruptions are characterized by lava flows of low to medium volume, with compositions similar to those erupted during the central eruptions.

Some of these flank eruptions, also known as *"eccentric"* (Rittmann, 1965) or DDF [*"deep dykes fed"*, (Corsaro et al., 2009)], are characterized by moderately to highly explosive activity, and are fed by magma rising through deep dykes, bypassing the central conduits region (Corsaro et al., 2009): they emit the least evolved (generally low porphyric and plagioclase-free) and undegassed products, offering the possibility to study the most primitive magmas. Between these eruptions (fig. 2.2b):

- **Mt Maletto** and **Mt. Spagnolo** eruptions [15-5 ky BP, (Armienti et al., 1988; Kamenetsky and Clocchiatti, 1996; Correale et al., 2014, Corsaro and Metrich, 2016)];
- **FS** eruption [~4 ky BP, (Coltelli et al., 2005, Kamenetsky et al., 2007)];
- **Montagnola** [1763, (Miraglia, 2002; Corsaro et al., 2009; Correale et al., 2014)];

- **Mts. De Fiore** [1974, (Corsaro et al., 2009; Correale et al., 2014)];
- and the recent **2001** and **2002/2003** eruptions (Métrich et al., 2004, Spilliaert et al., 2006a, 2006b; Corsaro and Métrich, 2016).

In historical times, and to a higher extent in the last decades, the volcanic activity of Mt. Etna became more frequent and more explosive as well, with increasing eruptive rate and gas emissions (Métrich et al., 2004; Allard et al., 2006).

Many geochemical features suggest another significant variation in the erupted trachybasalt since the 1971 eruption, considered as a benchmark in the recent magmatism of Mt. Etna. The composition of the eruptive products became more enriched in alkalis (K, Rb, Cs), and radiogenic Sr and B (Armienti et al., 2004; Métrich et al., 2004), so the affinity changed from sodic to potassic. This enrichment was inferred being due to the interaction between a HIMU-type mantle source and an enriched component (EM1), which could be a slab-derivated component (Schiano et al., 2001) or slab-derived fluids enriched in $\delta^{11}B$ (Tonarini et al., 2001; Armienti et al., 2004). Another hypothesis implies magma contamination with the uprising supercritical fluids carrying alkali and chlorine (Ferlito and Lanzafame, 2010; Ferlito et al., 2014). This new magma would have gradually mixed with and replaced the former resident magma.

2.3. Studied eruptions

Here, a brief description about the eruptions and the products selected for this PhD study.

Essentially the studied samples are primitive and more evolved lavas or pyroclastic products belonging to the Mongibello period (last 15 ky BP), from both ancient and very recent eruptions. These products have been sampled by INGV personal for previous studies (references are given in the following sessions).

2.3.1 Monte Spagnolo eruption

The Monte Spagnolo scoria cone is located about 6 km north of the present-day central crater (fig. 2.3a).

The studied eruption occurred after the Ellittico caldera collapse (~15 ky BP) and before the FS eruption (3930±60 BP). Armienti et al. (1988), Kamenetsky and Clocchiatti (1996) defined this eruption as *eccentric*, producing sub-aphyric alkali basaltic magma. Due to its mineralogical assemblage, principally olivine (Fo_{74-89}) and clinopyroxene, and to its radiogenic Sr and Nd composition, Mt. Spagnolo lava is considered as one of the most primitive product erupted in Etnean history (e.g., Kamenetsky and Clocchiatti, 1996; Correale et al., 2014). For its primitive character, and for the lack of information about volatile content in Mt. Spagnolo magma, the products of this eruption were chosen for the melt inclusions study. Mt. Spagnolo lava was also preferred as starting material for the experimental study.

The studied products, sampled in a lava flow, were previously investigated in Correale et al. (2014), for Sr-Nd and He isotopes.

2.3.2 FS eruption

FS eruption represents an important lithostratigraphic marker in the Etnean stratigraphy (Coltelli et al., 2005). The tephra deposit is located in the north flank of the volcano (fig. 2.3a), and reaches the thickness of 110 cm at 7 km from the summit craters. This suggests that a high (18-20 km) eruptive column was generated during a high explosive (sub-Plinian) activity [the volcanic explosive index VEI =4 (Walker, 1973)]. It was fed by a volatile-rich magma, with picritic composition [MgO ~ 13 wt.%, (Kamenetsky et al., 2007)]. The high contents of Ni (~250 ppm) and Cr (~900 ppm) corroborate the primitive character of this melt (Pompilio et al., 1995). Conversely, the high volatile content and the unusual enrichment of LILE in feeding magma suggest addition of fluids in the source zone. The high H_2O content of this picritic magma increases the magma buoyancy (Corsaro and Pompilio, 2004b) ensuring fast ascent, with the consequent vigorous degassing responsible of the explosive nature of this eruption (Coltelli et al., 2005).
The FS tephra chosen for the melt inclusions study, were previously studied in Correale et al. (2014) for Sr-Nd and He isotopes.

2.3.3 The 2002/2003 eruption

This flank eruption began on 27 October 2002, one year later the 2001 eruption, and finished on 28th January 2003. During this eruption, different fractures on the South rift (the same of the 2001 eruption) and on the Northeast rift were activated (Patanè et al., 2003; Andronico et al., 2005; Spilliaert et al., 2006; fig. 2.3a). Also the summit craters were active, with fire fountain and strombolian activity. The particularity of this eruption is the emission of two different magmas. A trachybasaltic lava, partially degassed, containing plagioclase phenocrysts was emitted from the NE rift, similar to the evolved trachybasalt plagioclase-rich produced from the summit crater, and the 2001 upper vent fissure eruption [> 2700 m a.s.l; (Métrich et al., 2004; Spilliaert et al., 2006; Corsaro et al., 2007)]. Conversely, undegassed basaltic lava flows and tephra (plagioclase-free) were produced from the S-rift, similar to the products of 2001 lower vent fissure eruption located along the lower southern flank [2600-2100 m a.s.l.; (Andronico et al., 2005; Corsaro et al., 2007)]. The latter products can be linked to a portion of the plumbing system deeper than that producing the trachybasalt of the northeast rift (Métrich et al., 2004; Rizzo et al., 2006; Spilliaert et al., 2006). Melt inclusions from this eruption have been already characterized for chemical composition and volatile content (Spilliaert et al., 2006), suggesting that the activity was fed by the ascent of primitive, volatile-rich (~4 wt %) basaltic magma. The observed CO_2 excess is ascribed to the magma flushing and dehydatation by a CO_2-rich gas phase of deeper derivation (e.g. Spilliaert et al., 2006).

COSPEC measurements indicate for SO_2 a total bulk output of ~$8.6x10^8$ kg, during the whole eruption (Caltabiano et al., 2003).
In this work, only the most primitive and undegassed tephra products from the South rift were studied (fig. 2.3a). The same products have been previously caractherized for the isotope signature of noble gas by Rosciglione (2008).

2.3.4 The 2006 eruption

This eruption started on 14th July and ended on 12th December of 2006. The activity took place on three new vents opened along the flank of the South East crater (SEC), producing several tephra cones and lava flow (fig. 2.3b), while lava fountaining occurred on the summit crater. It is therefore called sub-terminal eruption.

Melt and fluid inclusions were already characterized for volatile and trace elements abundance by Collins et al. (2009) and Schiavi et al. (2015). The observed CO_2 enrichment in the 2006 melt inclusions was explained as the consequence of a gas fluxing, derived from degassing at depth of a more primitive magma, or of the recirculation of degassed melt and subsequent mixing with a more primitive, undegassed melt (Collins et al., 2009).
For melt inclusions study, we used tepha sample, previously caractherized for the isotope signature of noble gas by Rosciglione (2008).

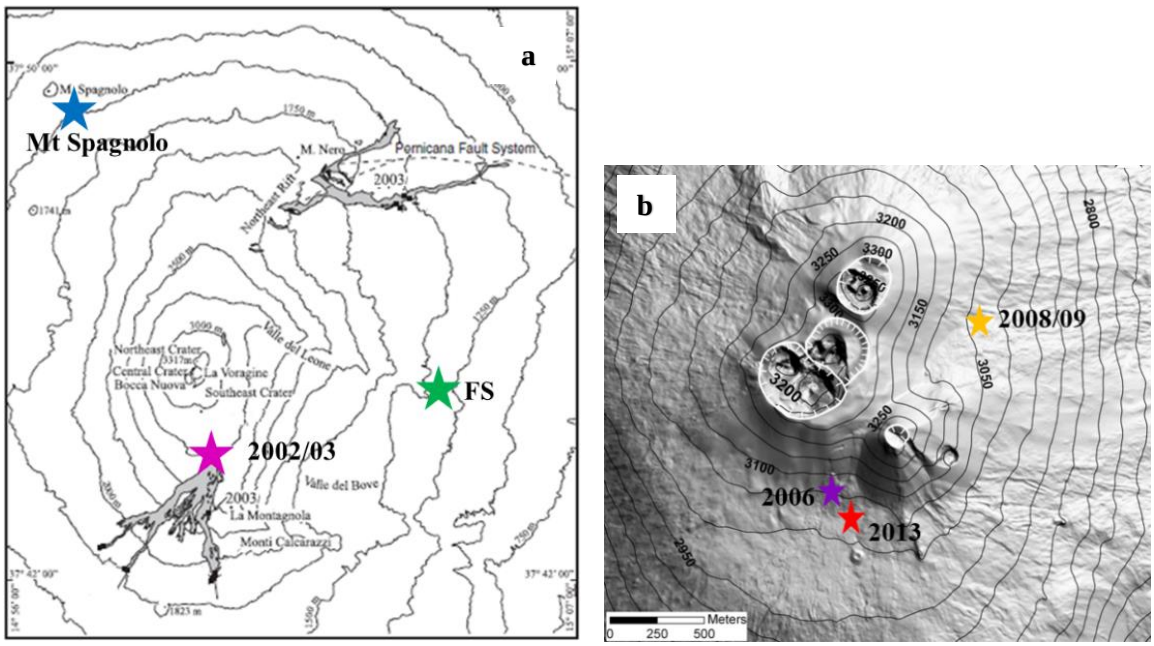

Fig. 2.3 - a) Etna map (from Coulson et al., 2011) and b) DEM (Digital Elevation Model) image of the summit area, with the sampling site.

2.3.5 The 2008/2009 eruption

This flank eruption began on 13th May 2008 and lasted until on 6th July 2009 (Bonaccorso et al., 2011; Corsaro and Miraglia, 2014). The eruption started with the opening of eruptive fissures propagating SE from the summit craters towards the western wall of the *Valle del Bove* (2620 m asl). From the lower portion of the eruptive fissures lava flows expanded in the *Valle del Bove* (Bonaccorso et al., 2011), reaching, 2 months after, the length of 6 km (James et al., 2012). Some intense explosion occurred also in the North East Crater (NEC). Tephra produced by the explosive activity, sampled by the INGV personal for other study, are preferred for this melt inclusion study.

2.3.6 The 2013 eruption

The 2013 is an intense eruptive year. After a rest period lasted 10 months, 19 paroxysms occurred at the New South East Crater (NSEC). Each episode was characterized by lava fountains and lava flows (fig. 2.3b) emission from fractures opened mostly along the NSEC cone. In 2013 it is noteworthy also the strombolian activity that occurred at Bocca Nuova crater (BC) and also the reactivation of the Voragine crater after 13 years. The lava flow associated at one paroxysm occurred on April 2013 was sampled by the INGV personal for this and other studies.

3. Experimental and analytical methods

The routinary petrographic methodologies (polarizing microscope, scanning electron microscope, electron microprobe) and more sophisticated methods were used during the PhD research activities. Each method required a different procedure of sample preparation. In many cases, the best analytical conditions were achieved through the collaboration with technicians and researchers with specific skill on the use of the instruments.

In this chapter (and appendix), basic information for used methodology is given, providing major details for some of those which required more technologically advanced procedures and longer set-up time.

3.1. Experimental strategy

Experiments were focused on the determination of sulfur solubility in Etna basalts, and were carried out using a vertically operating, internal heated pressure vessel (IHPV) at the ISTO.

For all the experiments, platinum capsules, 2 cm long and 2.5 mm inner diameter, were used. The use of platinum capsules presents both advantages and disadvantages. The advantages are that platinum capsules resist at high temperature (> 1050 ° C), and that the reaction between sulfur and this noble metal is less important with respect to the other capsules (such as AuPd, Au, AgPd). The disadvantage is that platinum capsules react with iron to form a Fe-Pt alloy (Jugo et al., 2005), and lower the Fe content of the melts during the experiment. However, this iron loss was minimized by adding iron to the starting material during the capsule preparation.

Mt. Spagnolo lava (one of the most primitive basalts erupted at Mt. Etna) was used as starting material. The rock was finely ground and then melted in a Pt crucible at 1400 °C, at atmospheric pressure for 3 hours and then rapidly quenched, in order to produce a degassed crystal- and bubble-free starting glass.

The average composition of the starting glasses, used for experimental runs, was determined by microprobe analysis and is given in table 3.1.

The glass was then crushed with acetone inside an agate mortar, and stored in an oven. About 50 mg of powdered starting material was loaded in Pt capsules, together with iron and volatiles ($H_2O \pm CO_2 + S$), added in different proportions (table 3.2). Iron was added as FeO (0 to 6 %) to minimize the iron loss and to study the effect of iron on sulfur content. Sulfur was added as elemental sulfur (1-4 wt.%). Distilled H_2O was added in the capsules, in order to attain water saturation. In some capsule (runs with $X_{H_2O} = 0.75$), CO_2 was also added as hydrous oxalic acid, to evaluate the effect of CO_2 on sulfur solubility.

Before filling the capsule, one end of the capsule was sealed. Then starting glass, FeO and volatiles were loaded, weighing every time the capsule, to check for the relative amounts. After loading, the other end of the capsule was sealed and the capsule was weighted to check for volatile lost.

Up to 4 capsules for each experiment run were placed in the hot spot of the molybdenum furnace (fig. 3.1), inside a Pt cage hung by a Pt or Re wire (0.2 and 0.1 mm diameter).

Mt. Spagnolo basalt, n=139		
oxide	wt.%	±
SiO_2	48.91	0.38
TiO_2	0.44	0.13
Al_2O_3	14.09	0.39
FeO	9.30	0.40
MnO	0.17	0.10
MgO	9.29	0.57
CaO	11.61	0.15
Na_2O	3.36	0.20
K_2O	1.27	0.10
P_2O_5	0.59	0.13

Table 3.1 - Composition of the starting glasses, determined by electron microprobe (number of analysis = 139). Major elements abundance were normalized to 100% (± = standard deviation of each oxide, 1σ).

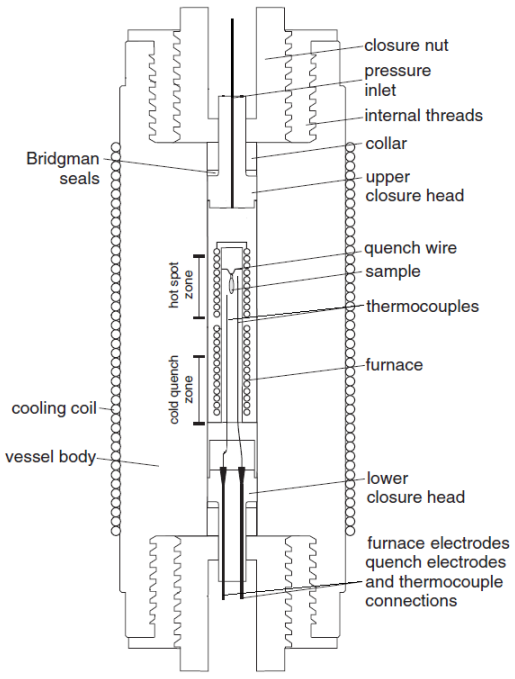

Fig. 3.1 - Sketch of a vertically operating, internal heated pressure vessel (IHPV), after Berndt et al. (2002).

Date of runs	charge number	FeO added	S added	X_{H_2O} added	X_{CO_2} added	P_{tot} (MPa)	T (°C)	time (hours)
17/02/2015	#1	0	1	1		180	1200	3
	#2	2	1	1		180	1200	3
	#3	3	1	1		180	1200	3
	#5	2	1	0.75	0.25	180	1200	3
27/03/2015	#1	4	2	1		210	1200	3
	#2	4	4	1		210	1200	3
	#3	4	2	0.75	0.25	210	1200	3
	#4	4	4	0.75	0.25	210	1200	3
27/04/2015	#1	5	2	1		193	1200	3
	#2	6	2	1		193	1200	3
	#3	5	4	1		193	1200	3
	#4	5	4	0.75	0.25	193	1200	3
29/02/2016	#1	4	2	1		200	1200	< 2
	#2	4	4	1		200	1200	< 2

Table 3.2 - Summary of the experimental conditions. (The added components are expressed in wt.%.)

The temperatures of the inner part of the furnace were checked by two S-type thermocouples in two points corresponding to the top and the bottom of the capsules. The temperature gradient along the capsules was always less than 10°C. Ar was used as pressurizing medium and mixed with variable amounts of H_2 in order to vary oxygen fugacity (fO_2).

The experiments were performed at constant temperature (1200 °C) and pressure (180-210 MPa) and under oxidized conditions (0.2 < NNO < 1.7, NNO means Nickel - Nickel Oxide), to evaluate the effects of fO_2 on sulfur solubility. The experiment runs lasted 3 hours, assuming that equilibrium between basalt and fluid phase is reached after 2 h, under these conditions (e.g. Jugo et al. 2005).

Experiments were ended by a drop quench (Di Carlo et al., 2006): the thin suspension wire (Pt or Re) was melted by an electrical current, allowing the capsules to fall into the cold part of the vessel (<100°C). The estimated cooling rate was about 100°C/sec (Di Carlo et al., 2006).

The redox conditions for each capsule were monitored using the Co-Pd-O solid sensor method consisting of two pellets of metal Co, Pd and CoO mixtures (each one with different Co^0/Pd^0 ratio), placed in a Pt capsule in the presence of excess H_2O (Taylor et al., 1992). The analyses of the composition of the metallic alloys after the experiment allowed the fO_2 of the sensor to be determined (Pownceby and O'Neill, 1994). The fH_2 of the sensor (identical to the fH_2 of the capsules) was then obtained from the fO_2 determined as above, the a_{H_2O} was calculated from the H_2O wt.% in the melt using the model of Burnham (1979), the dissociation constant of water (Robie et al.,1979) and the fugacity of pure water at the experimental P and T (Ferry and Baumgartner, 1987; Holloway, 1987). The fO_2 of each charge was then calculated from the fH_2 and fH_2O determined as above.

Typical uncertainty on log fO_2 is between 0.12 and 0.47 log units, defined by calculating the log fH_2 in an interval of PH_2 = 1 bar, around the introduced PH_2. In details, these uncertainty

values are the standard deviation of 3 estimated log fH_2 calculated using the introduced PH_2 and two value of PH_2 of 0.5 bar higher and minor than that really introduced. Interestingly, this uncertainty increase with the decreasing of H_2 used, therefore this is major for the oxidized values.

3.2. X-ray fluorescence spectroscopy (XRF)

Major elements analyses of the whole rocks (wr) were performed by *X-ray fluorescence* spectroscopy at the Actlabs Laboratories in Canada.
The analyses were performed on fine powders (< 10 μm) of Etnean rocks obtained by mechanical grinding vessel at the ISTO. The powders were prepared and analyzed at the Canadian laboratory following internal procedures (Norrish and Hutton, 1969).
Cl and S in the whole rocks were determined by INAA (Instrumental Neutron Activation Analysis) and IR (infrared) methods, respectively.
Detection limits for this analysis are 0.01 wt.% for all majors and volatiles elements. Analytical uncertainty (1σ) for major elements is < 1 wt.% SiO_2 and Al_2O_3, < 2 wt.% for Fe_2O_3, MgO, CaO, Na_2O and K_2O, <5 wt.% for MnO, TiO_2 and Cr_2O_3 and 5-10 wt.% for P_2O_5.

3.3. Scanning electron microscope (SEM)

Natural and experimental glass samples were observed by two scanning electron microscopes (SEM): a Tescan MIRA 3 XMU situated at the BRGM (*Bureau de Recherches Géologiques et Minières*) and a Zeiss Merlin Compact at the ISTO (fig. 3.2a).
Olivine hosted melt inclusions were polished one by one using abrasive papers with different granulometry (1200, 2500, 4000 mesch; 9; 3; 1 μm). They were then washed in acetone and ethanol solutions, occasionally using an ultrasonic bath, and mounted in epoxy resin. Some melt inclusions were double-polished and stuck on a thin section using the epoxy resin. All samples were coated with a carbon film to increase the surface conductivity.
Images and semi-quantitative spectra were acquired using 25 keV (Tescan MIRA 3 XMU) and 15 keV (Zeiss Merlin Compact) electron energy.
SEM observations were fundamentals for selecting the crystal-free inclusions prior to other analytical steps, and for assessing the homogeneity of experimental glasses.

3.4. Electron microprobe (EMP)

The Cameca SX FIVE (fig. 3.2b) electron microprobe of the ISTO was used to analyze the major element compositions of:

- olivine crystals,
- melt inclusions,
- glass embayments,
- matrix glasses,
- oxides,
- sulfide globules,
- experimental glasses,
- Pt experimental capsules,

mounted in epoxy resin, polished and previously carbon coated.

Major element, S, Cl, and F analyses were carried out using a beam energy of 15 keV, 6 nA beam current and a peak counting time of 10 seconds for all element, except for S (60 sec). A focused beam of 1 µm was used for olivine crystals, while a defocused beam of 6 µm size was used for melt inclusions for reducing Na loss, of 6-12 µm for experimental glasses, and 2-6 µm beam size for sulfides globules (to prevent S loss) and matrix glasses (because of the small size of sulfide and the microlites crystals in the matrix).

Natural minerals and oxides were used as internal standard during the measurements (Na and Si were calibrated on albite, K on anorthoclase, Ca on anhydrite, P on apatite, Cl on vanadinite, Mg on MgO, Al on Al_2O_3, Fe on Fe_2O_3, Ti and Mn on $MnTiO_3$). S was usually calibrated on a barite crystal ($BaSO_4$); in some melt inclusions, S was also calibrated on S-bearing MORB glasses (GMR-K512: S = 1680 ppm, VG-2: S = 1480 ppm, CY82-2903: S = 1028 ppm) using a 25 nA current, a defocused beam of 20 µm, and a counting time of 120 sec.

Fig. 3.2 - a) Scanning electron microscope and b) electron microprobe at the ISTO-CNRS used for observations and analyses of the samples.

Detection limits for major elements are very low (between 0.03 wt% for MgO and 0.4 wt.% for FeO), for S and Cl they are 120-450 ppm and 240-900 ppm, respectively (depending on the analytical conditions). Analytical uncertainty (1σ) is < 1% for all major elements and < 500 ppm for volatiles.

Sulfide globules in natural samples were analyzed using the same analytical condition; S and Fe were calibrated on a pyrite standard, Co, Ni and Cu on Co, Ni and Cu metals.

Pt-capsules used for experimental runs were also analyzed to evaluate Fe and S lost into the capsule during the experiment, using a beam energy of 20 keV, and 30 nA beam current (used standards: pyrite for S and Fe, native Pt for Pt).

3.5. Secondary ion mass spectrometry (SIMS)

Volatile abundances and $^{34}S/^{32}S$ ratio in melt inclusions and experimental glasses were determined using the Cameca IMS 1270 (fig. 3.3) and the new IMS 1280 HR2 ion microprobes of the CRPG (*Centre de Recherche de Petrologie et Geochimie)* of Nancy. The analyses were performed in collaboration with Etienne Deloule and Johan Villeneuve. More exhaustive information about this technique is given in the appendix (A1).

The first step for SIMS analysis was the accurate preparation of the samples. Olivine hosted melt inclusions and experimental glasses were pressed into indium within an aluminum disk (fig. 3.3). Indium is preferred to epoxy resin, due to its lower intrinsic volatile content.

Because many samples were previously analyzed by electron microprobe, they needed to be extracted from epoxy before inserting into indium. After removing their carbon coating, samples were extracted from epoxy resin using dichloromethane, then washed with acetone and ethanol solutions, and inserted into indium following standard procedures used at CRPG.

The indium mounts were gold coated to increase their conductivity and introduced through the airlock system in the SIMS chamber, where samples were outgassed until a pressure of 10^{-8}-10^{-9} Torr was reached.

Volatile (H_2O, CO_2, S, Cl, F) contents were measured using a Cs^+ primary beam of 5 nA, with an Impact Energy of 20 kV. The acquisition, preceded by a 30 seconds pre-sputtering period (to clean the surface's sample), was done in 12-15 cycles. The signals for all volatiles ($^{12}C^-$, $^{16}O^1H^-$, $^{19}F^-$, $^{32}S^-$, $^{35}Cl^-$) were collected in mono-collection mode during the same analysis, in about 12 minutes.

Fig. 3.3 - Cameca IMS 1270 used for SIMS analyses at the CRPG of Nancy. In the left small picture the usual Al-disk fill with indium, prepared for the SIMS analysis.

The secondary beam consists of both ionized atoms, commonly used as analytes for volatile determinations ($^{12}C^-$, $^{19}F^-$, $^{32}S^-$, $^{35}Cl^-$), and ionized hydride molecules that create numerous interferences. A good mass resolving power (MRP) must be used to separate these interfering species. The MRP is given by M/ΔM, where ΔM is the peak's width of the mass M (of interest) at 10 % of its high. We used a MRP of 7000 for the analyses of volatiles species.

For accurate determination of the elemental abundances, the matrix of the sample must be known, and standard glasses with a matrix composition similar to that of the sample must be preferred.

The concentrations of all the volatiles (except H_2O) were calculated comparing the $X^-/^{28}Si^-$ * SiO_2 in the sample to that in the reference glass (figs. 3.4), where X^- represent the volatiles species ($^{12}C^-$, $^{19}F^-$, $^{32}S^-$, $^{35}Cl^-$). Differently, H_2O was normalized to OH^- (figs. 3.4).

The basalts N72 from Kamchatka and the KL2-G basalt from Kilauea were used as standard for H_2O and CO_2 (Shishikina et al., 2010; Jochum et al., 2006), while VG-2 and A99 standard glasses (Jarosewich et al., 1979; Witter et al., 2005) were used for S, Cl (also KL2-G) and F (table 3.3 - 3.4).

	SiO_2	TiO_2	Al_2O_3	FeO	MnO	MgO	CaO	Na_2O	K_2O	P_2O_5
KL2-G	50.50	-	13.30	10.70	-	7.35	10.90	2.35	0.46	0.23
N72	50.07	0.92	18.38	9.35	0.17	7.02	11.32	2.45	0.22	0.15
A99	50.94	4.06	12.49	13.70	0.15	5.08	9.30	2.66	0.82	0.38
VG-2	50.81	1.85	14.06	11.84	0.22	6.71	11.12	2.62	0.19	0.20
CY82 31-2V	49.06	1.16	16.9	7.54	0.09	9.28	12.06	2.63	0.11	-
CH98DR12	49.95	1.62	14.91	10.75	0.21	7.99	11.31	2.83	0.06	0.13
EW9325-09	54.44	1.39	15.34	8.37	0.12	7.59	8.67	3.53	0.26	0.14

Table 3.3 - Chemical composition (wt.%) of the standard glasses used for SIMS investigation. N72 (from Shishikina et al., 2010) and KL2-G (Jochum et al., 2006) was used for creating calibration curves for H_2O and CO_2; A99 and VG-2 (from Jarosewich et al., 1979) for S, Cl (also KL2-G) and F concentrations. CY82 31-2V (Chaussidon et al., 1991), CH98DR12 and EW9325-09 (the major elements abundance were determined by electron microprobe) were using for IMF calculation for $^{34}S/^{32}S$ acquisition.

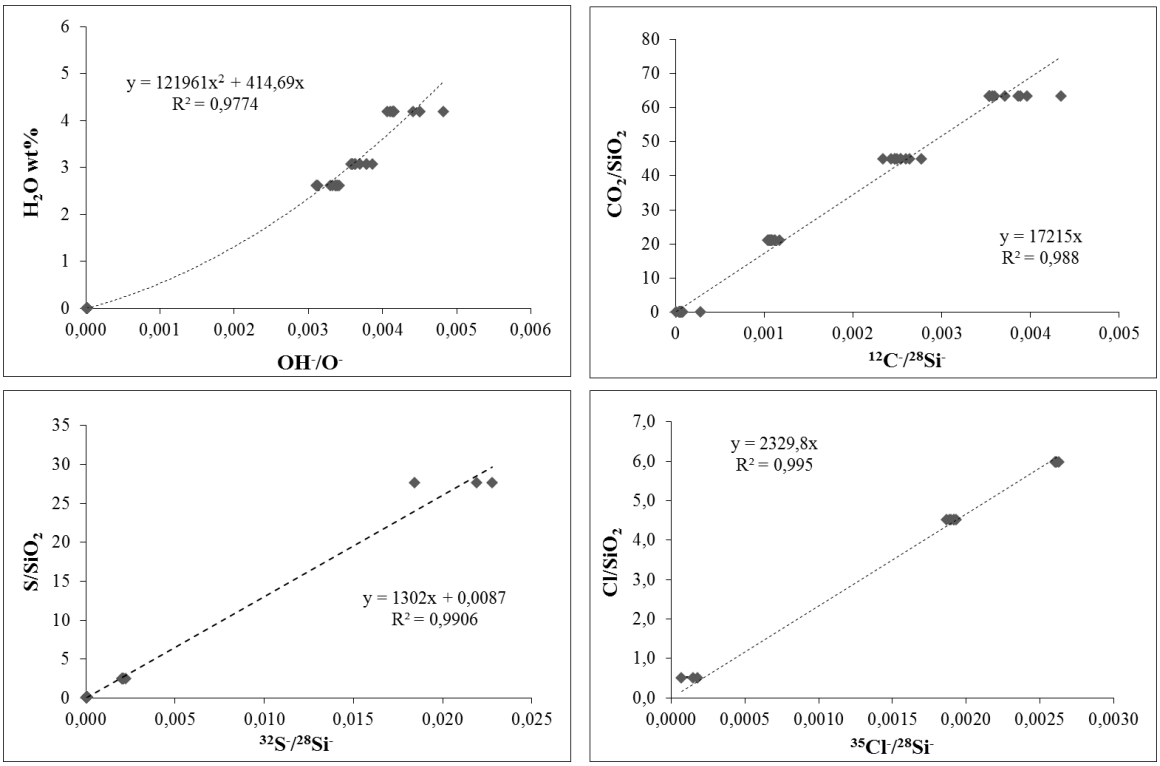

Fig. 3.4 - Calibration curves normalized to OH^- for H_2O and $^{28}Si^-$ for the other elements, used for the calculation of volatiles concentrations in Etnean MIs.

	H_2O (wt.%)	CO_2 (ppm)	S (ppm)	Cl (ppm)	F (ppm)
KL2-G	0.02	5.2	-	-	-
N72	0	0	-	-	-
N72-M34	5.70	375	-	-	-
N72-M35	4.20	1019	-	-	-
N72-M40	3.07	2183	-	-	-
N72-M43	2.52	3172	-	-	-
N72-M48	0.77	176	-	-	-
A99	-	-	130	230	225
VG-2	0.02	-	1406	304	288

Table 3.4 - Volatile concentrations in reference materials used for SIMS volatile acquisition. All N72 glasses are from Shishikina et al. (2010); A99 and VG-2 are from Witter et al. (2005).

$^{34}S/^{32}S$ ratios in melt inclusions and experimental glasses were acquired using a 20 kV Cs^+ primary beam of 1.5-5 nA, focused to 15-25 µm size spots. The pre-sputtering time was 50-150 sec. The acquisition time was 6-12 minutes during 30-50 cycles. Essentially, the same analytical conditions were used during the three sessions (November 2014, July and October 2015), except for the beam intensity and some secondary parameters as the number of cycles and the pre-sputtering time that varied.

Multicollection acquisitions were realized, using an electron multiplier for the less abundant isotope. The yield of the ions conversion into electrons decreases with time. Standard glasses and samples have therefore to be measured using the same conditions to correct this effect.

Moreover, the electron multiplier produces a dead time between two pulses, during which no electrical signals are emitted. The dead time is determinated doing a double acquisition in the multicollection mode, one with electron multiplier and the other without it: the dead time is the time at which the $^{32}S/^{34}S$ determined in the two acquisitions is the closest. The $^{32}S/^{34}S$ ratio is finally corrected for this dead time.

The isotopic ratio measured by ion microprobe is usually affected by an instrumental mass fractionation (IMF). It represent the difference between the expected isotopic ratio (δ_{real}) and the measured value (δ_{meas}):

$$IMF = \delta_{inst} = \delta_{meas} - \delta_{real}$$

Three MORB glasses [CY82-31-2V, CH98 DR12 and EW9325-09, (Chaussidon et al., 1991; Labidi et al., 2012)] were used as reference standards for calibrating the IMF and to calculate the dead time (table 3.5).

The calculated dead time was 66-70 ns for all session. The IMF was variable during the 3 sessions (7.9-10.9 ‰ in November 2014, 2.8-3.8 ‰ in July 2015, 4.5-9.5 ‰ in October 2015, fig. 3.5).

	S (ppm)	$\delta^{34}S$‰ (expected)	$\delta^{34}S$‰ (measured) November 2014	n.	$\delta^{34}S$‰ (measured) July 2015	n.	$\delta^{34}S$‰ (measured) October 2015	n.
CY82 31-2V	877	+1.30	11.32±1.37	36	-		-	
CH98DR12	1039	-1.20	-		2.30±1.22	18	-8.97 ±1.31	74
EW9325-09	625	+1.05	-		4.50 ±0.91	23	-6.40 ±1.70	53

Table. 3.5 - S content, predicted $\delta^{34}S$ and measured $\delta^{34}S$ for the MORB glasses (Chaussidon et al., 1991; Labidi et al., 2012 and Cartigny, personal communication) used for $\delta^{34}S$ determination (n= number of analyses performed during the entire analytical session). S content in EW9325-09 was determined by electron microprobe at the ISTO.

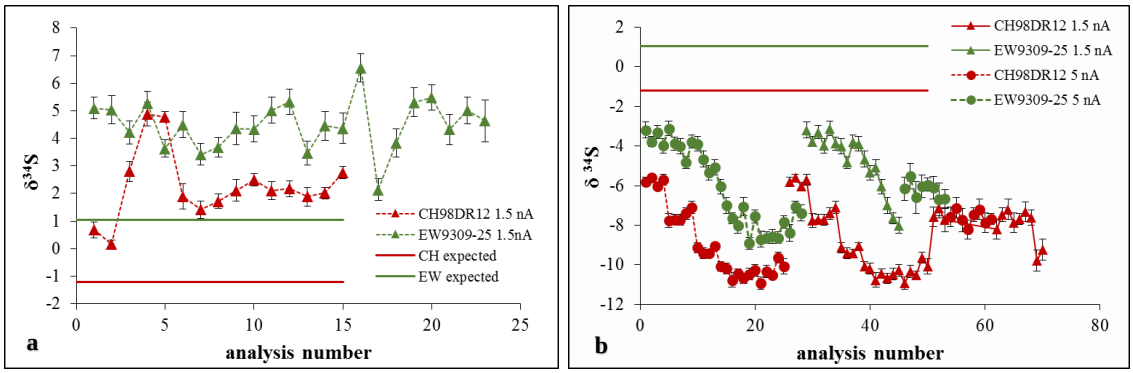

Fig. 3.5 - $^{34}S/^{32}S$ measured (and corrected for dead time) in the standard glasses: CH98 DR12 and EW9309-25 during the analytical sessions of a) July (Intensity of primary beam is 1.5 nA) and b) October 2015 (Intensity of primary beam is 1.5 and 5 nA). The expected values are also plotted for comparison.

3.6. Fourier transform infrared (FT-IR) spectroscopy

H_2O and CO_2 contents in some melt inclusions and in experimental glasses were estimated through transmission Fourier transform infrared spectroscopy (FT-IR) using a Nicolet 760 Magna spectrometer equipped with an IR microscope and a MCT detector at the ISTO.

The samples were accurately prepared and double-polished to obtain small chips of olivine hosted melt inclusions of 18-72 µm thickness and glasses of 7-52 µm thickness. For each sample, at least 2 (up to 7 for experimental glasses) spectra were acquired to check the homogeneity of H_2O and CO_2 dissolved contents.

Absorption spectra were acquired in the range 1000-6000 cm^{-1} with 128/560 scans and a resolution of $4cm^{-1}$, using a Globar internal IR source and a KBr beam-splitter.

The abundances of H_2O and CO_2 dissolved in glasses and MIs were calculated from the absorbancies of the 3530 cm^{-1} (OH^- stretching vibration) and 1430 cm^{-1} (CO_3^{2-} stretching) bands, respectively (fig. 3.6), using the modified Beer-Lambert law (Stolper, 1982):

$$C = ((MW*A)/(d*l*\varepsilon)*100)$$

in which *MW* is the molecular weight (g/mol) of each volatile specie, *A* is the absorbance (i.e. the height of the considered peak), *d* is the melt density (g/l), ε is the molar absorption coefficient (l/cm*mol), *l* is the optic path (i.e. the thickness of the sample, in cm) and *C* is the concentration of volatile specie.

Anhydrous melt density was evaluated using the starting glass of experimental runs (of Mt. Spagnolo composition) by the Archimedean method. Dry glass chips (0.45-1.5 g) were weighed successively in air and ethanol, using a Mettler balance equipped with a density accessory kit at the ISTO laboratory. The obtained dry density was used to calculate the hydrous density value for each sample (MIs and glasses) through the method of Richet et al. (2000), considering the amount of water dissolved in the glass [assuming that dissolved CO_2 does not affect density to any measurable extent (Lange,1994)].

An molar extinction coefficient (ε) of 63 l/mol*cm^{-1} was used for the 3530 cm^{-1} band (H_2Otot) (Dixon and Pan, 1995), while the coefficient for 1430 cm^{-1} band (CO_3^{2-}) was calculated for both MIs (300-416 L/mol*cm^{-1}) and experimental glasses (380 L/mol*cm^{-1}) using the Dixon and Pan (1995) method, which considers the Na/(Na+Ca) molar ratio of the melt.

The absorbancies of the carbonate doublet were estimated after subtraction of a spectrum of a CO_2-free glass (Dixon and Pan, 1995), with similar composition and H_2O content [fig. 3.6; (Lesne et al. 2011)].

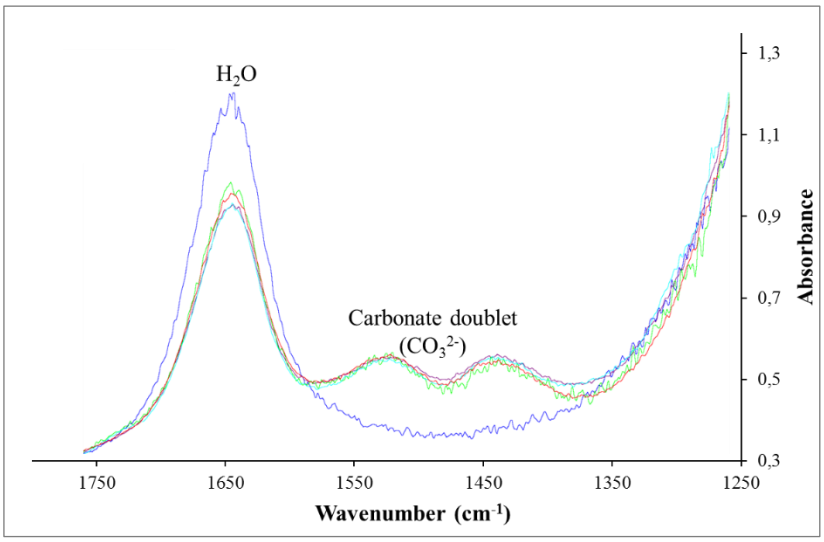

Fig. 3.6 - Example of infrared spectra in the region 1750-1000 cm^{-1} and the background correction (blue spectrum) for carbonate absorbance peek.

3.7. X-ray absorption near-edge structure (XANES) spectroscopy

The experimental glasses and the double polished melt inclusions were analyzed on the I18 beamline at Diamond Light Source (DSL) in the Oxfordshire in collaboration with Yves Moussallam and Nial Peters. We investigated the pre-edge structure of the Fe K-edge by synchrotron X-ray spectroscopy, in order to determine the $Fe^{3+}/\sum Fe$ ratio in 49 Etnean melt inclusions, 14 matrix glasses or embayments, and 13 experimental glasses.
The DLS is a 3 GeV third generation storage ring, and the synchrotron is a 24-cell machine with provision for about 40 beamline (Mosselmans et al., 2009). Measurements were carried out using the methods described in Moussallam et al. (2014) and Shorttle et al. (2015).
More exhaustive information about this technique is given in the appendix (A2).

XANES analyses at the Fe-edge were conducted over the energy range 7020-7500 eV, using a 2 micron (horizontal) x 2.5 micron (vertical) beam size. During the analytical session, the storage ring was operating at 3 GeV with an electron current of about 300 mA. The beamline utilizes liquid nitrogen - cooled double-crystal monochromator with silicon crystals, and Si (333) reflection was used to increase the energy resolution. Measurements were performed in fluorescence mode and the used energy-dispersive detector was a 6-element SGX Sensortech silicon drift detector positioned at 90 degrees with respect to the incident X-ray beam. The sample was positioned with the normal to the surface being at 10 degrees to the incident X-ray beam in order to improve the horizontal resolution and reduce potential self-absorption effects. The incident X-ray beam was filtered with Al foils (varying in thickness from 0.025 to 0.1 mm) with the aim to keep the detector count rate within the linear response region and to remove the effect of beam damage on the sample. The energy step sizes and dwell times used are given in Table 3.6.

In the acquired spectrum, the pre-edge region (7110-7118 eV) corresponds to the 1s => 3d electronic transition (fig. 3.7). This region of the spectra is very sensitive to the valence state of Fe (Wilke et al., 2005). The pre-edge position and the height of the two peaks composing it vary as a function of the Fe valence state (e.g. Wong et al., 1984; Bajt et al., 1994). These variations are used to calibrate the $Fe^{3+}/\Sigma Fe$ in unknown samples.

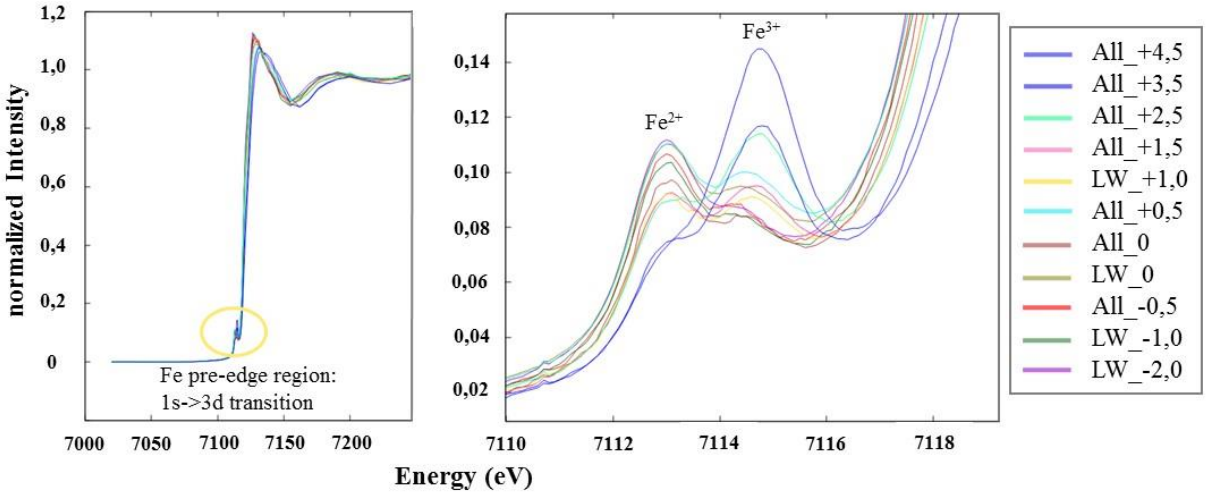

Fig. 3.7 - Edge-step normalized XANES spectra (drift-corrected in energy) for NMNH 117393 standard glass. The right plot shows the pre-edge region for Fe (related to 1s->3d metal electronic transition) in the same reference glasses. In the legend the names of the standard glasses (from Cottrell and Kelley, 2009), which indicate the relative fO_2, expressed as log units from the QFM buffer.

The pre-edge region was fitted using a combination of a linear function and a damped harmonic oscillator function (DHO) to fit the baseline (Cottrell et al., 2009; Moussallam et al., 2014). The centroid (area-weighted average) of the background-subtracted pre-edge region was then calculated and parametrised against the Fe valence state.

Energy range (eV)	Step size (eV)	Dwell time (s)
7020.0–7100.0	10	0.25
7101.0–7104.0	1	0.5
7104.1–7109.9	0.5	1
7110.0–7117.9	0.1	5
7118.0–7119.4	0.1	1
7119.5–7127.0	0.5	1
7128.0–7144.0	1	1
7148.0–7408.0	5	1
7410.0–7500.0	10	0.5

Table 3.6 - Acquisition parameters used during Fe K-edge XANES analysis

Smithsonian Expt.	log fO_2	ΔQFM	Single session drift corrected centroid energy (eV)	Cross session drift corrected centroid energy (eV)	$Fe^{3+}/\Sigma Fe$ predicted	$Fe^{3+}/\Sigma Fe$ measured by Mossbauer	centroid energy measured by XANES [a]
LW_−20	-8.72	-2.00	7112.108	7112.112	0.066	0.088	**7113.19**
LW_−10	-7.72	-1.00	7112.156	7112.156	0.099	0.130	**7113.26**
AII_−05	-7.20	-0.48	7112.211	7112.217	0.123	0.138	**7113.26**
LW_0	-6.68	0.01	7112.299	7112.299	0.149	0.162	**7113.34**
AII_0	-6.71	0.02	7112.276	7112.279	0.150	0.147	**7113.30**
AII_05	-6.24	0.48	7112.366	7112.355	0.181	0.194	**7113.39**
LW_10	-5.72	1.00	7112.438	7112.439	0.211	0.235	**7113.49**
AII_15	-5.24	1.48	7112.518	7112.511	0.257	0.247	**7113.53**
AII_25	-4.25	2.47	7112.730	7112.740	0.350	0.356	**7113.83**
AII_35	-3.22	3.50	7112.941	7112.937	0.462	0.484	**7114.09**
AII_45	-2.20	4.52	7113.168	7113.163	0.575	0.611	**7114.33**

Table 3.7 - Smithsonian NMNH 117393 basalt used for XANES calibration. Data from Cottrell et al. (2009). [a] centroid energy of the peaks acquired in this study by XANES.

Fe fluorescence spectra were acquired for the NMNH 117393 basalt rocks used for calibration (table 3.7). These experimental standard glasses, loaned by the Smithsonian Institution National Museum of Natural History, were equilibrated at 1350 °C at 1 atm, in a large fO_2 range (QFM -2.0 to QFM +4.5), and their $Fe^{3+}/\Sigma Fe$ ratios were measured by Mossbauer spectroscopy (Cottrell et al., 2009).
Almost 50 melt inclusions were analyzed, but many spectra showed olivine contamination (fig. 3.8), therefore they were not further considered.

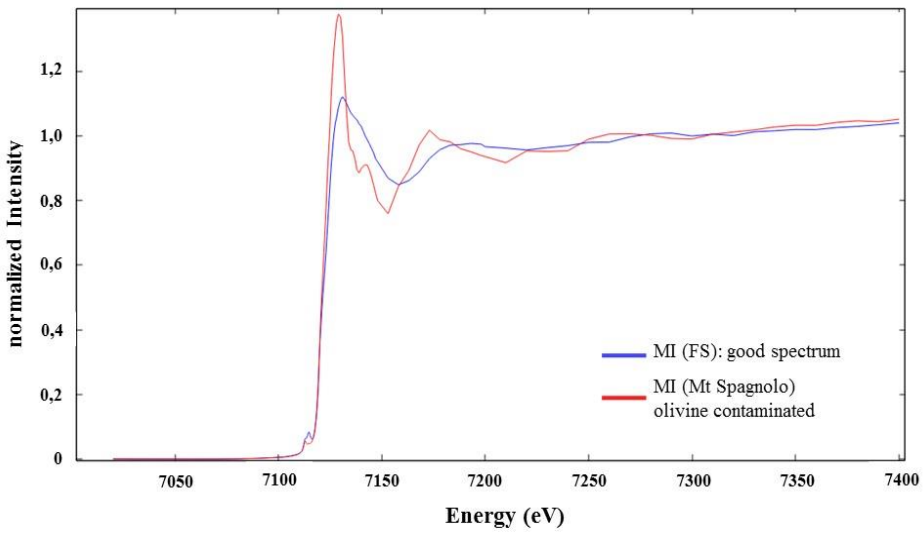

Fig. 3.8 - Examples of Fe K-edge spectra without (blue) and with (red) host olivine contamination (FS and Mt. Spagnolo melt inclusions).

4. RESULTS

In this chapter, we report the principal results obtained for the investigated melt inclusions and for the S-bearing experimental glasses, using the several methods described in the previous chapter.

4.1. Whole rocks composition

Major element composition of the studied lavas and tephras is reported in table 4.1 and plotted in a Total Alkali Silica (TAS) diagram (fig. 4.1). The rocks from 2006, 2008/2009 and 2013 eruptions present a trachybasaltic composition, the lavas from Mt. Spagnolo and 2002/2003 eruptions are at the limit between the basaltic and the trachybasaltic fields, while the FS tephras present a basaltic composition. All the rocks are in the field defined by historical alkaline lavas (e.g., Clocchiatti et al., 2004; Corsaro and Pompilio, 2004a; Métrich et al., 2004; Coltelli et al., 2005; Corsaro et al., 2006, 2009; Spilliaert et al., 2006a; Viccaro et al., 2006; Viccaro and Cristofolini, 2008; Correale et al., 2014), except the FS tephra, which are alkali-poorer and MgO-richer even than the oldest tholeiitic lavas (fig. 4.1 and 4.2). Due to their very high MgO content (up to 17.9 wt.%) FS tephras are generally classified as picritic basalts. They represent the most primitive magma that have been erupted at Mt. Etna [highest CaO/Al_2O_3 ratio and Mg number (Mg# = 100 x $Mg/(Mg+Fe_{tot})$, lowest alkali and silica contents; Table 4.1, figs. 4.1 and 4.2]. Both MgO and CaO/Al_2O_3 decreases from FS to Mt. Spagnolo composition and toward the most recent trachybasaltic compositions (fig. 4.2). The trachybasaltic lavas of Mt. Spagnolo eruption have a Na-alkaline affinity, while those erupted during 2002/2003, 2006, 2008/2009 and 2013 have a K-alkaline affinity, confirming the shift of the Etnean magmatism toward more alkaline potassic compositions observed in the last decades (e.g., Clocchiatti et al., 2004; Métrich et al., 2004; Corsaro and Métrich, 2016).

The SiO_2 content (46.5-48.4 wt.%) is very similar for all the studied rocks (Table 4.1) as, to a lesser extent, the Fe_2O_3* (Fe_2O_3 total = 10.3-12.20 wt.%) and CaO (9.9-11.7 wt.%) contents (figs. 4.3 b-d). Al_2O_3 varies from 9.3 wt.% in FS tephra to 17.6 wt.% in the most recent trachybasalts (fig. 4.3c). Using K_2O as differentiation index (figs. 4.3), the investigated products show a decreasing trend of MgO and increasing trends of Na_2O, Al_2O_3, Fe_2O_3 and TiO_2 with magma differentiation, from FS toward the most recent products. Essentially, FS rock with the lowest alkali and silica contents (fig. 4.1), the highest CaO/Al_2O_3 ratio (= 1.23; fig. 4.2) and Mg number (= 77.5; Table 4.1), represents the most primitive magma that have been erupted at Mt. Etna.

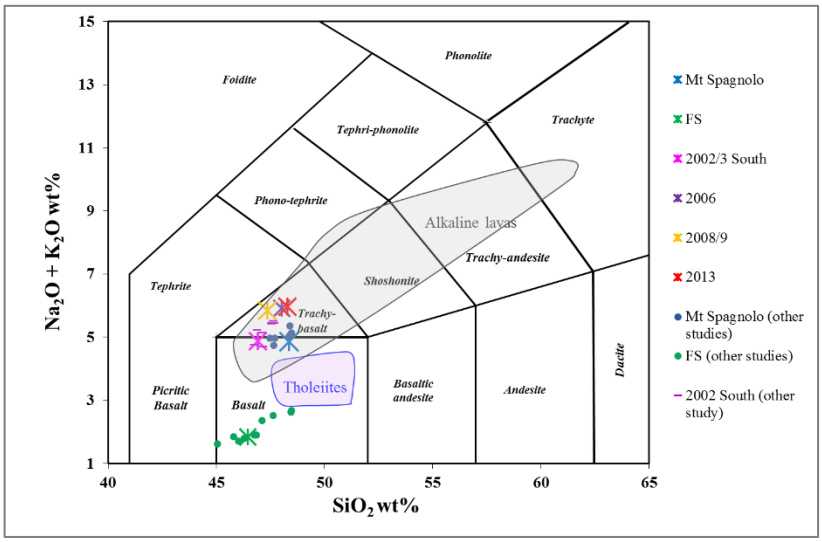

Fig. 4.1 - Total alkali versus silica classification diagram (Le Maitre, 2002) for the studied rocks. Also shown are whole rock compositions from the literature, for Mt. Spagnolo (Kamenetsky and Clocchiatti, 1996; Correale et al., 2014; Corsaro and Metrich, 2016), FS (Kamenetsky et al., 2007; Correale et al., 2014; Corsaro and Metrich, 2016) and 2002/2003 eruptions (Spilliaert et al., 2006a). The colored fields represent the oldest tholeiitic lavas (e.g., Kamenetsky and Clocchiatti, 1996; Tanguy et al., 1997; Armienti et al., 2004) and the alkaline ones (e.g., Clocchiatti et al., 2004; Coltelli et al., 2005; Corsaro and Pompilio, 2004a; Corsaro et al., 2006, 2009; Métrich et al., 2004; Spilliaert et al., 2006a; Viccaro et al., 2006; Viccaro and Cristofolini, 2008).

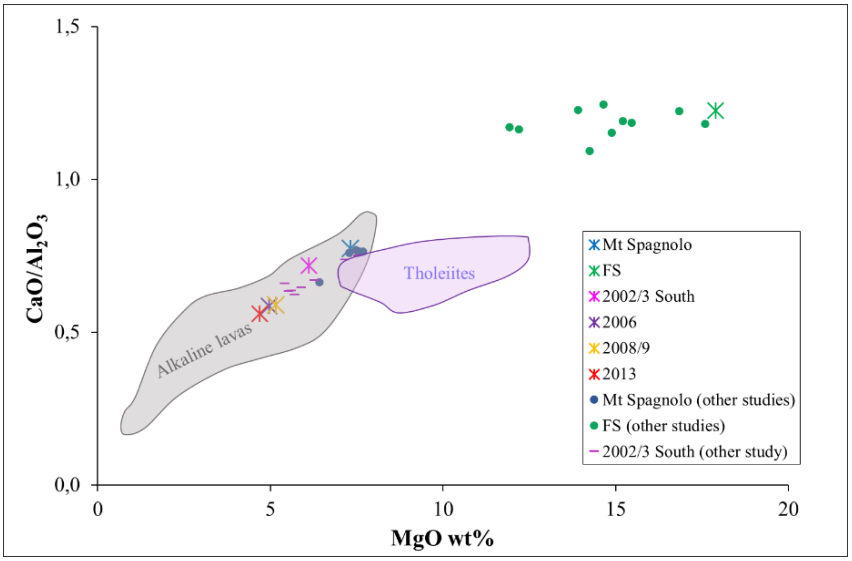

Fig. 4.2 - CaO/Al_2O_3 ratio versus MgO for whole rock studied samples. The colored fields (from Correale et al., 2014) represent the oldest tholeiitic lavas and the more recent alkaline ones (literature data are the same as in caption of fig. 4.1).

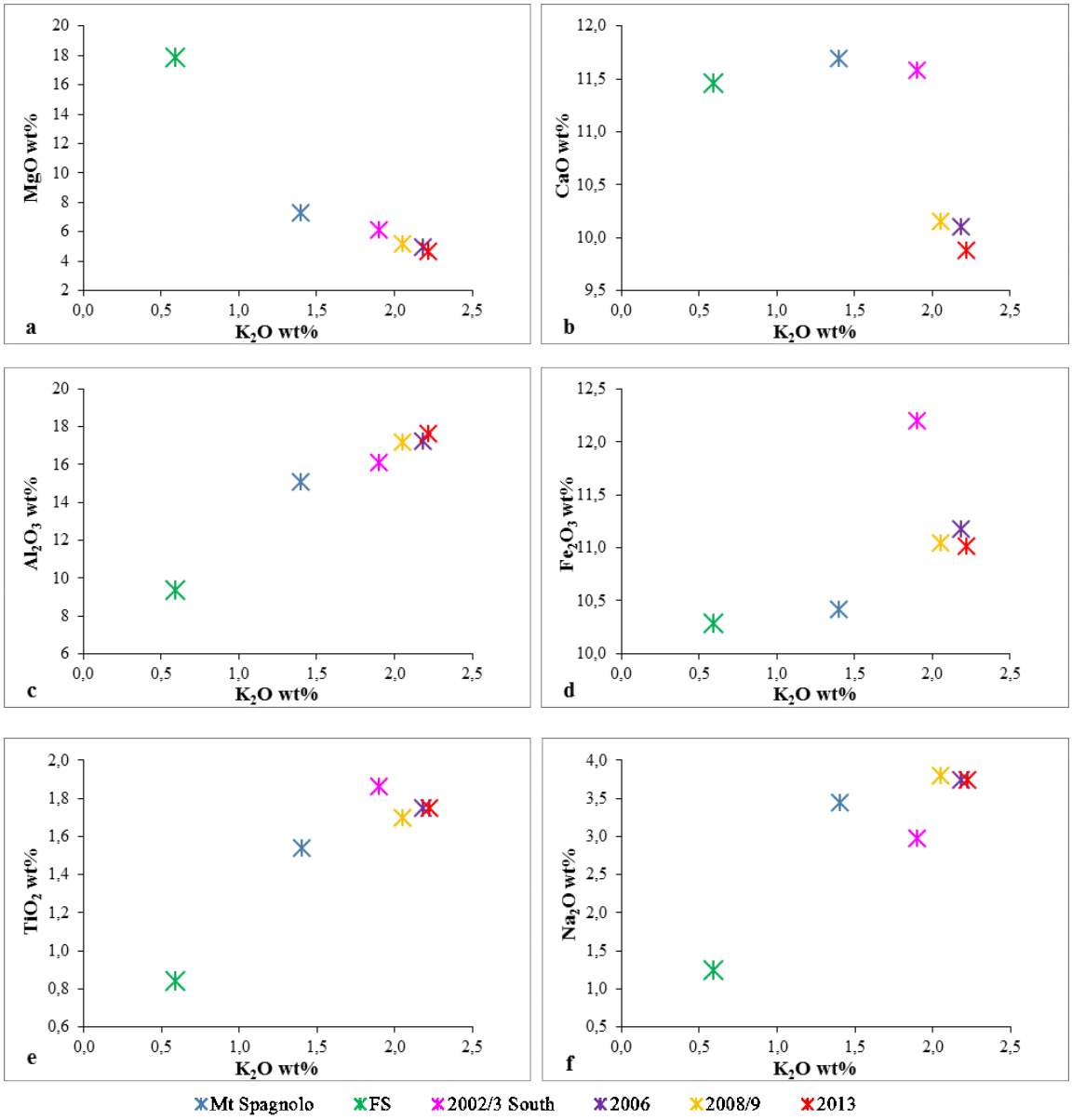

Fig. 4.3 - Whole rock major element variations for the studied Etnean products, in function of K_2O, used as differentiation index.

	Mt. Spagnolo	FS	2002/2003 South	2006	2008/2009	2013
SiO_2	48.37	46.46	46.93	48.02	47.50	48.29
TiO_2	1.54	0.84	1.86	1.75	1.70	1.75
Al_2O_3	15.09	9.35	16.11	17.25	17.30	17.62
Fe_2O_3	10.42	10.29	12.20	11.18	10.80	11.02
MnO	0.17	0.17	0.20	0.19	0.18	0.19
MgO	7.31	17.90	6.12	4.96	4.90	4.69
CaO	11.69	11.46	11.58	10.1	10.0	9.88
Na_2O	3.45	1.25	2.98	3.74	3.80	3.74
K_2O	1.40	0.59	1.90	2.18	2.10	2.22
P_2O_5	0.63	0.22	0.52	0.62	0.60	0.61
Cr_2O_3	0.04	0.19	0.02	b.d.l.	b.d.l.	0.03
LOI	0.06	1.86	-0.37	-0.29	0.24	-0.43
Total	100.2	100.6	100.0	99.7	99.1	99.6
Cl	0.16	0.08	0.12	0.11	0.077	0.12
S	0.01	b.d.l.	0.01	0.01	0.01	b.d.l.
Mg#	58.16	77.51	49.85	46.78	47.34	45.75
CaO/Al_2O_3	0.77	1.23	0.72	0.59	0.58	0.56

Table 4.1 - Major elements, chlorine, sulfur content in the studied rocks (expressed in wt.%). LOI = loss on ignition; Mg# = 100 x $Mg/(Mg+Fe_{tot})$; b.d.l. = below detection limit.

4.2. Petrography and minerals chemistry

Monte Spagnolo lavas

The products of the Monte Spagnolo lava flow are characterized by a low porphyric index (phenocrysts around 10-15 vol.%), with phenocrysts of clinopyroxene and euhedral to subhedral olivine (< 5 mm). Although clinopyroxene is the most abundant mineral phase, only olivine phenocrysts have been selected for the melt inclusion study (table 4.2).

There are different olivine phenocrysts with variable forsterite (Fo) contents (fig. 4.7): yellow olivine crystals with Fo_{70-76}, and transparent-pale olivine crystals with Fo_{82-88}. Some olivine phenocrysts present reverse zoning, with Fo_{75} in the core and Fo_{85} in the rim (fig. 4.4a). For our study only the most primitive (MgO-richer) olivine were selected, even if the yellow olivine entrapped more melt inclusions than the transparent ones. The chemical compositions of the melt inclusion-hosting olivine phenocrysts are reported in table A3.1 in Appendix (A3).

Abundant Cr-spinel microphenocrysts are observed inside the olivine phenocrysts and inside the melt inclusions (fig. 4.4 c-d, chemical composition in in table A3.8 in Appendix A3).

In the microcrystalline groundmass (fig. 4.4b) there are microlites of plagioclase, clinopyroxene (sometimes with skeletal textures), Ti-magnetite (dendritic textures) and olivine.

Eruption	Product	Bulk Rock composition	Vesicularity (vol.%)	Phenocrysts (vol.%)	Microphenocrysts/ Microlites	Groundmass
Mt. Spagnolo	lava	basalt/ trachybasalt		cpx (6-7) + ol (4-5) + plg (1-2) + ox (<0.5)	Cr-spinel and Ti-magnetite	microcrystalline
FS	tephra	picritic basalt	50	ol (7-8) + cpx (2-3) + ox (<0.5)	Cr-spinel	glassy
2002/2003 South	tephra	basalt/ trachybasalt	30	cpx (8) + ol (2-3) + plg (1) + ox (<0.1)	Ti-magnetite	microcrystalline
2006	tephra	trachybasalt	30-50	plg (10-12) + cpx (8-9) + ol (3-5) +ox (<0.5)	Ti-magnetite	microcrystalline
2008/2009	tephra	trachybasalt	40-50	plg (8) + cpx (7) + ol (2-4) + ox (<1)	Ti-magnetite	microcrystalline
2013	lava	trachybasalt		plg (8-10) + cpx (6-8) + ol (2-3) + ox (<3)	Ti-magnetite, apatite and Cu-sulfide	microcrystalline

Table 4.2 - Summary of the mainly features of the studied products.
(cpx = clinopyroxene, ol = olivine, plg = plagioclase, ox=oxides).

FS tephra

The tephra from FS eruption (table 4.2) are highly vesiculated (voids > 50 vol.%) and almost aphyric (~10 vol.%). The phenocrysts are principally represented by euhedral olivine (1 cm in size) with Fo_{89-91} (fig. 4.7), few subhedral clinopyroxene, and rare microphenocrysts of Cr-spinel (Cr_2O_3 = 38-52 wt.%). Cr-spinel microphenocrysts are often hosted within olivine phenocrysts and melt inclusions (figs. 4.5 a-b). The chemical composition of the melt inclusion-hosting olivine phenocrysts and of the Cr-spinel inclusions are reported in tables A3.2 and A3.8 in Appendix A3.

The groundmass is glassy, with some microlites of olivine, clinopyroxene, plagioclase and Cr-spinel.

2002/2003 South tephra

For this eruption, only the tephras located in proximity of the South Rift have been sampled and studied. Scoria samples are slightly vesiculated (voids ~ 30 vol.%, fig. 4.5d), poorly porphyritic (10-15 vol.%) with phenocrysts of (in order of decreasing abundance) clinopyroxene, olivine and plagioclase (table 4.2). Olivine phenocrysts are euhedral to subhedral and they have different colors and different Fo contents (74-83 mol.%; fig. 4.7), as in Monte Spagnolo lavas. They contain abundant melt inclusions, sometimes with big bubbles and daughter minerals. The chemical composition of the olivine phenocrysts (hosting the studied melt inclusions) are reported in table A3.3 in Appendix A3. Inside the olivine crystals, and sometimes inside the melt inclusions, Ti-magnetite crystals are frequently observed (fig. 4.5c, chemical composition in in table A3.8 in Appendix A3).

The groundmass (fig. 4.5d) is microcrystalline with microlites of clinopyroxene, plagioclase, and in minor amount of olivine and Ti-magnetite.

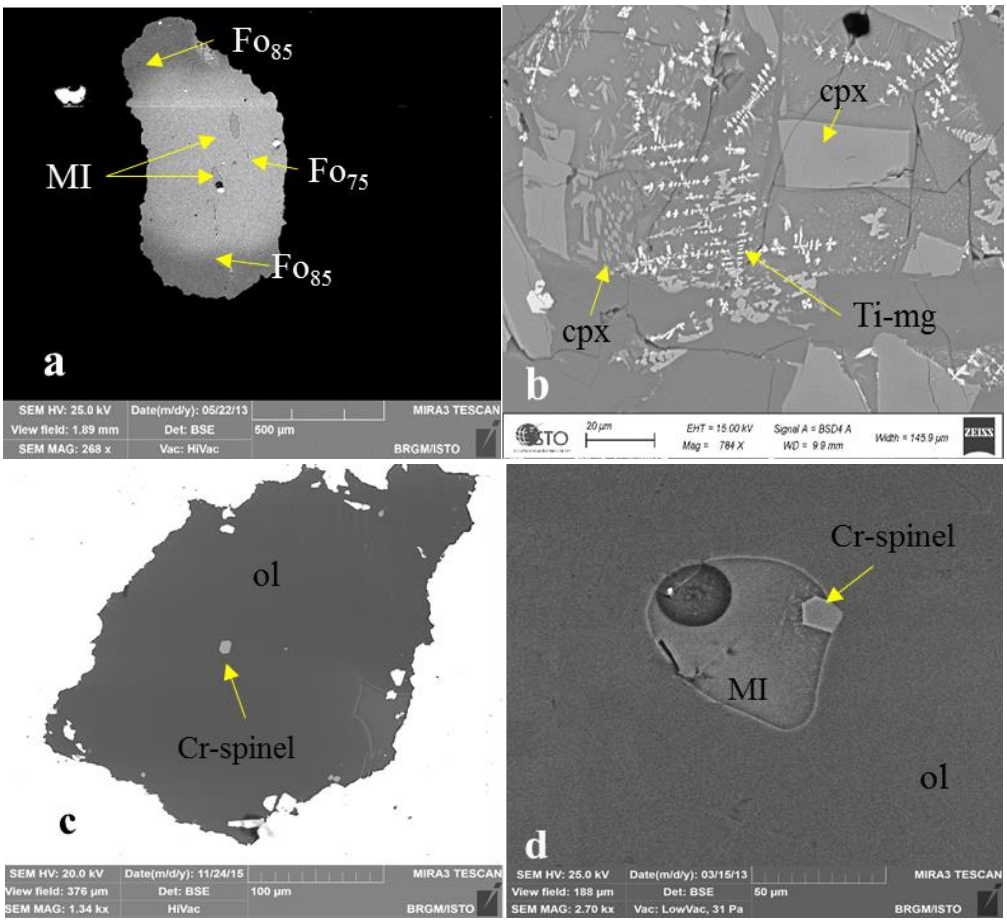

Fig. 4.4. a) Zoned Olivine phenocrysts in Mt. Spagnolo lava (core=Fo_{75}, rim=Fo_{85}); (MI =melt inclusions). b) Skeletal clinopyroxene (cpx) and dendritic Ti-magnetite (Ti-mg) microlites in the groundmass. c-d) Cr-spinel included in olivine crystals and melt inclusion. SEM images taken at the ISTO-BRGM laboratories.

2006 tephra

The products of the 2006 eruption are slightly vesiculated (voids ~ 30 vol.%) and porphyritic (~25 vol.%). The phenocrysts consist (in order of decreasing abundance) of plagioclase, clinopyroxene and olivine (table 4.2). Olivine phenocrysts (Fo_{69-81}; fig. 4.7) host many melt inclusions and Ti-magnetite (fig. 4.6a). The chemical composition of olivine phenocrysts (hosting the studied melt inclusions) and Ti-magnetite inclusions are reported in table A3.4 and A3.8 in Appendix A3.

The groundmass is microcrystalline with microlites of plagioclase, clinopyroxene, and less abundant olivine and Ti-magnetite.

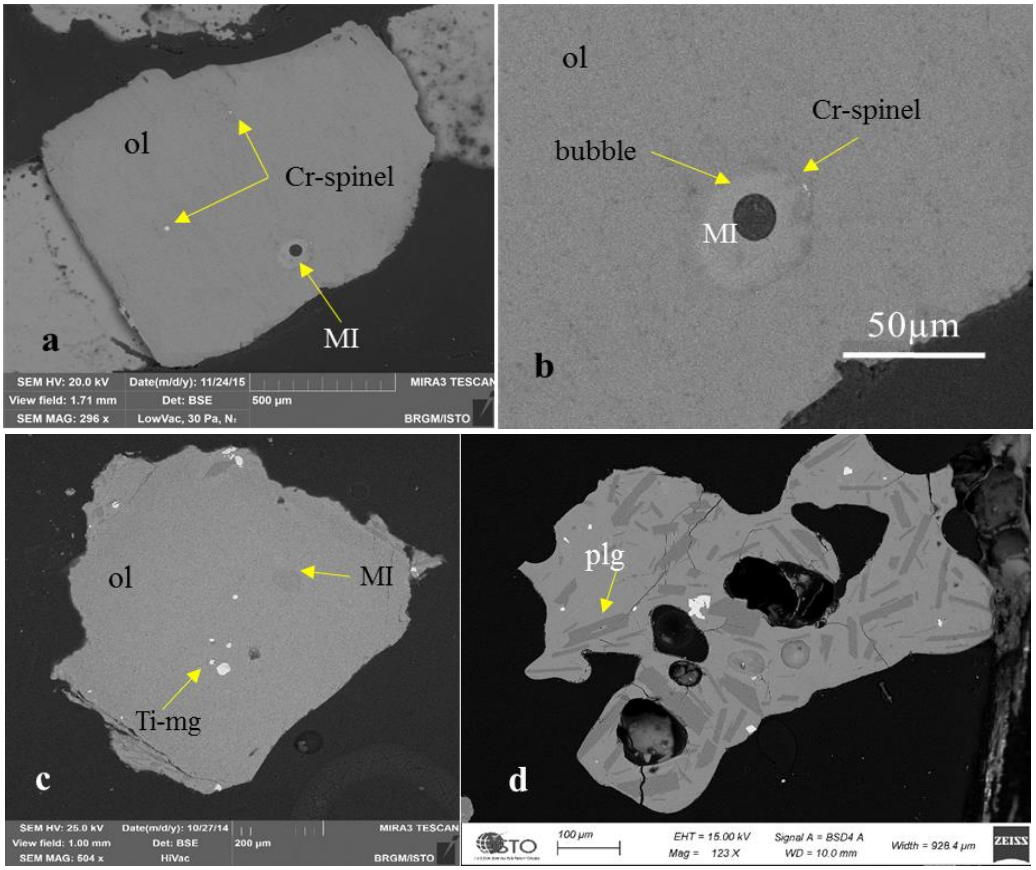

Fig. 4.5. a) Olivine phenocrysts in FS juvenile tephras (Fo_{91}), hosting Cr-spinel phases and a melt inclusion with bubble and a small Cr-spinel (b).
c) Olivine phenocrysts in 2002/2003 South tephras, hosting melt inclusion and several Ti-magnetite.
d) Microcrystalline groundmass of the tephras from 2002/2003 South eruption, with plagioclase (plg) microlites and large vesicles.
SEM images taken at the ISTO-BRGM laboratories.

2008/2009 bombs

For this eruption, volcanic bombs (juvenile) were sampled. They are highly vesiculated (voids ~ 45 vol.%) and slightly porphyritic (phenocrysts 20 vol.%, void free basis). The phenocrysts consist of plagioclase, clinopyroxene and olivine (table 4.2). The olivine crystals (Fo_{69-81}; fig. 4.7) host abundant melt and fluid inclusions, Ti-magnetite crystals and sulfide globules (chemical compositions in the tables A3.8 and A3.9 in Appendix A3). The chemical compositions of the olivine phenocrysts (hosting the studied melt inclusions) are reported in table A3.5 in Appendix A3.
The groundmass is microcrystalline with microlites of plagioclase, clinopyroxene, and less abundant olivine and Ti-magnetite (fig. 4.6b).

2013 lava

The trachybasaltic lava emitted along a southern fracture of the NSEC during the paroxysm of the 12th April 2013 is porphyric (phenocrysts 20-25 vol.%), with phenocrysts of plagioclase, clinopyroxene and olivine (table 4.2). The chemical composition of olivine phenocrysts (Fo_{72-80}) in this sample particularly rich in melt inclusions is reported in table A3.6 in Appendix A3.

The groundmass is microcrystalline with microlites of clinopyroxene, olivine, plagioclase, Ti-magnetite, and less abundant plagioclase, apatite and Cu-Fe sulfide (fig. 4.6c).

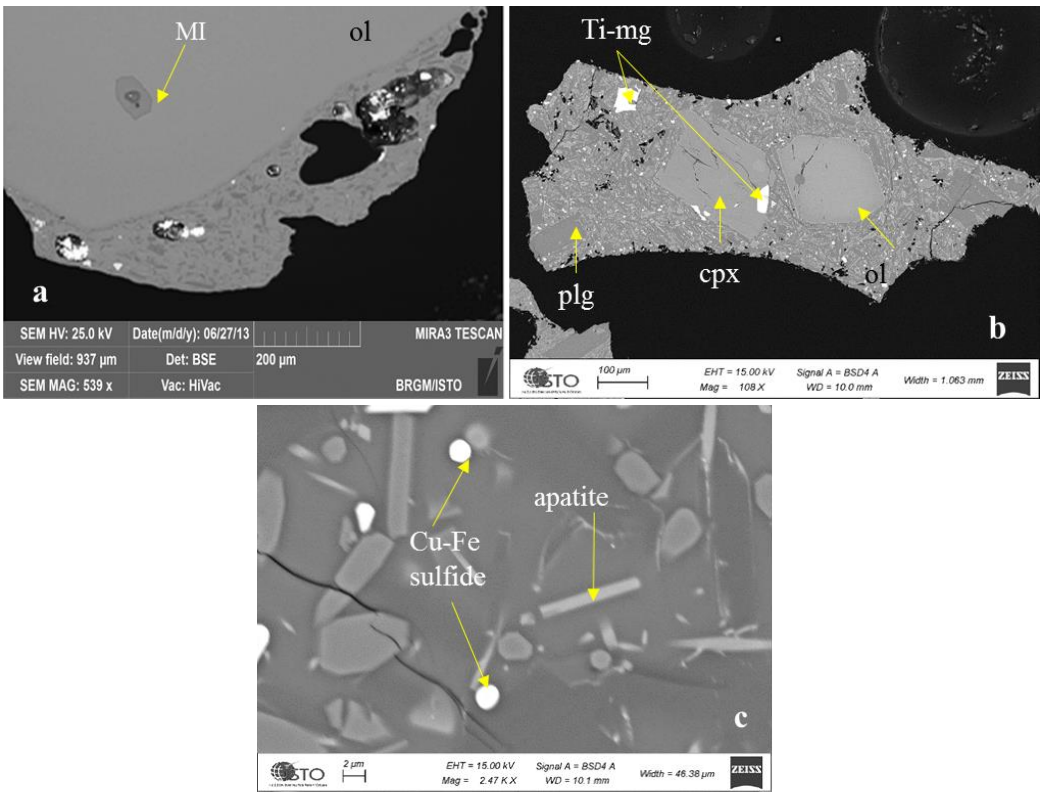

Fig. 4.6 - a) Olivine phenocrysts in 2006 tephra with a melt inclusions, surrounded by a microcrystalline groundmass. b) Microcrystalline groundmass of the tephras from 2008/2009 eruption, with plagioclase (plg), clinopyroxene (cpx), olivine (ol) microlites and Ti-magnetite oxide.
c) Cu-Fe sulfide and apatite microlites in the groundmass of the 2013 lava.
Pictures realized by scanning electron microprobe (SEM) at ISTO-BRGM laboratories.

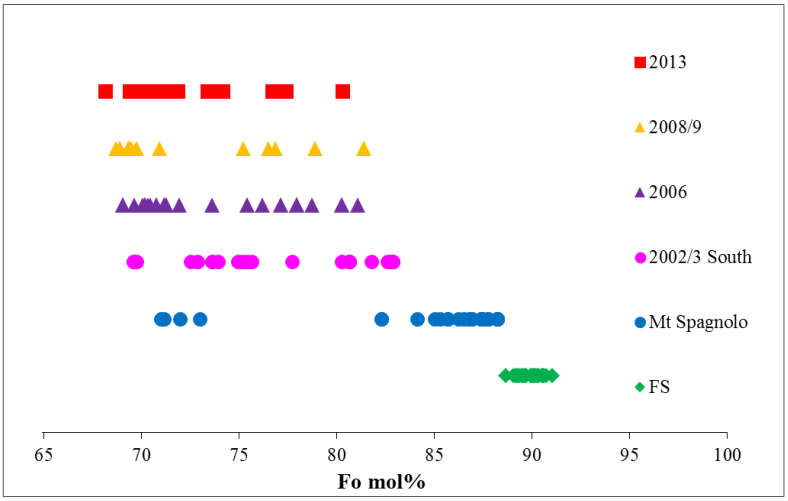

Fig. 4.7 - Forsterite (Fo mol.%) contents of the olivine phenocrysts for the investigated Etnean products. Note the two distinct groups of olivine composition (Fo_{70-76} and Fo_{82-88}) found in Mt. Spagnolo lavas.

4.3. Melt inclusions

More than 300 olivine hosted melt inclusions (hereafter **MIs**) were observed under binocular and petrographic microscopes. Among these, only the best primary melt inclusions (about 150), generally daughter mineral-free were selected for the study (fig. 4.8). These melt inclusions vary in size from 15 to 200 µm. Some of them contain bubbles of variable sizes. The bubble volume fraction for each melt inclusion are estimated, assuming a spherical shape for the bubble and the inclusion. The V_{bubble}/V_{MI} for most of the selected melt inclusions vary generally between 0.001 and 0.11. They are considered as shrinkage bubbles that result from the higher volume contraction of the silicate melt with respect to the hosting olivine during cooling (Frezzotti, 2001). In some inclusions, mainly from the FS and Mt. Spagnolo eruptions, the bubble volume fractions are higher (up to 0.2), and could imply volatile degassing before quenching. The influence of this possible degassing on the estimated volatile content of the inclusions will be discussed later (see paragraph 4.3.2). In some inclusions, very small Ti-magnetite (2002/2003, 2006, 2008/2009 and 2013) or Cr-spinel microphenocrysts (FS and Mt. Spagnolo) and sulfide globules (2006, 2008/2009 and 2013) are observed. Due to their small sizes, only few of them were characterized (Table. A3.8 and A3.9 in appendix).

Several studies deal with about *post-entrapment process* that can alter the chemical composition of the entrapment inclusions, their volatile contents and oxygen fugacity (e.g., Danyushevsky and Plechov, 2011; Frezzotti, 2001; Bucholz et al., 2013). The compositions of MIs could be modified by (i) the overgrowth of an olivine rim at the contact with the host olivine and (ii) the diffusion of Fe from the melt into the host mineral and the diffusion of Mg from the crystal into the melt during the re-equilibration of this rim with the host mineral

(e.g., Danyushevsky et al., 2000, 2002; Gaetani and Watson, 2002). These processes result in significantly higher distribution coefficient (K_D) relating the partitioning of ferrous iron and magnesium between olivine and liquid melt-olivine equilibrium than the well-established value of 0.30 (e.g., Roeder and Emslie, 1970).

The extent of *post-entrapment olivine crystallization (PEC)* on the walls of the inclusion upon cooling was calculated assuming olivine-liquid equilibrium and using a K_D $[(FeO/MgO)_{ol}/(FeO/MgO)_{melt}]$ of 0.26 for equilibrium partitioning of FeO and MgO between olivine and liquid in Etna basalts [with FeO calculated as FeO_{tot} (Di Carlo et al., 2006)]. For more details about calculations of post-entrapment crystallization, see the appendix A4. This correction (expressed as PEC % in table A3.7) varies between 0 and 23 %. The most important corrections were applied to some Mt. Spagnolo and FS melt inclusions. Despite their high PEC % (table A3.7) the inclusions selected for determination of their volatiles content do not show any magnetite daughter that could track post-trapping water loss and/or hydrogen migration (Sobolev et al., 1994; Bucholz et al., 2013), neither surrounding cracks or dislocations (indicating volatiles loss) in the host crystals, therefore suggesting a good preservation of their dissolved volatiles. However, volatiles loss mechanism in Mt. Spagnolo is not completely excluded.

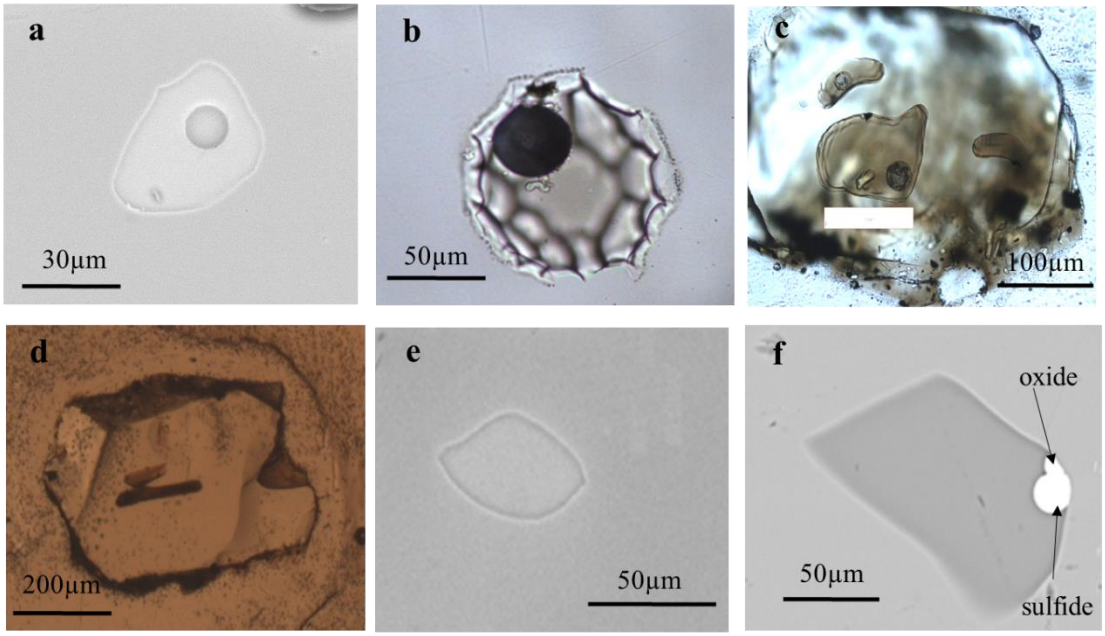

Fig. 4.8 - Example of some studied melt inclusions: a) Mt. Spagnolo, irregular shape with a small bubble; b) FS, typical scalloped edges and spherical vapor bubble (V_B/V_{MI}~0.03); c) 2002/2003 South, spherical and oval shapes; d) 2006, elongated melt inclusions and embayment; e) 2008/2009, oval; f) 2013, with Cu-sulfide and Ti-magnetite phases.
Images were obtained using a SEM (a, e, f), and a petrographic microscope in transmitted light (b, c, d).

4.3.1 Major elements characterization

The chemical compositions of the studied Etnean melt inclusions, after PEC correction, together with the uncorrected composition of some glass embayments and some matrix glasses are reported in table A3.7 in the appendix. Figure 4.9 shows the compositional variability of studied melt inclusions: their silica content varies between 42 wt.% (in Mt. Spagnolo inclusions) and 56 wt.% (in the 2008/2009 inclusions). The total alkalis content is also extremely variable for olivine-hosted melt inclusions, it ranges between 2.4 and 13.1 wt.% (fig. 4.9a).

The melts entrapped in the FS products have the lowest alkali contents (Na_2O = 1.4-2.4 wt.% and K_2O = 0.6-1.4 wt.%) and, similarly to the bulk rock, have a basaltic composition, and plot in the sub-alkaline field (fig. 4.9a). All MIs of the other eruptions, as their respective whole rocks, belong to the alkaline series. Particularly, the Mt. Spagnolo melt inclusions clearly show a sodic affinity (Na_2O-2 > K_2O), while the most recent products have not a clear affinity (fig. 4.9b).

The whole rock compositions are generally within the range of the MIs (fig. 4.11), with the exception of the higher MgO content of the FS bulk-rock, probably due to some accumulation of olivine phenocrysts.

Melt inclusions also show large variations in the content of the other major elements. Particularly, MgO spans between 2 and 12 wt.%, while CaO between 3 and 15 wt.%, with the highest values characterizing FS inclusions (figs. 4.10 a-b): they both display a decreasing trend with the K_2O content, used as differentiation index. Conversely, SiO_2, Na_2O and Al_2O_3 increase with the K_2O content (figs. 4.10 c-e-f), from FS to the most recent compositions, through Mt. Spagnolo melt inclusions.

No clear trends of FeO, TiO_2 and P_2O_5 contents versus K_2O are observed (figs. 4.10 d-g-h).

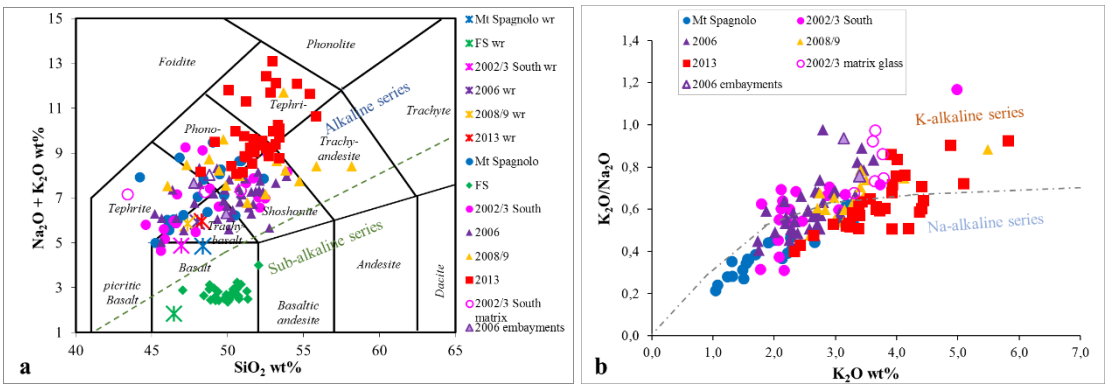

Fig. 4.9 - a) Total alkali vs. silica (TAS) diagram (Le Maitre, 2002) showing the compositions of the studied melt inclusions with the respective whole rocks (wr), some embayments for the 2006 eruption and the matrix glasses for the 2002/2003 South eruption. The dashed green line indicates the separation between the alkaline and the sub-alkaline fields (Irvine and Baragar, 1971). b) K_2O/Na_2O ratio versus K_2O content plot showing the sodic or potassic affinity of the Etnean studied glass inclusions (except the sub-alkaline FS products). The dashed line indicates the separation of the two fields after (Innocenti et al., 1999). All data are normalized to 100 %, and melt inclusion data are corrected for post-entrapment crystallization.

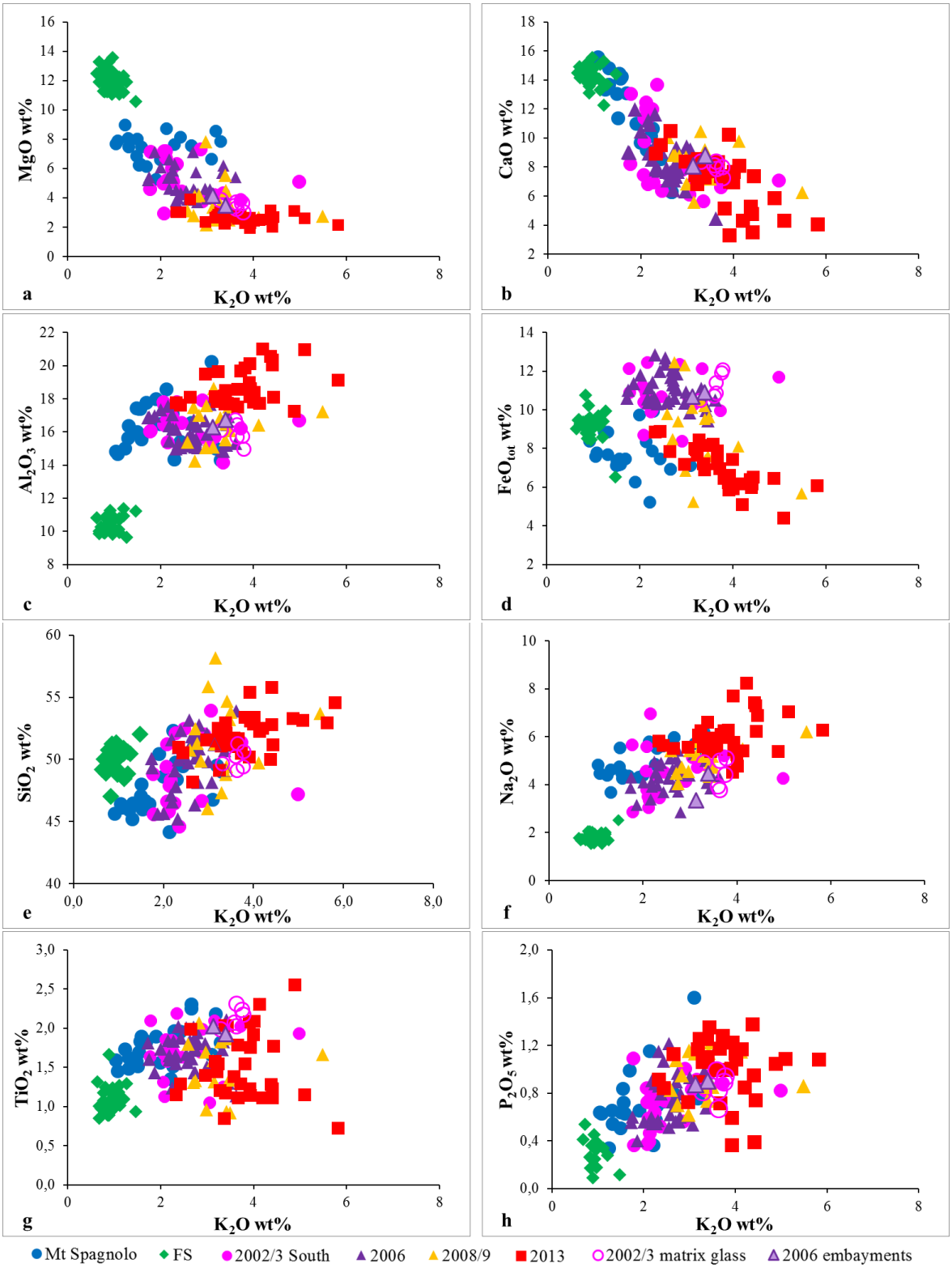

Fig. 4.10 - Major element composition in the studied melt inclusions, as a function of K_2O, used as differentiation index. All data are normalized to 100 % and melt inclusion data are corrected for *post-entrapment crystallization (PEC)*.

The composition of the studied MIs are in a good agreement with the previous studies on similar compositions (e.g., Kamenetsky and Clocchiatti, 1996; Métrich et al., 2001; Spilliaert et al., 2006a; Kamenetsky et al., 2007; Collins et al., 2009; Corsaro and Métrich, 2016), our study revealing 2013 melt inclusions as the Mg-poorest olivine-hosted melts. The figure 4.11 shows that among all Etnean products, FS melt inclusions seems to be the most primitive liquid ever erupted at Etna with the highest CaO/Al_2O_3 ratio (~ 1.5), followed by Maletto and Mt. Spagnolo MIs (Kamenetsky and Clocchiatti, 1996).

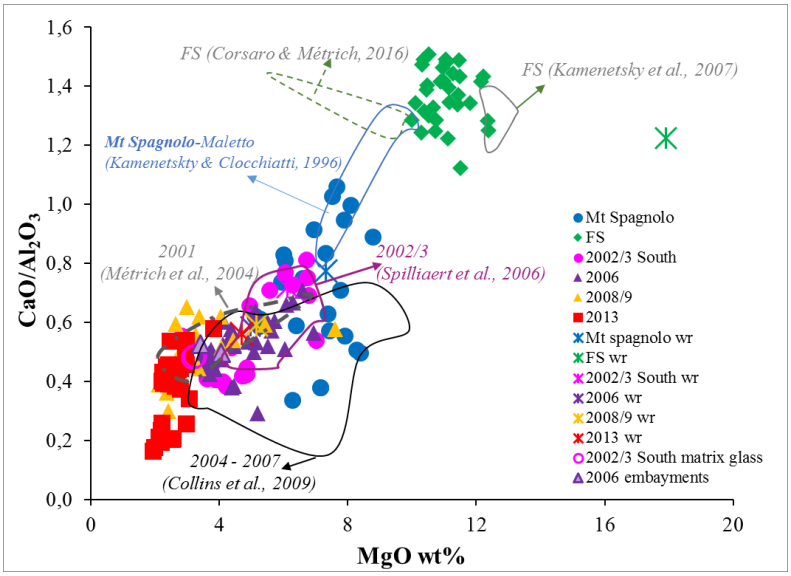

Fig. 4.11 - CaO/Al_2O_3 ratio versus MgO plot, with bulk rocks, melt inclusions (*PEC corrected*), embayments and matrix glasses investigated in this study and MIs from literature (Kamenetsky and Clocchiatti, 1996; Métrich et al., 2001; Spilliaert et al., 2006; Kamenetsky et al., 2007; Collins et al., 2009; Corsaro and Métrich, 2016).

4.3.2 Volatile content

Major volatiles (H_2O, CO_2, S and Cl) in melt inclusions and glass embayments were determined using the different analytical method described in the chapter 3 (SIMS, FTIR, EMP). All data are reported in table 4.3; data that will be used in the discussions are in bold. For more details about data elaboration, see appendix A5.

H_2O content of Etnean glass inclusions is extremely variable, between 0 and 5.9 wt.%. These contents are not correlated with the estimated PEC %, neither with the inclusion size, (figs. 4.12 a-b). No clear relation exists between the water content and the Fo content of the hosting olivine or the melt K_2O content (figs. 4.12 c-d). The H_2O-richest melt inclusions are from the FS eruption. On the contrary, Mt. Spagnolo, 2008/2009 and 2013 melt inclusions have extremely low H_2O contents (< 0.5 wt.%). The 2002/2003 and 2006 melt inclusions present variable H_2O contents (between 0.1 and 3.2 wt.%, the maximum value is found in 2006 MI).

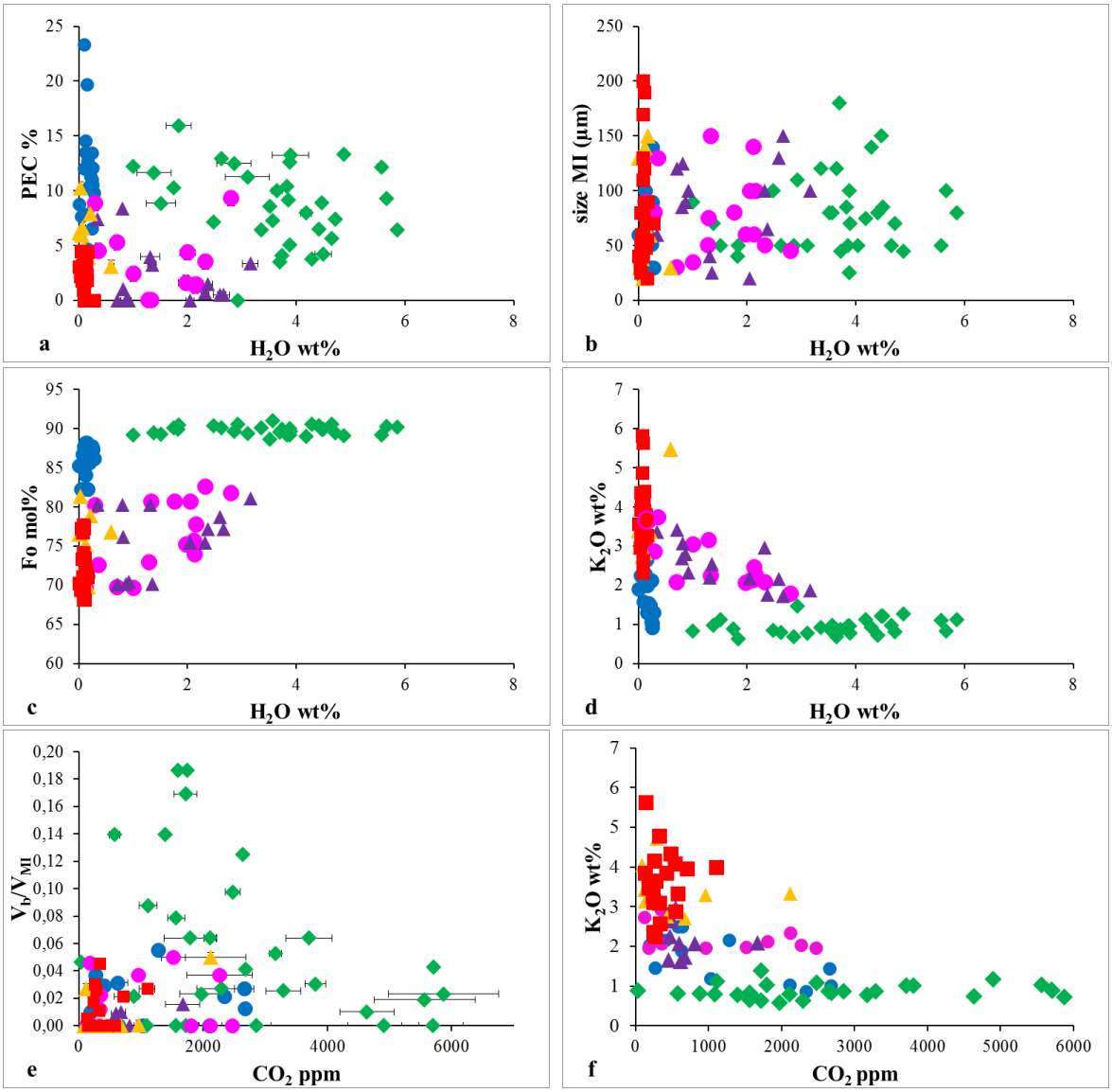

Fig. 4.12 - Water content in the studied melt inclusions are not affected by PEC (a) or the inclusions size (b). There is any clear relation between the H_2O content and the Fo content of the hosting olivine (c) or the K_2O content of the inclusions (d). Any clear relation exists between the bubbles inside the MI (V_b/V_{MI}) and the CO_2 estimated in the MIs (e), neither with the K_2O (f).
For symbols, see legend in the figure 4.11. Error bars, indicating the standard deviation, are reported for H_2O and CO_2 only in the plot 4.12a and 4.12e.

CO_2 contents measured by SIMS in some FS inclusions (up to 5872 ppm) are much higher than those previously estimated by Kamenetsky et al. (2007) (3300 ppm), but are not corroborated by FTIR estimations (fig. 4.13), suggesting possible carbon contamination during SIMS analyses (see the Appendix 5). Mt. Spagnolo melt inclusions show a large range of CO_2 abundance, between 0 and 2674 ppm. The highest CO_2 contents was determined in some melt inclusions H_2O-free, e.g. Mt. Spagnolo sample, corroborating the hypothesis of carbon contamination during SIMS analyses. The inclusions from the other eruptions have CO_2 contents (between 87 ppm in 2008/2009 MIs and 2470 ppm of

2002/2003 South MIs) similar to those measured by previous authors (e.g., Métrich et al., 2004; Spilliaert et al., 2006a; Collins et al., 2009) as shown in figure 4.13.

Bubble-bearing melt inclusions do not clearly show lower CO_2 contents if compared with the bubble-free ones (fig. 4.12e). No systematic relation exists between the CO_2 content and the ratio between the estimated bubble and melt inclusion volumes (V_b/V_{MI},), although the MIs from FS with the highest CO_2 contents seems to have the lowest V_b/V_{MI} (< 0.05), while the MIs with the highest V_b/V_{MI} (> 0.12) have a low CO_2 content (< 2000 ppm).

H_2O and CO_2 contents were used to determine melt inclusions entrapment pressures using the solubility model of Iacono-Marziano et al. (2012) under the assumption of magma volatile saturation (see fig. 4.13, table 4.3). Results translate in a large range of pressures (76-477 MPa) for FS melt inclusions (the lower values very likely resulting from H_2O loss after entrapment), but narrower for all the other eruptions: Mt. Spagnolo (3-173 MPa), 2002/2003 South (11-254 MPa), 2006 (0-153 MPa), 2008/2009 (5-161 MPa), 2013 (0-81 MPa).

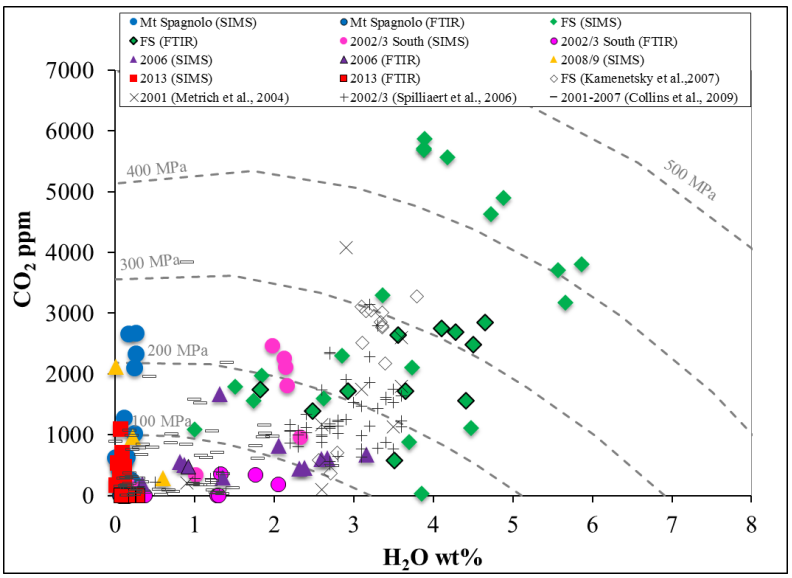

Fig. 4.13 - Evolution of CO_2 and H_2O contents of melt inclusions (estimated by SIMS and FTIR). Isobars are calculated at 1200 °C using the model of Iacono-Marziano et al. (2012), using as composition the average of studied melt inclusions.

Sulfur content in the investigated melt inclusions is extremely variable, reaching 4100 ppm, which is higher than previously estimated abundance (e.g., Métrich and Clocchiatti, 1989; Métrich et al., 2004; Spilliaert et al., 2006; Kamenetsky et al., 2007; Collins et al., 2009; Corsaro and Métrich, 2016). The highest S abundance is in the Mt. Spagnolo inclusions (table 4.3, fig. 4.14). The H_2O and CO_2 -rich melt, entrapped in the primitive olivine from FS eruption, contains a lower sulfur content (up to 3473 ppm), but slightly higher than previously estimated [1700-3000 ppm respectively in Kamenetsky et

al. (2007) and Corsaro and Métrich (2016)]. In 2002/2003 South inclusions, S abundance is between 128 and 3000 ppm, 113-3410 ppm in 2006 magma, while in the most recent magma of 2008/2009 and 2013, the maximum estimated sulfur content is 1100 ppm, which reasonably indicates a higher extent of magmatic degassing.
There is no systematic correlation with the other estimated volatiles contents (H_2O, CO_2, Cl, figs. 4.14 a-b-c). Conversely, S decreases with the increasing of the K_2O content (fig. 4.14d), which is an indication of melt evolution.

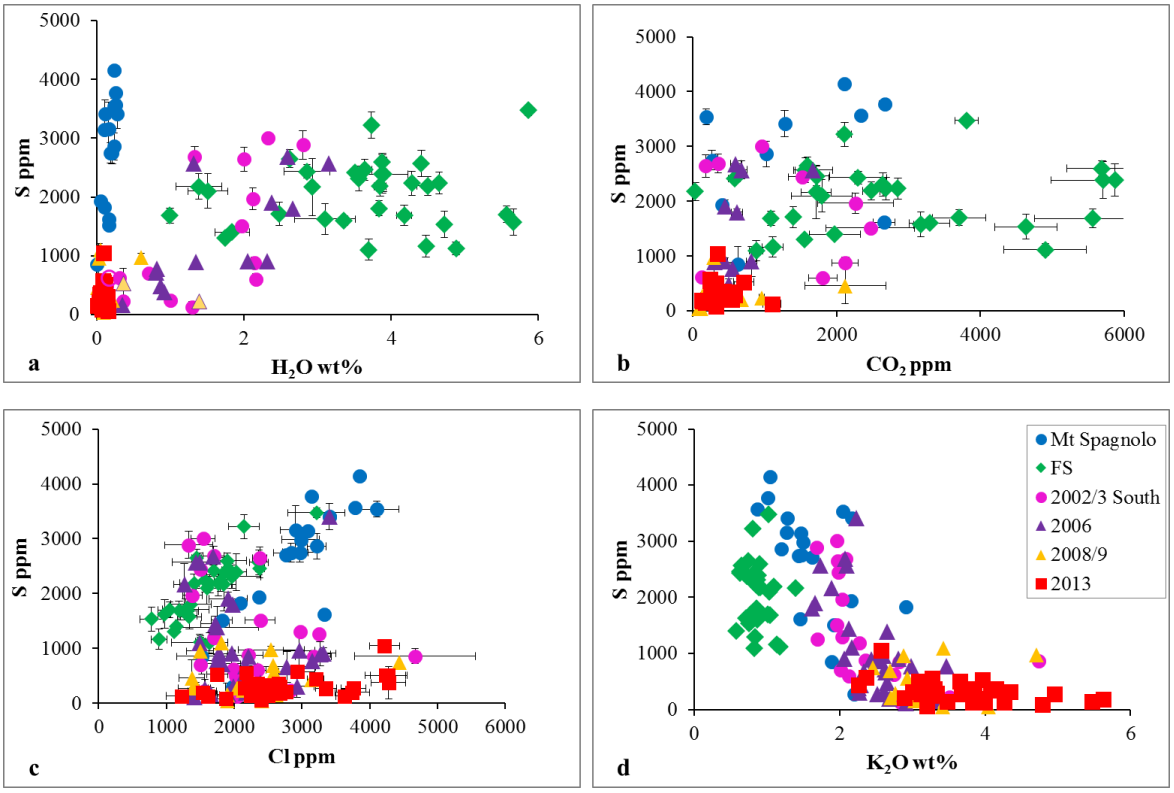

Fig. 4.14 - S content versus other volatiles abundance (a-b-c) and K_2O (d) in olivine hosted melt inclusions. Error bars indicate standard deviations.

Chlorine content is also highly variable, between 793 and 4670 ppm in the 2002/2003 South melt inclusions, perfectly in agreement with previous estimate (e.g., Métrich and Clocchiatti, 1989; Métrich et al., 2004; Spilliaert et al., 2006; Kamenetsky et al., 2007; Collins et al., 2009; Corsaro and Métrich, 2016). Even more than for sulfur, there is a lack of correlation between Cl and the other volatiles, or the K_2O content (fig. 4.15a). Cl/K_2O ratio in the studied melt inclusions varies from 0.03 to 0.44. Normally, this ratio should be constant during the melt differentiation, being both incompatible elements. The highest Cl/K_2O ratio values are for some MIs from Mt. Spagnolo and FS eruptions, higher than previously estimated in other DDF [=*Deep Dyke Fed* (Corsaro et al., 2009)] magmas (2001-2003) by Corsaro and Métrich (2016). The authors find that the Cl/K_2O ratio of the older DDF eruptions is around 0.21 ± 0.03, while those occurred after the 1970's have a Cl/K_2O ratio around 0.08. Indeed, Cl/K_2O ratios of the studied DDF magmas (Mt Spagnolo,

FS and 2002/2003 eruptions) fill the field limited by the Cl/K_2O ratio values defined in Corsaro and Métrich (2016) (0.08 and 0.21, fig. 4.15a-b), while the others magmas (2006, 2008/2009 and 2013) are caractherized by more variable values of the Cl/K_2O ratio.

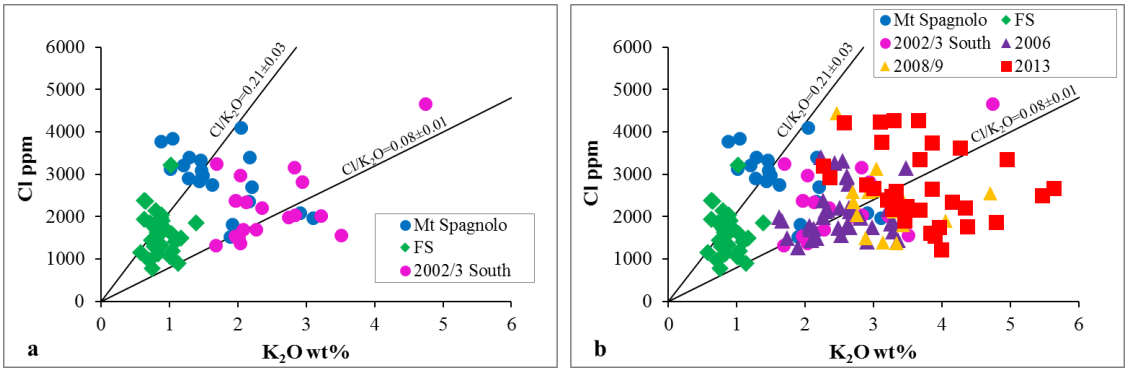

Fig. 4.15 - Cl abundance versus K_2O in the melt inclusions: a) of the studied DDF [=*Deep Dyke Fed* (Corsaro et al., 2009)] eruptions, and b) of all studied magmas. The black lines in the figures indicate the mean values (0.21 and 0.08) defined by Corsaro and Métrich (2016) respectively for the oldest DDF eruptions and for those post-1970.

4.3.3 Phenocryst embayments and matrix glasses

Three glass embayments in olivines were also analyzed (two from 2006 and one from 2002/2003 eruptions). Among these, one embayment ("2006-7emb") is more evolved (CaO/Al_2O_3 = 0.53 versus 0.71 in the MI) and water-poor (0.36 wt.% H_2O in the embayment and 3.16 wt.% H_2O in the MI) than the melt inclusion in the same olivine, suggesting a slightly more superficial entrapment, than the MI (fig. 4.11, table A3.7 and 4.3). The other two embayments ("2006-E2emb" and "2002/3S-24emb") present a similar composition and water contents of the inclusions entrapped in the same olivine (table 4.3), and in one case also very similar S and Cl contents, suggesting that MIs and embayments were entrapped inside the crystal at similar depth. Few matrix glasses were also analyzed, they have a more evolved composition (CaO/Al_2O_3 = 0.49±0.02 for 2002/2003 glasses, and 0.48 for 2006) than their related melt inclusions, but S and Cl contents are very similar to those of the MIs (table 4.3). H_2O and CO_2 were not measured in the matrix glasses.

sample name	Fo mol.%	H_2O (SIMS) wt.%	H_2O (FTIR) wt.%	CO_2 (SIMS) ppm	CO_2 (FTIR) ppm	S (EMP) ppm	S^* (EMP) ppm	S (SIMS) ppm	Cl (EMP) ppm	Cl (SIMS) ppm	P (MPa)	Depth (km)	Bubble inside MI
Spa-1a	87.76	**0.24**		**185** (±9)		**3539** (±141)	4068	3190 (±118)	**4104** (±331)	4080 (±214)	12.0	0.5	yes
Spa-1b	87.76	**0.10 (±0.01)**				**3140**			**3090**				yes
Spa-3	82.27	**0.05 (±0.01)**		**410** (±17)		**1935** (±35)		1466 (±281)	**2370** (±14)	1728 (±300)	39.5	1.5	yes
Spa-3n	82.27		**0.16 (±0.07)**		b.d.l.	**1515** (±49)			**1820** (±156)		5.9 [a]	0.2	yes
Spa-4n	86.85	**0.21**				**2745** (±176)			**2840** (±254)				no
Spa-5	86.95	**0.16 (±0.01)**				**3160** (±446)		3533 (±283)	**2907** (±229)	3360 (±332)			yes
Spa-5n	86.21	**0.28**				**3410** (±240)			**3405** (±63)				yes
Spa-6	85.70	**0.19**		**267** (±30)		**2750** (±176)			**2970** (±254)		21.4	0.8	yes
Spa-7	85.29	**0**		**626** (±162)		**857** (±320)			**1523** (±370)		76.9	3.0	yes
Spa-7n	87.48	**0.11**		**1279** (±16)		**3410** (±240)		1022 (±15)	**3405** (±63)	1748 (±30)	109.4	4.2	yes
Spa-9	85.67					**2985** (±219)	2895		**2985** (±276)				yes
Spa-11	85.00					**2710**			**2760**				no
Spa-D	86.77		**0.07 (±0.01)**		b.d.l.	**310**			**1980**		2.9 [a]	0.1	no
Spa-L	86.50		**0.1**		b.d.l.	**1830**			**2090**		3.5 [a]	0.1	no
Spa-O1	84.12		**0.12**		b.d.l.	**280**			**2700**		3.9 a	0.2	yes
Spa-R	71.17	**0.16**		**2660** (±153)		**1620**		1886 (±40)	**3330**	3198 (±67)	173.3	6.7	yes
Spa-T1	87.42	**0.26**		**2336** (±63)		**3570**(±14)		3885 (±75)	**3785** (±21)	3948 (±78)	154.2	5.9	yes
Spa-T2	87.42	**0.26**		**2674** (±76)		**3770**		4552 (±63)	**3140**	4581 (±54)	144.1	5.5	yes
Spa-T3	87.42	**0.24**		**2107** (±48)		**4150**		3906 (±58)	**3850**	3952 (±55)	119.8	4.6	no
Spa-T4	87.42	**0.24**		**1025** (±27)		**2863** (±231)		3000 (±66)	**3220** (±139)	3195 (±68)	74.4	2.9	no
Spa-U1	88.21	**0.12**		**583** (±29)		b.d.l.		184 (±4)	**2655** (±304)	3696 (±80)	44.9	1.7	no
Spa-U2	88.21	**0.15**		**635** (±21)		b.d.l.		258 (±6)	**2570**	3865 (±54)	48.5	1.9	no
Spa-U3	88.21					b.d.l.			**3163** (±476)				no
Spa-U4	88.21					b.d.l.			**3040**				no
FS-00	89.54	**3.70 (±0.05)**	3.11	**882** (±72)	b.d.l.	**1100** (±179)		1281 (±36)	**1633** (±151)	2024 (±65)	158.1	6.1	yes
FS-01	89.49	**1.39 (±0.31)**				**2178** (±222)	2913		**1767** (±206)				yes
FS-03b	89.37	**3.10 (±0.41)**				**1625** (±263)		1076 (±153)	**975** (±96)	940 (±174)			yes
FS-03c	89.48	**4.72 (±0.07)**		**4635** (±434)		**1533** (±225)		1461 (±158)	**783** (±172)	930 (±27)	408.6	15.7	yes
FS-05	89.15	**4.88 (±0.02)**		**4903** (±575)		**1120** (±110)	1571	1133	**1500** (±71)	1673 (±73)	398.7	15.4	no
FS-06b	90.12	**3.36**		**3294** (±283)		**1600** (±82)	2132	1510 (±28)	**1329** (±125)	1105 (±24)	323.9	12.5	yes
FS-06c	90.11	**2.62 (±0.03)**		**1599** (±71)		**2650** (±154)		1129 (±22)	**1450** (±71)	1450	180.1	6.9	yes
FS-06n	90.11	**1.74 (±0.05)**		**1560** (±43)		**1300**		1026 (±11)	**1120**	726 (±13)	201.4	7.8	no
FS-07	89.72	**3.85 (±0.08)**		**34** (±3)		**2180** (±164)		2118	**1640** (±152)	2331	75.9	2.9	yes
FS-08b	89.03	**4.18 (±0.10)**		**5564** (±814)		**1689** (±169)		2006 (±42)	**1189** (±127)	1592 (±28)	477.3	18.4	yes
FS-08c	89.23	**5.57 (±0.08)**		**3706** (±372)		**1700** (±141)		1660 (±58)	**1050** (±173)	1323	342.8	13.2	yes
FS-09 n	90.73	**3.88**	1.59	**5709**	1116	**2390** (±332)		1589	**2033** (±152)	1319 (±42)	454.7	17.5	yes
FS-09	90.00	**3.88 (±0.06)**		**5694** (±493)		**2600** (±141)		1584 (±44)	**1900** (±283)	1667 (±49)	429.1	16.5	no
FS-10b	90.26	**5.66 (±0.02)**		**3170** (±96)		**1575** (±226)	2235	1504 (±50)	**1342** (±178)	1475 (±61)	305.5	11.8	yes
FS-10c	90.50	**1.84 (±0.23)**		**1977** (±356)		**1400** (±63)	1828	813 (±115)	**1150** (±55)	802 (±118)	224.1	8.6	yes
FS-11	89.97	**4.47 (±0.05)**		**1112** (±143)		**1164** (±186)	1629	1216 (±32)	**891** (±114)	1100 (±40)	186.4	7.2	yes
FS-12a	89.21	**0.99 (±0.01)**		**1089** (±30)		**1683** (±130)		1710 (±36)	**1310** (±160)	1936 (±44)	109.1	4.2	no
FS-12b	89.21	**3.83 (±0.05)**				**1805** (±131)		2378 (±150)	**1360** (±300)	2192 (±138)			yes
FS-13b	89.63	**3.89 (±0.33)**		**5872** (±885)		**2386** (±291)	3037	1874 (±202)	**1857** (±79)	1915 (±227)	456.0	17.6	yes
FS-13c	89.63	**2.86 (±0.31)**		**2300** (±402)		**2433** (±115)	3062	1631 (±210)	**1933** (±115)	1521 (±214)	243.0	9.4	yes
FS-14	89.32	**1.51 (±0.27)**		**1796** (±424)		**2100** (±292)	3058	1197 (±231)	**1600** (±158)	915(±189)	210.5	8.1	yes
FS-21	90.17	**5.86 (±0.03)**		**3808** (±165)		**3473** (±90)		3723 (±111)	**3217** (±420)	2737 (±84)	306.0	11.8	yes
FS-23													no

FS-24	88.64		**3.51 (±0.04)**		**580** (±83)	**2420**			**1700**		114.0 [a]	4.4	yes
FS-25	90.56		**3.65 (±0.10)**		**1720** (±186)	**2463** (±175)			**2380** (±66)		190.1 [a]	7.3	yes
FS-26	89.96	**3.73 (±0.03)**		**2111** (±96)		**3223** (±220)		2640 (±73)	**2145** (±231)	1941 (±63)	243.4	9.4	yes
FS-28a	90.35		**4.41 (±0.02)**		**1567** (±138)	**2570** (±226)			**2365** (±134)		184.0 [a]	7.1	yes
FS-28b	90.35		**2.48**		**1396**	**1710** (±198)			**1285** (±346)		162.0 [a]	6.2	yes
FS-B	90.53		**4.65**		**2853**	**2235** (±190)			**1800** (±98)		262.2 [a]	10.1	no
FS-D	90.6		**4.28**		**2687**	**2235** (±205)			**1570** (±42)		271.2 [a]	10.4	yes
FS-E	90.56		**2.93 (±0.03)**		**1718** (±210)	**2169** (±488)			**1851** (±177)		203.3 [a]	7.8	no
FS-Xa	89.92		**4.50 (±0.15)**		**2482** (±123)	**2190** (±160)			**1410** (±216)		240.3 [a]	9.3	yes
FS-Xb	89.92		**1.82**		**1741**								yes
FS-Z	91.02		**3.56**		**2645**	**2310** (±212)			**1965** (±430)		231.5 [a]	8.9	yes
ET2002/3S-1	75.21	**1.97 (±0.14)**		**2470** (±618)		**1513** (±61)		2025 (±27)	**2383** (±223)	2709 (±56)	238.7	9.2	no
ET2002/3S-3	75.69	**2.12 (±0.05)**		**2262** (±527)		**1964** (±187)		1268 (±26)	**1382** (±143)	1148 (±43)	254.3	9.8	yes
ET2002/3S-5	81.79	**2.80 (±0.07)**				**2885** (±247)		1295 (±45)	**1330** (±354)	890 (±29)			yes
ET2002/3S-6	77.76	**2.16 (±0.04)**		**1810** (±201)		**603** (±97)		435 (±17)	**2343** (±129)	1972 (±119)	225.0	8.7	no
ET2002/3S-7	74.96					**860** (±141)			**4670** (±890)				no
ET2002/3S-9	75.43					**855** (±35)			**3170** (±269)				no
ET2002/3S-10	73.94	**2.14 (±0.03)**		**2122** (±182)		**878** (±100)		777 (±21)	**2208** (±216)	1528 (±37)	238.8	9.2	no
ET2002/3S-11b	82.90					**1190**			**1700**				yes
ET2002/3S-13	82.68			**1520** (±195)		**2445** (±49)		403 (±33)	**1505** (±35)	263 (±23)			yes
ET2002/3S-16a	73.65					**1260** (±98)			**3250** (±74)				yes
ET2002/3S-16b	73.65					1300			**2970**				yes
ET2002/3S-23	82.61	**2.33 (±0.01)**		**963** (±16)		**3005** (±50)		3068 (±12)	**1545** (±177)	1507 (±7)	122.9	4.7	yes
ET2002/3S-24	80.26	**0.3**		**119** (±3)		**620** (±28)		896 (±15)	**1995** (±49)	1766 (±27)	11.3	0.4	no
ET2002/3S-25			**1.28**		b.d.l.								yes
ET2002/3S-26	72.57		**0.36 (±0.02)**		b.d.l.	**225** (±78)			**1560** (±184)				yes
ET2002/3S-29a	69.64	**1**		**348** (±10)		130		**237** (±2)	**2830**	2049 (±15)	50	1.9	yes
ET2002/3S-29b	69.64	**0.13**		**236** (±5)		**490** (±113)		116 (±2)	**2020** (±14)	395 (±6)	20.1	0.8	no
ET2002/3S-31	69.77	**0.70 (±0.01)**				**700**		513(±37)	**1500**	1109 (±89)			yes
ET2002/3S-32	72.90		**1.30**		b.d.l.	**128** (±92)			**2043** (±161)		27.4 [a]	1.1	yes
ET2002/3S-33a	80.68		**1.33**		**353**	**2687** (±172)			**1697** (±155)		52.4 [a]	2.0	yes
ET2002/3S-33b	80.68		**2.0 (±0.14)**		**181**	**2643** (±207)			**2380** (±104)		52.6 [a]	2.0	yes
ET2002/3S-33c			**1.76 (±0.09)**		**336**								no
ET2002/3S-14 secondary MI	67.96					b.d.l.			**1300**				yes
ET2002/3S-24 embayment	80.26	**0.17**				**620** (±367)		595(±8)	**2410** (±70)	1714 (±21)	0.5 [ab]	0	
ET2002/3S-6 gm						b.d.l.			b.d.l.				
ET2002/3S-10 gm						b.d.l.			b.d.l.				
ET2002/3S-13 gm						b.d.l.			b.d.l.				
ET2002/3S-23 gm						b.d.l.			**2100**				
ET2002/3S-32 gm						**130**			**1330**				
ET2006-1 a	69.64					**310** (±210)	601		**2930** (±250)				no
ET2006-1 b	70.35					**910** (±100)	656		**3320** (±180)				no
ET2006-4	70.48		**0.92 (±0.02)**		**470**	**380** (±28)			**2390** (±226)		62.4 [a]	2.4	no
ET2006-7	81.08	**3.16 (±0.14)**	2.19 (±0.08)	**678** (±77)	1193 (±151)	**2573** (±159)		2664 (±101)	**1493** (±400)	1221 (±56)	130.6	5.0	yes
ET2006-12	78.75	**2.60 (±0.11)**		**598** (±75)		**2683**		3475 (±179)	**1693**	1725 (±106)	126.3	4.9	yes
ET2006-B3a	77.15	**2.38 (±0.08)**	1.82	**450** (±49)	b.d.l.	**1903** (±127)	2355	2384 (±116)	**1910** (±284)	2129 (±121)	106.9	4.1	no
ET2006-B3b	77.15	**2.66 (±0.11)**		**618** (±78)		**1800** (±67)	2494	2589 (±122)	**1984** (±123)	2153 (±116)	145.5	5.6	no
ET2006-B5a	80.24	**1.32 (±0.18)**		**1673** (±275)		**2570**		2515 (±436)	**1437**	1301 ±1237)	153.2	5.9	yes

ET2006-B5c	80.24	**0.34**		**192** (±28)		127 (±112)		**161** (±7)	**1913** (±156)	2841 (±158)	22.4	0.9	no
ET2006-B5d	80.24	0.80				**720** (±104)	1082	1288 (±48)	1827 (±263)	2286 (±102)	0	0	yes
ET2006-B5n	80.24					**3410**			**3405**		0	0	yes
ET2006-B6	76.20	**0.81 (±0.02)**		**554** (±59)		**773** (±114)	1092	1166 (±47)	**1750** (±213)	2153 (±100)	48.9	1.9	no
ET2006-B8a	75.42	**2.32 (±0.07)**		**441** (±43)		**907** (±58)	1064	1455 (±68)	**1967**(±55)	2718 (±144)	112.9	4.3	no
ET2006-B8b	75.42	**2.05 (±0.07)**		**817** (±73)		**905** (±276)	756	1622 (±65)	**1780** (±226)	2287 (±110)	140.1	5.4	no
ET2006-C7a	70.20					b.d.l.	142		**1730** (±57)				no
ET2006-C7b	70.20					**300** (±226)			1995 (±120)				no
ET2006-C8	73.62					**663** (±280)	632		**2780** (±427)				no
ET2006-C11	71.96					**270** (±168)	278		**1570** (±79)				no
ET2006-D9	70.06	**0.71 (±0.03)**				b.d.l.	213	123 (±8)	**1840** (±71)	1113 (±70)			no
ET2006-E2a	70.19	**0.87 (±0.10)**		**500** (±79)		**480** (±110)	240	444 (±65)	**2130** (±50)	2565 (±394)	89.0	3.4	no
ET2006-E2b	70.19	**1.35 (±0.08)**		**300** (±40)		**895** (±219)		1004 (±88)	**3270** (±156)	3875 (±375)	57.4	2.2	no
ET2006-F5a	77.95					**1387** (±384)			**1750** (±613)				no
ET2006-F5b	77.95					**520**			**2170**				no
ET2006-F5c	77.95					**2167** (±385)			**1267** (±158)				no
ET2006-F5d	77.95					**1105** (±148)			**1495** (±417)				no
ET2006-F5e	77.95					**1443** (±140)			**1720** (±213)				no
ET2006-F5n	71.28					**765**			**3155**				no
ET2006-H2	71.18					**957** (±298)			**2960** (±236)				no
ET2006-H4a	71.21					**190** (±160)			**2177** (±245)				no
ET2006-H4b	71.21					**677** (±165)			**2163** (±182)				no
ET2006-H4c	71.21					b.d.l.			**2210** (±57)				no
ET2006-H7a	69.06					**223** (±152)			**1437** (±116)				no
ET2006-H7b	69.06					**165** (±120)			**1655** (±78)				no
ET2006-H7c	69.06					b.d.l.			**1417** (±169)				no
ET2006-18a	70.76					**860**			**2210**				no
ET2006-18b	70.76					**440**			**2130**				no
ET2006-7 embayment	81.08		**0.36**		b.d.l.	**525** (±262)			**2240** (±240)		2.4 [ab]	2.2	
ET2006-E2 embayment	70.19		**1.39**		b.d.l.	**220**			**1497**		30.1 [ab]	3.2	
ET2006-B6 gm						b.d.l.							
ET2008/9-1	75.24	**0.13**		**430** (±64)		207 (±121)	115	**284** (±6)	**2046** (±132)	2146 (±44)	42.8	1.6	no
ET2008/9-10a	68.72					**750**			**4440**				yes
ET2008/9-10b	69.49					**430**			**3140**				no
ET2008/9-5	76.52	**0.01**		**2121** (±567)		**461** (±324)			**1376** (±193)		160.9	6.2	yes
ET2008/9-6a	69.77					**153** (±216)			**1897** (±107)				yes
ET2008/9-6b	69.77	**0.17**		**129** (±18)		224 (±161)		**273** (±10)	**1394** (±223)	1654 (±84)	9.0	0.3	no
ET2008/9-7a	69.34	**0.09 (±0.02)**		**118** (±17)		b.d.l.		**42** (±8)	**2410**	778 (±175)	11.3	0.4	yes
ET2008/9-7b	69.34	**0.1**		**87** (±11)		b.d.l.		**46** (±2)	**1905** (±106)	2249 (±109)	5.6	0.2	no
ET2008/9-8	76.85	**0.60 (±0.01)**		**291** (±41)		**975** (±64)		1107 (±84)	**2545** (±488)	3630 (±239)	23.9	0.9	no
ET2008/9-9b	81.38	**0.03**				**953** (±256)			**1500** (±200)				no
ET2008/9-11	69.37					**690**			**2580**				no
ET2008/9-12a	68.90					**150**			**2620**				no
ET2008/9-12b	68.90					**560**			**2590**				yes
ET2008/9-16	70.91	**0.05**				**1100**			**1810**				yes
ET2008/9-18	78.89	**0.22**		**964** (±37)		**240**			**2130**	1697 (±33)	61.3	2.4	yes
ET2008/9-23	69.36	**0.07**		**675** (±14)		**210**			**2350**		35.4	1.4	no
													no
ET2013-1	73.46	**0.11**		**281** (±47)		402 (±106)	371	**508** (±23)	**4272** (±257)	5814 (±296)	17.6	0.7	yes

ET2013-2a	77.28	**0.09**		**339** (±38)		420 (±198)	856	**1047** (±42)	**4220** (±226)	5168 (±246)	25.3	1.0	yes
ET2013-2b	77.28	**0.04 (±0.01)**		**543** (±79)		450		**347** (±117)	n.d.	3562 (±1181)	21.7	0.8	no
ET2013-3a	70.26	**0.01**		**175** (±17)		**147** (±38)	176		**2243** (±136)	407 (±60)	14.1	0.5	no
ET2013-3b	70.26	**0.05 (±0.01)**		**250** (±50)		216 (±147)	282	**275** (±65)	**3760** (±181)	2805 (±671)	19.4	0.7	no
ET2013-3c	70.26	**0.05**		**426** (±40)		320		**364** (±7)	**2650**	3583 (±141)	33.5	1.3	no
ET2013-4	73.47					**128** (±45)	198		**1618** (±207)				yes
ET2013-6a	70.14	**0.08**		**243** (±57)		414 (±142)	381	**576** (±19)	**2928** (±267)	4030 (±149)	21.3	0.8	no
ET2013-6b	70.14	**0.09**		**270** (±44)		310(±135)	434	**440** (±19)	**3202** (±122)	4012 (±192)	23.2	0.9	no
ET2013-7a	68.17					b.d.l.			**3627** (±131)				yes
ET2013-7b	68.17	**0.08**		**581** (±96)		200 (±139)		**292** (±29)	**2607** (±156)	3070 (±348)	49.9	1.9	no
ET2013-7c	68.17					**375** (±290)			**4280** (±255)				no
ET2013-7n	69.62	**0.11**		**126** (±3)		150 (±14)		**197** (±4)	**3740** (±254)	3917 (±75)	6.3	0.2	no
ET2013-11	80.30					**274** (±14)	300		**3356**(±167)				yes
ET2013-12a	71.10	**0.16**				b.d.l.		**63** (±2)	**2400**	3370 (±77)			yes
ET2013-12b	71.10					**250**			**2450**				yes
ET2013-12c	71.10	**0.07**		**139** (±27)		b.d.l.		**180** (±11)	**2677** (±40)	3685 (±258)	6.7	0.3	no
ET2013-12d	71.10					**330**			**2490**				yes
ET2013-14a	74.18	**0.08**		**709** (±139)		161(±87)	100	**528** (±16)	**1749** (±153)	3342 (±122)	65.7	2.5	yes
ET2013-14b	74.18					**284** (±59)	259		**2152** (±85)				no
ET2013-16	76.69	**0.07**		**323** (±59)		b.d.l.		**85** (±4)	**1874** (±163)	2485 (±109)	23.7	0.9	no
ET2013-17a	69.40	**0.09**		**321** (±43)		332 (±200)	397	**509** (±20)	**4242** (±306)	5796 (±252)	23.8	0.9	yes
ET2013-17b	69.40	**0.09**		**233** (±31)		308 (±48)	426	**554** (±24)	**2182** (±173)	2600 (±125)	19.7	0.8	yes
ET2013-17c	69.40					**190**			**1540**				yes
ET2013-17d	69.40	**0.03 (±0.01)**		**545** (±61)		**210**			**2760**		45.8	1.8	no
ET2013-19a	73.39	**0.06**		**1102** (±128)		136 (±41)		**132** (±5)	**1228** (±232)	1680 (±71)	81.4	3.1	yes
ET2013-24			**0.09**		b.d.l.								yes
ET2013-27	77.42	**0.1**		**254** (±8)		320		**364** (±8)	**2340**	3619 (±81)	9.5	0.4	yes
ET2013-30	71.87		**0.14**		b.d.l.	**310**			**2675**		3.7 [ab]	0.1	yes
ET2013-31			**0.28**		b.d.l.								no
ET2013-32	71.51		**0.15**		b.d.l.	b.d.l.			**1910** (±353)		3.9 [ab]	0.2	yes
ET2013-33			**0.17**		b.d.l.								no
ET2013-34	70.97		**0.13**		b.d.l.	**270**			**3350**		3.7 [ab]	0.1	no
ET2013-36	71.58	**0.11**		**483** (±13)		210 (±28)		**320** (±6)	**2210**(±170)	2680 (±55)	21.6	0.8	no
ET2013-37	73.93					b.d.l.			**1770**				yes
ET2013-40			**0.16**		b.d.l.								yes
ET2013-41	77.70		**0.08**		b.d.l.	**145**			**2495** (±78)		2.0 [ab]	0.1	yes

Table 4.3 - Volatile contents in the studied etnean melt inclusions, glass embayments and matrix glasses. Fo = forsteritic content (mol.%) of hosting olivine Numbers inside brackets indicate the standard deviations Data in bold are considered more reliable and therefore used in the discussions. Pressures are calculated using Iacono-Marziano et al. (2012) model; entrapment depths are estimated using a density of 2.65 g cm^{-3} for the basement rocks (Corsaro and Pompilio, 2004).

b.d.l. = below detection limit; n.d. = not determined

* S content estimated by EMP using MORB glasses as reference materials.

[a] = pressure and relative depth (below crater level) calculated using FTIR data. [b] = CO_2 content fixed at 50 ppm (FT-IR detection limit) to calculate pressure, considering the estimated CO_2 detection limit (e.g. Cecchetti et al., 2002; Von Aulock et al., 2014).

4.4. Experimental glasses

The principal goal of these experimental series was to reproduce the high S content measured in the natural etnean melt inclusions in order to understand the conditions that constrained the S contents of the natural melts, and the formation of sulfide globules.

Experimental runs were performed in Internally Heated Pressure Vessels (IHPV) at T = 1200 ± 2°C and P in the range 180-210 MPa, the oxygen fugacity was kept between NNO+0.19 and NNO+1.73, at volatile saturation (H_2O±CO_2+S), using the Mt. Spagnolo composition as starting material. This latter is preferred, among the studied products, because it represent the lava with the most primitive composition (FS products are low-density pyroclastic products, whose bulk composition is more difficult to establish). Moreover, Mt. Spagnolo melt inclusions have the highest sulfur contents.

All experimental charges contained a free fluid phase at the end of the experiment that was documented by the weight loss after piercing the capsules. Using the weight loss the calculated amounts of fluid phase inside the experimental charge are about 6 - 10 wt.%.

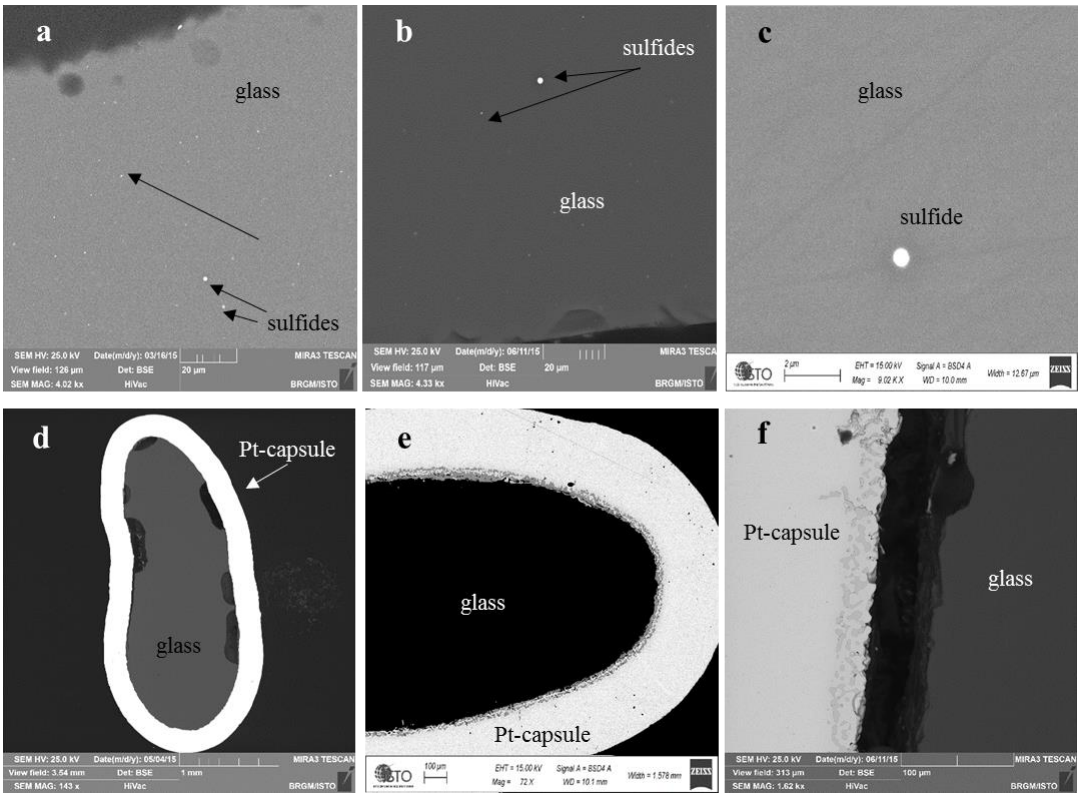

Fig. 4.16 - Backscattered electron images of experimental products: a-b-c) glasses (1702#3-2704#4 - 1902#1) with small sulfide globules. d) Bubbles located at the glass-capsule interface (2703#3); e-f) reaction rims (S-Pt-Fe) in the Pt capsules.

The run products were brown glasses, homogeneous and crystal-free, except small (less than 2-3 μm in diameter) sulfide globules in some runs (figs. 4.16 a-b-c). The sulfide globules appear as bright spheres at the petrographic optical microscope and SEM. Their size did not

allow EMP analysis, only semiquatitative SEM-EDS spectra, which confirmed that they are mainly constituted of Fe, and Pt. Their presence confirm the saturation of the melt with a sulfide phase for the experimental charges performed at the most reducing condition (fO_2 < NNO+1).
Sometimes, few microbubbles were observed in the melt, while larger bubbles are frequently located at the glass-capsule interface, indicating fluid saturation (fig. 4.16d).
The internal walls of all Pt-capsules present a thin rim (up to 60 µm) in which Pt-Fe-S aggregates were found (figs. 4.16 e-f and fig. 4.17).

Major element composition and volatiles contents of the 14 experimental glasses are reported in table 4.4. All glasses have a basaltic composition. Standard deviation for all major elements is generally low (< 0.35), except for FeO (0.24-0.78).
During the experimental run, part of the iron of the melt is indeed lost into the capsule rim (figs. 4.16 e-f). Despite the fact that the capsules were FeO-doped before the runs, the iron contents of the experimental melts are generally lower than the starting material (except for the 2704#2 and 1902#1 runs). The total iron loss during the experiments is between 3 and 30 %, probably depending on the redox conditions, the total FeO content of the melt and the amount of sulfide droplets segregated. Any clear effect is observed between the iron loss and other parameters, only CO_2-bearing glasses obtained at the lowest fO_2 (NNO+0.19 and NNO+0.26) show the highest iron loss.

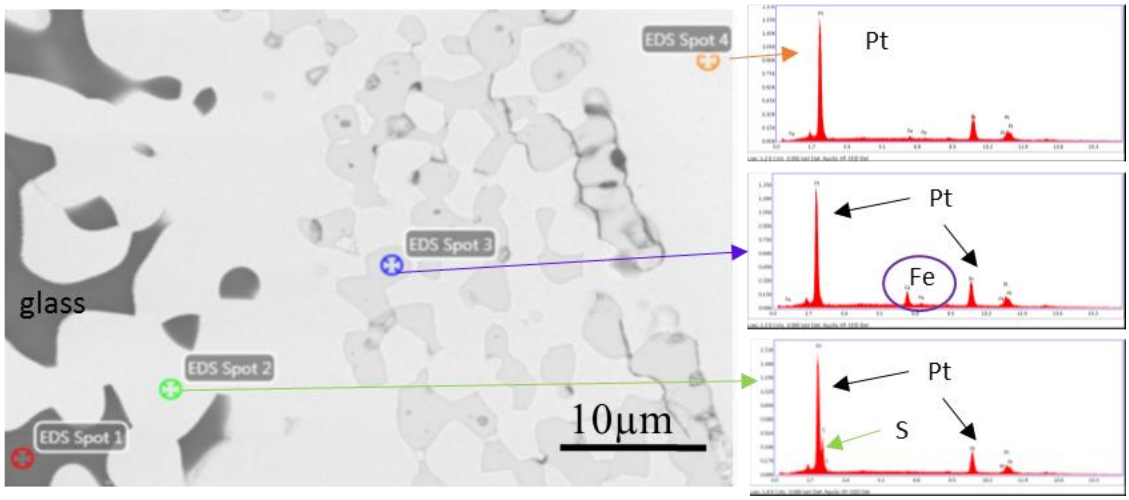

Fig. 4.17 - Backscattered electron image of the capsule rim with the Pt-Fe-S aggregates. On the right 3 spectra acquired by SEM, which confirms the presence of FeO (S and) globules.

Dissolved H_2O content estimated by SIMS (see appendix A5 for comparison with FTIR data) varies between 4.4 and 5.2 wt.% in the glasses without CO_2, while CO_2-bearing glasses (SPA 1702#5, 2703#3, 2703#4, 2704#4) have lower water dissolved (3.4-3.6 wt.%). CO_2 contents of these glasses (also measured by SIMS) are 751-1578 ppm.

The standard deviations associated to water measurements are very low (0.02-0.22wt.% for SIMS and ~0.3wt% for FTIR measurements), indicating that experimental charges are homogeneous also for dissolved water contents.

The sulfur content of quenched glasses estimated by EMP (see appendix A5 for comparison with SIMS data) vary between 759 ppm and 6454 ppm. Standard deviations are between 87 and 410 ppm, with the highest values being associated to the highest S contents. The maximum sulfur contents are found in the glasses prepared at the highest oxygen fugacity (NNO+1.7, table 4.4).

It is very difficult to evaluate the role of the single oxide components of the melt on the S content in these sulfide saturated glasses, given the extremely low variability observed in their major element composition (table 4.4). A general negative correlation of the S content with the SiO_2 content, and a positive correlation with the total FeO content is observed when samples at the same fO_2 are selected (figs. 4.18 a-b). This in agreement with previous studies (e.g., Carroll and Webster, 1994; Liu et al., 2007; Moune et al., 2009; Lesne et al., 2015). The good correlation between the dissolved sulfur (as sulfide) and the FeO in the melt is due to an exchange of S^{2-} with O^{2-} anions associated with Fe^{2+} in melt as described by the equilibrium $FeO_{(melt)} + 1/2S_{2(gas)} = FeS_{(melt)} + 1/2O_{2(gas)}$ (Carroll and Webster, 1994; and references therein).

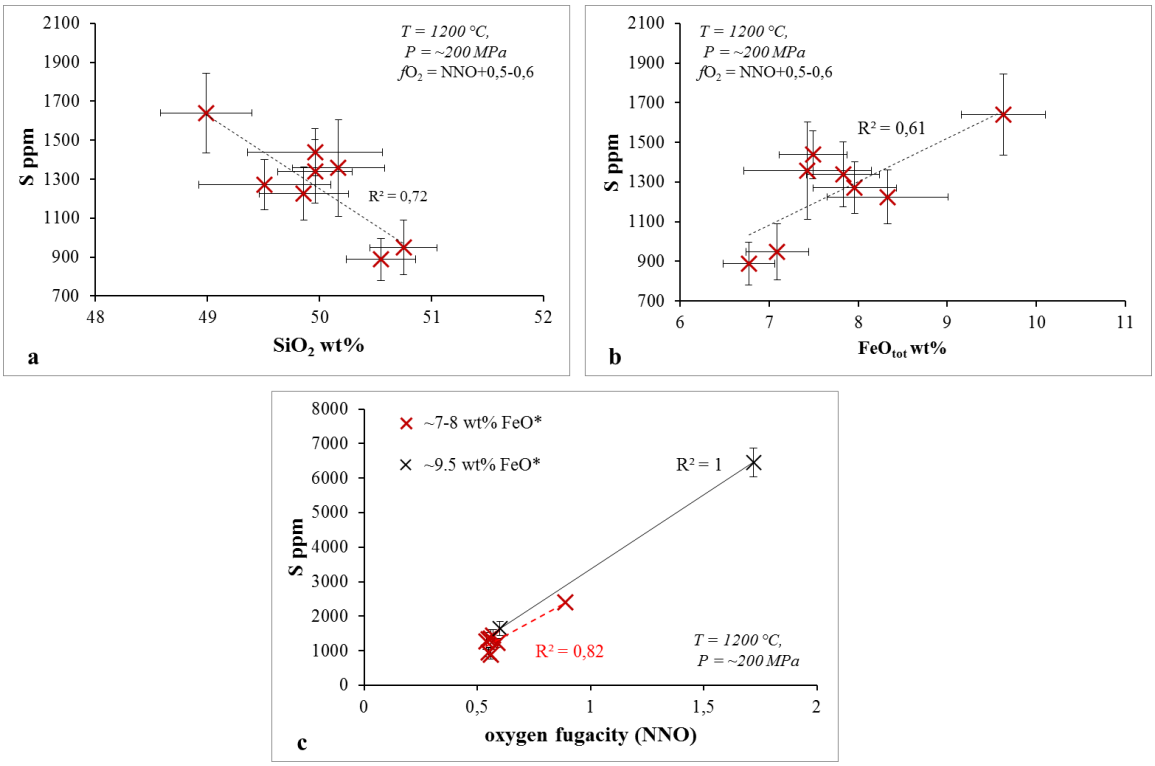

Fig. 4.18 - S content in the experimental basaltic glasses (with FeO_{tot} content of 7-8 wt.%), as a function of a) SiO_2, b) FeO_{tot} and c) fO_2. The oxygen fugacity (expressed as deviation from the Nickel-Nickel Oxide buffer at the give T) seems to be the principal parameter affecting S solubility (highlighted by the highest coefficient of determination, R^2). All data are normalized to 100 %. The error bars indicate the standard deviation.

If we select samples with similar FeO* (= FeO total) and SiO_2 content, but different fO_2 (fig. 4.18c), we can appreciate that oxygen fugacity is the parameter that mostly affect sulfur solubility in our experiments, in agreement with previous authors (e.g., Jugo et al., 2005; and reference therein).

Indeed the effect of the FeO* content varying between 7-8 wt.% and 9.5 wt.% is negligible respect to that of fO_2 varying from ~ NNO+0.6 (888-1438 ppm S) to ~ NNO+0.9 (~ 2395 ppm S) or NNO+1.7 (~ 6454 ppm S).

If compared with the natural products, the experimental glass compositions seem to approach some MIs from Mt. Spagnolo and FS eruptions, above all for FeO contents (fig. 4.19a). In detail, the dissolved water in the experimental glasses approach the most undegassed studied melt inclusions (FS eruption, fig. 4.19b). S contents in the experimental glasses (759-6454 ppm) reproduce those measured in most of the investigated melt inclusions (from FS and Mt. Spagnolo eruptions) and part of those from 2002/2003, 2006 and 2008/2009 eruptions (fig. 4.19).

These experimental glasses were used also as standards for $Fe^{3+}/\Sigma Fe$ XANES acquisitions and $\delta^{34}S$ estimations by SIMS.

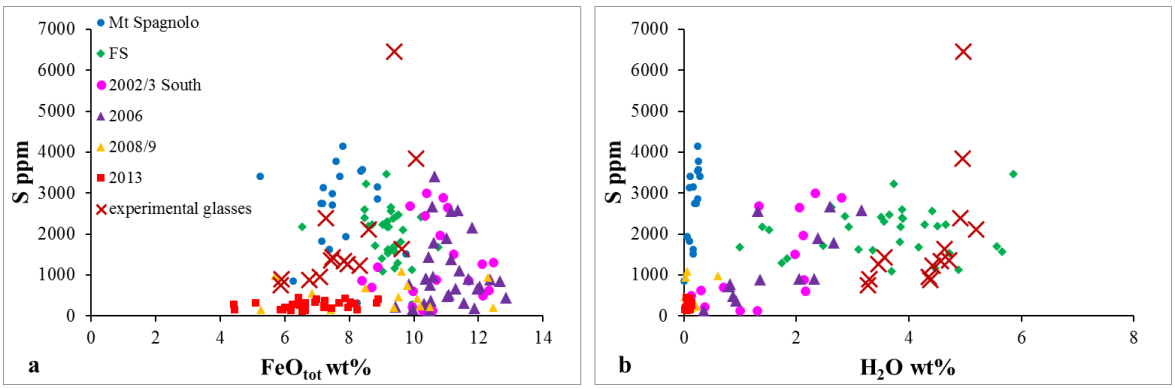

Fig. 4.19 - S content versus FeO and H_2O abundance in the experimental glasses and etnean studied melt inclusions (FeO content corrected for PEC)..

4.4.1 Calculation of S content in the fluid phase and fluid/melt partitioning

The concentrations of sulfur in the volatile phase at run conditions were determined by mass balance calculations

$$S_{tot} = (\%_{fluid} \cdot S_{fluid}) + (\%_{melt} \cdot S_{melt})$$

between the added sulfur in the experimental charge (S_{tot}) and the sulfur measured in the quenched melt (S_{melt}), neglecting the sulfur entrapped in the sulfide globules and in the reaction capsule's wall (length < 20 µm, except for the chips 2704 #3 and #4 for which the length of reaction's wall is slightly higher). The gas phase ($\%_{fluid}$) is calculated from the weight loss evaluated between the weight of the capsule after-experiment and the weight of the opened capsules, after heating at 100 °C. The melt phase ($\%_{melt}$) is the difference of the fluid phase ($\%_{fluid}$) to 100.

Therefore, $D_S^{fluid/melt}$ (= S_{fluid}/S_{melt}) is calculated using the amount of the sulfur dissolved in the experimental glasses (S_{melt}) and the sulfur exsolved in the gas phase (S_{fluid}). This value is extremely variable, from 58.5 to 394. These values are in the range of those previously estimated for basaltic composition and similar experimental condition, but exceed the upper limit ($D_S^{fluid/melt}$ = 10-209 (e.g. Beermann et al., 2010; Lesne et al., 2011; Fiege et al., 2015). Considering that the P-T experimental conditions are constant, and neglecting any compositional effect (mainly of FeO^*_{melt} content in the melt), the only variable parameters affecting $D_S^{fluid/melt}$ are the oxygen fugacity and the added S. At constant content of added sulfur, the S partition coefficient values decreases with the increase of oxygen fugacity (fig. 4.20) according with previous studies (e.g. Fiege et al., 2015). The minor values are for the experimental glasses more oxidized, while the highest values are in the experimental glasses (2704 #3 and #4) with 4 wt.% of S added, and with an oxygen fugacity of $0.2 \leq NNO \geq 0.9$. These glasses had shown the largest reaction capsule's wall (figs. 4.16e-f and 4.17), indicating that probably high S amount is lost in the capsule and therefore the calculated $D_S^{fluid/melt}$ is not very representative of the fluid/melt sulfur partitioning. The average value of $D_S^{fluid/melt}$ is 175±108.

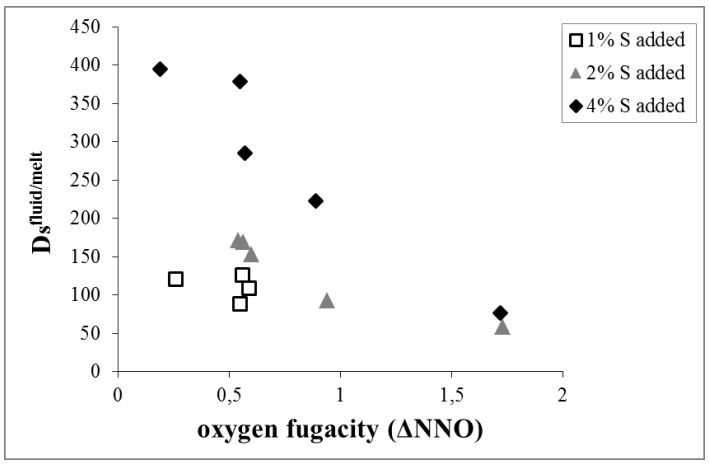

Fig. 4.20 - Sulfur partition coefficient between fluid and melt as function of the oxygen fugacity in the experimental glasses at constant temperature (1200 °C) and pressure (200 MPa).

run	SiO_2	TiO_2	Al_2O_3	FeO	MnO	MgO	CaO	Na_2O	K_2O	P_2O_5	Tot	Fe loss%	Mg#[a]	MFM[b]	H_2O	CO_2	S	log f_{O_2}	ΔNNO	$D_S^{fluid/melt}$ [c]
Spa1702#1	50.55 (±0.31)	1.49 (±0.11)	14.60 (±0.19)	6.77 (±0.29)	0.16 (±0.09)	9.31 (±0.16)	11.80 (±0.13)	3.38 (±0.10)	1.30 (±0.09)	0.57 (±0.13)	94.0	-27.3	71.0	4.44	4.38 (±0.10)		888 (±108)	-7.15	0.56 (±0.13)	126
Spa1702#2	50.75 (±0.30)	1.50 (±0.13)	14.64 (±0.19)	7.09 (±0.35)	0.19 (±0.10)	9.02 (±0.11)	11.71 (±0.13)	3.26 (±0.08)	1.28 (±0.07)	0.5 (±0.14)	93.3	-23.8	69.4	4.35	4.35 (±0.04)		948 (±140)	-7.16	0.55 (±0.13)	88
Spa1702#3	49.86 (±0.40)	1.43 (±0.02)	14.30 (±0.08)	8.33 (±0.68)	0.15 (±0.12)	9.07 (±0.05)	11.57 (±0.15)	3.35 (±0.05)	1.30 (±0.02)	0.56 (±0.02)	94.4	-10.4	66.0	4.57	4.42 (±0.03)		1225 (±136)	-7.12	0.59 (±0.13)	109
Spa1702#5	51.85 (±0.37)	1.55 (±0.12)	14.61 (±0.23)	5.88 (±0.24)	0.17 (±0.09)	8.88 (±0.07)	12.01 (±0.08)	3.20 (±0.08)	1.32 (±0.08)	0.48 (±0.14)	94.0	-36.8	72.9	4.25	3.27 (±0.04)	850 (±27)	759 (±87)	-7.45	0.26 (±0.13)	121
Spa2703#1	49.36 (±0.58)	1.47 (±0.13)	14.36 (±0.24)	8.61 (±0.42)	0.16 (±0.10)	9.08 (±0.26)	11.71 (±0.19)	3.26 (±0.13)	1.30 (±0.09)	0.61 (±0.12)	90.9	-7.4	65.3	4.56	5.19 (±0.03)		2116 (±173)	-6.76	0.94 (±0.14)	93
Spa2703#2	50.11 (±0.83)	1.45 (±0.10)	14.52 (±0.20)	7.28 (±0.78)	0.17 (±0.08)	9.35 (±0.14)	11.85 (±0.13)	3.34 (±0.10)	1.31 (±0.10)	0.61 (±0.15)	90.6	-21.7	69.6	4.48	4.92 (±0.14)		2395 (±260)	-6.81	0.89 (±0.14)	222
Spa2703#3	49.51 (±0.59)	1.50 (±0.13)	14.58 (±0.32)	7.96 (±0.47)	0.16 (±0.09)	9.35 (±0.16)	11.68 (±0.19)	3.36 (±0.08)	1.31 (±0.08)	0.60 (±0.13)	92.6	-14.4	67.7	4.59	3.46 (±0.03)	1578 (±14)	1271 (±130)	-7.16	0.54 (±0.14)	172
Spa2703#4	49.96 (±0.60)	1.45 (±0.11)	14.56 (±0.27)	7.49 (±0.38)	0.18 (±0.10)	9.30 (±0.15)	11.78 (±0.17)	3.36 (±0.09)	1.32 (±0.10)	0.58 (±0.14)	92.9	-19.8	68.9	4.54	3.56 (±0.03)	1242 (±16)	1438 (±120)	-7.13	0.57 (±0.14)	285
Spa2704#1	50.17 (±0.41)	1.45 (±0.10)	14.54 (±0.28)	7.43 (±0.72)	0.15 (±0.10)	9.22 (±0.16)	11.72 (±0.19)	3.46 (±0.09)	1.26 (±0.08)	0.61 (±0.12)	94.0	-21.8	68.9	4.51	4.71 (±0.03)		1357 (±247)	-7.15	0.56 (±0.12)	170
Spa2704#2	48.99 (±0.41)	1.40 (±0.10)	14.07 (±0.19)	9.63 (±0.47)	0.16 (±0.08)	9.13 (±0.12)	11.33 (±0.15)	3.42 (±0.09)	1.27 (±0.09)	0.61 (±0.15)	93.7	1.4	62.8	4.79	4.63 (±0.22)		1640 (±205)	-7.10	0.60 (±0.12)	153
Spa2704#3	49.96 (±0.33)	1.46 (±0.12)	14.37 (±0.17)	7.83 (±0.41)	0.17 (±0.10)	9.26 (±0.10)	11.60 (±0.14)	3.47 (±0.09)	1.29 (±0.08)	0.58 (±0.15)	94.0	-17.6	67.8	4.61	4.56 (±0.10)		1338 (±163)	-7.15	0.55 (±0.12)	379
Spa2704#4	50.94 (±0.51)	1.49 (±0.11)	14.84 (±0.21)	5.90 (±0.33)	0.17 (±0.10)	9.48 (±0.17)	11.66 (±0.15)	3.63 (±0.21)	1.33 (±0.10)	0.56 (±0.15)	94.6	-37.9	74.1	4.40	3.30 (±0.02)	751 (±8)	896 (±164)	-7.51	0.19 (±0.12)	394
Spa1902#1	49.44 (±0.34)	1.41 (±0.14)	14.00 (±0.18)	10.07 (±0.41)	0.16 (±0.04)	9.08 (±0.14)	11.36 (±0.14)	3.22 (±0.11)	1.26 (±0.09)	n.d.	92.8	4.1	61.7	4.45	4.96 (±0.08)		3849 (±341)	-5.98	1.73 (±0.47)	59
Spa1902#2	49.93 (±0.33)	1.41 (±0.13)	14.11 (±0.19)	9.40 (±0.36)	0.16 (±0.04)	9.07 (±0.10)	11.39 (±0.13)	3.26 (±0.15)	1.27 (±0.07)	n.d.	92.4	-2.9	63.2	4.35	4.97 (±0.10)		6454 (±410)	-5.98	1.72 (±0.47)	77

Table 4.4 - Major elements and S contents in the experimental glasses measured by EMP. H_2O and CO_2 content from SIMS measurements. Numbers in brackets indicate the standard deviations (1σ). Major elements, H_2O and CO_2 content are expressed in wt.%; S and Cl in ppm.

[a] Mg# = 100 x $Mg/(Mg+Fe_{tot})$;

[b] MFM = $Na+K+2(Ca+Mg+Fe^{2+})/Si(Al+Fe^{3+})$ as defined in Fortin et al. (2015);

[c] $D_S^{fluid/melt}$ = S partition coefficient between the fluid and melt.

(n.d. = not determined)

4.4.2 Sulfur Content at Sulfide Saturation (SCSS) models

The sulfur content measured in the sulfide-saturated glasses synthetized for this study represent the maximum amounts of sulfur that the melt can dissolve at the different oxygen fugacity, and is indicated as *sulfur content at sulfide saturation* [SCSS, (Liu et al., 2007; Fortin et al., 2015)].

Many studies have investigated the SCSS at various temperatures, pressures, melt compositions, and oxygen fugacities, generally at anhydrous conditions (e.g., Haughton et al., 1974; Wallace and Carmichael, 1992; Mavrogenes and O'Neill, 1999; O'Neill and Mavrogenes, 2002; Li and Ripley, 2005; Jugo, 2009).

Only Liu et al. (2007), Li and Ripley (2009), and Fortin et al. (2015) incorporate the effect of water in their models for calculating the SCSS in basaltic magma.

We calculated the SCSS in our experimental glasses using these models. The Liu et al. (2007) model is based on the reaction describing the dissolution of sulfide:

$$FeS_{sulfide} + FeO_{melt} + O^{2-}{}_{melt} <==> S^{2-}{}_{melt} + 2FeO_{sulfide}$$

where $FeS_{sulfide}$ and $FeS_{sulfide}$ represent the FeS and FeO present in the sulfide phase, and FeO_{melt} represents the FeO in the silicate melt. The effect of the melt composition on the SCSS is approximated by the MFM parameter:

$$[Na+K+2(Ca+Mg+Fe^{2+})] / [Si*(Al+Fe^{3+})]$$

where Na, K, Ca, Mg, Fe^{2+}, Si, Al, Fe^{3+} indicate the mole fractions of these elements in the melt. The MFM parameters is a revised version of the FM parameter created by Ryerson and Watson (1987), used as a compositional factor to predict rutile saturation in magmas, and itself was modified from the M parameter of Watson and Harrison (1983) designed for predicting zircon saturation (Liu et al., 2007).

Li and Ripley (2009) updated the previously anhydrous SCSS model of Li and Ripley (2005) by incorporating hydrous experimental results from the literature. The algorithm calculates the SCSS as a function of temperature, pressure, some oxides constituting the melt (FeO, TiO_2 CaO, SiO_2) and H_2O. Fortin et al. (2015) use their experimental data and other data from literature to define a further SCSS model, giving greater importance to the water effect.

Comparing calculated values with the measured ones for our samples (fig. 4.21), shows that Fortin et al. (2015) generally overestimate measured S contents, while the others models generally well reproduce measured S content for values lower than 1400 ppm (Li and Ripley, 2009) and 1000 ppm (Liu et al., 2007). This is most likely due to the fact that these three models do not consider the effect of fO_2 on the SCSS, which represents the primary factor affecting the S content of our oxidized glasses.

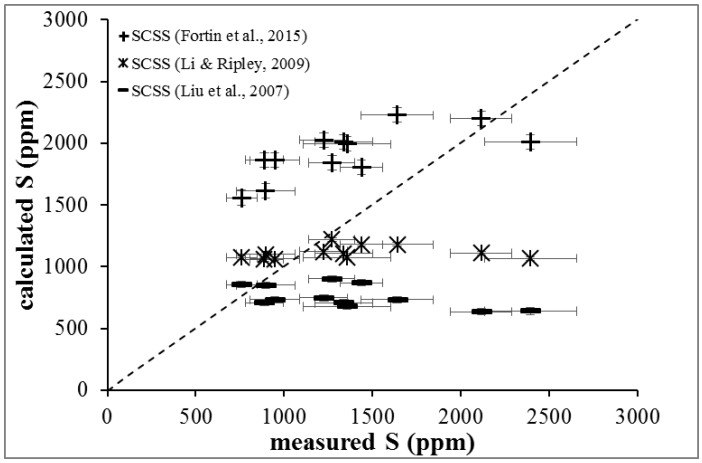

Fig. 4.21 - SCSS calculated in our experimental glasses using the models of Liu et al. (2007), Li and Ripley (2009), Fortin et al. (2015). The error bars indicate the standard deviation. The dashed line indicate the 1:1 continuous line.

4.5. XANES measurement of $Fe^{3+}/\Sigma Fe$ ratios and fO_2 calculation

Speciation of iron (or other polyvalent elements) strongly depends on the redox condition of the system. XANES spectra of $Fe^{3+}/\Sigma Fe$ ratio of melt inclusions were acquired in order to evaluate the oxygen fugacity and therefore the redox condition of Etnean magmas.

XANES results for some of the experimental glasses (except for the 1902#1 and 1902#2, prepared afterwards) and for double-polished melt inclusions are reported in tables 4.5 and 4.6. The calculated $Fe^{3+}/\Sigma Fe$ ratios, using the calibration of Cottrell et al. (2009), range from 0.32 to 0.39 for the experimental products. The precision (1σ) of the XANES $Fe^{3+}/\Sigma Fe$ ratio is 0.0045 (Cottrell et al., 2009; Moussallam et al., 2016). Measured values are systematically higher than those calculated using the empirical formulation of Kress and Carmichael (1991) from the experimental fO_2 (named "experimental" in table 4.5 and fig. 4.22). This formulation relates the $Fe^{3+}/\Sigma Fe$ ratio of the silicate melt to the oxygen fugacity, and accounts for the effects of melt compositions, pressure and temperature. Both the measured (XANES) and the calculated (experimental) $Fe^{3+}/\Sigma Fe$ ratios increase with the H_2O and S contents of the melt (figs. 4.23 a-b). The error associated with the calculated "experimental" $Fe^{3+}/\Sigma Fe$ ratio was estimated from the uncertainty in the experimental fO_2 (see the paragraph 3.1), which is in turn calculated from the amount (in bar) ± 0.5 bar of H_2 loaded in the vessel. Typical uncertainties on $Fe^{3+}/\Sigma Fe$ ratios are between 0.010 and 0.013 for more reduced samples and 0.052 for the most oxidized ones.

The discrepancy between measured (XANES) and calculated (experimental) $Fe^{3+}/\Sigma Fe$ ratios (0.09±0.02) significantly exceeds estimated uncertainties (figs. 4.22, 4.23 a-b). Consequently, fO_2 values calculated from XANES $Fe^{3+}/\Sigma Fe$ ratios are almost one log unit above the experimental fO_2.

A possible explanation for this discrepancy is that the exposure of volatile-rich basaltic samples to a µ-XANES X-ray beam could cause Fe oxidation, as observed in H_2O-rich basalts by Cottrell et al. (2016). This effect has not been observed in dry glasses, despite specific investigations (Cottrell and Kelley, 2009; Moussallam et al., 2014). Considering that the standard glasses used for XANES analyses are volatile-free while the etnean experimental glasses are H_2O and S-rich, we looked for a possible effect of H_2O or S, without finding any clear one (figs. 4.23 a-b-c-d). One the contrary, we observed a clear negative correlation between the difference between the XANES and the experimental calculated $Fe^{3+}/\Sigma Fe$ ratios and the FeO_{tot} content (R^2=0.70, fig. 4.23e), the lowest differences being observed for FeO_{tot} contents close to 10 wt.%. This could be a consequence of the difference in FeO_{tot} content between the experimental glasses (5.88-10.07 wt.%; table 4.4) and the standard glasses used for the calibration (9.53-10.17 wt.%; Cottrell et al., 2009).

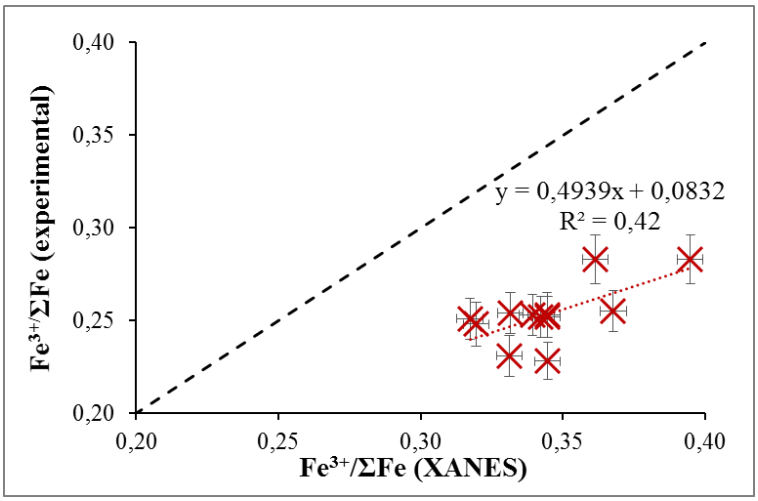

Fig. 4.22 - $Fe^{3+}/\Sigma Fe$ ratios estimated by XANES spectroscopy in the etnean experimental glasses, and those calculated using Kress and Carmichael (1991) and the experimental fO_2. Error bars indicate the precisions (1σ) of XANES measurements (=0.0045) as defined in Cottrell et al. (2009) and Moussallam et al. (2016); while the errors in the experimental $Fe^{3+}/\Sigma Fe$ ratios are calculated from the error associated at the experimental fO_2 (as described in the text).

Although we are not sure about the reason of the discrepancy observed in figure 4.22, we think that our experimental glasses are more similar to the Etnean melt inclusions than the standard glasses used for the calibration, in terms of H_2O, S and FeO_{tot} contents.
Consequently, we used the experimental glasses to provide a further correction for the XANES $Fe^{3+}/\Sigma Fe$ ratios of the studied Etnean volatile-rich melt inclusions. We used the equation of the regression line in figure 4.22 to obtain the "corrected $Fe^{3+}/\Sigma Fe$" values in table 4.6.

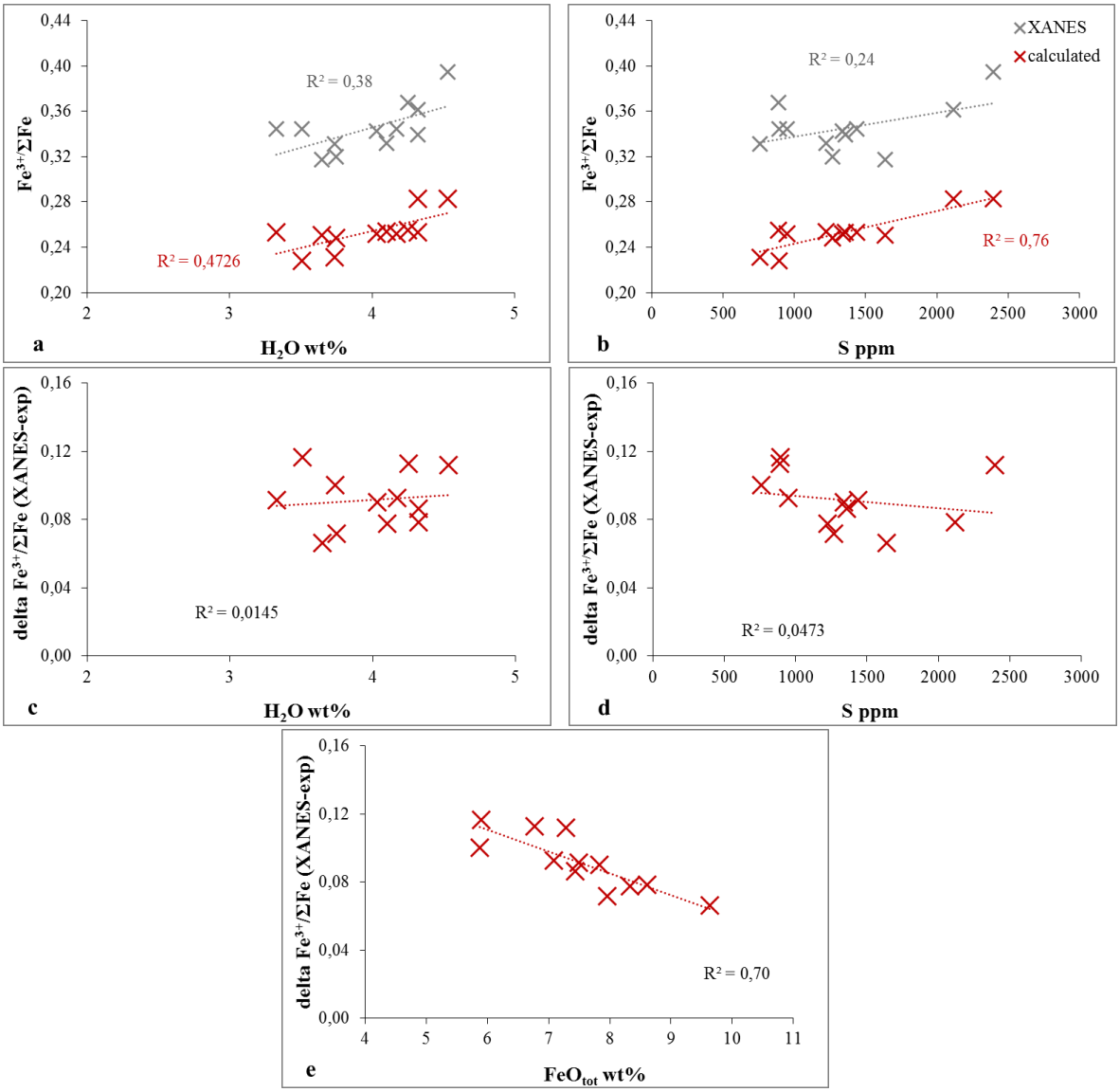

Fig. 4.23 - a-b) $Fe^{3+}/\Sigma Fe$ ratios estimated by XANES spectroscopy (gray symbols) and those previously calculated from the experimental fO_2 (using Kress and Carmichael, 1991) in the experimental glasses (red symbols), versus H_2O and S contents. The difference between XANES $Fe^{3+}/\Sigma Fe$ ratios and experimental $Fe^{3+}/\Sigma Fe$ ratios versus H_2O (c), S (d) and FeO_{tot} (e) contents in the experimental glasses.

The major limit of this approach is that the range of measured $Fe^{3+}/\Sigma Fe$ ratios is narrower for the experimental glasses (0.2-0.3) than for the MIs (0.1-0.5). This implies that the applied correction is less robust for some MIs with $Fe^{3+}/\Sigma Fe$ ratios higher or lower than those of experimental glasses.

Both corrected and directly measured $Fe^{3+}/\Sigma Fe$ ratios do not show any correlation with the estimated values of PEC %, therefore we exclude any effect of post-entrapment crystallization (PEC) on the $Fe^{3+}/\Sigma Fe$ evaluation (fig. 4.24a). This is more evident for the FS inclusions, characterized by a large interval of PEC% (0-10), that present a similar $Fe^{3+}/\Sigma Fe$ ratio (mean of 0.32±0.01), but also a rather constant K_2O content (0.87±0.21 wt.%)

and CaO/Al_2O_3 ratio (1.36±0.08) (figs. 4.24 b-c). Only the $Fe^{3+}/\Sigma Fe$ ratio estimated for the MI "Spa-O1" (0.14) could be affected by post entrapment process, considering that the corrected value of the other inclusions is 0.26 while for the embayment "Spa-N" is 0.18. The embayments and matrix glasses from 2002/2003 and 2006 eruptions generally present $Fe^{3+}/\Sigma Fe$ ratios lower than those of melt inclusions.

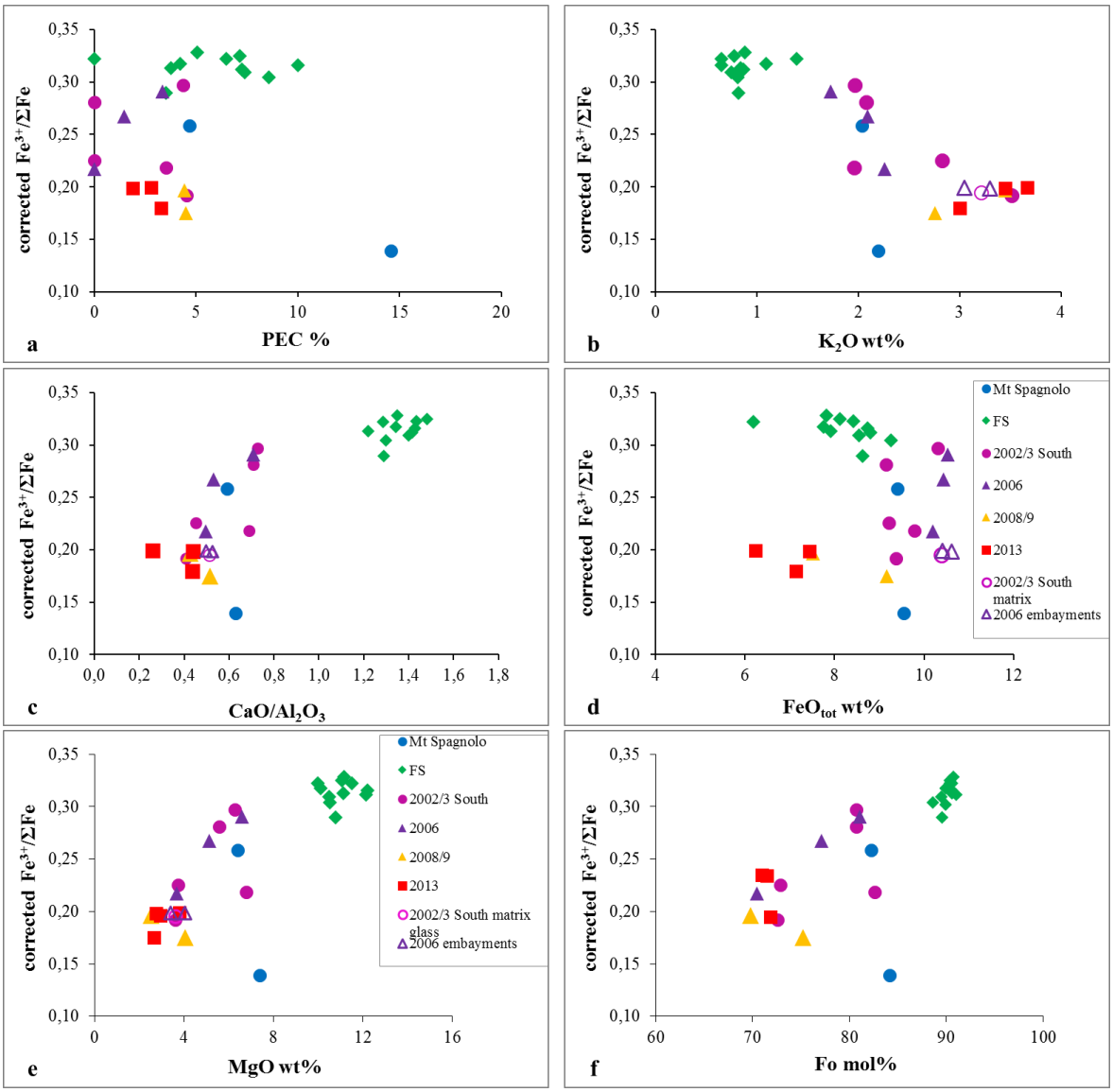

Fig. 4.24 - a) Plot of $Fe^{3+}/\Sigma Fe$ ratios with calculated amount of post-entrapment crystallization (in %) for each melt inclusion. b) $Fe^{3+}/\Sigma Fe$ ratios versus K_2O contents, used as index of melt differentiation. c) $Fe^{3+}/\Sigma Fe$ ratios versus CaO/Al_2O_3 ratio and d) FeO_{tot} content. The absence of correlation between the $Fe^{3+}/\Sigma Fe$ ratios and PEC shows that post-entrapment processes are unlikely to have exerted a strong influence on the measured Fe oxidation state. The slight correlation with K_2O contents and CaO/Al_2O_3 ratio indicate a possible change in the $Fe^{3+}/\Sigma Fe$ ratio with differentiation.

A general inverse correlation with the degree of differentiation is evident, except for sample Spa O1: $Fe^{3+}/\Sigma Fe$ ratios decrease with the decrease of the forsteritic content of the host olivine crystal, of the CaO/Al_2O_3 ratio and of the MgO content, and with the increase of the K_2O content (figs. 4.24 b-c-e-f). Considering the results all-together, FS and 2008/2009-2013 MIs have respectively the highest (~0.31±0.01) and the lowest (~0.19±0.01) $Fe^{3+}/\Sigma Fe$ ratios. Less clear is the trend with the total FeO content (fig. 4.24d), revealing a tricky effect of the crystallization of Fe-bearing minerals on the $Fe^{3+}/\Sigma Fe$ ratio.

In figure 4.25 $Fe^{3+}/\Sigma Fe$ ratios of MIs are plotted versus their volatiles contents (H_2O, CO_2, S and Cl). Despite the important scatter in the data, $Fe^{3+}/\Sigma Fe$ generally decreases with the decrease of H_2O and less clearly with the decrease of S and CO_2 dissolved in the melt. This good relation seems suggesting a reduction of $Fe^{3+}/\Sigma Fe$ ratio in the melt during the degassing process. No clear correlation exists between the Fe oxidation state and the Cl content.

These corrected values of $Fe^{3+}/\Sigma Fe$ ratio were translated into oxygen fugacity using the semi empirical equation of Kress and Carmichael (1991). Considering the temperature range of 1100-1200 °C and the range of pressure values, previously estimated for each melt inclusions from H_2O-CO_2 content (table 4.3), the calculated fO_2 for the investigated etnean melt inclusions vary from 1.3 log units above the Nickel - Nickel Oxide buffer (NNO) to 0.9 log units below the same NNO buffer.

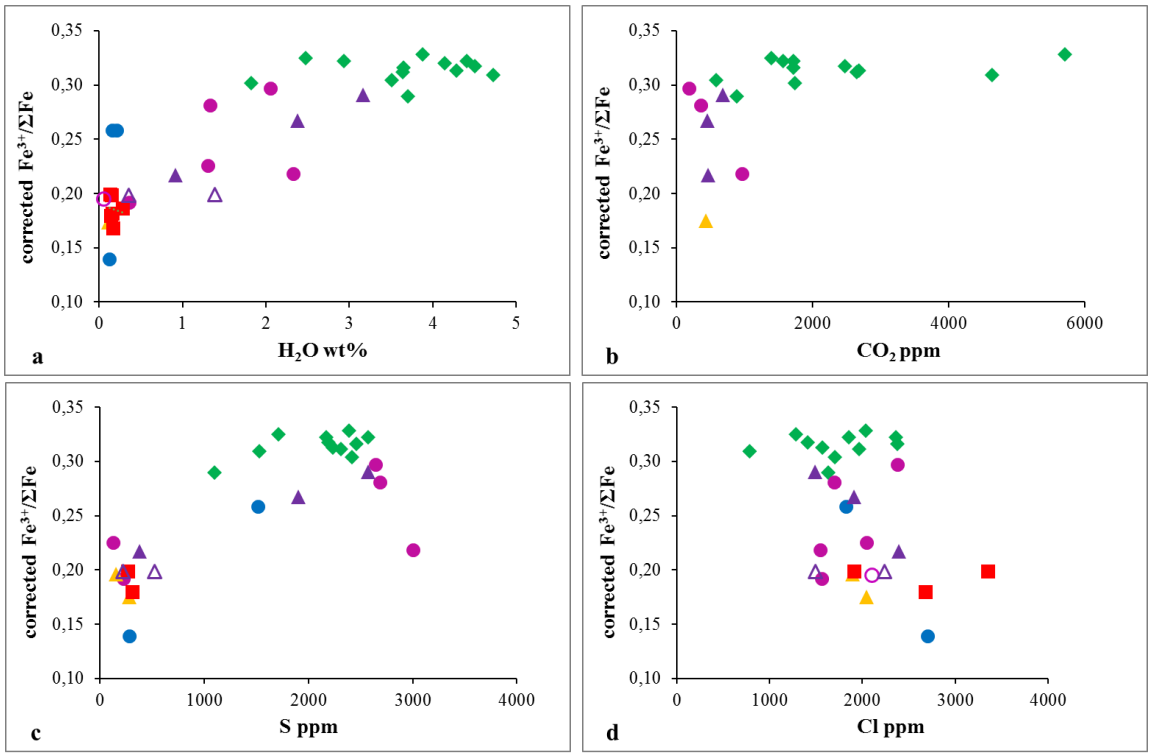

Fig. 4.25 - The corrected $Fe^{3+}/\Sigma Fe$ ratios compared with H_2O (a), CO_2 (b), S (c) and Cl (d) abundance determined in the glassy inclusions. For the symbols, see the caption of figure 4.24.

					experimental estimation			from XANES spectra		
name run	**P_{tot} (MPa)**	**H_2O (wt.%)**	**CO_2 (ppm)**	**S (ppm)**	**log fO_2**	**ΔNNO**	**$Fe^{3+}/\Sigma Fe$**	**centroid energy**	**$Fe^{3+}/\Sigma Fe$**	**log fO_2**
Spa1702#1	180	4.38 (±0.10)		888 (±108)	-7.15	0.56 (±0.13)	**0.26**	7113.839	**0.37**	-5.99
Spa1702#2	180	4.35 (±0.04)		948 (±140)	-7.16	0.55 (±0.13)	**0.25**	7113.786	**0.34**	-6.24
Spa1702#3	180	4.42 (±0.03)		1225 (±136)	-7.12	0.59 (±0.13)	**0.25**	7113.755	**0.33**	-6.32
Spa1702#5	180	3.27 (±0.04)	850 (±27)	759 (±87)	-7.45	0.26 (±0.13)	**0.23**	7113.754	**0.33**	-6.39
Spa2703#1	210	5.19 (±0.03)		2116 (±173)	-6.76	0.94 (±0.14)	**0.28**	7113.824	**0.36**	-6,00
Spa2703#2	210	4.92 (±0.14)		2395 (±260)	-6.81	0.89 (±0.14)	**0.28**	7113.900	**0.39**	-5.77
Spa2703#3	210	3.46 (±0.03)	1578 (±14)	1271 (±130)	-7.16	0.54 (±0.14)	**0.25**	7113.727	**0.32**	-6.42
Spa2703#4	210	3.56 (±0.03)	1242 (±16)	1438 (±120)	-7.13	0.57 (±0.14)	**0.25**	7113.785	**0.34**	-6.23
Spa2704#1	193	4.71 (±0.03)		1357 (±247)	-7.15	0.56 (±0.12)	**0.25**	7113.773	**0.34**	-6.25
Spa2704#2	193	4.63 (±0.22)		1640 (±205)	-7.10	0.60 (±0.12)	**0.25**	7113.722	**0.32**	-6.37
Spa2704#3	193	4.56 (±0.10)		1338 (±163)	-7.15	0.55 (±0.12)	**0.25**	7113.780	**0.34**	-6.24
Spa2704#4	193	3.30 (±0.02)	751 (±8)	896 (±164)	-7.51	0.19 (±0.12)	**0.23**	7113.786	**0.34**	-6.30
Spa1902#1	200	4.96 (±0.08)		3849 (±341)	-5.98	1.73 (±0.47)	**0.36**	n.d.	n.d.	
Spa1902#2	200	4.97 (±0.10)		6454 (±410)	-5.98	1.72 (±0.47)	**0.36**	n.d.	n.d.	

Table 4.5 - $Fe^{3+}/\Sigma Fe$ ratios and log fO_2 in the experimental glasses estimated by Kress and Carmichael (1991). XANES $Fe^{3+}/\Sigma Fe$ ratios are estimated using the MORB standard glasses in Cottrell et al. (2009). The precision (1σ) of the centroid energy and XANES $Fe^{3+}/\Sigma Fe$ ratio are 0.011 and 0.004 (Cottrell et al., 2009; Moussallam et al., 2016).

sample name	**Fo mol. %**	**H_2O wt.%**	**CO_2 (ppm)**	**S (ppm)**	**Cl (ppm)**	**P (MPa)**	**Depth (km)**	**centroid energy**	**$Fe^{3+}/\Sigma Fe$**	**corrected $Fe^{3+}/\Sigma Fe$**	**log fO_2**	**ΔNNO**
Spa-3n	82.27	0.16 (±0.07)	b.d.l.	1515	1820	5.9	0.2	7113.81	0.35	0.26	-7.46	0.50
Spa-N								7113.81	0.35	0.26		
Spa-N embayment								7113.42	0.20	0.18		
Spa-O1	84.12	0.12	b.d.l.	280	2700	3.9	0.2	7113.20	0.11	*0.14*	-10.05	-2.09
FS-00	89.54	3.70 (±0.05)	882 (±72)	1100 (±179)	1633	158.1	6.1	7113.95	0.42	0.29	-6.76	0.95
FS-03c	89.48	4.72 (±0.07)	4635 (±434)	1533 (±225)	783	408.6	15.7	7114.04	0.46	0.31	-6.4	1.27
FS-09 n	90.73	3.88	5709	2390 (±332)	2033	454.7	17.5	7114.12	0.5	0.33	-6.42	1.29
FS-23								7114.14	0.51	0.33		
FS-24	88.64	3.51 (±0.04)	580 (±83)	2420	1700	114	4.4	7114.02	0.45	0.30	-6.61	1.11
FS-25	90.56	3.65 (±0.10)	1720 (±186)	2463 (±175)	2380	190.1	7.3	7114.07	0.47	0.32	-6.45	1.26
FS-28a	90.35	4.41 (±0.02)	1567 (±138)	2570 (±226)	2365	184	7.1	7114.09	0.48	0.32	-6.44	1.27
FS-28b	90.35	2.48	1396	1710 (±198)	1285	162	6.2	7114.11	0.49	0.33	-6.49	1.23

FS-A								7114.08	0.48	0.32		
FS-D	90.60	4.28	2687	2235 (±205)	1570	271.2	10.4	7114.05	0.47	0.31	-6.42	1.25
FS-E	90.56	2.93 (±0.03)	1718 (±210)	2169 (±488)	1851	203.3	7.8	7114.09	0.48	0.32	-6.61	1.09
FS-Xa	89.92	4.50 (±0.15)	2482 (±123)	2190 (±160)	1410	240.3	9.3	7114.07	0.47	0.32	-6.53	1.17
FS-Xb	89.92	1.82	1741					7114.01	0.44	0.30		
FS-Z	91.02	3.56	2645	2310 (±212)	1965 (±430)	231.5	8.9	7114.05	0.46	0.31	-6.52	1.18
ET2002/3S-23	82.61	2.33 (±0.01)	963(±16)	3005	1545	122.9	4.7	7113.62	0.27	0.22	-8.18	0.1
ET2002/3S-26	72.57	0.36 (±0.02)		225 (±78)	1560			7113.48	0.22	0.19	-8.7	-0.43
ET2002/3S-32	72.90	1.30	b.d.l.	128 (±92)	2043	27.4	1.1	7113.65	0.29	0.23	-7.95	0.32
ET2002/3S-33a	80.68	1.33	353	2687 (±172)	1697	52.4	2.0	7113.91	0.4	0.28	-7.42	0.85
ET2002/3S-33b	80.68	2.0 (±0.14)	181	2643 (±207)	2380	52.6	2.0	7113.98	0.43	0.30	-7.2	1.07
ET2002/3S-32 gm				b.d.l.	2100			7113.5	0.23	0.19	-9.41	-0.51
ET2002/3S-33 gm								7113.61	0.27	0.22		
ET2006-4	70.48	0.92 (±0.02)	470	380	2390	62.4	2.4	7113.61	0.27	0.22	-8.25	0.05
ET2006-7	81.08	3.16 (±0.14)	678 (±77)	2573 (±159)	1493	130.6	5.0	7113.96	0.42	0.29	-7.29	0.74
ET2006-B3a	77.15	2.38 (±0.08)	450 (±49)	1903 (±127)	1910	106.9	4.1	7113.85	0.37	0.27	-7.51	0.79
ET2006-7 embayment	81.08	0.36	b.d.l.	525	2240	2.4	2.2	7113.52	0.23	0.20	-9.35	-0.41
ET2006-E2 embayment	70.19	1.39	b.d.l.	220	1497	30.1	3.2	7113.52	0.23	0.20	-9.12	-0.18
ET2008/9-1	75.24	0.13	430(±64)	284	2046	42.8	1.6	7113.39	0.19	0.18	-9.25	-0.31
ET2008/9-6a	69.77			153	1897			7113.51	0.23	0.20	-9.32	-0.38
ET2013-24		0.09	b.d.l.					7113.48	0.22	0.19		
ET2013-30	71.87	0.14	b.d.l.	310	2675	3.7	0.1	7113.42	0.2	0.18	-9.84	-0.90
ET2013-31		0.28	b.d.l.					7113.46	0.21	0.19		
ET2013-32	71.51	0.15	b.d.l.	b.d.l.	1910	3.9	0.2	7113.52	0.23	0.20	-9.58	-0.64
ET2013-33		0.17	b.d.l.					7113.36	0.17	0.17		
ET2013-34	70.97	0.13	b.d.l.	270	3350	3.7	0.1	7113.52	0.23	0.20	-9.37	-0.43
ET2013-40		0.16	b.d.l.					7113.43	0.20	0.18		

Table 4.6 - Centroid position, XANES $Fe^{3+}/\Sigma Fe$ ratios and corrected $Fe^{3+}/\Sigma Fe$ for some of the studied melt inclusions, together with the ΔNNO values, calculated using the corrected $Fe^{3+}/\Sigma Fe$ and the equation of Kress and Carmichael (1991). The precision (1σ) of the centroid energy and XANES $Fe^{3+}/\Sigma Fe$ ratio are 0.011 and 0.004 (Cottrell et al., 2009; Moussallam et al., 2016). In the tables are reported also the forsterite contents (Fo mol.%) of the olivine, the volatile contents of the melt inclusions and the calculated pressure (using Iacono-Marziano et al., 2012).

4.6. Sulfur isotopes

In order to verify the precision of the SIMS method for $\delta^{34}S$ analyses, several tests were conducted on standard glasses. Then the S isotopic compositions of twelve experimental glasses were determined (table 4.7).

Once determined the precision of the method we characterized the Etnean melt inclusions, for which it is difficult a multiple acquisition (because of the small size of the inclusions). The experimental glasses were synthesized in a similar pressure-temperature range, using the same S source (elemental S of unknown composition), and similar proportions of fluid phase, but at variable oxygen fugacity, FeO, S and H_2O contents in the melt (see paragraph 4.4).

The $\delta^{34}S$ in the experimental glasses varies from -0.17 ‰ to +1.74 ‰. The standard deviation of a single sample varies from 0.09 to 0.61 $\delta^{34}S$ ‰, while the analytical uncertainty is between 0.2 and 0.4‰). In the figure 4.26 (a-b-c-d), $\delta^{34}S$ values are plotted versus the H_2O, S, FeO, and oxygen fugacity. Oxygen fugacity shows the best correlation and is probably the crucial parameter controlling the $\delta^{34}S$ in the glass, by controlling the partitioning of S between the melt and the fluid phase. The S and FeO_{tot} contents are directly related to fO_2 in these experiments (the S content of the melt increases with fO_2, and also the total FeO content due to a decrease in the Fe loss to the capsule). The variability of the measured $\delta^{34}S$ ‰ in the experimental glasses is lower than 2 δ ‰.

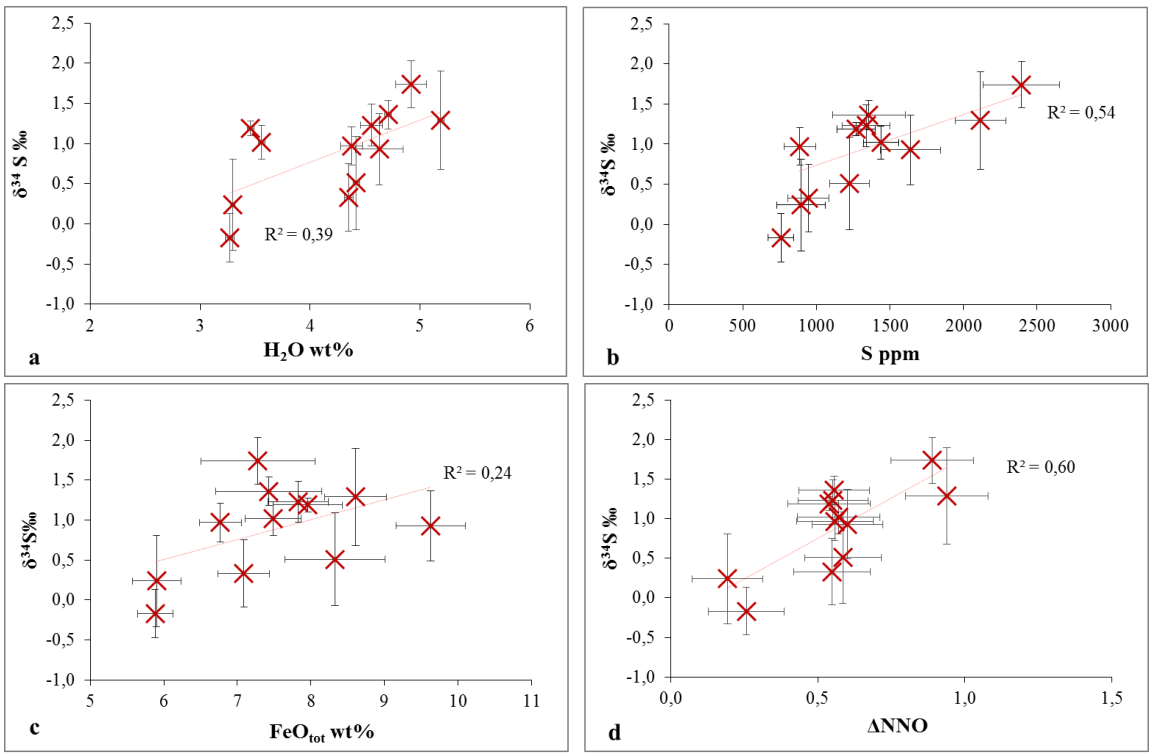

Fig. 4.26 - S isotopic composition (expressed as $\delta^{34}S$ ‰) plotted against (a) H_2O, (b) S and (c) FeO contents and (d) the experimental fO_2 (expressed as deviation from NNO buffer). Error bars indicate the standard deviations for H_2O, S, FeO_{tot} and $\delta^{34}S$ ‰; for the NNO values see the text.

The $\delta^{34}S$ values of the melt inclusions vary strongly, ranging from -4.4 to +4.1 ‰ (table 4.8, fig. 4.27). This large range overlaps the previous few measurements of S isotopic ratio in the volcanic gases (Allard, 1978, 1983, 1986; Liotta et al., 2012), in the bulk rocks (Gambardella, 2000) and in the melt inclusions from 2002/3 eruption (Spilliaert, 2006).

The presence of bubbles inside some of the melt inclusions seems not to affect the measured $\delta^{34}S$ (fig. 4.28a).

There is no clear difference between the studied products and the variability inside one eruption is extremely high (table 4.8). The highest value ($\delta^{34}S$ = 4.06 ‰) was measured in one MI from Mt. Spagnolo basalt (the other two give a mean $\delta^{34}S$ value of 0.83 ± 0.1 ‰), the lowest values ($\delta^{34}S$ = -4.42 and -3.50 ‰) are determined in MIs from 2002/2003 South eruption. All data from this latter eruption, having a mean $\delta^{34}S$ ratio of -1.1 ± 2.3 ‰, are more negative than those reported in the Spilliaert (2006) ($\delta^{34}S$ between 0.5 and 4.7 ‰). $\delta^{34}S$ value in the 2002/2003 embayments (-2.1 ‰) is more positive than the inclusions (-3.5 ‰) entrapped in the same olivine crystal (2002/3-24). The other eruptions have intermediate values (FS: -1.9 - 2.3 ‰; 2006: -0.9 – 2.4 ‰; 2008/2009: -1.1 - 1.9 ‰; 2013: -2.0 -2.2 ‰). In the 2006 products, the embayments show a $\delta^{34}S$ more positive than the inclusions in the same olivine, as in the 2002/2003.

name run	P_{tot} (MPa)	experimental log fO_2	ΔNNO	S (ppm)	$\delta^{34}S$ ‰ (1σ)	n. analyses	average uncertainty
Spa1702#1	180	-7.15	0.56 (±0.13)	888 (±108)	**0.97 (±0.24)**	5	0.31
Spa1702#2	180	-7.16	0.55 (±0.13)	948 (±140)	**0.33 (±0.42)**	5	0.32
Spa1702#3	180	-7.12	0.59 (±0.13)	1225 (±136)	**0.51 (±0.58)**	5	0.32
Spa1702#5	180	-7.45	0.26 (±0.13)	759 (±87)	**-0.17 (±0.30)**	5	0.39
Spa2703#1	210	-6.76	0.94 (±0.14)	2116 (±173)	**1.29 (±0.61)**	5	0.23
Spa2703#2	210	-6.81	0.89 (±0.14)	2395 (±260)	**1.74 (±0.29)**	5	0.23
Spa2703#3	210	-7.16	0.54 (±0.14)	1271 (±130)	**1.19 (±0.09)**	5	0.26
Spa2703#4	210	-7.13	0.57 (±0.14)	1438 (±120)	**1.02 (±0.21)**	4	0.24
Spa2704#1	193	-7.15	0.56 (±0.12)	1357 (±247)	**1.36 (±0.18)**	5	0.27
Spa2704#2	193	-7.10	0.60 (±0.12)	1640 (±205)	**0.93 (±0.44)**	5	0.28
Spa2704#3	193	-7.15	0.55 (±0.12)	1338 (±163)	**1.23 (±0.26)**	5	0.29
Spa2704#4	193	-7.51	0.19 (±0.12)	896 (±164)	**0.24 (±0.57)**	5	0.32

Table 4.7 - $^{34}S/^{32}S$ ratio (expressed as $\delta^{34}S$ ‰) for twelve experimental glasses together with the main experimental conditions (pressure, experimental fO_2) and the S contents. The isotopic ratio values are reported with the standard deviation (1σ) of 4-5 acquisitions and the average uncertainty determined by the full propagation of counting statistics and instrument background.

Any clear relation exists between the $^{34}S/^{32}S$ ratios and the volatiles contents dissolved in MIs (H_2O, S; figs. 4.28 b-c), the K_2O content or the forsteritic content of the host olivine (figs. 4.28 d-e).

The large variability of the isotope ratios in the MIs could depend on the analytical uncertainties as well as on sample treatment and post entrapment processes that are difficult

to be assessed exhaustively. Following this reasoning, we will not further discuss isotope composition of sulfur.

We just underline that gases not affected by secondary processes and collected in different periods are characterized by very narrow $\delta^{34}S$ ranging between -1 and + 1 $\delta^{34}S‰$ (Liotta et al 2012). The relative homogeneity of the emitted gases over time let us suppose a more restricted range for the isotope ratios in the melt.

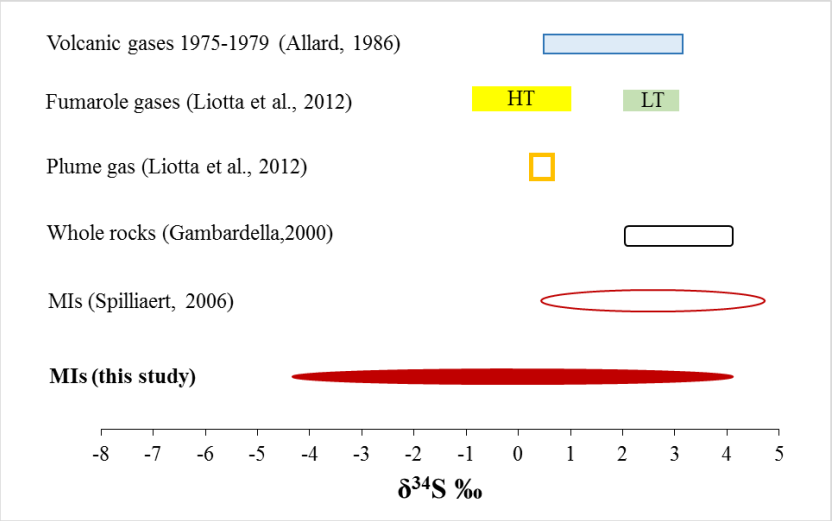

Fig. 4.27 - $\delta^{34}S$ data existing for Etna volcano. $\delta^{34}S$ values for etnean volcanic gases are from Allard (1986), Liotta et al. (2012); for the bulk rocks from Gambardella (2000), and for the melt inclusions from of the 2002/2003 eruption from Spilliaert (2006). The fumarole of high and low temperature ("HT" and "LT" in the plot) and plume gases characterized in Liotta et al. (2012) were sampled during the 2008/2009 eruption.

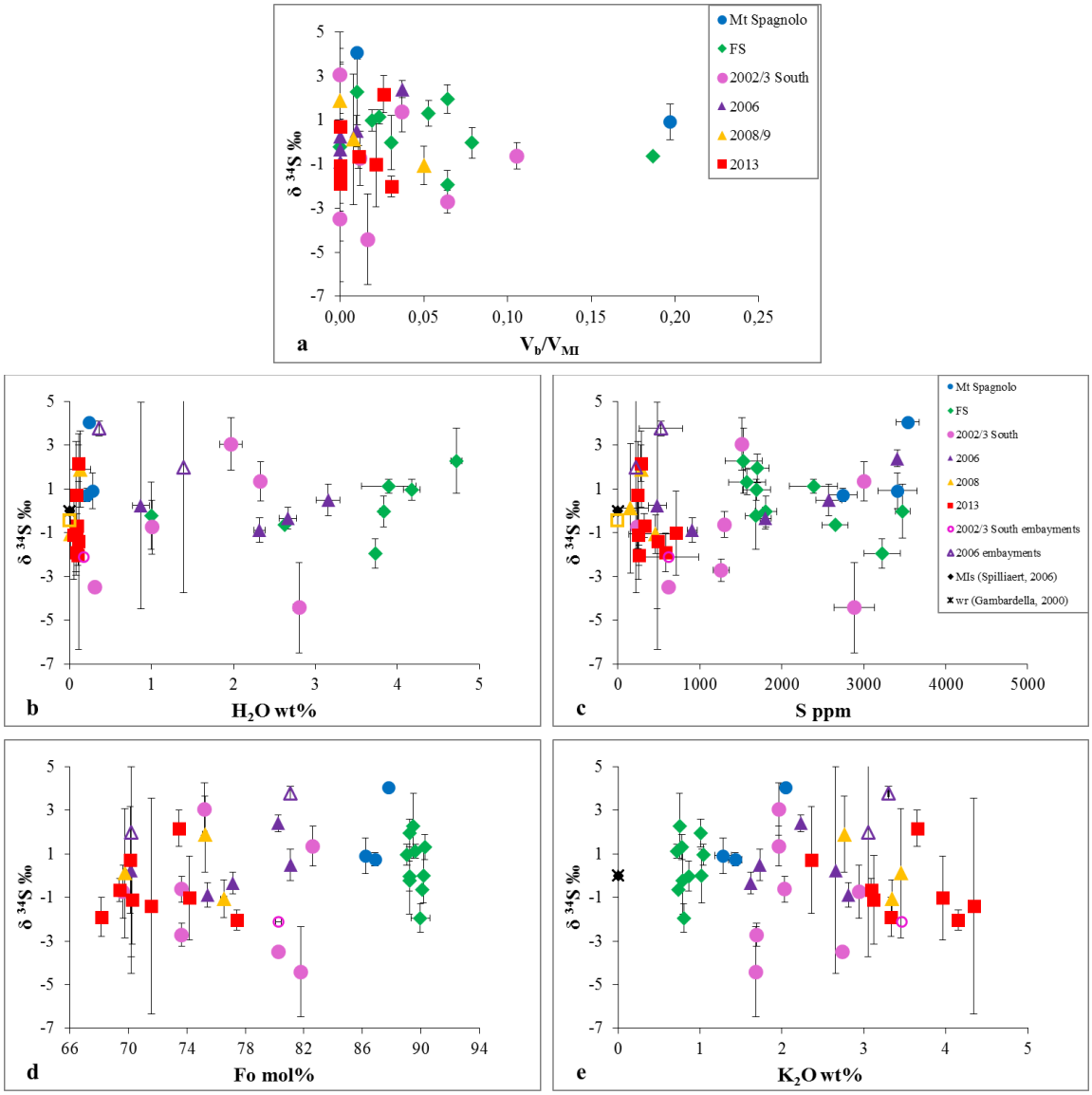

Fig. 4.28 - $\delta^{34}S$ determined in some of the studied melt inclusions. The values are extremely variable (-4.4 to +4.1 ‰) and any clear relation is evident between the $\delta^{34}S$, the volatiles (H_2O and S) contents, the K_2O and olivine composition (Fo mol.%). In all plots, error bars for volatiles and K_2O contents indicate the standard deviations, while those for the $\delta^{34}S$ are the sum of the standard deviations and the instrumental errors.

sample name	Fo (mol.%)	session	Intensity of primary beam	S (ppm)	$\delta^{34}S$ ‰ (1σ)	n. analysis	average uncertainty
Spa-1a	87.76	Oct 2015	1.5 nA	3539 (±141)	**4.06**	1	0.19
Spa-4n	86.85	Oct 2015	1.5 nA	2745 (±176)	**0.73**	1	0.30
Spa-5n	86.21	Oct 2015	1.5 nA	3410 (±240)	**0.92**	1	0.81
FS-03c	89.48	July 2015	1.5 nA	1533 (±225)	**2.28 (±1.26)**	4	0.23
FS-06c	90.11	Oct 2015	5 nA	2650 (±154)	**-0.65**	1	0.14
FS-08b	89.03	July 2015	1.5 nA	1689 (±169)	**0.97 (±0.23)**	3	0.25
FS-08c	89.23	July 2015	1.5 nA	1700 (±141)	**1.95 (±0.47)**	2	0.18
FS-10b	90.26	July 2015	1.5 nA	1575 (±226)	**1.31 (±0.27)**	2	0.30
FS-12a	89.21	Oct 2015	5 nA	1683 (±130)	**-0.23 (±1.29)**	2	0.25
FS-12b	89.21	July 2015	5 nA	1805 (±131)	**-0.03 (±0.44)**	3	0.26
FS-13b	89.63	July 2015	1.5 nA	2386 (±291)	**1.13 (±0.07)**	2	0.24
FS-21	90.17	July 2015	5 nA	3473 (±90)	**-0.02 (±1.04)**	3	0.19
FS-26	89.96	July 2015	5 nA	3223 (±220)	**-1.95 (±0.49)**	2	0.18
ET2002/3S-1	75.21	Oct 2015	1.5 nA	1513 (±61)	**3.05 (±0.93)**	2	0.27
ET2002/3S-5	81.79	Oct 2015	1.5 nA	2885 (±247)	**-4.42**	1	2.06
ET2002/3S-16a	73.65	Oct 2015	1.5 nA	1260 (±98)	**-0.63**	1	0.59
ET2002/3S-16b	73.65	Oct 2015	1.5 nA	1300	**-2.71**	1	0.51
ET2002/3S-23	82.61	Oct 2015	1.5 nA	3005 (±50)	**1.35 (±0.57)**	2	0.33
ET2002/3S-24	80.26	Oct 2015	5 nA	620 (±28)	**-3.50**	1	0.23
ET2002/3S-29a	69.64	Oct 2015	1.5 nA	237 (±2)	**-0.74**	1	1.23
ET2002/3S-24 embayments	80.26	Oct 2015	5 nA	620 (±367)	**-2.11**	1	0.14
ET2006-7	81.08	July 2015	1.5 nA	2573 (±159)	**0.49 (±0.46)**	2	0.26
ET2006-B3b	77.15	July 2015	1.5 nA	1800 (±67)	**-0.34 (±0.21)**	2	0.28
ET2006-B5n	80.24	Oct 2015	1.5 nA	3410	**2.40**	1	0.39
ET2006-B8a	75.42	July 2015	1.5 nA	907 (±58)	**-0.89 (±0.19)**	2	0.38
ET2006-E2a	70.19	July 2015	1.5 nA	480 (±110)	**0.25 (±4.2)**	2	0.53
ET2006-7 embayment	81.08	July 2015	1.5 nA	525 (±262)	**3.77**	1	0.33
ET2006-E2 embayment	70.19	July 2015	1.5 nA	220	**1.97 (±4.1)**	3	1.61
ET2008/9-1	75.24	July 2015	1.5 nA	284 (±6)	**1.90 (±1.12)**	3	0.63
ET2008/9-5	76.52	July 2015	1.5 nA	461 (±324)	**-1.07 (±0.37)**	3	0.51
ET2008/9-6a	69.77	July 2015	1.5 nA	153 (±216)	**0.12 (±1.85)**	3	1.11
ET2013-1	73.46	Oct 2015	1.5 nA	508 (±23)	**2.17**	1	0.83
ET2013-3b	70.26	Oct 2015	1.5 nA	275 (±65)	**-1.10 (±0.83)**	2	1.21
ET2013-6a	70.14	Oct 2015	1.5 nA	576 (±19)	**0.71 (±1.38)**	3	1.07
ET2013-7b	68.17	Oct 2015	5 nA	292 (±29)	**-1.90**	1	0.89
ET2013-14a	74.18	Oct 2015	5 nA	528 (±16)	**-1.02 (±1.42)**	1	0.50
ET2013-17a	69.40	Oct 2015	5 nA	509 (±20)	**-0.67**	1	0.53
ET2013-27	77.42	Oct 2015	5 nA	364 (±8)	**-2.03**	1	0.47
ET2013-36	71.58	Oct 2015	5 nA	320 (±6)	**-1.40 (±4.35)**	3	0.58

Table 4.8 - S content and isotopic compositions of olivine-hosted glass inclusions from the studied etnean products. In the table, the standard deviation (1σ, in case of multiple acquisition) is reported together with average uncertainty as determined by full propagation of counting statistics, instrument background, associated to the $^{34}S/^{32}S$ ratio given by ionic microprobe (SIMS).

5. DISCUSSION

In this chapter, we discuss chemical trends observed in the studied Etnean melt inclusions, using the experimental results, XANES data and MELTS modeling.

5.1. Geochemical features of Etnean magmas

The composition of the investigated olivine-hosted melt inclusions confirms that the FS eruption emitted the most primitive sub-alkaline magma erupted from Mt. Etna, having the highest CaO/Al_2O_3 ratio and MgO content (figs. 4.11 and 5.1), in agreement with previous studies (e.g., Kamenetsky et al., 2007). Due to the high MgO content (~17wt.%) of the bulk rock, FS magma is defined as picritic basalt (fig. 4.2). This melt is also very volatile- rich (H_2O contents up to 5.7 wt.%, CO_2 contents up to > 5000 ppm, and S contents between 1100 and 3473 ppm , fig. 4.14).

Mt. Spagnolo melt, already recognized as primitive (Armienti et al., 1988; Kamenetsky and Clocchiatti, 1996; Correale et al., 2014), is here, for the first time, characterized for its volatile content using melt inclusions. H_2O contents are very low (< 0.3 wt.%), while S contents reach 4150 ppm, being the highest measured in the Etnean melts (fig. 4.14a). CO_2 contents are variable (180-1300 ppm, excluding the highest values probably affected by C contamination, see paragraph 4.3.2 and appendix A.5), as well as chlorine contents (1523-4104 ppm). If compared with FS melt, Mt. Spagnolo composition is more evolved in terms of major elements (higher alkali content and lower MgO content), and highly degassed in water and carbon dioxide, but not in sulfur and chlorine, which both degas at low pressures (140 and 100 MPa, respectively according to Spilliaert et al., 2006a-b). Sulfur contents observed in Mt. Spagnolo melt inclusions are higher than the sulfur content at sulfide saturation calculated at T=1200°C and P<200 MPa using the model of Fortin et al. (2015) (< 2000 ppm), or at the typical magmatic redox condition (fO_2 < NNO+1) using the model of Jugo (2009) for anhydrous basalts. Moreover, no sulfide globules are observed inside Mt. Spagnolo melt inclusions, suggesting more oxidizing conditions to explain the high measured sulfur contents.

The studied melt inclusions of the recent eruptions (2002 to 2013) are significantly more evolved than FS and Mt. Spagnolo melts (lower MgO and CaO contents and higher alkali contents; fig. 4.10). The MIs from 2002/2003 and 2006 eruptions are very similar in terms of major elements and volatile contents to those previously studied (e.g. Spilliaert et al., 2006; Collins et al., 2009; Schiavi et al., 2015).

The 2008/2009 and 2013 melt inclusions, here investigated for the first time, show more evolved compositions, higher alkali contents and lower volatile abundances (H_2O, CO_2, and S) than the other studied Etnean magmas. The olivine phenocrysts in 2013 lava are less abundant than in the other products [see paragraph 4.2 and Viccaro et al. (2015)] and have variable Fo content (68-80 mol.%). Olivine trapped highly evolved melt

inclusions, showing the highest K_2O and the lowest FeO* content, among the studied compositions (fig. 4.10).

The $Fe^{3+}/\Sigma Fe$ ratios measured by synchrotron spectroscopy are extremely variable in the investigated Etnean magmas, from 0.33 in FS melt inclusions to 0.17 in the 2013 ones (excluding the lowest value of 0.14 in the MI SPA-O1, probably affected by post-entrapment crystallization, fig. 4.24, paragraph 4.6).

The prominent geochemical features emerging from this study are therefore (i) the high H_2O (S and CO_2) content of FS melt inclusions; (ii) the low H_2O and the exceptionally high S content of Mt. Spagnolo melt inclusions; (iii) the variability of FeO* (4.3-12.6 wt.%, fig. 5.1) and S (166-4150 ppm, fig. 4.14) contents of the entrapped melts; (iv) the continuous enrichment in K_2O of the melt, up to 5.6 wt.% in the 2013 melts; (v) the important variation of the $Fe^{3+}/\Sigma Fe$ ratio. We are going to discuss these features in terms of crystallization and degassing processes of Etnean magmas, paying particular attention to the variations in the redox conditions.

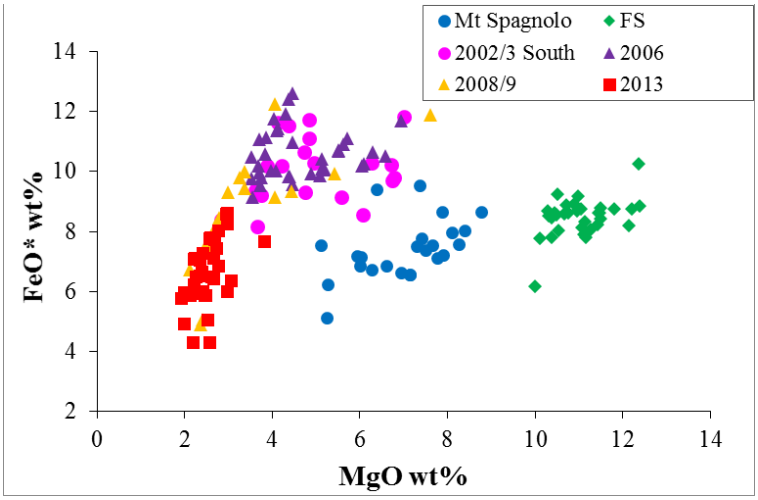

Fig 5.1 - FeO* (= FeO total) and MgO content in the studied Etnean melt inclusions from the eruptions of FS, Mt. Spagnolo, 2002/2003, 2006, 2008/2009 and 2013.

5.2. Depth of storage and degassing pattern of the erupted magmas

H_2O and CO_2 contents in the studied melt inclusions were used to determine their entrapment pressures using the solubility model of Iacono-Marziano et al. (2012), which is calibrated for different mafic composition, including specifically Etnean alkali-basalt and CaO-K_2O-rich rocks for pressures up to 1 GPa (table 4.3, fig. 5.2). Calculated pressures were then converted into depths using as rock density an average value of 2.65 g cm^{-3}, taking into consideration the different density of the lithologies in the crustal basement [from 2.57 to 2.70 g cm^{-3} in the first 22 km of the crust, as reported in Corsaro and Pompilio (2004b)]. The depth calculated via this average density value, rather than the exactly values of

lithology's density for each depth, could probably yield a relatively small error (up to 350 m).

FS melt inclusions are entrapped in a large range of pressures (76-477 MPa, fig. 5.2, table 4.3), corresponding to depths of 3-18 km below crater level ("bcl"). The inclusions from the other eruptions (Mt. Spagnolo, 2002/2003 South, 2006, 2008/2009 and 2013) are entrapped in a narrower range of pressures, indicating shallower depths, less than 7 km bcl (table 4.3 in paragraph 4.3.2, and fig. 5.2).

We used the model of Iacono-Marziano et al. (2012) to simulate the degassing of the deepest (~15-18 km bcl), volatile-rich (5000-5700 ppm CO_2 and 4.5±0.5 wt.% H_2O) primitive FS magma, considering an initial X_{CO_2} of 0.7-0.8. In order to reproduce most of the H_2O and CO_2 contents of FS melt inclusions, we performed two distint degassing simulations (starting from 4 wt.% H_2O - 5700 ppm CO_2 and 5wt.% H_2O - 5000 ppm CO_2). We use the highest CO_2 content, even if it is characterized by a large error (1σ, fig 5.2) and possibly affected by analytical problem during SIMS acquisition (see paragraph 4.3.2 and appendix A5), in order to reproduce H_2O and CO_2 contents of most of the inclusions.

Following the study of Métrich et al. (2004) and Spilliaert et al. (2006a), we simulated the degassing process only in closed system, with different excess of fluid phase (0-20 wt.%). These authors exclude the presence of an open system degassing at Mt. Etna because (i) this process would require an early bubble-melt separation, hampered during the fast and likely turbulent ascent of buoyant water-rich Etna basalt; (ii) it cannot explain the volatile-depleted and more evolved glass embayments.

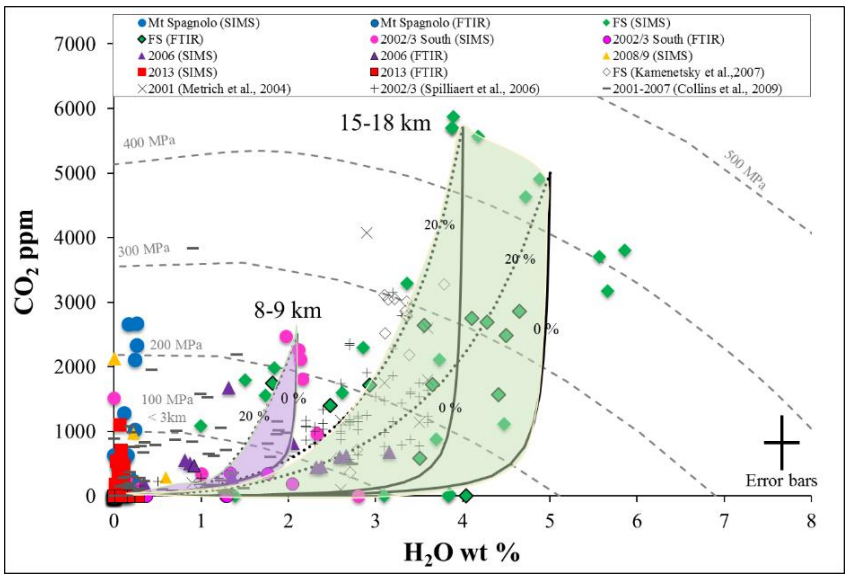

Fig. 5.2 - CO_2 and H_2O contents of melt inclusions (estimated by SIMS and FTIR), and isobars calculated at 1200 °C using the model of Iacono-Marziano et al., 2012, and an average composition of the studied melt inclusions. The depths are derived from the density of the sedimentary basement of Mt. Etna (Corsaro and Pompilio, 2004b). For comparison, data from previous studies are also reported. The green area is obtained from degassing calculation starting from the highest H_2O and CO_2 contents for FS composition at different initial volatile excess (0-20 %). The violet area is obtained for 2002 MI composition with H_2O and CO_2 contents of 2 wt.% and 2500 ppm. The error bars represent the highest standard deviations obtained for the volatile-richest inclusions.

Two degassing trends are shown for the deepest FS inclusions (green area in fig. 5.2) entrapped at 400-480 MPa, accounting for most of FS inclusions, but also for the products of the 2001-2006 period (this study; Metrich et al., 2004; Spilliaert et al., 2006; Collins et al., 2009) and suggesting a deep ponding zone for magmas at 15-8 km bcl. An additional trend describes the degassing of a primitive (already partially degassed) melt entrapped at 220-250 MPa in the 2002/2003 inclusions, indicating a ponding magma depth of 8-9 km bcl (i.e. ~5-6 km bsl), similarly to Spilliaert et al., 2006a.

Some melt inclusions from the studied 2013, 2008/2009 and Mt. Spagnolo eruptions, and 2002/2003 and 2006 from Spilliaert et al. (2006) and Collins et al. (2009), are anomalously enriched in CO_2 (fig. 5.2). In addition to a possible C contamination during SIMS analyses (discussed in paragraph 4.3.2 and appendix A5), other possible causes can be evoked to explain this CO_2 enrichment. Previous studies on Etna (e.g., Spilliaert et al., 2006a; Collins et al., 2009; and reference therein) attribute the CO_2 enrichment in some 2001-2002 and 2001-2007 inclusions to a rising CO_2-rich fluid from a degassing deep magmatic body (CO_2 fluxing). This deep fluid could impose re-equilibration and dehydration of a shallow ponding magma (100-200 MPa), resulting in the formation of the H_2O-poor and CO_2-rich melt.
Pichavant et al. (2013) give another explication for the high CO_2 content of some melt inclusions, on the basis of decompression experiments on Stromboli basalts. These authors found, in the basaltic melt, CO_2 contents well above the solubility values and suggested that CO_2-oversaturated melts could be generated during magma ascent as the result of a disequilibrium degassing.

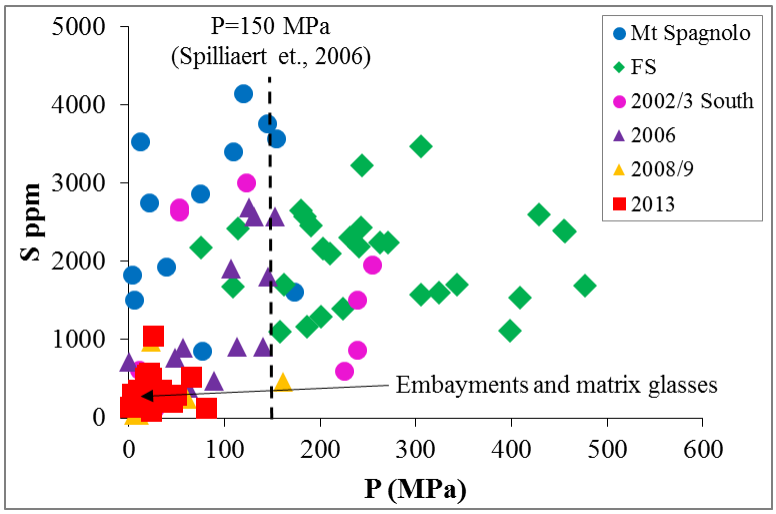

Fig. 5.3 - Pressure-related evolution of S in melt inclusions, embayments and matrix glasses from the studied eruptions. Entrapment pressures are inferred from the dissolved H_2O and CO_2 contents using the model of Iacono-Marziano et al. (2012) (table 4.3 and paragraph 4.3.2).

Regarding sulfur, Spilliaert et al., 2006a suggest that sulfur degassing beneath Etna becomes significant only in the upper part of the plumbing system, i.e. in the last 150 MPa. This is mainly due to the increase in the sulfur content at sulfide saturation (**SCSS**) with decreasing pressure (e.g., Mavrogenes and O'Neill, 1999), which can lead sulfur to be enriched in the melt during magma rising. In our melt inclusions, S content is not clearly correlated with the estimated pressure (fig. 5.3), as predicted in Spilliaert et al., 2006. In addition, several melt inclusions from Mt. Spagnolo, 2002/2003 and 2006 products, entrapped at pressure below 150 MPa have sulfur contents higher than those measured in melt inclusions (for example FS) entrapped at higher pressure. This suggests that S degassing in the hydrous Etnean magma is controlled not only by magma decompression, but also by the redox conditions, as discussed in paragraph 5.5.

5.3. Fractional crystallization processes

In this paragraph, we model the fractional crystallization processes associated with the genesis of the investigated Etnean products, by using the MELTS code (Ghiorso and Sack, 1995; Smith and Asimow, 2005), in order to evaluate the effects of fractional crystallization on the geochemistry of major and volatile elements and on the redox conditions of the magma. We select the most primitive composition of FS olivine-hosted melt inclusions (see table 5.1) for checking by means of MELTS simulations if the compositions of the other investigated products may be explained through a simple melt differentiation by fractional crystallization. The higher pressure values are determined by H_2O and CO_2 contents in FS melt inclusions (see paragraph 4.3.2, table 4.3 and fig. 5.2), which provide a maximum pressure of about 477 MPa. Accordingly, and in order to reproduce the deepest magmatic conditions, MELTS simulations were carried out by using an initial pressure fixed between 400 and 500 MPa. The initial temperature values used for the simulations are between 1200 (Mollo et al., 2015) and 1300 °C [anhydrous conditions (Armienti et al., 2007; Armienti et al., 2012)]. The final temperatures are 1050-1100 °C, similar to the direct measurements of lava temperatures [980-1080 °C (Calvari et al., 1994)] and to those calculated by other studies (Kahl et al., 2011, 2015). The initial redox conditions used are between NNO+1.5 and NNO+2, in agreement with the $Fe^{3+}/\Sigma Fe$ ratios determined by XANES in the most primitive inclusions (see paragraph 4.6 and table 4.6), and to previous estimations [~ NNO+1.8, Kamenetsky and Clocchiati (1996); NNO>1, Métrich et al. (2009); NNO>1, Liotta et al. (2012)].

We have performed several MELTS calculations by using different combinations of the initial P-T-fO_2-H_2O values within the previously given ranges. Generally, fractional crystallization processes are calculated through MELTS code in *"isothermal"* and *"geothermal"* mode (as termed in the *alphaMELTS* manual by P. Antoshechkin). In *geothermal* simulations pressure and temperature decrease according to the imposed pressure-temperature gradient (dP/dT), while in isothermal simulations pressure decreases

at a constant temperature. In this chapter, we discuss only the most representative MELTS simulations, reported in table 5.2, and shown in figs. 5.4 and 5.8. Additional information is in the appendix A6.
We show the simulations starting from two different combination of fO_2-H_2O parameters (NNO+2, 4 wt.% H_2O, and NNO+1.5, 5 wt.% H_2O), at the same initial temperature (1200°C), pressure (400 MPa) and melt composition (in table 5.1). The most representative *geothermal* simulations have dP/dT slopes of 3 and 5 MPa $°C^{-1}$ that are in agreement with those proposed in Armienti et al. (2012).

The starting composition that we used for most of the simulations is the average of the two most primitive melt inclusions in FS products (table 5.1). We initially checked the liquidus temperature of this melt, by means of two *geothermal* simulations, one starting from an initial fO_2 of NNO+2, a H_2O content of 4 wt.% (simulation n° 1 in table 5.2), the other starting from an initial fO_2 of NNO+1.5 and a H_2O content of 5 wt.% (simulation n° 6 in table 5.2), both with an initial temperature of 1300°C and pressure of 500 MPa. We then modeled fractional crystallization in *"isothermal"* mode (adiabatic process at 1200°C, to simulate a rapid ascent, simulations n° 2 and 7), and in *"geothermal"* mode, with a slope dP/dT of 3 and 5 MPa $°C^{-1}$ (= 30-50 bar/ °C, to simulate a slow ascent, simulations nunber 3, 4, 8 and 9).

We finally performed an additional simulation to reproduce Mt. Spagnolo melt inclusions: an almost *isobaric* process using a dP/dT of 0.066 MPa $°C^{-1}$ (=0.7 bar/ °C), starting from the composition obtained at 10 MPa from the "*isothermal"* model (for details see table 5.2, simulations n° 5 and 10). This was aimed at simulating fractional crystallization at shallow depth, after a rapid ascent.

SiO_2	TiO_2	Al_2O_3	FeO_{tot}	MnO	MgO	CaO	Na_2O	K_2O	P_2O_5	Cr_2O_3	NiO	CaO/ Al_2O_3	Mg#
43.84	1.00	9.00	8.15	0.10	11.71	12.88	1.59	0.87	0.26	0.12	0.04	1.43	72

Table 5.1 - The initial primitive composition used for most of the MELTS simulations, represented by the average of the 2 most primitive FS-B and FS-Z olivine-host melt inclusions (with the highest Mg#, CaO/Al_2O_3 ratio and Cr_2O_3 content of the FS-D MI) recalculated for post entrapment crystallization (5-7 % of PEC). All oxides are expressed in wt.%.

In the plot CaO/Al_2O_3 versus K_2O (fig. 5.4), all the performed simulations almost overlap, and very well reproduce the trend described by the Etnean melt inclusions, with the exception of the most evolved 2013 inclusions. Independently on the initial parameters (fO_2, H_2O), MELTS simulations reproduce the evolution of Etnean magmas, starting from the FS composition by fractional crystallization of olivine, spinel, clinopyroxene, and plagioclase in the final steps (table A6.1 and A6.2 in Appendix A6).

The *geothermal* processes (n° 1 and 6 in table 5.2) simulated at temperatures between 1300 and 1200 °C, and pressure between 500 and 400 MPa, suggest that for a FS liquid, olivine is the liquidus phase at 1250 °C and 450 MPa. MELTS also predicts Cr-spinel

crystallization at the same T-P conditions, for highly oxidizing conditions (NNO+2) and dissolved water content of 4 wt.% H_2O. If starting from less oxidizing conditions (NNO+1.5) and 5wt.% H_2O, the Cr-spinel appears at a temperature of 1210 °C and a pressure of 410 MPa. These pressure values are very close to those determined for FS melt inclusions in which Cr-spinel inclusions are observed (e.g. figs. 4.5 a-b).

The following *isothermal (~ adiabatic) simulations* (n° 2 and 7 in table 5.2) are characterized by the irrelevant crystallization of olivine + clinopyroxene + Cr(Mg)-spinel. The *geothermal* simulations (n° 3, 4, 8 and 9, table 5.2) starting from a temperature of 1200°C are also characterized by the crystallization of clinopyroxene and plagioclase at shallower pressures. The nucleation of these minerals yields at the decrease of the CaO/Al_2O_3 ratio (fig. 5.4), MgO (fig. 5.6d), and CaO content (fig. 5.6e), and the increase of SiO_2 (fig. 5.6a), alkali (fig. 5.6f) and P_2O_5 (fig. 5.6h) contents, as shown by the studied glass inclusions (and bulk rocks, fig. 4.3).

The fractional crystallization, simulated in these different modes, well reproduces the scatter in the H_2O contents measured in the melt inclusions (fig. 5.5). Fractional crystallization of olivine and Cr(Mg)-spinel at high T-P (1300-1200°C and 500-400 MPa, simulations n° 1 and 6 in table 5.2) produces an increase in water dissolved in the residual melt, independently on the initial couple of fO_2-H_2O considered (figs. 5.5a-b). The amount of water dissolved in the melt strongly decreases during the *isothermal (~ adiabatic)* process (simulations n° 2 and 7), characterized by a negligible fractional crystallization of olivine (0.04 %) and Cr(Mg)-spinel (0.5-1.1 %) and by abundant crystallization of clinopyroxene (30-33 %), at shallow depth (30 MPa).

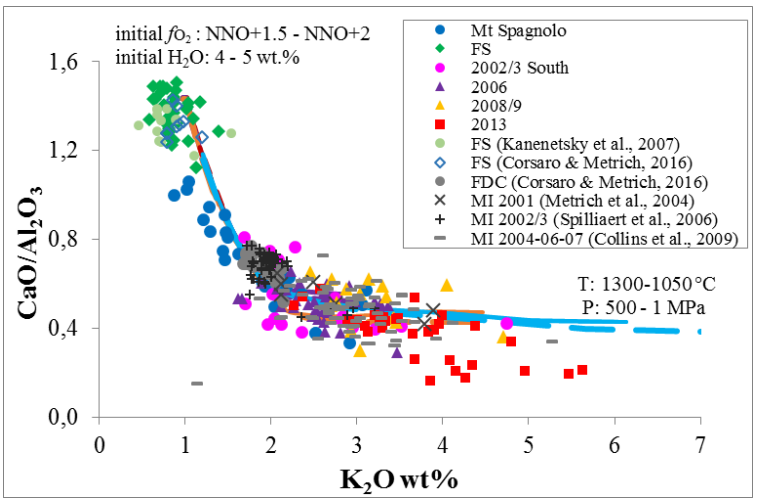

Fig. 5.4 - CaO/Al_2O_3 ratio versus K_2O content measured in the investigated melt inclusions. Etnean MIs from previous studies (Métrich et al., 2004; Spilliaert et al., 2006; Collins et al., 2009; Corsaro and Métrich, 2016) are also shown. The evolution of the CaO/Al_2O_3 ratio and the K_2O content calculated by MELTS is also shown (see text for explanation). Several MELTS curves were obtained using variable initial conditions (T, P, fO_2 and water content), and the *geothermal* or the *isothermal* mode, they all overlap (simulations 1-11 in table 5.2).

The (*isothermal*) adiabatic decompression describes rather well the fast rising of the FS primitive magma (e.g., Coltelli et al., 1998; 2005) associated to an important H_2O degassing (indicated by the large range of H_2O content measured in the FS melt inclusions fig. 5.5), but a minor differentiation (revealed by the constant K_2O content, and CaO/Al_2O_3 ratio, figs. 5.4 - 5.7). Also an adiabatic decompression seems to explain the low water contents (< 0.5 wt.% H_2O) observed in Mt. Spagnolo melt inclusions (fig. 5.5).

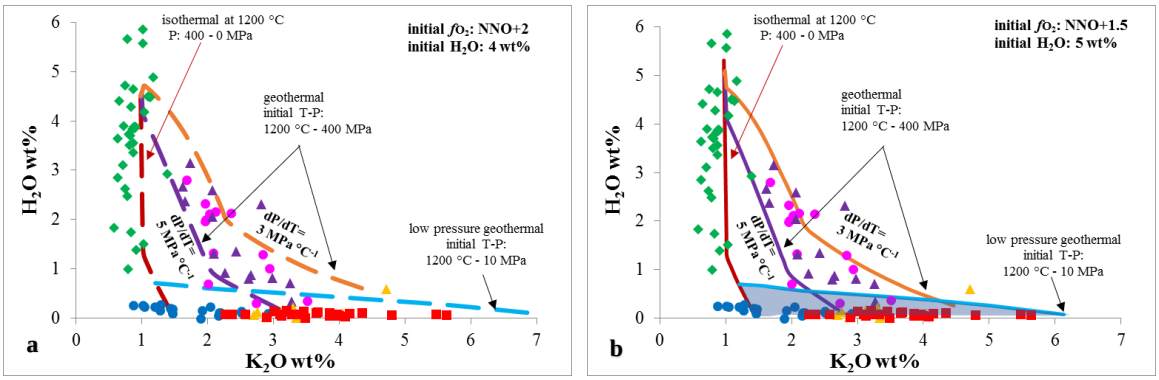

Fig. 5.5 - H_2O versus K_2O content measured in the investigated melt inclusions and calculated by MELTS (see text for details). In the plot (a) the simulations using an initial fO_2 of NNO+2 and a H_2O content of 4 wt.%. In the plot (b) the simulations using an initial fO_2 of NNO+1.5 and a H_2O content of 5 wt.%. The red curves indicate the *isothermal* simulations starting from 1200 °C and 400 MPa. The violet and orange curves show the *geothermal* simulations with a slope dP/dT of 3 and 5 MPa $°C^{-1}$, respectively. The light blue curves illustrate the superficial *geothermal* simulations (pressure < 10 MPa). For the MIs, symbols see the caption of figure 5.4.

Therefore, both the decrease in the water content of FS inclusions and the extremely low H_2O contents measured in Mt. Spagnolo MIs could be the result of a rapid decompression from the deeper parts of the plumbing system to the most superficial ones, accompanied by a minor fractional crystallization of olivine + spinel + clinopyroxene. To reproduce the compositional evolution shown by Mt. Spagnolo inclusions, a following almost *isobaric* cooling (simulations n° 5 and 10) at pressures lower than 10 MPa is needed (figs. 5.5 a-b), characterized by the fractional crystallization of clinopyroxene + spinel + olivine + plagioclase (table A6.1 and A.6.2 in appendix A6). Such a simulation reproduces, at least partially, the decrease in MgO, CaO and the increase in K_2O, SiO_2, Al_2O_3, TiO_2, and P_2O_5 shown by Mt. Spagnolo melt inclusions, but not the strong decrease in FeO* (fig. 5.6c), which is probably due to a significant magnetite crystallization, not simulated by MELTS. MELTS simulations, after all, were not able to reproduce the important scatter shown by the MIs, especially in the SiO_2 contents (fig. 5.6a)

The fractional crystallization process simulated by *geothermal modes* with dP/dT gradients of 3 and 5 MPa $°C^{-1}$ (n° 3, 4, 8 and 9), starting from 1200 °C and 400 MPa, generally well reproduces the water and the major element contents measured in the 2002/2003, 2006, 2008/2009 and partially in the 2013 trachybasaltic MIs. These simulations well describe the decrease in MgO and CaO contents accompanied by an increase in K_2O of recent melt

inclusions with respect to the FS primitive melt (figs. 5.6d-e). Only the most evolved 2013 inclusions are generally richer in MgO and poorer in CaO than predicted by MELTS. The enrichment of the 2002/2003, 2006, and 2008/2009 residual liquids in Al_2O_3, Na_2O, TiO_2 and P_2O_5, is also generally well accounted for by MELTS *geothermal* simulations, although the important scatter in the data (figs. 5.6 b-f-g-h). For the SiO_2 content, it must be noted that the initial value normalized by MELTS is higher than that originally used.
Therefore, the MELTS curves are shifted with respect to the trend described by melt inclusions, more importantly for SiO_2 (fig. 5.6a), than for the other elements. Once again, the natural data are characterized by an important scatter. The compositions of 2013 melt inclusions, and in particular those of the most evolved ones, are generally not well reproduced by MELTS simulations starting from high T and P (fig. 5.6): Al_2O_3 and Na_2O contents calculated by MELTS are significantly lower than those measured in MIs, while CaO and FeO* are higher than the measured ones. The low pressure simulations (continue and dashed light blue curves in figure 5.6, simulations n° 5 and 10 in table 5.2) do not reproduce either Al_2O_3 and Na_2O contents of the 2013 melt inclusions, but better account for the evolution of the FeO* content (fig. 5.6c). These two simulations yield a crystallization of clinopyroxene (up to 15 %) and plagioclase (up to 67 %) (table A6.1 and A6.2) higher than those really observed in the rocks (8 and 10 % respectively, table 4.2). To better reproduce the higher Al_2O_3 and Na_2O contents in 2013 melts respect the simulations, MELTS should produce a minor crystallization of plagioclase.

The differences in the initial values of fO_2 and dissolved H_2O content do not influence the evolution of the CaO/Al_2O_3 ratio, of most of the major elements (as SiO_2, K_2O, MgO, CaO, Na_2O), and of the dissolved water contents calculated by MELTS simulations (figs. 5.4, 5.5, 5.6; and tables A6.1 and A.6.2 in the appendix). In contrast, they strongly control the evolution of the iron content (FeO* = FeO total), as illustrated by figure 5.7 (and figs. A5.6), by affecting the crystallization of the spinel.

The studied Etnean melt inclusions show a large range of FeO* contents (4.3-12.6 wt.%). MELTS simulations in the *geothermal mode* generally properly reproduce the variations in the FeO* content of MIs (figs. 5.6c, 5.7a-b), with the exceptions of Mt. Spagnolo and the more evolved 2013 inclusions. MELTS simulations, starting from NNO+2 and 4 wt.% H_2O, or from NNO+1.5 and 5 wt.% H_2O, at 1300°C and 500 MPa (red curves in figs. 5.7a-b; simulations n° 1 and 6 in table 5.2), well describe the first steps of differentiation of the primitive FS melt, branded by the crystallization of olivine (maximum 18.5 wt.% at higher fO_2 and lower H_2O) and, in minor abundance, of Cr-spinel (0.3 wt.%). This crystallization only slightly decreases the FeO* content of the residual melt. The following *isothermal* simulation (~ adiabatic process; n° 2 and 7 in table 5.2) that reproduces the decompression of the FS magma and the decrease in H_2O of the melt, is characterized by an increase in the FeO* content in the melt. This increase in the FeO* content is not observed either in FS or in Mt. Spagnolo melt inclusions, which on the contrary show an important decrease in their FeO* content during melt differentiation (fig. 5.7).

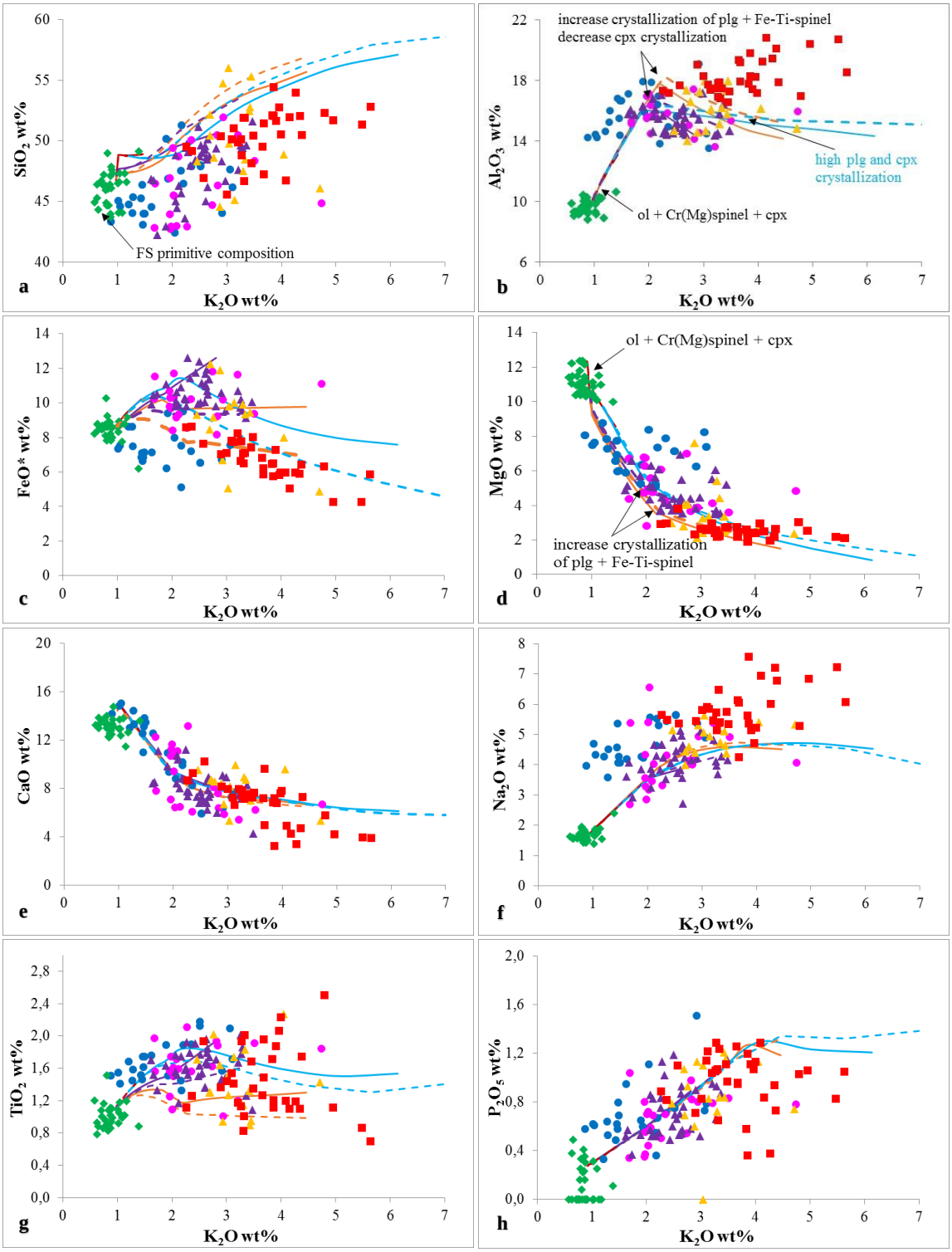

Fig. 5.6 - Major element contents measured in the etnean melt inclusions and calculated by MELTS simulations described in the text and reported in table 5.2. The red curves indicate the *isothermal* simulations starting from 1200 °C and 400 MPa. The violet and orange curves show the *geothermal* simulations with a slope dP/dT of 3 and 5 MPa °C^{-1}, respectively. The light blue curves illustrate the superficial *geothermal* simulations (pressure < 10 MPa). The continue curves are from the starting condition of fO_2-H_2O of NNO+1.5 and 5 wt.%. The dashed curves are from the starting condition of fO_2-H_2O of NNO+2 and 4 wt.%. For the MIs symbols see the caption of figure 5.4.

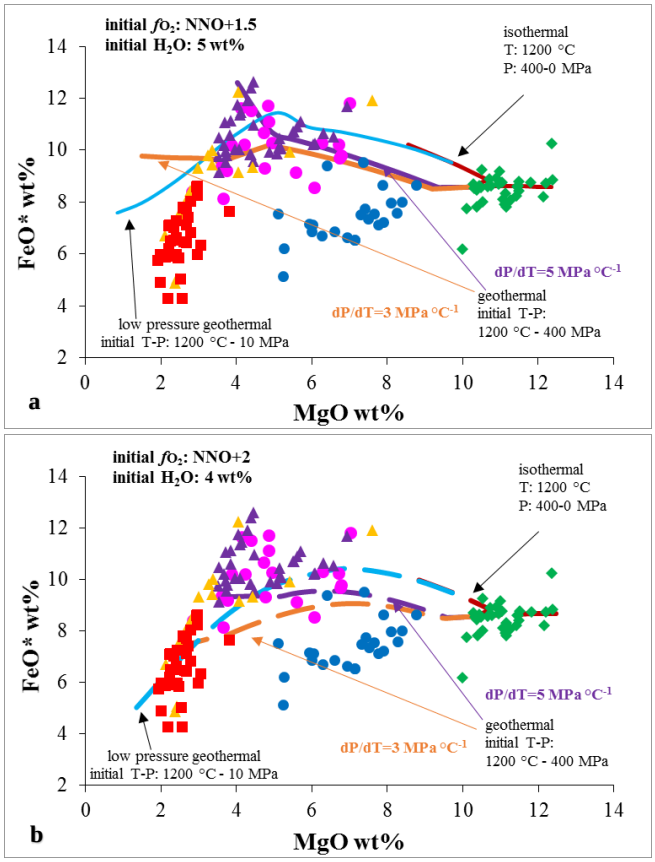

Fig. 5.7 - FeO* versus MgO contents measured in melt inclusions and calculated by MELTS. In (a) the simulations calculated from an initial fO_2 and H_2O of NNO+2 and 4 wt.%. In (b) the simulations with an initial fO_2 and H_2O of NNO+1.5 and 5 wt.%.

The red curves indicate the *geothermal* simulations at high temperature and pressure, and the following *isothermal* processes at 1200 °C. The violet and orange curves represent the *geothermal* simulation with a slope dP/dT of 3 and 5 MPa °C^{-1}, respectively. In light blue the superficial *geothermal* (pressure < 10 MPa). For the MIs, symbols see the caption of figure 5.4.

We believe that a more important co-crystallization of olivine and Cr-spinel, at high temperature and pressure, would lead the FS melt to evolve towards the most primitive Mt. Spagnolo melt compositions (table A6.1 and A6.2). Indeed, phenocrysts of Cr-rich spinel are observed (< 1 vol.%) in the Mt. Spagnolo basalt (as in FS products), as inclusions in the olivine and inside melt inclusions, confirming an early crystallization together with or before olivine crystallization. The important decrease in the FeO* content recorded by Mt. Spagnolo MIs could be then explained by the change in composition of the spinel, due to Cr depletion in the melt.

The other *geothermal* simulations starting from lower T and P (1200 °C - 400 MPa) and simulating a slow cooling of 1°C each 3-5 MPa (*geothermal* processes performed with a slope dP/dT of 3 - 5 MPa °C^{-1}, simulations n° 3, 4, 7, 8 in table 5.2), bracket the different FeO* contents measured in 2002/2003, 2006, 2008/2009 melt inclusions. In particular, the simulation (n° 8 in table 5.2) of the fastest fractional crystallization, with an initial oxygen fugacity of NNO+1.5 (violet curve in fig. 5.7a) reproduces the highest values of FeO* of

some MIs of the 2002/2003 and 2006 products. The FeO* increase is due to low spinel crystallization during the differentiation. These high FeO* values (~ 12.6 wt.%) are attained in the final steps at the superficial pressure of <10 MPa, slightly lower than the pressure estimated for these MIs from H_2O-CO_2 contents (P = 0-58 MPa, table 4.3, paragraph 4.3.2). The difference in the pressure values is likely due to the CO_2 effect, not considered in the MELTS model. The other *geothermal* simulations starting from 1200°C and 400 MPa produce melts with lower FeO* contents (fig. 5.7). The low pressure *geothermal* (< 10 MPa) simulation (n° 10 in table 5.2) shown in the figure 5.7a (dashed light blue curve), better reproduces the lowest FeO* content measured in the MIs from 2013 lava.

In conclusion, starting from a primitive FS composition, MELTS simulations generally reproduce the more evolved compositions of the 2002/2003, 2006, 2008/2009 and 2013 magmas, by fractional crystallization of olivine + clinopyroxene ± spinel ± plagioclase.

An *adiabatic* decompression of the primitive FS melt, followed by a rapid cooling at superficial levels could instead account for H_2O contents and major element compositions observed in Mt. Spagnolo melt inclusions.

This conclusion is based only on the major elements compositions of the investigated melt inclusions. Conversely, recent studies on trace and isotope elements (e.g. Correale et al., 2014; Corsaro and Métrich, 2016) suggest that both FS, Mt. Spagnolo and other recent DDF magma are the result of different degree of melting of a heterogeneous mantle and so, not linked to fractional differentiation.

5.3.1 Alkali enrichment?

Our investigated melt inclusions highlight a consistent K_2O increase, from the most primitive FS toward the most differentiated and degassed samples of 2013 eruption (up to 5.6 wt.% of K_2O). Fractional crystallization modeled through MELTS code yields to melt enriched in K_2O up to 7 wt.% (e.g., figs. 5.4 - 5.5 - 5.6 and 5.8). The good correspondence between MELTS simulations and the K_2O contents of MIs suggests that the K_2O increase could mainly be ascribed to the crystal fractionation of K-free mineral phases. However, figures 5.6f and 5.8 show a discrepancy between the MIs data and the MELTS simulations mainly concerning the Na_2O content of Mt. Spagnolo and 2013 melt inclusions, but also that of some 2002/2003 and 2008/2009 inclusions. This observation suggests the existence of another mechanism, influencing at local scale the magma composition of Mt. Etna during the last 15 ky. Several mechanisms were proposed, for example (i) assimilation of sediments underlying the volcanic edifice, or of magma contamination during its migration to the surface, by assimilation of basement rocks (carbonates, shales, quartzarenites) (e.g., Joron and Treuil, 1984; Clocchiatti et al., 1988; Tonarini et al., 1995). Others studies attributed this enrichment to source-related processes, such as the partial melting of a heterogeneous mantle source (e.g., Armienti et al., 1989; Corsaro and Cristofolini, 1996), or the mixing of a mantle-derived-magmas with a melt K- and Si-enriched (Schiano and Clocchiatti, 1994).

Recently, Ferlito and Lanzafame (2010) explain the enrichment in K_2O, Na_2O and Cl of Etnean lava, through the extraction of alkalis (and metals as Ti, Fe) from the magma ponding in the lower portion of the plumbing system, through stripping by a Cl, H_2O, CO_2-bearing phase (Frank et al., 2003). Nevertheless, according to these authors, as pressure decreases, Cl exsolves, with the Na that could be easily accommodated within the lattice of the crystallizing plagioclase, enriching the melt only in K_2O. Therefore, the enrichment in Na_2O observed in some samples respect MELTS simulations is not well coinstrained and needs further investigations.

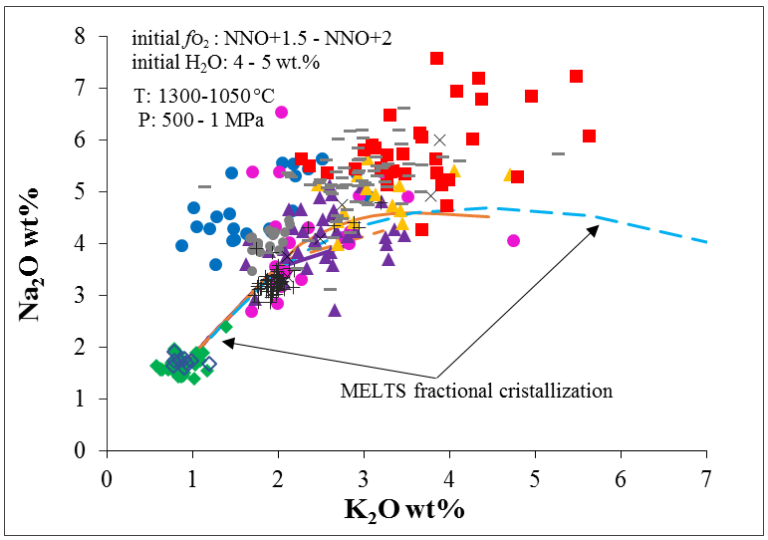

Fig. 5.8 - Na_2O-K_2O content in the Etnean melt inclusions. In this plot, Etnean MIs from previous studies (Métrich et al., 2004; Spilliaert et al., 2006; Collins et al., 2009; Corsaro and Métrich, 2016) are also shown. For the MIs symbols, see the caption of figure 5.4. For the MELTS curve, see description in the text, and the caption in the figure 5.4 and 5.5.

5.3.2 Mt. Spagnolo: primitive magma evolution by FC and magma mixing

In the previous paragraphs, we described the Mt. Spagnolo lava as the result of a fast rising of a primitive FS-type magma, experiencing an early fractional crystallization (FC) of olivine and Cr-spinel at high oxygen fugacity (around NNO+1.5) and at high pressure (400-500 MPa). In these conditions, H_2O and S increase in the residual melt. Conversely, the following fast decompression at intermediate and superficial levels, associated with the fractional crystallization of olivine + Cr-spinel + clinopyroxene, induces a relevant water exsolution.

This water loss is partially observed in FS melt inclusions, because FS magma was rapidly erupted, triggering one of the few subplinian eruptions of Etna magmatic record (Coltelli et al., 2005). In the case of Mt. Spagnolo eruption, the high temperature oxidized magma was not erupted and cooled down in the last kilometers of the shallow system, continuing to crystallize clinopyroxene and plagioclase, as calculated by MELTS code. The occurrence of typical textures dictated by a high degree of undercooling, e.g. skeletal

clinopyroxenes and dendritic oxides in the groundmass (paragraph 4.2) of Mt. Spagnolo lava, corroborate this fast superficial cooling. However, the melt inclusions from Mt. Spagnolo eruption have sensibly lower FeO* contents (figs. 5.6c, 5.9).

We propose that Mt. Spagnolo magma could be the result of an important fractional crystallization of olivine and Cr-spinel from a primitive magma FS-like, followed by a mixing process with a more evolved and degassed magma at very superficial depths (<0.5 km). We calculate the magma mixing by using the end-member compositions obtained by the *adiabatic (isothermal)* fractional crystallization at 1200 °C and 10 MPa. Conversely, as evolved composition we use the last one of the low-pressure *geothermal* models (0.1 MPa). The resulted mixing line (in red color) is shown in figure 5.9. The melt inclusions data of Mt. Spagnolo and Mt. Frumento delle Concazze ["FdC" (Corsaro and Métrich, 2016)] seem to depict the combined influences of fractional crystallization and mixing mechanism. In effect, the occurrence in the Mt. Spagnolo lava of the large compositional range of olivine (Fo_{70-88}, paragraphs 4.2 and figure 4.7), some of which with inverse zonation, could indicate the presence at least of two batches of magma, one with primitive composition FS-type and another more evolved.

The existence of mixing process in the shallow plumbing system of Mt. Etna has been already reported in previous studies (e.g., Corsaro and Pompilio, 2004a; Métrich et al., 2004) for the eruptions after 1970's, as well as, for the Mt. Frumento (FdC) lava (Clocchiatti and Métrich, 1986).

The decrease of FeO* content in the melt inclusions from the 2006 products toward those of the 2013 eruption could also reflect some mixing process in the very shallow volcanic system, as shown by the black line in figure 5.9.

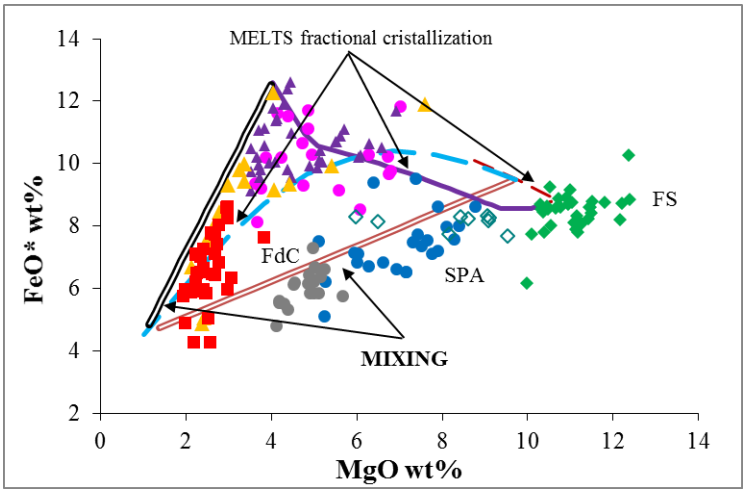

Fig. 5.9 - FeO versus MgO content in the Etnean melt inclusions. The plot shows the MELTS models approaching to the highest and the lowest FeO^* contents of the studied melt inclusions, and the mixing line to explain Mt. Spagnolo compositions. The mixing is calculated between the last composition of the MELTS *isothermal model* (primitive end member) and the last one of the *almost isobaric simulation* (evolved composition). MIs of FS and FdC (Frumento delle Concazze) are from Corsaro and Metrich (2016). For the MIs symbols see the caption of figure 5.4. For description of MELTS curves see the caption of figure 5.6.

N°	**MELTS simulation**	**Initial redox condition**	**T_i (°C)**	**T_f (°C)**	**P_i (MPa)**	**P_f (MPa)**	**dT**	**dP**	**Initial H_2O (wt.%)**	***final* redox condition**	***note***
1	*High T-P geothermal*	NNO+2	1300	1200	500	400	1	10	4	NNO+2	
2	*Isothermal/ adiabatic*	NNO+2	1200	1200	400	0.1	0	10	4.5	NNO+1.6	*Starting composition from the last one of previous geothermal model.*
3	*Geothermal dP/dT = 5 MPa °C^{-1}*	NNO+2	1200	1120	400	0.1	1	5	4.5	NNO	*Starting composition from the last one of previous geothermal model.*
4	*Geothermal dP/dT = 3 MPa °C^{-1}*	NNO+2	1200	1067	400	1	1	3	4.5	NNO-1.4	*Starting composition from the last one of previous geothermal model.*
5	*low pressure geothermal (almost isobaric)*	NNO+1.6	1200	1050	100	0.1	1.5	0.1	0.7	NNO-2.6	*Starting composition from the second-last one of the isothermal model.*
6	*High T-P geothermal*	NNO+1.5	1300	1200	500	400	1	10	5	NNO+1.5	
7	*Isothermal*	NNO+1.5	1200	1200	400	0.1	0	10	5.3	NNO+0.9	*Starting composition from the last one of previous geothermal model.*
8	*Geothermal dP/dT = 5 MPa °C^{-1}*	NNO+1.5	1200	1120	400	0.1	1	5	5.3	NNO+0.3	*Starting composition from the last one of previous geothermal model.*
9	*Geothermal dP/dT = 3 MPa °C^{-1}*	NNO+1.5	1200	1067	400	1	1	3	5.3	NNO-2.6	*Starting composition from the last one of previous geothermal model.*
10	*low pressure geothermal (almost isobaric)*	NNO+1	1200	1050	100	0.1	1.5	0.1	0.7	NNO-2.6	*Starting composition from the second-last one of the isothermal model.*

Table 5.2 - Summary of the MELTS models described in the text and reported in the figures 5.4, 5.5, 5.6, 5.7 and 5.10.

5.4. Redox conditions variation

The $Fe^{3+}/\Sigma Fe$ ratio of the Etnean glass inclusions decreases significantly during the investigated period of differentiation (from FS to 2013 melt, figs. 4.24 and 5.10, suggesting that the magma experienced a reduction during evolutive processes and ascent. In this paragraph, we explore two possible processes that could influence the $Fe^{3+}/\Sigma Fe$ ratio of Etnean magmas.

5.4.1 Volatile degassing effect

Many recent studies discuss the effect of volatile degassing on the variation of the magmatic redox state (e.g., Burgisser and Scaillet, 2007; Moussallam et al., 2014; 2016; Gaillard et al., 2011; Waters and Lange, 2016).

The degassing of H_2O and CO_2 was proposed either to oxidize the melt (e.g., Mathez, 1984; Burgisser and Scaillet, 2007; Humphreys et al., 2015), or to have no effect on its redox state (Waters and Lange, 2016). However, the relations between these two volatiles and the $Fe^{3+}/\Sigma Fe$ ratio in etnean melt inclusions (figs. 4.25a-b) seem to indicate a reduction of the melt during H_2O and CO_2 degassing. This does not mean that H_2O and CO_2 degassing causes directly the reduction of the melt, but probably that the oxidation conditions of the magma are controlled by another process occurring concurrently.

Sulfur is known to have a more important influence on the redox conditions of a magma, due to its different oxidation state in the silicate melt and in the fluid phase (e.g. Burgisser and Scaillet, 2007; Gaillard and Scaillet, 2009; Métrich et al., 2009; Gaillard et al., 2011). Indeed, S is the only volatile species with several oxidation states, and a difference of 8 electrons between the oxidized (S^{6+}) and the reduced form (S^{2-}).

The dominant S species among the volcanic gases is SO_2, while H_2S and S_2 are minor species (e.g. Oppenheimer, 2003). In the silicate melt S^{2-} and S^{6+} generally coexist in different proportions depending on the oxygen fugacity (e.g., Jugo et al., 2010).

The degassing of S in an *oxidized melt*, in which the dominant dissolved S species is sulfate [$(SO_4)^{2-}$], releases oxygen in the FeO-bearing melt, provoking an oxidation of the melt (Métrich et al., 2009):

$$SO_4^{2-}{}_{(melt)} + 2Fe^{2+}O_{(melt)} = SO_{2(gas)} + Fe^{3+}{}_2O_{3(melt)} + O^{2-}{}_{(melt)}$$

Conversely, at *more reduced conditions* (fO_2 < NNO+1), the exolution of S^{2-} from a FeO-bearing melt could induce a decrease of Fe^{3+}/Fe^{2+} (Métrich et al., 2009):

$$S^{2-}{}_{(melt)} + 3Fe^{3+}{}_2O_{3(melt)} = SO_{2(gas)} + 6Fe^{2+}O_{(melt)} + O^{2-}{}_{(melt)}$$

Moussallam et al. (2014, 2016) observe at Erebus and Kilauea volcanos respectively, a strong reduction of the melt driven by sulfur degassing (i.e. at Erebus $Fe^{3+}/\Sigma Fe$ ratio decrease from 0.4 to 0.1).

In the investigated etnean melt inclusions a decrease of the $Fe^{3+}/\Sigma Fe$ ratio with the decrease of the S content is observed (fig. 4.25c).
In order to verify the effect of degassing on the iron speciation, we model H_2O (the most abundant volatile in magma) and S (the only polyvalent volatile species) degassing using the gas-melt equilibrium model of Gaillard and Scaillet (2009). Two simulations have been performed starting from an oxygen fugacity not higher than one log unit above the NNO buffer, at which S in melt is preferentially in its reduced form (S^{2-}). The initial conditions before degassing are: pressure = 300-400 MPa, temperature = 1110-1200°C (kept constant during the decompression), H_2O and S content of 3-4 wt.% and 2700-2900 ppm, respectively (neglecting the CO_2 degassing effect), oxygen fugacity = NNO+0.3, or NNO+1 (details of the calculations in table 5.3). The results are shown in figures 5.10. The modeled curves reproduce the degassing of H_2O and S observed in the melt inclusions and predict a slight decrease of the $Fe^{3+}/\Sigma Fe$ ratio, which is less important than that observed in the melt inclusions at high oxygen fugacity (~ NNO+1; green curves in figs. 5.10 a-b). The model performed at more reduced conditions (~ NNO+0.3, at 300 MPa and 1100 °C), better reproduces the decrease of $Fe^{3+}/\Sigma Fe$ ratio with S and H_2O degassing (figs. 5.10 a-b).
These simulations suggest that the degassing of S and H_2O could explain the decrease of the $Fe^{3+}/\Sigma Fe$ ratio from 0.25 to 0.18 but not that from 0.33 to 0.25. Hence, degassing *is probably not the only process* responsible for the important reduction trend recorded by melt inclusions.

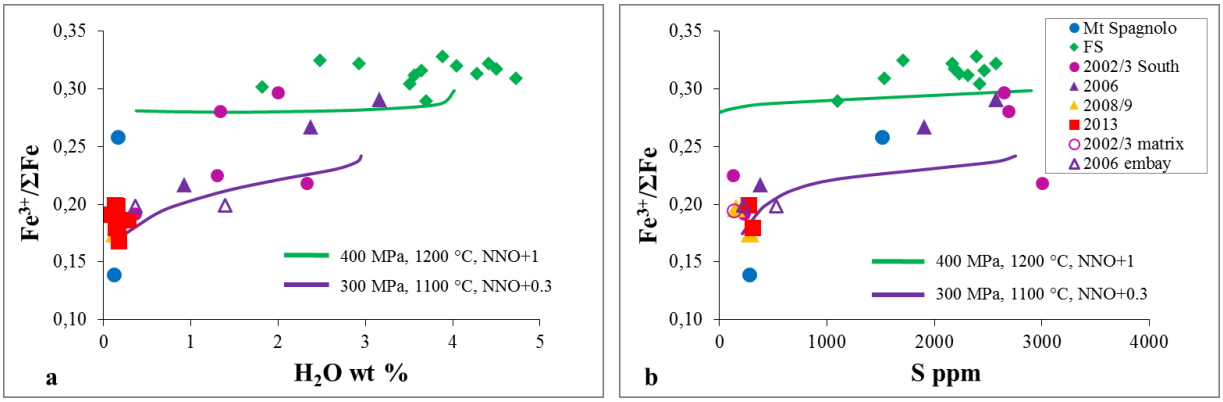

Fig. 5.10 - $Fe^{3+}/\Sigma Fe$ ratio versus S and H_2O content in MIs, embayments and matrix glasses from Mt. Etna. The modelled degassing curves for the two volatiles species are reported for initial fO_2 of NNO+1 and NNO+0.3 (table 5.3 for other details).

	Oxygen fugacity (ΔNNO)	Pressure (MPa)	Temperature (°C)	FeO* (wt.%)	S (ppm)	H_2O (wt.%)
Oxidized	+1.05	400	1200	9	2900	4
Reduced	+0.35	300	1100	10.4	2750	3

Table 5.3 - Starting conditions used for modelling degassing of S and water by Gaillard and Scaillet (2009) shown in the figure 5.10.

5.4.2 Magma differentiation effect

A very important upshot of MELTS simulations is that the $Fe^{3+}/\Sigma Fe$ ratio of the residual liquid decreases during the fractional crystallization (fig. 5.11). For each simulation, the $Fe^{3+}/\Sigma Fe$ ratio was then converted into oxygen fugacity using Kress and Carmichael (1991) equation (labels in fig. 5.11). In figure 5.11a, we show MELTS simulations with an initial fO_2 of NNO+2, while in the figure 5.11b, MELTS simulations with an initial fO_2 of NNO+1.5. In both cases the initial crystallization of olivine (0.1-0.4 %) and Cr-spinel (0.5-1.1 %) at high T-P conditions, preferentially removing Fe^{2+} into lattice sites, induces a slight increase of the $Fe^{3+}/\Sigma Fe$ ratio in the residual melt. The $Fe^{3+}/\Sigma Fe$ ratio then begins to decrease in all simulations due to clinopyroxene crystallization, which probably consumes more Fe^{3+} than Fe^{2+}. This is visible for instance in the *adiabatic (isothermal)* simulation (red curves in fig.5.11), in which 30-32 % clinopyroxene crystallizes. In the *geothermal processes*, included the almost *isobaric* calculations, the most important decrease in the $Fe^{3+}/\Sigma Fe$ ratio (a kink is visible in orange, violet and blue curves) is caused by spinel crystallization, which depends on oxygen fugacity (it occurs at higher temperature when the fO_2 is higher). Magnetite crystallization strongly decreases the $Fe^{3+}/\Sigma Fe$ ratio down to values of 0.15-0.20, which are comparable to those measured in 2013, 2008/2009, 2002 MIs and glass embayments (figs. 5.11 a-b and 5.12).

The effect of the magmatic differentiation on $Fe^{3+}/\Sigma Fe$ ratio of the residual liquid is also shown in the figures 5.12 (a-b-c-d), in which the effect of the different phases crystallizing is clearer. The MELTS geothermal simulations (violet and orange curves in figs. 5.12) well reproduce melt inclusion data in the $Fe^{3+}/\Sigma Fe$ versus MgO diagram (fig. 5.12a), and generally in the $Fe^{3+}/\Sigma Fe$ versus total FeO one (except for 2013 MIs, as already noted in fig. 5.7), but less clearly the variations in the TiO_2 content (fig. 5.12b).

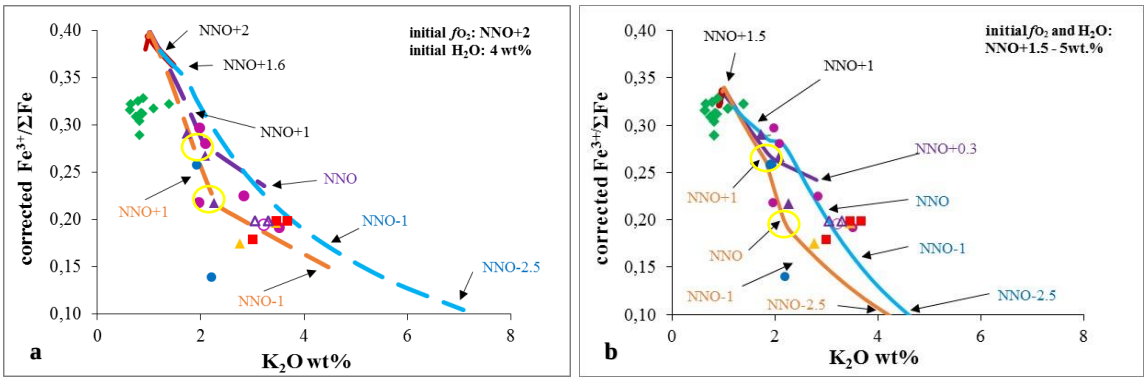

Fig. 5. 11 - Corrected $Fe^{3+}/\Sigma Fe$ ratio versus K_2O content for the studied Etnean melt inclusions, together with those calculated by the MELTS code. The conditions of the simulations are described in the text (table 5.2). a) MELTS curves performed using an initial oxygen fugacity of NNO+2 (and H_2O = 4 wt.%). b) MELTS curve obtained with an initial fO_2 of NNO+1.5 (and H_2O = 5 wt.%). For each simulation, fO_2 values, expressed as deviation from the NNO buffer, are calculated using Kress and Carmichael (1991) equation. Red curves indicate the *geothermal* simulations at high temperature and pressure, and the following *isothermal* processes at 1200 °C. The violet and orange curves the *geothermal* simulation with a slope dP/dT of 3 and 5 MPa $°C^{-1}$, respectively. In light blue the superficial *geothermal* (pressure < 10 MPa). For the MIs symbols, see the caption of figure 5.4.

These trends are interpreted to be the results of the spinel crystallization. At high oxygen fugacity ($Fe^{3+}/\Sigma Fe$ ratio in melt > 0.25 figures 5.12 b-c-d) there is the crystallization of a Cr(Mg)-rich spinel, that contribute to the decrease in MgO content of the melt and the increase in FeO*. Under more reduced condition ($Fe^{3+}/\Sigma Fe$ ratio in melt < 0.25) Ti-magnetite crystallization prevails, decreasing FeO*, FeO, Fe_2O_3, $Fe^{3+}/\Sigma Fe$, and slightly also of TiO_2 in the residual melt. In particular, the *low-pressure geothermal* calculations yield an important magnetite crystallization (9-53 %), above all when the initial redox condition are high (dashed light blue curve in fig. 5.10). This produce a FeO-poor residual liquid and the decrease of its $Fe^{3+}/\Sigma Fe$ ratio during differentiation.

To summarize, fractional crystallization modeled by MELTS, reveals a decrease of $Fe^{3+}/\Sigma Fe$ ratio during melt differentiation, well reproducing the trends observed in the investigated melt inclusions (figs. 5.11, 5.12). This suggests that the effect of the fractional crystallization in decreasing the $Fe^{3+}/\Sigma Fe$ ratio of the residual melt is predominant with respect to that of degassing, at least at high T, P, and fO_2. At more reduced condition (fO_2 < NNO+1), lower temperatures and pressures, the decrease of the $Fe^{3+}/\Sigma Fe$ ratio in the melt is probably induced by the increasing of clinopyroxene and magnetite crystallization (figs. 5.11, 5.12) coupled to the degassing of water and sulfur (figs. 5.11 a-b).

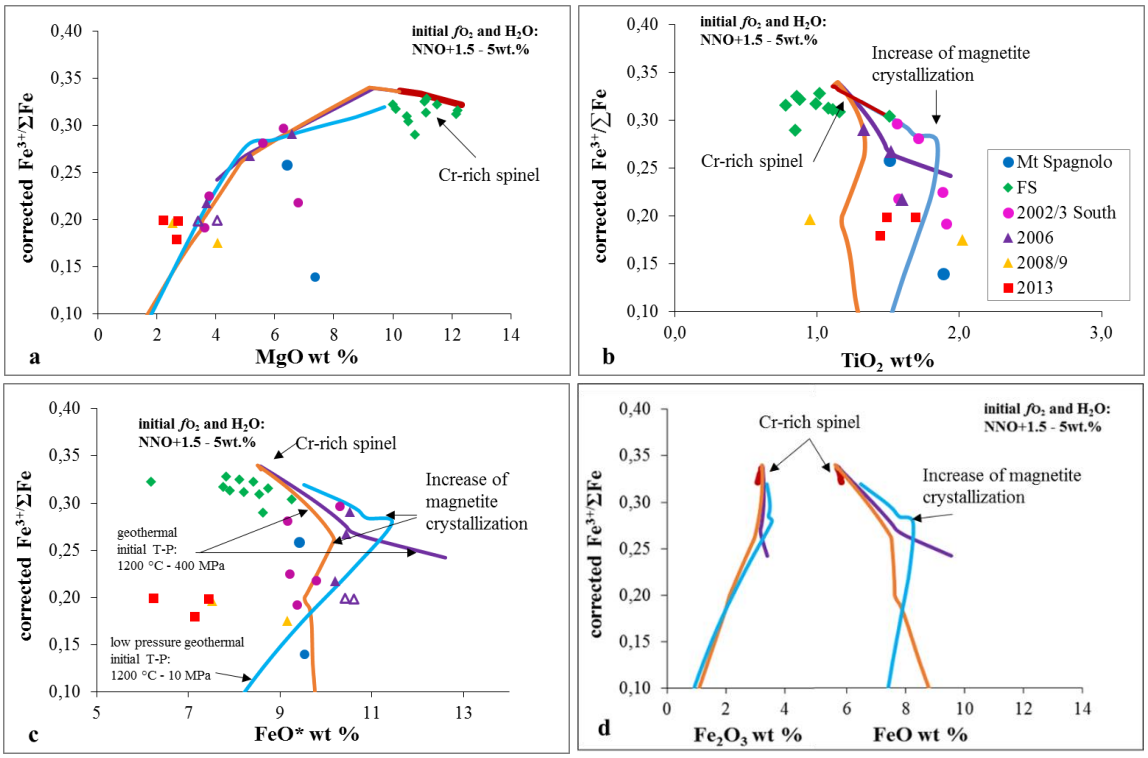

Fig. 5.12 - $Fe^{3+}/\Sigma Fe$ ratio, FeO*, FeO, Fe_2O_3, MgO contents modelled by MELTS code at initial fO_2 of NNO+1.5. Legend: the red curves indicate the *isothermal* processes at 1200 °C. The violet and orange curves the *geothermal* simulation with a slope dP/dT of 3 and 5 MPa $°C^{-1}$, respectively. In light blue the superficial *geothermal* (pressure < 10 MPa).

5.5. Sulfur behavior in the Etnean magma

In the Etnean hydrous basaltic magmas, the sulfur content in the melt is extremely variable, from few ppm in degassed magmas to more than 4000 ppm, in the melt inclusions from Mt. Spagnolo lava (fig. 5.13). In addition, the sulfur content of the Etnean melt inclusions well correlates with the estimated $Fe^{3+}/\Sigma Fe$ ratio (fig. 5.10b), that decreases during the melt differentiation (and degassing).

Our experiments with water-rich Etnean basalts (Mt. Spagnolo as starting composition), carried out at constant temperature and pressure, but different fO_2, show that the Etnean hydrous-basalt may dissolve more than 6000 ppm of sulfur when the redox conditions are oxidizing (~ NNO+1.7). This support that the high sulfur contents (up to 4150 ppm) measured in the melt inclusions of Mt. Spagnolo are attained for oxygen fugacity higher than NNO+1 (fig. 5.13). In addition, our experiments confirm the positive effect of fO_2 on the sulfur content dissolved in the silicate melt (fig. 5.13), as previous described (e.g., Fincham and Richardson, 1954; Carroll and Rutherford, 1985, 1987; Jugo et al., 2005; Jugo, 2009), and ascribed to the speciation of dissolved sulfur in the silicate melt changing from sulfide (S^{2-}) to sulfate (S^{6+}), the solubility of S^{2-} being significantly lower than that of S^{6+} (Fincham and Richardson, 1954; Carroll and Webster, 1994; Jugo, 2009; and reference therein).

In our experiments, fO_2, reducing from NNO+1.7 to NNO+0.5, decreases the S content of the melt from ~6500 ppm (in sulfide undersaturated conditions) to ~1300 ppm at sulfide saturation (fig. 5.13). One of the major deductions of this study is the belief that the variation of sulfur content observed in the Etnean melt inclusions is due to the decrease in fO_2, resulting predominantly from melt differentiation process. S degassing would be therefore triggered by melt reduction and would in turn enhance melt reduction.

MELTS software gives also the possibility for checking the behavior of sulfur during fractional crystallization mechanism. In MELTS, sulfur is treated like an incompatible element, therefore the residual melt tend to enrich in it during the early stages of fractional crystallization. Nevertheless, once the sulfide saturation is reached, the sulfur content in the melt cannot incree further, but it should exsolve in a fluid phase, triggering the S degassing. MELTS is not able to reproduce the variation of the S behavior from "dissolved" to "exsolved" in the residual melt.

We use a simple calculation to model the behavior of the dissolved sulfur in the Etnean magma during the fractional crystallization, and the following degassing. For each MELTS simulation (table 5.2), we have calculated the sulfur content in the residual melts, for each step of crystallization, assuming a constant S/K_2O ratio, considering that both elements are incompatible during the fractional crystallization:

$$S = S/K_2O \cdot K_2O_{melt} \qquad \textbf{\{1\}}$$

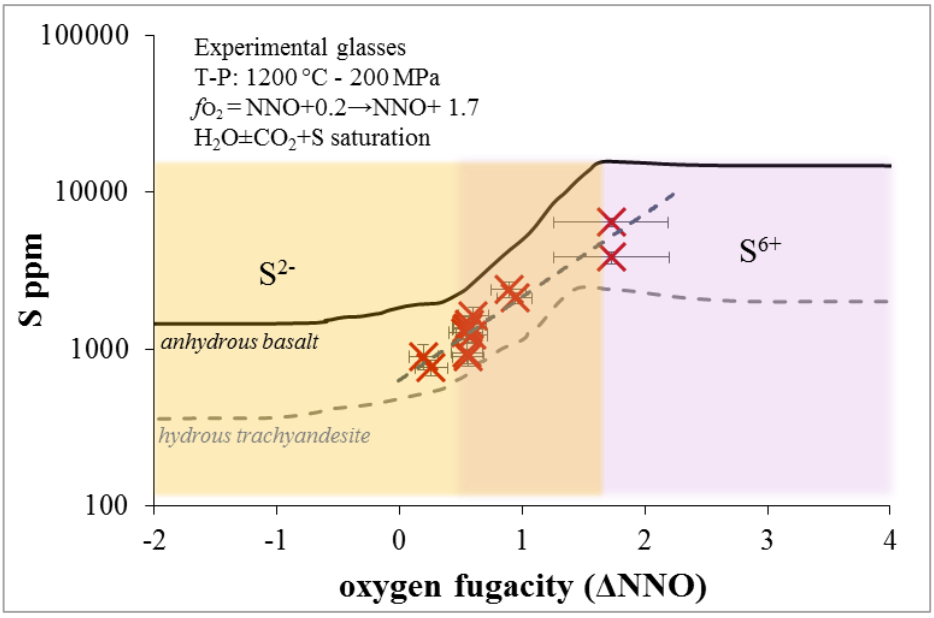

Fig. 5.13 - S content in the Etnean experimental glasses as a function of the oxygen fugacity. The black and dashed grey curves are from Jugo, 2009 for anhydrous basalt (Jugo et al., 2005) and for hydrous trachyandesite (Carroll and Rutherford, 1985, 1987), respectively. Our experimental glasses at fO_2 < NNO+1 present small sulfide globules, while the more oxidized glasses have not achieved the sulfide saturation.

The used value (S/K_2O = 0.27) is calculated from the S and K_2O content in the two melt inclusions of FS (B and Z) used as starting composition for the MELTS calculations (table 5.1). As predictable, the sulfur content, calculated in this way, increases in the residual melt during the fractional crystallization of S-free phases (fig. 5.14).

In order to model the sulfur degassing from the MELTS calculations, we use the mean value of the partition coefficient $Ds^{fluis/melt}$ (175±108) calculated from the experimental study (see paragraph 4.4.1). This value is used in each step of MELTS simulations to calculate the sulfur content in the residual melt (S^*_{melt}) during a probable degassing process, as in the following mass balance:

$$S^*_{melt} = [S_{melt} \cdot M_{syst}] / [M_{melt} + M_{gas} \cdot Ds^{fluid/melt}] \qquad \{2\}$$

in which M_{syst}, M_{melt} and M_{gas} are the total mass of the system, of the residual melt and of the fluid phase calculated by MELTS, respectively. The fluid phase, in this case, consists only of the water exsolved during the decompression and the fractional crystallization simulated through MELTS code.

The first algorithm (**{1}**) is used to evaluate the S increase in the residual melt up to oxygen fugacity around NNO+1. Starting from this oxygen fugacity, the second one (**{2}**) is applied for describing the S degassing in the same MELTS calculations. The results of these two calculations for some MELTS simulations are shown in the plot of figure 5.14. In this plot we reported the calculated S and the MgO content for the models starting from an initial

oxygen fugacity of NNO+2, considering that the MgO content calculated by MELTS in the 2 series (fO_2-H_2O: NNO+1.5-5wt.% and NNO+2-4wt.%) of simulations is very similar (independently of the initial fO_2, see figure 5.4 and appendix A6).

The *geothermal* models at high T-P and the following *isothermal/adiabatic* (at 1200 °C) simulations, are accompanied by a continue increase of S content in the melt during the fractional crystallization, since that the fO_2 maintains high values (> NNO+1.5). The other *geothermal* models (at initial T and fO_2 of 1200 °C and NNO+1.5), being characterized by an important fO_2 reduction, get both the enrichment of sulfur in the melt during the fractional crystallization, and the subsequent sulfur degassing. The results obtained from the two algorithms (**{1}** and **{2}**) well reproduce the sulfur content measured in the melt inclusions within the grey area of the figure 5.14.

The first algorithm achieves, at oxygen fugacity around NNO+1.1, a high S content (> 4000 ppm), near the maximum content measured in the melt inclusions of Mt. Spagnolo (fig. 5.14). This simple algorithm confirms that Mt. Spagnolo magma is the result of the fast ascent of a FS primitive melt at redox condition enough high to maintain the sulfur dissolved in the melt during the fractional crystallization. The following rapid cooling at superficial depth induces the rapid S degassing. Unfortunately, we have no XANES results for the Mt. Spagnolo melt inclusions with the highest sulfur content.

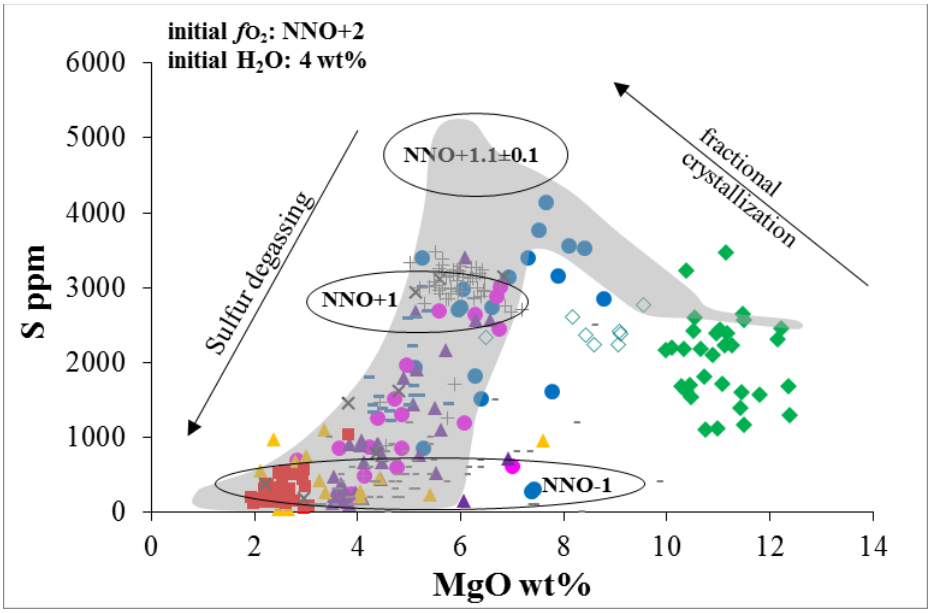

Fig. 5.14 - S versus MgO content of the investigated melt inclusions and those from previous studies (e.g., Métrich et al., 2004; Spilliaert et al., 2006; Collins et al., 2009; Corsaro and Métrich, 2016). In this plot, the gray area indicates the S content calculated using the equation {1} and {2} described in the text, for the MELTS simulations, modeling fractional crystallization starting from an oxygen fugacity of NNO+2. For the MIs symbols, see the caption of figure 5.4.

Therefore, taking into account i) the MIs and experimental data, ii) the XANES $Fe^{3+}/\Sigma Fe$ ratio in MIs and iii) the MELTS results, we suggest that a *coupled fractional*

crystallization-decompression process is the principal responsible of the variable sulfur content observed in the Etnean melt inclusions. This melt differentiation induces initially the enrichment in sulfur by fractional crystallization of S-free phases when the oxygen fugacity of the magmatic system remains constantly high or is enhanced by olivine fractionation (around NNO+1-NNO+1.5). This process can explain the exceptionally high sulfur content measured in the MIs of Mt. Spagnolo (up to 4150 ppm), even if the H_2O contents and the related entrapment pressures are extremely low. This could be the result of the enrichment of sulfur in the FS parental melt at high fO_2 (in agreement with the experimental glasses at NNO+1.7), in which the dissolved sulfur in the melt is principally in its oxidized form (S^{6+}) as confirmed qualitatively by Raman spectra (fig. 5.15 from *Morizet et al., submitted*).

Subsequently, the contemporaneous crystallization of olivine + clinopyroxene + spinel yield the reduction of the magma and the consequent degassing of S. This leads to the sulfide saturation of the melt, as indicated by the occurrence of sulfide globules inside some melt inclusions from the recent products (2006, 2008/2009 and 2013). Anyway, sulfide globules in the natural glasses are not abundant, as confirmed by the low sulfur content in the bulk rock ($\leq$ 0.01wt.%, fig. 5.3, table 4.1), indicating that most of the sulfur initially dissolved in the hydrous melt is degassed when the redox conditions drop (fO_2 < NNO+1).

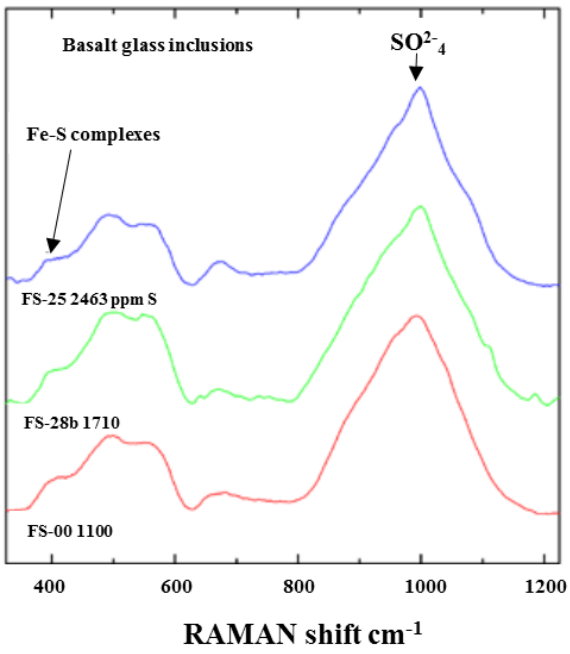

Fig. 5.15 - Raman spectra obtained on some FS melt inclusions (from *Morizet et al., submitted;* see also appendix A5 for details about Raman spectroscopy).

CONCLUSIONS

In order to improve knowledge of sulfur solubility in the hydrous basalts and of the S behavior and redox conditions in the basaltic to picritic magmas, we have carried out a melt inclusion study, coupled with an experimental investigation on S solubility in the Etnean alkali basalt.

Olivine hosted melt inclusions were accurately selected from rocks formed during Etnean eruptions of the last 15000 years. In particular, from the oldest and most primitive magmas (Mt. Spagnolo basalt and FS picrite) up to more "evolved" basalts erupted during the recent paroxysm event of April 2013, and from the trachybasalts of 2002/2003, 2006 and 2008/2009 eruptions.

Melt inclusions were characterized for their major elements compositions and volatiles contents by electron microprobe, ionic probe, and infrared spectroscopy.

The experimental glasses were obtained, from Mt. Spagnolo basalts, at supra-liquidus conditions (T=1200 °C, P=200 MPa), at water (and sulfide) saturation, and at carefully constrained oxygen fugacity (variable from NNO+0.2 to NNO+1.7).

XANES $Fe^{3+}/\sum Fe$ spectra were acquired for some natural and experimental glasses, in order to calculate the $Fe^{3+}/\sum Fe$ ratio, proportional to the redox conditions.

The chemical composition of Etnean melt inclusions was interpreted using MELTS code, while the interpretation of the S content and Fe speciation has used the hydrous basaltic experimental glasses.

Here the principal remarks obtained from this research:

- ✓ Sulfur solubility experiments have shown the important control of the oxygen fugacity on the sulfur content in the Etnean hydrous basaltic glasses. In particular, at the lower investigated fO_2 (ΔNNO = 0.2-0.9), sulfur solubility reached 2400 ppm at sulfide saturation; while at the higher fO_2 (ΔNNO = 1.7) the highest S content (6454 ppm) was measured, but without sulfide or sulfate solid phases saturating.
  The variability of the fluid/melt partitioning for S ($D_S^{fluid/melt}$ = 175±108) suggests that at higher redox conditions (fO_2 > NNO+1), sulfur partitions preferably in the melt phase, while at lower fO_2 (ΔNNO = 0.2 to 0.9), sulfur strongly partitions in the fluid (*and the sulfide*) phase.

- ✓ The most primitive melt inclusions, among the investigated Etnean products, are those entrapped in FS and Mt. Spagnolo olivine phenocrysts (Fo_{91} and Fo_{87}, respectively). MIs in FS are the most undegassed and oxidized ($Fe^{3+}/\Sigma Fe$ = 0.3) at Mt. Etna, with high volatile content (H_2O up to 5.7 wt.%, CO_2 up to more than 5000 ppm, S up to 3500 ppm), while Mt. Spagnolo MIs have the lower water (< 0.5 wt.%) and the highest sulfur (4150 ppm) contents.

- ✓ The investigated Etnean melt inclusions are characterized by large variability of FeO* (4.3-12.6 wt.%) and S (166-4150 ppm) contents, with a continuous increase of alkali

content from FS to 2013 magma (K_2O up to 5.6 wt.%, and Na_2O up to 8.2 wt.%). Concurrently, the $Fe^{3+}/\Sigma Fe$ ratios (determined by XANES spectroscopy) decrease from the most primitive FS picrite toward the evolved and degassed basalts of 2013.

- ✓ Petrogenetic modeling (MELTS code), using only major elements compositions in melt inclusions, allowed to assess that FS could represent the parental, oxidized (sulfur undersaturated) magma, with the Mt. Spagnolo and the others recent basalts that could represent derivate melts, after fractional crystallization of olivine + clinopyroxene ± spinel ± plagioclase. Furthermore, Mt. Spagnolo melt shows features of a low-pressure mixing process with a more evolved composition.

- ✓ The melt differentiation, simulated by MELTS with a starting oxygen fugacity, fixed at ΔNNO = +1.5 and +2, shows a decreases of $Fe^{3+}/\Sigma Fe$ ratios, as measured in melt inclusions. In particular, the early appearance on the liquidus at high pressure of olivine + Cr(Mg)-spinel resulted in an initial increase of the $Fe^{3+}/\Sigma Fe$ ratio in the melt. Then, at lower temperature, the clinopyroxene and Ti-magnetite-spinel crystallization resulted in a clear decrease in the $Fe^{3+}/\Sigma Fe$ ratio (melt reduction).

- ✓ The sulfur content determined in Etnean melt inclusions is the result of a coupled fractional crystallization-decompression process. The melt differentiation at higher oxygen fugacity (between NNO+1 and NNO+2, when S^{6+} prevails on S^{2-}) induces initially the enrichment of the melt in sulfur, as could be represented by the highest S content measured in Mt. Spagnolo MIs (4150 ppm). Afterward, the contemporaneous crystallization of olivine + clinopyroxene + Ti-magnetite-spinel at lower fO_2 (< NNO+1, when S^{2-} prevails on S^{6+}), yield the decrease of sulfur solubility (and the sulfide saturation of the melt), resulting in the sulfur outgassing.

We believe that the results coming from this research could shed light on the several issues still opened about the complex Etnean (oxidized) magmatic source, and onto the evolutionary scenario of the present-day volcanic activity of Mount Etna, although further investigation are necessary to better understand the sulfur isotopic composition and sulfur speciation in the melt inclusions.

This PhD data could be useful to estimate the atmospheric S discharge, occurred during the studied eruptions, both for the oldest eruptions, for which direct measurement are missing; both for the recent ones to estimate the magma budgets.

Data could be valuable to improve a quantitative model of magma degassing incorporating these new volatile contents and redox condition constraints, to use for volcanic surveillance.

Finally, the determination of sulfur solubility and Fe speciation in basaltic magmas, and the application to the Etnean magmatic system, will represent a reference and a step forward for the scientific community working on this research field.

References

Acocella, V., Behncke, B., Neri, M., and D'Amico, S., 2003. Link between major flank slip and 2002-2003 eruption at Mt. Etna (Italy). Geophysical Research Letters, 30 (24), 2286, doi: 10.1029/2003GL018642.

Aiuppa, A., Moretti, R., Federico, C., Giudice, G., Gurrieri, S., Liuzzo, M., Papale, P., Shinohara, H., and Valenza, M., 2007. Forecasting Etna eruptions by real-time observation of volcanic gas composition, Geology, 35, 1115–1118, doi:10.1130/G24149A.1.

Aiuppa, A., Giudice, G., Gurrieri, S., Liuzzo, M., Burton, M., Caltabiano, T., McGonigle, A.J.S., Salerno, G., Shinohara, H., and Valenza, M., 2008. Total volatile flux from Mount Etna. Geophysical Research Letters, 35, L24302, doi: 10.1029/2008GL035871.

Allard, P., 1978. Composition isotopique et origine des constituants majeurs des gaz volcaniques, thesis, 214 pp., Paris Univ., Paris.

Allard, P., 1983. The origin of hydrogen, carbon, sulphur, nitrogen and rare gases in volcanic exhalations: Evidence from isotope geochemistry, in Forecasting Volcanic Events, edited by H. Tazieff and J. C. Sabroux, pp. 337-386, Elsevier, Amsterdam.

Allard, P., 1986. Isotopic composition and origin of water, carbon, and sulfur in volcanic gases: Rift zones, continental margins and island arcs, PhD thesis, Paris Univ., Paris.

Allard, P., Behncke, B., D'Amico, S., Neri, M., Gambino, S., 2006. Mount Etna 1993-2005: anatomy of an evolving eruptive cycle. Earth-Science Reviews 78, 85-114.

Andronico, D., Branca, S., Calvari, S., Spampinato, L., 2005. A multi-disciplinary study of the 2002-03 Etna eruption: Insights into a complex plumbing system. Bulletin of Volcanology 67, 314-330, doi: 10.1007/s00445-004-0372-8.

Armienti, P., Innocenti, F., Petrini, R., Pompilio, M., Villari, L., 1988. Sub-aphyric alkali basalt from Mt Etna: inferences on the depth and composition of the source magma. Rendiconti della Società Italiana di Mineralogia e Petrologia 43, 877-891.

Armienti, P., Innocenti, F., Petrini, R., Pompilio, M., Villari, L., 1989. Petrology and Sr-Nd isotope geochemistry of recent lavas from Mt. Etna: bearing on the volcano feeding system. Journal of Volcanology and Geothermal Research 39, 315–327.

Armienti, P., Paresehi, M.T., Innocenti, F., and Pompilio, M., 1994. Effects of magma storage and ascent of crystal growth: The case of the 1991-93 Mt. Etna eruption. Contributions to Mineralogy and Petrology, 115:402-414.

Armienti P., Tonarini S., D'Orazio M., Innocenti F., 2004. Genesis and Evolution of Mt Etna alkaline lavas: petrological and Sr-Nd-B isotope costraints. Periodico di Mineralogia 73, 29-52.

Armienti, P., Tonarini, S., Innocenti, F. and D'Orazio, M., 2007. Mount Etna pyroxene as tracer of petrogenetic processes and dynamics of the feeding system. In: Beccaluva, L., Bianchini, G. and Wilson, M. (eds) Cenozoic Volcanism in the Mediterranean Area, Geological Society of America, Special Papers 418, 265^276, doi:10.1130/2007.2418(13).

Armienti, P., Perinelli, C., Putirka, K.D., 2012. A new model to estimate deep-level magma ascent rates, with applications to Mt. Etna (Sicily, Italy). Journal of Petrology 54, 795-813.

Azzaro, R., 1999. Earthquake surface faulting at Mount Etna volcano (Sicily) and implication for active tectonics. Journal of Geodynamics 29, 193-213.

Bajt S., Sutton S.R., Delaney J.S., 1994. X-ray microprobe analysis of iron oxidation states in silicates and oxides using X-ray absorption near edge structure (XANES). Geochimica e Cosmochimica Acta 58, 5209-5214.

Ballhaus, C., 1993. Redox states of lithospheric and asthenospheric upper mantle: Contributions to Mineralogy and Petrology, v. 114, p. 331–348, doi: 10.1007/BF01046536.

Beermann, O., Botcharnikov, R.E., Holtz, F., Diedrich, O., Nowak,M., 2011. Temperature dependence of sulfide and sulfate solubility in olivine-saturated basaltic magmas. Geochim. Cosmochim. Acta 75 (23), 7612-7631.

Behncke, B., Branca, S., Corsaro, R.A., De Beni, E., Miraglia, L., Proietti, C., 2014. The 2011-2012 summit activity of Mount Etna: birth, growth and products of the new SE crater. Journal of Volcanology and Geothermal Research 270:10-21.

Berndt, J., Liebske, C., Holtz, F., Freise, M., Nowak, M., Ziegenbein, D., Hurkuck, W., And Koepke, J., 2002. A combined rapid-quench and H_2-membrane setup for internally heated pressure vessels: Description and application for water solubility in basaltic melts. American Mineralogist, Volume 87, Pages 1717-1726.

Bonaccorso, A., Bonforte, A., Calvari, S., Del Negro, C., Di Grazia, G., Ganci, G., Neri, M., Vicari, A., Boschi, E., 2011. The initial phases of the 2008-2009 Mt. Etna eruption: a multi-disciplinary approach for hazard assessment. Journal of Geophysical Research, Vol. 116, B03203, doi: 10.1029/2010JB007906.

Botcharnikov, R.E., Behrens, H., Holtz, F., Koepke, J., Sato, H., 2004. Sulfur and chlorine solubility in Mt. Unzen rhyodacitic melt at 850 °C and 200 MPa. Chem. Geol. 213, 207-225.

Bousquet, J.C., and Lanzafame, G., 2004. The tectonics and geodynamics of Mt. Etna: synthesis and interpretation of geological and geophysical data. In: Bonaccorso, A., Calvari, S., Coltelli, M., Del Negro, C., Falsaperla, S. (Eds.), Mt. Etna: Volcano Laboratory. American Geophysical Union, Washington, D. C. http://dx.doi.org/10.1029/143GM03.

Branca, S., and Del Carlo, P., 2004a. Eruptions of Mt. Etna during the past 3200 years: a revised compilation integrating the historical and stratigraphic records. In: Bonaccorso, A., Calvari, S., Coltelli, M., Del Negro, C., Falsaperla, S. (Eds.),Mt. Etna: Volcano Laboratory. American Geophysical Union, Washington, D. C. http://dx.doi.org/10.1029/143GM02.

Branca S., Coltelli M., Groppelli G., 2004b. Geological evolution of Etna volcano. In: Mt. Etna: Volcano Laboratory, Bonaccorso, A., Calvari, S., Coltelli, M., Del Negro, C., Falsaperla, S., pp. 49-63, American Geophysical Union, Geophysical Monograph 143.

Branca, S., Coltelli, M., De Beni, E., Wijbrans, J., 2008. Geological evolution of Mount Etna volcano (Italy) from earliest products until the first central volcanism (between 500 and 100 ka ago) inferred from geochronological and stratigraphic data. Intern. Journal of Earth Science, 97:135-152. doi: 10.1007/s00531-006-0152-0.

Branca, S., Coltelli, M., Groppelli, G., 2011. Geological evolution of a complex basaltic stratovolcano: Mount Etna, Italy. Italian Journal of Geosciences 130, 306-317.

Bucholz, C.E., Gaetani, G. A., Behn, M.D., Shimizu N., 2013. Post-entrapment modification of volatiles and oxygen fugacity in olivine-hosted melt inclusions. Earth and Planetary Science Letters. http://dx.doi.org/10.1016/j.epsl.2013.05.033i.

Burgisser, A., Scaillet, B., 2007. Redox evolution of a degassing magma rising to the surface. Nature445, 194-197.

Burnham, C.W., 1979. The importance of volatile constituents. In: Yoder, H. S., Jr (ed.). The Evolution of Igneous Rocks. Princeton, NJ: Princeton University Press, pp. 439-482.

Caltabiano, T., Salerno, G.G., Bruno, N. and Longo, V., 2003. Mt. Etna SO_2 emissions during the 2002-2003 eruption, paper presented at AGUEGS- EGU Assembly, Nice, 6-11 April.

Calvari, S., Coltelli, M., Neri, M., Pompilio, M., and Scribano, V., 1994. The 1991–1993 Etna eruption: chronology and lava flow-field evolution. Acta Vulcanologia 4, 1-14.

Calvari, S., Tanner, L.H., Groppelli, G., Norini, G., 2004. A comprehensive model for the opening of the Valle del Bove depression and hazard evaluation for the eastern flank of Etna volcano. In Mt Etna: Volcano Laboratory. Geophysical Monograph Series 143, 65-75.

Carroll, M.R., Rutherford, M.J., 1985. Sulfide and sulfate saturation in hydrous silicate melts. Journal of Geophysical Research, 90, C601-C612.

Carroll, M.R., Rutherford, M.J., 1987. The stability of igneous anhydrite. Experimental results and implications for sulfur behaviour in the 1982 El-Chichon trachyandesite and other evolved magmas. Journal of Petrology 28 (5), 781-801.

Carroll, M.R., and Webster, J.D., 1994. Solubilities of Sulfur, Noble Gases, Nitrogen, Chlorine, and Fluorine in Magma Reviews in Mineralogy and Geochemistry Chapter 7. p. 231-280.

Cecchetti, A., Marianelli, P., Sbrana, A., 2002. L'eruzione Di Astroni (Caldera Dei Campi Flegrei): Dati Preliminari Dallo Studio Di Inclusioni Silicatiche. Atti Soc. tosc. Sci. nat., Mem., Serie A, 108 (2002-2003) pagg. 59-63.

Chaussidon, M., Sheppard, S., Michard, A., 1991. Hydrogen, sulphur and neodymium isotope variations in the mantle beneath the EPR at 12°50' N. Stable Isotope Geochemistry: a Tribute to Samuel Epstein: Geochemical Society, Special Publication, 3, pp. 325-337.

Clemente, B., Scaillet, B., Pichavant, M., 2004. The solubility of sulphur in hydrous rhyolitic
melts. Journal of Petrology 45 (11), 2171-2196.

Clocchiatti, R., Métrich, N., 1986. Refilling and mineralogical disequilibrium in Etnean lava-the Monte Frumento delle Concazze eruption. Comptes Rendus De L Academie Des Sciences Serie Ii 303, 1117-1122.

Clocchiatti, R., Joron, J.L., Treuil, M., 1988. The role of selective alkali contamination in the evolution of recent historical lavas of Mt. Etna. Journal of Volcanology and Geothermal Research 34, 241-249.

Clocchiatti, R., Schiano, P., Ottolini, L., Bottazzi, P., 1998. Earlier alkaline and transitional magmatic pulsation of Mt Etna volcano. Earth and Planetary Science Letters 163, 399-407.

Clocchiatti, R., Condomines, M., Guénot, N., Tanguy, J.C., 2004. Magma changes at Mount Etna: the 2001 and 2002-2003 eruptions. Earth and Planetary Science Letters 226, 397-414.

Cocina, O., Neri, G., Privitera, E., Spampinato, S., 1997. Stress tensor computations in the Mount Etna area (Southern Italy) and tectonic implications. Journal Geodynamics 23, 109-127.

Cocina, O., Neri G., Privitera, E., Spampinato, S., 1998. Seismogenic stress field beneath Mt Etna (South Italy) and possible relationships with the volcano-tectonic features. Journal of Volcanology and Geothermal Research 83, 335-348.

Collins, S.J., Pyle, D.M., Maclennan, J., 2009. Melt inclusions track pre-eruption storage and dehydration of magmas at Etna. Geology 37, 571-574.

Coltelli, M., Del Carlo, P., Pompilio, M., Vezzoli, L., 1998. Discovery of a Plinian basaltic eruption of Roman age at Etna volcano, Italy. Geology 26, 1095-1098.

Coltelli, M., Del Carlo, P., Vezzoli, L., 2000. Stratigraphic constrains for explosive activity in the last 100 ka at Etna volcano, Italy. International Journal of Earth Sciences 89, 665-677.

Coltelli, M., Del Carlo, P., Pompilio, M., Vezzoli, L., 2005. Explosive eruptions of a picrite: The 3930 BP subplinian eruption of Etna volcano (Italy). Geophysical Research Letter 32, L23307, doi:10.1029/2005GL024271.

Continisio, R., Ferrucci, F., Gaudiosi, G., Lo Bascio, D., Ventura, G., 1997. Malta Escarpment Mt Etna: early stages of an asymmetric rifting process? Evidences from geophysical and geological data. Acta Vulcanologica 9, 45-53.

Correale, A., Paonita, A., Martelli, M., Rizzo, A., Rotolo, S.G., Corsaro, R.A., Di Renzo, V., 2014. A two-component mantle source feeding Mt. Etna magmatism: Insights from the geochemistry of primitive magmas Lithos 184–187, 243-258.

Corsaro, R.A., and Cristofolini, R., 1996. Origin and differentiation of recent basaltic magmas from Mount Etna. Mineralogy and Petrology 57, 1-21.

Corsaro, R.A., and Cristofolini, R., 1997. Geology, geochemistry and mineral chemistry of tholeiitic to transitional Etnean magmas. Acta Vulcanologica 9, 55-66.

Corsaro, R.A., and Cristofolini, R., 2000. Sub-aqueous volcanism in the Etnean area: evidence for hydromagmatic activity and regional uplift inferred from the Caste Rock of Acicastello. Journal of Volcanology and Geothermal Research 95, 209-225.

Corsaro, R.A., and Pompilio, M., 2004a. Dynamics of magmas at Mount Etna. In: Mount Etna: Volcano Laboratory. Geophysical Monograph Series 143, 91-110.

Corsaro, R.A., and Pompilio M., 2004b. Buoyancy-controlled eruption of magmas at Mt Etna. Terra Nova, 16, 16-22.

Corsaro, R.A., Miraglia, L., Pompilio, M., 2006. Petrologic evidence of a complex plumbing system feeding the July-August 2001 eruption of Mt. Etna, Sicily, Italy. Bulletin of Volcanology 69, 401-421.

Corsaro, R.A., Métrich, N., Allard, P., Andronico, D., Miraglia, L., Fourmentraux, C., 2009. The 1974 flank eruption of Mount Etna: an archetype for deep dike-fed eruptions at basaltic volcanoes and a milestone in Etna's recent history. Journal of Geophysical Research 114, B07204. http://dx.doi.org/10.1029/2008JB006013.

Corsaro, R. A., and Métrich, N., 2016. Chemical heterogeneity of Mt. Etna magmas in the last 15 ka. Interferences on their mantle sources. Lithos 252-253, 123-134.

Cottrell, E., Lanzirotti, A., Kelley, K. A., Newville, M., Birner, S., Davis, F.A., Mysen, B., and Botcharnikov, R., 2016. Radiation-induced oxidation of Fe in hydrous basalt glasses. Goldschmidt 2016, Conference Abstracts 550.

Cottrell, E., Kelley, K.A., Lanzirotti, A., Fischer, R.A., 2009. High-precision determination of iron oxidation state in silicate glasses using XANES. Chem. Geol. 268 (3-4), 167-179.

Coulson, I.A., Finlay M. Stuart, F.M., MacLean, N.J., 2011. Assessing the link between mantle source and sub-volcanic plumbing in the petrology of basalts from the 2001 and 2002/2003 eruptions of Mount Etna, Sicily: Evidence from geochemical and helium isotope data. Lithos 123, 254–261.

Danyushevsky, L.V., Della-Pasqua, F.N., Sokolov, S., 2000. Re-equilibration of melt inclusions trapped by magnesian olivine phenocrysts from subduction-related magmas: petrological implications. Contributions to Mineralogy and Petrology 138: 68-83.

Danyushevsky, L.V., 2001. The effect of small amounts of H_2O on crystallisation of midocean ridge and backarc basin magmas: Journal of Volcanology and Geothermal Research, v. 110, p. 265-280.

Danyushevsky, L.V., Sokolov, S. and Falloon, T.J., 2002. Melt inclusions in olivine phenocrysts: Using diffusive re-equilibration to determine the cooling history of a crystal, with implications for the origin of olivine-phyric volcanic rocks, Journal of Petrology, 43, 1651–1671, doi:10.1093/petrology/ 43.9.1651.

Danyushevsky, L.V., and Plechov, P., 2011. Petrolog3: Integrated software for modeling crystallization processes. Geochemistry Geophysics Geosystems 12, Q07021, doi:10.1029/2011GC003516.

De Beni, E., Branca, S., Coltelli, M., Groppelli, G., Wijbrans, J.R., 2011. 40Ar/39Ar isotopic dating of Etna volcanic succession. Italian Journal of Geosciences 130, 292–305.

De Rita, D., Frazzetta, G., Romano, R., 1991. The Biancavilla-Montalto ignimbrite (Etna, Sicily). Bulletin of Volcanology 53, 121-131.

Devine, J.D., Gardner, J.E., Brack, H.P., Layne, G.D., Rutherford, M.D., 1995. Comparison of microanalytical methods for estimating H_2O contents of silicic volcanic glasses. Am Mineral 80: 319-328.

Di Carlo, I., Pichavant, M., Rotolo, S., G., and Scaillet, B., 2006. Experimental Crystallization of a High-K Arc Basalt: the Golden Pumice, Stromboli Volcano (Italy). Journal of Petrology v. 47 - 7, 1317-1343, doi:10.1093/petrology/egl011.

Dixon, J. E. and Pan, V., 1995. Determination of the molar absorptivity of dissolved carbonate in basanitic glass. Am. Mineral. 80, 1339-1342.

Doglioni, C., Innocenti, F., Mariotti, G., 2001. Why Mt Etna? Terranova 13, 25-31.

Ferlito, C., and Lanzafame, G., 2010. The role of supercritical fluids in the potassium enrichment of magmas at Mount Etna volcano (Italy). Lithos 119, 642-650.

Ferlito, C., Coltorti, M., Lanzafame, G., Giacomoni, P.P., 2014. The volatile flushing triggers eruptions at open conduit volcanoes: evidence from Mount Etna volcano (Italy). Lithos 184, 447-455.

Ferry, J.M. and Baumgartner, L., 1987. Thermodynamic models of molecular fluids at the elevated pressures and temperatures of the crustal metamorphism. In: Eugster, H.P. and Carmichael, I.S.E. (eds) thermodynamic Modelling of Geological Materials: Minerals, Fluids and Melts. Mineralogical Society of America, Reviews in Mineralogy 17, 323-365.

Fincham, C.J.B., and Richardson, F.D., 1954. The behaviour of sulphur in silicate and aluminate melts: proceedings of the Royal Society of London, ser. A, Mathematical and Physical Sciences, v. 223, p. 40-62.

Fortin, M.A., Riddle, J., Desjardins-Langlais, Y., Baker, D. R., 2015. The effect of water on the sulfur concentration at sulfide saturation (SCSS) in natural melts. Geochimica e Cosmochimica Acta 160, 100-116.

Frank, M.R., Candela, P.A., Piccoli, P.M., 2003. Alkali exchange equilibria between a silicate melt and coexisting magmatic volatile phase: an experimental study at 800 °C and 100 MPa. Geochimica et Cosmochimica Acta 67, 1415-1427.

Frezzotti, M. L., 2001. Silicate-melt inclusions in magmatic rocks: applications to petrology. Lithos 55, 273-299.

Gaetani, G., A., and Watson, B., E., 2002. Modeling the major-element evolution of olivine-hosted melt inclusions a Chemical Geology 183, 25-41.

Gambardella, B., 2000. Abbondanza e composizione isotopica dello zolfo nelle vulcaniti etnee. Quantificazione degli equilibri ossido-riduttivi in atto, MSc thesis, Univ. of Genoa, Genoa, Italy.

Gaillard, F., Scaillet, B., 2009. The sulfur content of volcanic gases on Mars. Earth and Planetary Science Letters, 279, 34-43.

Gaillard, F., Scaillet, B., Arndt, N.T., 2011. Atmospheric oxygenation caused by a change in volcanic degassing pressure. Nature478, 229-232.

Ghiorso, M.S., and Sack, R.O., 1995. Chemical Mass-Transfer in Magmatic Processes IV. A Revised and Internally Consistent Thermodynamic Model for the Interpolation and Extrapolation of Liquid-Solid Equilibria in Magmatic Systems at Elevated-Temperatures and Pressures, Contributions to Mineralogy and Petrology, 119 (2-3), 197-212.

Guo, S., Bluth, G.J.S., Rose, W,I,, Watson, I.M., Prata, A.J., 2004. Re-evaluation of SO_2 release of the 15 June 1991 Pinatubo eruption using ultraviolet and infrared satellite sensors. Geochemistry Geophysics Geosystems 5:Q04001, doi: 101029/2003GC000654

Gvirtzman, Z., and Nur, A., 1999. The formation of Mount Etna as the consequence of the slab rollback. Nature 401, 782-785.

Haughton, D.R., Roeder, P.L. and Skinner, B.J., 1974. Solubility of sulfur in mafic magmas. Econ. Geol. 69, 451-467.

Holloway, J. R., 1987. Igneous fluids. In: Eugster H. P. and Carmichael I. S. E. (eds) Thermodynamic Modelling of Geological Materials: Minerals, Fluids and Melts. Mineralogical Society of America, Reviews in Mineralogy 17, 211-233.

Humphreys, M.C.S., Brooker, R.A., Fraser, D.G., Burgisser, A., Mangan, M.T., McCammon, C., 2015. Coupled interactions between volatile activity and Fe oxidation state during arc crustal processes. Journal of Petrology, egv017.

Iacono-Marziano, G., Morizet, Y., Le Trong, E., Gaillard, F., 2012. New experimental data and semi-empirical parameterization of H_2O-CO_2 solubility in mafic melts. Geochimica et Cosmochimica Acta 97, 1-23.

Innocenti, F., Rocchi, S., Trigila, R., 1999. La classificazione delle rocce vulcaniche e subvulcaniche: schema operativo per il progetto CARG. Atti Soc. tosc. Sci. Nat., Mem., Serie A, 106, pagg. 113-124, figg. 17, tabb. 8.

Irvine, T.N., and Baragar, W.R.A., 1971. A guide to the chemical classification of the common volcanic rocks: Canadian Journal of Earth Sciences, v. 8, p. 523-548.

James, M.R., Applegarth, L.J., Pinkerton, H., 2012. Lava channel roofing, overflows, breaches and switching: insights from the 2008–2009 eruption of Mt. Etna. Bullettin of Volcanology, 74, 107-117. http://dx.doi.org/10.1007/s00445-011-0513-9.

Jarosewich E., Parkes A.S., Wiggins L.B., 1979. Microprobe analyses of four natural glasses and one mineral: an interlaboratory study of precision and accuracy. Smithsonian Contrib Earth Science, 22:53-67.

Jochum K.P., Stoll B., Hervig K., Willbold M., Hofmann A.W., Amini M., Aarburg S., Abouchami W., Hellebrand E., Mocek B., Raczek I., Strake A., Alard O., Bouman C., Becker S., Ducking M., Bratz H., Klemd R., de Bruin D., Canil D., Cornell D., De Hoog C-J., Dalpé C., Danyushevsky L., Eisenhauer A., Gao Y., Snow J., Groschopf N., Gunther D., Latkoczy C., Guillong M., Hauri E.H., Hofer H.E., Lahaye Y., Horz K., Jacob D.E., Kasemann S.A., Kent A.J.R., Ludwig T., Zack T., Mason P.R.D., Meixner A., Rosner M., Misawa K., Nash B.P., Pfander J., Premo W.R., Sun W.D., Tiepolo M., Vannucci R., Vennemann T., Wayne D., Woodhead J.D., 2006. MPI-DING reference glasses for in situ microanalysis: New reference values for element concentrations and isotope ratios. Geochemistry Geophysics Geosystems 7, Q02008, doi:10.1029/2005GC001060.

Joron, J.L., and Treuil, M., 1984. Etude géochimique et pétrogenése des laves e l'Etna, Sicilie, Italie. Bulletin of Volcanology 47 (4), 1125-1144.

Jugo, P.J., Luth, R.W. and Richards, J.P., 2005. An experimental study of sulfur content in basaltic melts saturated with immiscible sulfide of sulfate liquids at 1300 °C and 1.0 GPa. Journal of Petrology 46, 783-798, doi: 10.1016/j.gca.2004.07.011.

Jugo, P.J., 2009. Sulfur content at sulfide saturation in oxidized magmas. Geology 37, 415-418.

Jugo, P. J., Wilke, M., and Botcharnikov, R. E., 2010. Sulfur K-edge XANES analysis of natural and synthetic basaltic glasses: Implications for S speciation and S content as function of oxygen fugacità, Geochim. Cosmochim. Acta, 74, 5926–5938, doi:10.1016/j.gca.2010.07.022.

Kahl, M., Chakraborty, S., Costa, F., Pompilio, M., 2011. Dynamic plumbing system beneath volcanoes revealed by kinetic modeling, and the connection to monitoring data: an example from Mt. Etna. Earth and Planetary Science Letters 308, 11-22. http://dx. doi.org/10.1016/j.epsl.2011.05.008.

Kahl, M., Chakraborty, S., Pompilio, M., and Costa, F., 2015. Constraints on the Nature and Evolution of the Magma Plumbing System of Mt. Etna Volcano (1991-2008) from a Combined Thermodynamic and Kinetic Modelling of the Compositional Record of Minerals Journal of Petrology, 2015, Vol. 0, No. 0, 1-43, doi: 10.1093/petrology/egv063.

Kamenetsky, V.S., and Clocchiatti, R., 1996. Primitive magmatism of Mt. Etna: insights from mineralogy and melt inclusions. Earth and Planetary Science Letters 142, 553-572.

Kamenetsky, V.S., Pompilio, M., Métrich, N., Sobolev, A.V., Kuzmin, D.V., Thomas, R., 2007. Arrival of extremely volatile-rich high-Mg magmas changes explosivity of Mount Etna. Geology 35, 255-258.

Kelley, K.A., Cottrell, E., 2012. The influence of magmatic differentiation on the oxidation state of Fe in a basaltic arc magma. Earth and Planetary Science Letters 329-330, 109-121.

Kress, V.C., Carmichael, I.S.E., 1991. The compressibility of silicate liquids containing Fe_2O_3 and the effect of composition, temperature, oxygen fugacity and pressure on their redox states. Contributions to Mineralogy and Petrology, 108, 82-92.

Labidi, J., Cartigny, P., Birck, J., Assayag, N. and Bourrand, J., 2012. Determination of multiple sulfur isotopes in glasses: a reappraisal of the MORB $\delta^{34}S$. Chem. Geol. 334, 189-198.

Lange, R.A., 1994. The effect of H_2O, CO_2 and F on the density and viscosity of silicate melts. In: Volatiles in Magmas, vol 30. Mineralogical Soc America, Washington, pp 331-369.

Lanzafame, G., Neri, M., Coltelli, M., Lodato, L., Rust, D., 1997. North-south compression in the Mt Etna region (Sicily): spatial and temporal distribution. Acta Vulcanologica 9, 121-133.

Le Maitre, R.W. (Ed.) 2002. Igneous rocks. A classification and glossary of terms, 2nd ed. Recommendations of the IUGS Subcomission on the Systematics of Igneous Rocks. Cambridge University Press, p. 236.

Lesne, P., Scaillet, B., Pichavant, M. and Beny, J. M., 2011. The carbon dioxide solubility in alkali basalts: an experimental study. Contributions to Mineralogy and Petrology, 162, 153-168. http://dx.doi.org/10.1007/s00410-010-0585-0.

Lesne, P., Scaillet, B., Pichavant, M., 2015. The solubility of sulfur in hydrous basaltic melts Chemical Geology 418, 104-116.

Li, C., and Ripley, E. M., 2005. Empirical equations to predict the sulfur content of mafic magmas at sulfide saturation and applications to magmatic sulfide deposits. Mineral. Deposita 40, 218-230.

Li, C., and Ripley, E.M., 2009. Sulfur contents at sulfide-liquid or anhydrite saturation in silicate melts: empirical equations and example applications. Econ. Geol. 104, 405-412.

Liotta, M., Rizzo, A., Paonita, A., Caracausi, A., Martelli, M., 2012. Sulfur isotopic compositions of fumarolic and plume gases at Mt. Etna (Italy) and inferences on their magmatic source. Geochemistry Geophysics Geosystems 13, doi: 10.1029/2012GC004118.

Liu, Y. N., Samaha, N.T., and Baker D. R., 2007. Sulfur concentration at sulfide saturation (SCSS) in magmatic silicate melts. Geochimica e Cosmochimica Acta 71, 1783-1799.

Luhr, J.F., 1990. Experimental phase-relations of water-saturated and sulphur saturated arc magmas and the 1982 eruptions of El Chichon volcano. Journal of Petrology, 31 (5), 1071-1114.

Marini, L., Moretti, R., and Accornero, M., 2011. Sulfur isotopes in magmatic-hydrothermal systems, melts, and magmas, in Sulfur in Magmas and Melts: Its Importance for Natural and Technical Processes, edited by J. Webster and H. Behrens, Reviews in Mineralogy and Geochemistry, 73, 423-492.

Martelli, M., Caracausi, A., Paonita, A., and Rizzo, A., 2008. Geochemical variations of air-free crater fumaroles at Mt Etna: New inferences for forecasting shallow volcanic activity. Geophysical Research Letter, 35, L21302, doi: 10.1029/2008GL035118.

Mathez, E.A., 1984. Influence of degassing on oxidation states of basaltic magmas. Nature310, 371-375.

Mavrogenes, J.A. and O'Neill, H. St., 1999. The relative effects of pressure, temperature and oxygen fugacity on the solubility of sulfide in mafic magmas. Geochimica e Cosmochimica Acta 63, 1173-1180.

McGuire, W.J., Stewart, I.S., Saunders, S.J., 1997. Intra-volcanic rifting at Mount Etna in the context of regional tectonics. Acta Volcanologica 9, 147-156.

Mercier, M., Di Muro, A., Giordano, D., Métrich, N., Lesne, P., Pichavant, M., Scaillet, B., Clocchiatti, R., Montagnac, G., 2009. Influence of glass polymerisation and oxidation on micro-Raman water analysis in alumino-silicate glasses Geochimica et Cosmochimica Acta 73, 197-217.

Métrich, N., and Clocchiatti, R., 1989. Melt inclusion investigation of the volatile behavior in historic alkaline magmas of Etna. Bulletin of Volcanology 51, 185-198.

Métrich, N., and Clocchiatti, R., 1996. Sulfur abundance and its speciation in oxidized alkaline melts. Geochimica et Cosmochimica Acta 60, 4151–4160.

Métrich, N. and Rutherford, M. J., 1998. Low pressure crystallization paths of H_2O-saturated basaltic hawaiitic melts from Mt Etna: Implications for open-system degassing of basaltic volcanoes. Geochimica et Cosmochimica Acta 62, 1195^1205, doi:10.1016/ S0016-7037(98)00048-9.

Métrich, N., Allard, P., Spilliaert, N., Andronico, D., Burton, M., 2004. 2001 flank eruption of the alkali and volatile-rich primitive basalt responsible for Mount Etna's evolution in the last three decades. Earth and Planetary Science Letters 228, 1-17.

Métrich, N., Berry, A.J., O'Neill, H. S. C., and Susini, J., 2009. The oxidation state of sulfur in synthetic and natural glasses determined by X-ray absorption spectroscopy, Geochimica e Cosmochimica Acta, 73, 2382-2399, doi:10.1016/j.gca.2009.01.025.

Miraglia, L., 2002. Evidence for heterogeneous magmas in the feeding system of the 1763 "La Montagnola" eruption at Mount Etna. Plinius 27, 108-112.

Mollo, S., Giacomoni, P.P., Coltorti, M., Ferlito, C., Iezzi, G., Scarlato, P., 2015. Reconstruction of magmatic variables governing recent Etnean eruptions: Constraints from mineral chemistry and P-T-fO_2-H_2O modeling. Lithos 212-215, 311-320.

Morizet, Y., Gennaro, E., Jégo, S., Zajacz, Z., Iacono-Marziano, G., Pichavant, M., Di Carlo, I. Ferraina, C., Lesne, P., (*submitted*). A Raman calibration for the quantification of SO_4^{2-} groups dissolved in silicate glasses: Application to natural melt inclusions. American Mineralogist.

Mosselmans, J.F.W., Quinn, P. D., Dent, A.J., Cavill, S.A., Diaz Moreno, S., Peach, A., Leicester P.J, Keylock, S.J., Gregory, S.R., Atkinson, K.D., and Roque Rosell, J., 2009. I18 - the microfocus spectroscopy beamline at the Diamond Light Source. Journal of Synchrotron Radiation, 16, 818-824.

Moune, S., Holtz, F. and Botcharnikov, R. E., 2009. Sulfur solubility in andesitic to basaltic melts: implications for Hekla volcano. Contributions to Mineralogy and Petrology 157, 691-707.

Moussallam, Y., Oppenheimer, C., Scaillet, B., Gaillard, F., Kyle, P., Peters, N., Hartley, M., Berlo, K., Donovan, A., 2014. Tracking the changing oxidation state of Erebus magmas, from mantle to surface, driven by magma ascent and degassing. Earth and Planetary Science Letters 393, 200-209.

Moussallam, Y., Edmonds, M., Scaillet, B., Peters, N., Gennaro, E., Sides, I., Oppenheimer, C., 2016. The impact of degassing on the oxidation state of basaltic magmas: A case study of Kılauea volcano. Earth and Planetary Science Letters 450, 317-325.

Neri, M., Acocella, V., and Behncke, B., 2004. The role of the Pernicana Fault System in the spreading of Mt. Etna (Italy) during the 2002–2003 eruption. Bulletin of Volcanology, 66(5), 417 -430, doi:10.1007/s00445-003-0322-x.

Nicolich, R., Laigle, M., Hirn, A., Cernobori, L., Gallart, J., 2000. Crustal structure of the Ionian margin of Sicily: Etna volcano in the frame of regional evolution. Tectonophysics 329, pp. 121-139.

Norrish, K., Hutton, J. T., 1969. An accurate X-ray spectrographic method for the analysis of a wide range of geological samples Geochimica et Cosmochimica Acta, Volume 33, Issue 4, p. 431-453.

O'Neill, H.St. and Mavrogenes, J.A., 2002. The sulfide capacity and the sulfur content at sulfide saturation of silicate melts at 1400 °C and 1 bar. Journal of Petrology 43, 1049-1087.

Oppenheimer, C., 2003. Volcanic degassing, treatise on geochemistry, pp. 123-166.

Oppenheimer, C., Scaillet, B., and Martin, R.S., 2011. Sulfur Degassing From Volcanoes: Source Conditions, Surveillance, Plume Chemistry and Earth System Impacts. Reviews in Mineralogy and Geochemistry, Vol. 73 pp. 363-421.

Paonita, A., Caracausi, A., Iacono-Marziano, G., Martelli, M., and Rizzo, A., 2012. Geochemical evidence for mixing between fluids exsolved at different depths in the magmatic system of Mt Etna (Italy), Geochim. Cosmochim. Acta, 84, 380-394, doi:10.1016/j.gca.2012.01.028.

Parkinson, I.J., and Arculus, R.J., 1999. The redox state of subduction zones: Insights from arcperidotites: Chemical Geology, v. 160, p. 409-423, doi: 10.1016/S0009-2541(99)00110-2.

Patane`, D., De Gori, P., Chiarabba, C., and Bonaccorso A., 2003. Magma ascent and the pressurization of Mount Etna's volcanic system, Science, 299, 2061-2063, doi:10.1126/Science.1080653.

Patané, D., Aliotta, M., Cannata, A., Cassisi, C., Coltelli, M., Di Grazia, G., Montalto, P., Zuccarello, L., 2011. Interplay between Tectonics and Mount Etna's Volcanism: Insights into the Geometry of the Plumbing System, New Frontiers in Tectonic Research - At the Midst of Plate Convergence, Dr. Uri Schattner (Ed.), ISBN: 978-953-307-594-5.

Pompilio, M., Coltelli, M., Del Carlo, P., Vezzoli, L., 1995. How do basaltic magmas, feeding explosive eruption, rise and differentiate at Mt. Etna? Periodico di Mineralogia, 64, 253-254.

Pownceby, M. I. and O'Neill, H. St. C., 1994. Thermodynamic data from redox reactions at high temperatures. III. Activity–composition relations in Ni–Pd alloys from EMF measurements at 850–1250 K and calibration of the NiO þ Ni–Pd assemblage as a redox sensor. Contributions to Mineralogy and Petrology 116, 327-339.

Ryerson, F.J., and Watson, E.B., 1987. Rutile saturation in magmas, implications for Ti-Nb–Ta depletion in island-arc basalts. Earth and Planetary Science Letters, 86, 225-239.

Richet, P., Whittington, A., Holtz, F., Behrens, H., Ohlhorst, S., Wilke, M., 2000. Water and the density of silicate glasses. Contributions to Mineralogy and Petrology 138(4): 337-347.

Rittman, A., 1965. Notizie sull'Etna. Suppl. Nuovo Cimento, 3(I), 1117-1123.

Rittmann, A., 1973. Structure and evolution of Mount Etna. Philos. Trans. R. Soc. Lond., 274, 5-16.

Rizzo, A. Caracausi, A., Favara, R., Martelli, M., Paonita, A., Paternoster, M., Nuccio, P.M., and Rosciglione, A., 2006. New insights into magma dynamics during last two eruptions of

Mount Etna as inferred by geochemical monitoring from 2002 to 2005. Geochemistry Geophysics Geosystems 7, doi:10.1029/2005GC001175.

Rizzo, A.L., Caracausi, A., Liotta, M., Paonita, A., Barnes, J.D., Corsaro, R.A., Martelli, M., 2013. Chlorine isotope composition of volcanic gases and rocks at Mount Etna (Italy) and inferences on the local mantle source Earth andPlanetaryScienceLetters371-372, 134-142.

Rizzo, A. L., Jost, H.-J., Caracausi, A. Paonita, A., Liotta, M., and Martelli, M., 2014. Real-time measurements of the concentration and isotope composition of atmospheric and volcanic CO_2 at Mount Etna (Italy), Geophys. Res. Lett., 41, 2382–2389, doi:10.1002/2014GL059722.

Robie, R. A., Hemingway, B. S. and Fisher, J. R., 1979. Thermodynamic properties of minerals and related substances at 298_15 K and 1 bar (105 pascals) pressure and at higher temperatures. US Geological Survey Bulletin 1452, 456.

Roeder, P.L., and Emslie, R. F., 1970. Olivine-Liquid Equilibrium. Contributions to Mineralogy and Petrology 29, 275-289, by Springer-Verlag 1970.

Rollion-Bard, C., 2001. Variabilité des isotopes de l'oxygene dans les coraux Porites: developpement et implications des microanalyses d'isotopes stables (B, C et O) par sonde ionique. These CRPG-INPL.

Rosciglione, A., 2008. Evidences of Enriched Mantle (EM-2) source contribution to Etnean magmas: a comprehensive study on fluid and melt inclusions of 2001-2006 eruptions. PhD thesis, University of Palermo.

Salerno, G.G., Burton, M.R., Oppenheimer, C., Caltabiano, T., Randazzo, D., Bruno and Longo, V., 2009. Three-years of SO_2 flux measurements of Mt. Etna using an automated UV scanner array: Comparison with conventional traverses and uncertainties in flux retrieval. Journal of Volcanology and Geothermal Research 183, 76-83.

Schiano, P., Clocchiatti, R., 1994. Worldwide occurrence of silica-rich melts in subcontinental and sub-oceanic mantle minerals. Nature 368, 621-624.

Schiano, P., Crocchiati, R., Ottolini, L., Busà, T., 2001. Transition of Mount Etna lavas from a mantle-plume to an island-arc magmatic source. Nature 412, 900-904.

Schiano, P., 2003. Primitive mantle magmas recorded as silicate melt inclusions in igneous minerals, Earth Science Reviews 63, 1-2, 121-144.

Schiavi, F., Rosciglione, A., Kitagawa, H., Kobayashi, K., Nakamura, E., Nuccio, P. M., Ottolini, L., Paonita, A., Vannucci, R., 2015. Geochemical heterogeneities in magma beneath Mount Etna recorded by 2001-2006 melt inclusions, Geochemistry Geophysics Geosystems 16, doi:10.1002/2015GC005786.

Shishkina, T.A., Botcharnikov, R.E., Holtz, F., Almeev, R.R., Portnyagin, M.V., 2010. Solubility of H_2O- and CO2 -bearing fluids in tholeiitic basalts at pressures up to 500MPa. Chemical Geology 277, 115-125.

Shorttle, O., Moussallam, Y., Hartley, M. E., Maclennan, J, Edmonds, M., Murton, B. J., 2015. Fe-XANES analyses of Reykjanes Ridge basalts: Implications for oceanic crust's role in the solid Earth oxygen cycle. Earth and Planetary Science Letters 427, 272-285.

Smith, P.M., and Asimow, P.D., 2005. Adiabat_1ph: A new public front-end to the MELTS, pMELTS, and pHMELTS models. Geochemistry Geophysics Geosystems 6, art. no. Q02004, doi:10.1029/2004GC000816.

Sobolev, A.V., and Danyushevsky, L.V., 1994. Petrology and Geochemistry of boninites from the North termination of the Tonga Trench: constraints on the generation conditions of primary high-Ca boninite magmas. Journal of Petrology 35, 1183 - 1211.

Spilliaert, N., Allard, P., Métrich, N., Sobolev, A.V., 2006a. Melt inclusion record of the conditions of ascent, degassing, and extrusion of volatile-rich alkali basalt during the powerful 2002 flank eruption of Mount Etna (Italy). Journal of Geophysical Research, 111, B04203, http://dx.doi.org/10.1029/2005JB003934.

Spilliaert, N., Metrich, N. and Allard, P., 2006b. S-Cl-F degassing pattern of water-rich alkali basalt: modelling and relationship with eruption styles on Mount Etna volcano. Earth and Planetary Science Letters 248, 772-786.

Spilliaert, N., 2006. Dynamiques de remontée, dégazage et eruption des magmas basaltiques riches en volatils : Traçage par les inclusions vitreuses et modélisation des processus dans le cas de l'Etna, 2000-2002, thesis, 294 pp., Univ. Paris, Paris.

Stolper, E., 1982. Water in silicate glasses: an infrared spectroscopic study Contributions to Mineralogy and Petrology 81, 1-17.

Stormer, J. C. Jr., 1983. The effects of recalculation on estimates of temperature and oxygen fugacity from analyses of multicomponent iron-titanium oxides. American Mineralogist, 68. 586-594.

Tanguy, J.C., Condomines, M., Kieffer, G., 1997. Evolution of Mount Etna magma: Constraints on the present feeding system and eruptive mechanism. Journal of Volcanology and Geothermal Research 75, 221-250.

Taylor, J. R., Wall, V. J., and Pownceby, M. I., 1992. The calibration and application of accurate redox sensors. American Mineralogist 77, 284–295.

Tonarini, S., Armenti, P., D'Orazio, M., Innocenti, F., Pompilio, M., Petrini, R., 1995. Geochemical and isotopic monitoring of Mt. Etna 1989–1993 eruptive activity: bearing on the shallow feeding system. Journal of Volcanology and Geothermal Research 64, 95-115.

Tonarini, S., Armienti, P., D'Orazio, M., Innocenti, F., 2001. Subduction-like fluids in the genesis of the Mt Etna magmas: evidence from boron isotopes and fluid mobile elements. Earth and Planetary Science Letters 5989, 1-13.

Torelli, L., Grasso, M., Mazzoldi, G., Peis, D., 1998. Plio-Quaternary tectonic evolution and structure of the Catania foredeep, the northern Hyblean Plateau and the Ionian shelf (SE Sicily). Tectonophysics 298, 209-221.

Trigila, R., Spera, F.J., and Aurisicchio, C., 1990. The 1983 Mount Etna eruption: thermochemical and dynamical inferences. Contributions to Mineralogy and Petrology, 104:594-608.

Viccaro, M., Ferlito, C., Cortesogno, L., Cristofolini, R., Gaggero, L., 2006. Magma mixing during the 2001 event at Mount Etna (Italy): effect on the eruptive dynamics. Journal of Volcanology and Geothermal Research 149, 139-159.

Viccaro, M., and Cristofolini, R., 2008. Nature of mantle heterogeneity and its role in the short-term geochemical and volcanological evolution of Mt Etna (Italy). Lithos 105, 272-288.

Viccaro, M., Calcagno, R., Garozzo, I., Giuffrida, M., Nicotra, E., 2015. Continuous magma recharge at Mt. Etna during the 2011–2013 period controls the style of volcanic activity and compositions of erupted lavas. Mineralogy and Petrology, 109:67-83, DOI 10.1007/s00710-014-0352-4.

Von Aulock, F.W., Kennedy, B.M., Schipper, C.I., Castro, J.M., Martin, D.E., Oze, C., Watkins, J.M., Wallace, P.J., Puskar, L., Bégué, F., Nichols, A.R.L., Tuffen, H., 2014. Advances in Fourier transform infrared spectroscopy of natural glasses: From sample preparation to data analysis. Lithos 206-207, 52-64

Walker, G. P. L., 1973. Explosive volcanic eruptions - A new classification scheme, Geol. Rundsch., 62, 431-446.

Wallace, P. and Carmichael, I.S.E., 1992. Sulfur in basaltic magmas. Geochimica e Cosmochimica Acta 56, 1863-1874.

Wallace, P., Edmonds, M., 2011. The Sulfur Budget in Magmas: Evidence from Melt Inclusions, Submarine Glasses, and Volcanic Gas Emissions. Reviews in Mineralogy and Geochemistry, Vol. 73 pp. 215-246.

Waters, L.E., Lange, R.A., 2016. No effect of H_2O degassing on the oxidation state of magmatic liquids. Earth and Planetary Science Letters, 447, 48-59.

Watson, E.B., and Harrison, T.M., 1983. Zircon saturation revisited, temperature and composition effects in a variety of crustal magma types. Earth and Planetary Science Letters, 64, 295-304.

Webster, J.D., and Botcharnikov, R.E., 2011. Distribution of sulfur between melt and fluid in SOHC-Cl-bearing magmatic systems at shallow crustal pressures and temperatures. Rev. Mineral. Geochem. 73 (1), 247-283.

Wilke, M., Partzsch, G.M., Bernhardt, R., Lattard, D., 2005. Determination of the iron oxidation state in basaltic glasses using XANES at the K-edge. Chemical Geology, 220 (1-2), 143-161.

Witter, J.B. Kress, V. C., and Newhall, C. G., 2005. Volcan Popocatepetl, Mexico. Petrology, Magma Mixing, and Immediate Sources of Volatiles for the 1994 Present Eruption. Journal of Petrology, 11, 2337-2366.

Wong, J., Lytle, F.W., Messmer, R.P., Maylotte, D.H., 1984. K-edge absorption spectra of selected vanadium compounds. Physical Review, B30, 5596-5610.

Appendix

A1. SIMS: Principle and instrumental apparatus

The secondary ion mass spectrometry (SIMS) is a technique useful to determine elemental and isotopic compositions of many known elements (up to U), even at very low concentration levels.
In an ionic probe, a beam of primary ions is accelerated through an electrical sector and focused on the sample surface, producing an ablation of the sample. Part of the produced ions constitutes the so-called "secondary ion beam" that is transferred to the spectrometer sector of the instrument.

The instrumental apparatus (fig. A1.1) consists of:

- ✓ airlock system,
- ✓ source,
- ✓ primary column,
- ✓ secondary column,
- ✓ mass spectrometry.

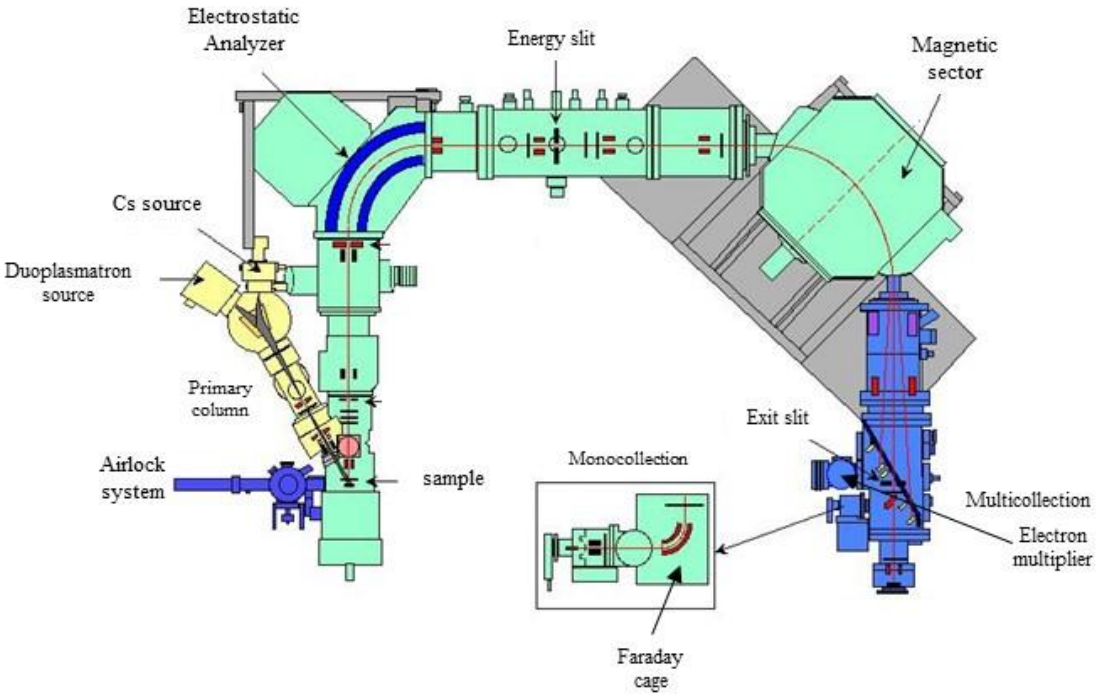

Fig. A1.1 - Modified scheme of Cameca 1270 IMS (from Cameca and Rollion-Bard. 2001).

The "Airlock system" is the tool for the introduction of the samples (two sample-holders for IMS 1270 and up to six for IMS 1280).

An ionic probe is equipped with two different sources: a "duoplasmatron" device, generating a primary O^- (or O_2^-, O_2^+, or Ar^+) beam commonly used for the lightest element, and a "Cs source". We used the latter for all the analyses realized in this PhD study, for both the determination of volatile abundances, and S isotopic composition. The primary beam of Cs^+ is created heating a reservoir of carbonate of cesium, and ionized after a contact with a tungsten plate a T = 1100 °C. It goes through a primary column and a series of electrostatic lenses to be accelerated and focused toward the sample surface.

The impact generates an ablation of the sample, with a depth of some microns (6-15 µm), and producing a collision cascade of atoms (sputtering). A part of these atoms forms the "secondary beam", which is accelerated and focused through a second series of lens (secondary column) toward an electrostatic analyzer and subsequently toward the magnetic sectors of the mass spectrometer. Here, the ions are separated depending their mass and sent in the collector sector.

The collection of the signal can be done in two modes: mono-collection (in a sequential manner) or multi-collection. The multi-collection consists of 7 ion detectors with two Faraday cages and five mobile detectors (Faraday cages or electron multipliers). It thus allows the simultaneous analysis of different isotopes of the same element.

A2. XANES: Principle and instrumental apparatus

X-ray absorption near-edge structure (XANES) spectroscopy is a method, based on a synchrotron source, suitable to determine the valence state of elements.
A synchrotron light is a very intense, continuous, polarized and collimated radiation, with a large emission band (from infrared to X-ray). This radiation is created inside particle accelerator or storage rings, in which the charged particles move at high speed. Typically, they are accelerated by an electron field and move on a circular direction under the effect of a magnetic field. When particles are forced to change theirs directions they produce a synchrotron radiation, which is sent to a specific beamline.
When this radiation is absorbed by the sample, it excites the sample atoms generating the displacement of electrons toward the external orbitals, and releasing energy.

The core of the XANES investigation is the experimental hutch (fig. A2.1) that is the analytical chamber, where the sample (mounted on an aluminium plate) is exposed at the radiation. The experimental hutch is completely isolated and remains so during all acquisition.

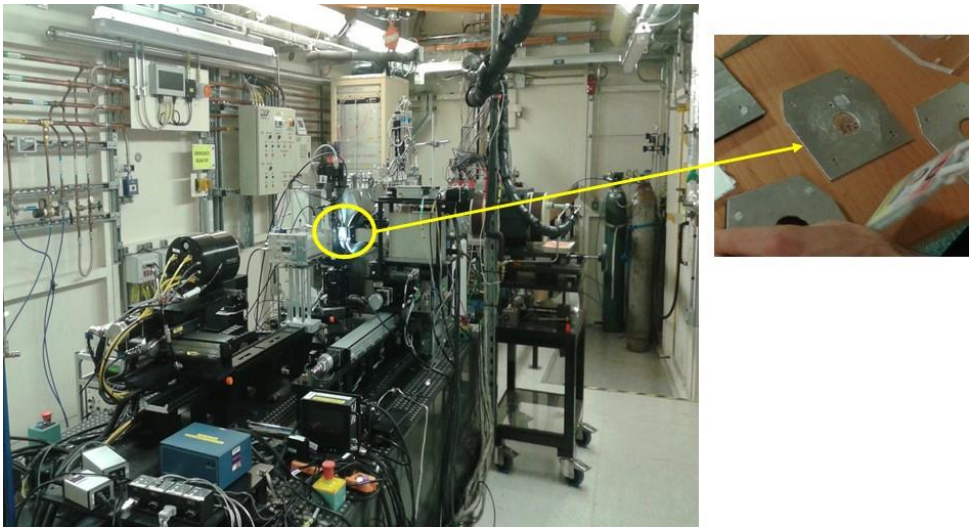

Fig. A2.1 - Experimental hutch of the I18 beamline at Diamond Light Source (DLS). In the small picture, the typical aluminum plate used to mount the sample.

A3. Chemical composition of mineral phase in the investigated products.

Table A3.1 - Olivine from monte Spagnolo lava.

sample name	SiO_2	FeO	MnO	MgO	CaO	total	Fo mol.% [#]
Spa-1a	39.83	11.86	0.24	47.70	0.29	99.92	87.76
Spa-1b	39.83	11.86	0.24	47.70	0.29	99.92	87.76
Spa-3	38.62	16.79	0.32	43.72	0.26	99.71	82.27
Spa-3n	38.62	16.79	0.32	43.72	0.26	99.71	82.27
Spa-4n	39.13	12.75	0.31	47.25	0.34	99.77	86.85
Spa-5	40.84	12.56	0.16	46.97	0.26	100.8	86.95
Spa-5n	40.84	12.92	0.24	45.33	0.31	99.64	86.21
Spa-6	38.68	13.86	0.25	46.59	0.35	99.73	85.70
Spa-7	41.98	13.50	b.d.l.	43.91	0.23	99.62	85.29
Spa-7n	39.93	12.44	0.22	48.77	0.19	101.5	87.48
Spa-9	39.22	13.78	0.22	46.20	0.32	99.74	85.67
Spa-11	39.26	14.33	0.18	45.57	0.29	99.63	85.00
Spa-D	39.26	12.83	0.20	47.19	0.27	99.75	86.77
Spa-L	36.66	13.65	0.13	49.06	0.22	99.72	86.50
Spa-O1	42.27	14.40	0.19	42.81	0.31	99.98	84.12
Spa-R	37.81	26.37	0.51	36.52	0.37	101.6	71.17
Spa-T1	40.52	12.46	0.07	48.58	0.27	101.9	87.42
Spa-T2	40.52	12.46	0.07	48.58	0.27	101.9	87.42
Spa-T3	40.52	12.46	0.07	48.58	0.27	101.9	87.42
Spa-T4	40.52	12.46	0.07	48.58	0.27	101.9	87.42
Spa-U1	40.71	11.29	0.15	47.40	0.28	99.83	88.21
Spa-U2	40.71	11.29	0.15	47.40	0.28	99.83	88.21
Spa-U3	40.71	11.29	0.15	47.40	0.28	99.83	88.21
Spa-U4	40.71	11.29	0.15	47.40	0.28	99.83	88.21

b.d.l. = below detection limit.
[#]Fo mol = Fo content of the host olivine

Table A3.2 - Olivine from FS tephra.

sample name	SiO_2	FeO	MnO	MgO	CaO	total	Fo mol.% [#]
FS-00	41.59	10.05	0.16	48.24	0.26	100.3	89.54
FS-01	42.35	9.89	0.20	47.23	0.22	99.89	89.49
FS-03b	41.30	10.18	0.20	48.03	0.23	99.94	89.37
FS-03c	41.20	10.11	b.d.l.	48.26	0.22	99.79	89.48
FS-05	41.50	10.31	0.18	47.53	0.25	99.77	89.15
FS-06b	41.85	9.4	b.d.l.	48.09	0.23	99.57	90.12
FS-06c	41.03	9.55	b.d.l.	48.84	0.27	99.69	90.11
FS-06n	41.03	9.55	b.d.l.	48.84	0.27	99.69	90.11
FS-07	42.20	9.68	0.21	47.39	0.24	99.72	89.72
FS-08b	41.70	10.42	b.d.l.	47.45	0.25	99.82	89.03
FS-08c	41.05	10.36	0.33	48.17	0.22	100.1	89.23
FS-09 n	40.09	9.14	0.27	50.17	0.21	99.88	90.73
FS-09	41.95	9.51	0.16	48.04	0.22	99.88	90.00
FS-10b	40.98	9.41	0.18	48.9	0.20	99.67	90.26
FS-10c	41.24	9.15	0.24	48.9	0.24	99.77	90.50
FS-11	41.18	9.65	0.26	48.58	0.23	99.90	89.97
FS-12a	40.46	10.59	0.13	49.10	0.25	100.53	89.21
FS-12b	40.46	10.59	0.13	49.10	0.25	100.53	89.21
FS-13b	41.94	9.82	0.07	47.60	0.31	99.74	89.63

FS-13c	41.94	9.82	0.07	47.60	0.31	99.74	89.63
FS-14	40.77	10.29	0.14	48.30	0.25	99.75	89.32
FS-21	40.56	9.76	0.06	50.24	0.27	100.89	90.17
FS-23	-	-	-	-	-	-	-
FS-24	40.56	10.95	0.12	47.91	0.29	99.83	88.64
FS-25	40.84	9.10	0.23	48.95	0.25	99.38	90.56
FS-26	41.88	9.69	0.10	48.71	0.25	100.63	89.96
FS-28a	40.82	9.40	0.05	49.37	0.22	99.86	90.35
FS-28b	40.82	9.40	0.05	49.37	0.22	99.86	90.35
FS-A	-	-	-	-	-	-	-
FS-B	39.17	9.46	0.10	50.75	0.27	99.75	90.53
FS-D	40.53	9.18	0.29	49.62	0.20	99.82	90.60
FS-E	40.94	9.19	0.09	49.45	0.24	99.91	90.56
FS-Xa	38.51	10.12	0.10	50.65	0.32	99.70	89.92
FS-Xb	38.51	10.12	0.10	50.65	0.32	99.70	89.92
FS-Z	39.57	8.94	0.14	50.86	0.23	99.74	91.02

b.d.l. = below detection limit.
[#]Fo mol = Fo content of the host olivine

Table A3.3 - Olivine from 2002/2003 South tephra.

sample name	**SiO_2**	**FeO**	**MnO**	**MgO**	**CaO**	**total**	**Fo mol.% [#]**
ET2002/3S-1	37.22	22.91	0.53	38.99	0.23	99.88	75.21
ET2002/3S-3	38.18	22.24	0.50	38.85	0.21	99.98	75.69
ET2002/3S-5	39.60	17.03	0.21	42.91	0.25	99.99	81.79
ET2002/3S-6	38.02	20.72	0.39	40.63	0.19	99.95	77.76
ET2002/3S-7	38.21	22.78	0.47	38.25	0.19	99.89	74.96
ET2002/3S-9	40.08	21.72	0.34	37.41	0.27	99.81	75.43
ET2002/3S-10	39.00	23.21	0.55	36.95	0.23	99.94	73.94
ET2002/3S-11a	40.67	15.79	0.26	42.97	0.22	99.91	82.90
ET2002/3S-11b	40.67	15.79	0.26	42.97	0.22	99.91	82.90
ET2002/3S-13	40.06	16.17	0.15	43.31	0.24	99.92	82.68
ET2002/3S-16a	38.53	24.64	0.43	38.64	0.23	102.5	73.65
ET2002/3S-16b	38.53	24.64	0.43	38.64	0.23	102.5	73.65
ET2002/3S-23	40.34	16.98	0.18	45.25	0.22	102.97	82.61
ET2002/3S-24	37.33	18.75	0.32	42.77	0.23	99.40	80.26
ET2002/3S-25	-	-	-	-	-	-	-
ET2002/3S-26	37.62	24.76	0.41	36.74	0.36	99.88	72.57
ET2002/3S-29a	37.43	28.05	0.64	36.10	0.31	102.52	69.64
ET2002/3S-29b	37.43	28.05	0.64	36.10	0.31	102.52	69.64
ET2002/3S-31	37.60	27.75	0.42	35.94	0.26	101.98	69.77
ET2002/3S-32	37.85	24.26	0.77	36.62	0.34	99.84	72.90
ET2002/3S-33a	38.69	18.33	0.26	42.95	0.27	100.5	80.68
ET2002/3S-33b	38.69	18.33	0.26	42.95	0.27	100.5	80.68
ET2002/3S-33c	38.69	18.33	0.26	42.95	0.27	100.5	80.68

[#]Fo mol = Fo content of the host olivine

Table A3.4 - Olivine from 2006 tephra.

sample name	**SiO_2**	**FeO**	**MnO**	**MgO**	**CaO**	**total**	**Fo mol.% [#]**
ET2006-1 a	37.38	26.93	0.49	34.65	0.38	99.83	69.64
ET2006-1 b	38.01	26.20	0.47	34.87	0.36	99.91	70.35

ET2006-4	38.50	25.88	0.40	34.66	0.41	99.85	70.48
ET2006-7	39.51	17.87	0.25	42.97	0.28	100.88	81.08
ET2006-12	40.01	19.99	0.34	41.56	0.23	102.13	78.75
ET2006-B3a	37.64	21.32	0.27	40.39	0.21	99.83	77.15
ET2006-B3b	37.64	21.32	0.27	40.39	0.21	99.83	77.15
ET2006-B5a	37.97	18.62	0.44	42.43	0.23	99.69	80.24
ET2006-B5c	37.97	18.62	0.44	42.43	0.23	99.69	80.24
ET2006-B5d	37.97	18.62	0.44	42.43	0.23	99.69	80.24
ET2006-B5n	37.97	18.62	0.44	42.43	0.23	99.69	80.24
ET2006-B6	37.49	21.98	0.38	39.48	0.34	99.67	76.20
ET2006-B8a	37.36	22.61	0.56	38.91	0.23	99.67	75.42
ET2006-B8b	37.36	22.61	0.56	38.91	0.23	99.67	75.42
ET2006-C7a	36.63	25.92	0.63	34.25	0.41	97.84	70.20
ET2006-C7b	36.63	25.92	0.63	34.25	0.41	97.84	70.20
ET2006-C8	37.12	24.18	0.35	37.86	0.29	99.80	73.62
ET2006-C11	36.59	25.55	0.57	36.79	0.37	99.87	71.96
ET2006-D9	36.58	26.04	0.53	34.19	0.40	97.74	70.06
ET2006-E2a	37.57	26.42	0.50	34.89	0.39	99.77	70.19
ET2006-E2b	37.57	26.42	0.50	34.89	0.39	99.77	70.19
ET2006-F5	37.38	20.74	0.35	41.14	0.20	99.81	77.95
ET2006-F5	37.38	20.74	0.35	41.14	0.20	99.81	77.95
ET2006-F5	37.38	20.74	0.35	41.14	0.20	99.81	77.95
ET2006-F5	37.38	20.74	0.35	41.14	0.20	99.81	77.95
ET2006-F5	37.38	20.74	0.35	41.14	0.20	99.81	77.95
ET2006-F5n	37.00	25.92	0.57	36.09	0.26	99.84	71.28
ET2006-H2	36.46	26.18	0.54	36.27	0.38	99.83	71.18
ET2006-H4	38.01	25.47	0.65	35.35	0.38	99.86	71.21
ET2006-H4	38.01	25.47	0.65	35.35	0.38	99.86	71.21
ET2006-H4	38.01	25.47	0.65	35.35	0.38	99.86	71.21
ET2006-H7	36.22	27.8	0.55	34.81	0.41	99.79	69.06
ET2006-H7	36.22	27.8	0.55	34.81	0.41	99.79	69.06
ET2006-H7	36.22	27.8	0.55	34.81	0.41	99.79	69.06
ET2006-18a	37.44	26.1	0.43	35.43	0.37	99.77	70.76
ET2006-18b	37.44	26.1	0.43	35.43	0.37	99.77	70.76

[#]Fo mol = Fo content of the host olivine

Table A3.5 - Olivine from 2008/2009 tephra.

sample name	**SiO_2**	**FeO**	**MnO**	**MgO**	**CaO**	**total**	**Fo mol.% [#]**
ET2008/9-1	38.48	22.45	0.41	38.28	0.32	99.93	75.24
ET2008/9-10a	36.51	27.99	0.53	34.49	0.38	99.90	68.72
ET2008/9-10b	36.19	27.5	0.61	35.13	0.38	99.81	69.49
ET2008/9-5	38.63	21.39	0.34	39.10	0.31	99.77	76.52
ET2008/9-6a	37.63	26.68	0.52	34.55	0.37	99.75	69.77
ET2008/9-6b	37.63	26.68	0.52	34.55	0.37	99.75	69.77
ET2008/9-7	37.12	27.14	0.63	34.44	0.43	99.76	69.34
ET2008/9-7	37.12	27.14	0.63	34.44	0.43	99.76	69.34
ET2008/9-8	31.66	23.56	0.48	43.87	0.24	99.81	76.85
ET2008/9-9a	38.20	17.62	0.21	43.21	0.25	99.49	81.38
ET2008/9-9b	38.20	17.62	0.21	43.21	0.25	99.49	81.38
ET2008/9-11	38.31	26.59	0.54	33.78	0.36	99.58	69.37
ET2008/9-12	36.92	27.61	0.66	34.32	0.29	99.80	68.90
ET2008/9-12	36.92	27.61	0.66	34.32	0.29	99.80	68.90
ET2008/9-16	38.07	25.65	0.79	35.08	0.38	99.97	70.91

ET2008/9-18	37.39	20.05	0.20	42.03	0.22	99.89	78.89
ET2008/9-23	39.00	26.48	0.32	33.62	0.37	99.79	69.36

[#]Fo mol = Fo content of the host olivine

Table A3.6 - Olivine from 2013 lava.

sample name	SiO_2	FeO	MnO	MgO	CaO	total	Fo mol.% [#]
ET2013-1	38.16	23.87	0.42	37.07	0.25	99.77	73.46
ET2013-2a	38.12	21.01	0.36	40.09	0.27	99.85	77.28
ET2013-2b	38.12	21.01	0.36	40.09	0.27	99.85	77.28
ET2013-3a	37.38	26.38	0.70	34.96	0.39	99.81	70.26
ET2013-3b	37.38	26.38	0.70	34.96	0.39	99.81	70.26
ET2013-3c	37.38	26.38	0.70	34.96	0.39	99.81	70.26
ET2013-4	37.37	24.13	0.45	37.49	0.37	99.81	73.47
ET2013-6a	37.47	26.52	0.54	34.94	0.40	99.87	70.14
ET2013-6b	37.47	26.52	0.54	34.94	0.40	99.87	70.14
ET2013-7a	37.02	28.07	0.70	33.72	0.38	99.89	68.17
ET2013-7b	37.02	28.07	0.70	33.72	0.38	99.89	68.17
ET2013-7c	37.02	28.07	0.70	33.72	0.38	99.89	68.17
ET2013-7n	37.50	27.82	0.41	35.77	0.40	101.9	69.62
ET2013-11	38.61	18.49	0.21	42.28	0.24	99.83	80.30
ET2013-12	37.89	25.72	0.39	35.50	0.45	99.95	71.10
ET2013-12	37.89	25.72	0.39	35.50	0.45	99.95	71.10
ET2013-12	37.89	25.72	0.39	35.50	0.45	99.95	71.10
ET2013-12	37.89	25.72	0.39	35.50	0.45	99.95	71.10
ET2013-14	39.71	22.70	0.56	36.59	0.32	99.88	74.18
ET2013-14	39.71	22.70	0.56	36.59	0.32	99.88	74.18
ET2013-16	39.26	21.09	0.36	38.93	0.29	99.93	76.69
ET2013-17	37.39	27.11	0.56	34.50	0.32	99.88	69.40
ET2013-17	37.39	27.11	0.56	34.50	0.32	99.88	69.40
ET2013-17	37.39	27.11	0.56	34.50	0.32	99.88	69.40
ET2013-17	37.39	27.11	0.56	34.50	0.32	99.88	69.40
ET2013-19	38.58	23.73	0.58	36.72	0.28	99.89	73.39
ET2013-19	38.58	23.73	0.58	36.72	0.28	99.89	73.39
ET2013-24	-	-	-	-	-	-	-
ET2013-27	38.94	21.80	0.50	41.92	0.30	103.45	77.42
ET2013-30	36.23	25.73	0.64	36.88	0.45	99.93	71.87
ET2013-31	-	-	-	-	-	-	-
ET2013-32	35.53	26.12	0.67	36.78	0.46	99.56	71.51
ET2013-33	-	-	-	-	-	-	-
ET2013-34	36.72	26.06	0.78	35.74	0.39	99.69	70.97
ET2013-36	38.13	25.85	0.40	36.53	0.36	101.26	71.58
ET2013-37	38.65	24.31	0.66	38.67	0.34	102.63	73.93
ET2013-40	-	-	-	-	-	-	-
ET2013-41	38.27	20.64	0.78	40.34	0.29	100.32	77.70

[#]Fo mol = Fo content of the host olivine

Table A3.7 - Corrected chemical composition of melt inclusions and uncorrected compositions of glass embayments and matrix glasses from the studied products of Mt Spagnolo (SPA). FS. 2002/2003 (ET2002/3S). 2006 (ET2006). 2008/2009 (ET2008/9) and 2013 (ET2013) eruptions. Mg# is the Mg number= 100 x Mg/(Mg+Fe_{tot}). PEC% is the estimated amount of post-entrapment crystallization and the Fo is the forsteritic content of the hosting olivine. Numbers in brackets indicate the standard deviations.

sample name	n.	SiO_2	TiO_2	Al_2O_3	FeO	MnO	MgO	CaO	Na_2O	K_2O	Cr_2O_3	NiO	P_2O_5	tot	Mg#	CaO/ Al_2O_3	PEC %	Fo mol.%
Spa-1a	4	42.44 (±0.92)	1.59 (±0.06)	17.83 (±0.40)	8.02 (±0.50)	0.17 (±0.04)	8.39 (±0.19)	8.85 (±0.58)	5.57 (±0.40)	2.04 (±0.06)	n.d.	n.d.	1.11 (±0.20)	96.01	65.09	0.5	6.6	87.76
Spa -1b	1	43.10	1.75	14.38	6.64	0.24	6.93	13.15	4.07	1.46	n.d.	n.d.	0.58	92.3	65.04	0.91	12	87.76
Spa-3	2	47.56 (±0.56)	1.45 (±0.12)	16.37 (±0.16)	7.54 (±0.80)	b.d.l.	5.10 (±0.31)	10.21 (±1.03)	4.64 (±0.06)	2.16 (±0.04)	n.d.	n.d.	0.55	95.58	54.66	0.62	7.7	82.27
Spa-3n	1	46.93 (±0.04)	1.51 (±0.15)	15.90 (±0.01)	9.41 (±0.75)	0.17 (±0.08)	6.39 (±0.20)	9.37 (±0.13)	4.24 (±0.02)	1.92 (±0.06)	n.d.	n.d.	0.60 (±0.12)	96.44	54.76	0.59	4.7	82.27
Spa -4n	3	45.30 (±1.34)	1.52 (±0.16)	16.81 (±0.40)	6.86 (±0.04)	0.08 (±0.07)	6.60 (±0.15)	12.59 (±0.08)	4.58 (±0.04)	1.43 (±0.08)	n.d.	n.d.	0.49 (±0.02)	96.26	63.17	0.75	11.3	86.85
Spa-5	3	44.09 (±0.04)	1.45 (±0.10)	15.24 (±0.25)	8.65 (±0.45)	0.20 (±0.16)	7.88 (±0.27)	14.46 (±0.25)	3.60 (±0.12)	1.27 (±0.09)	n.d.	n.d.	0.64	97.48	61.89	0.95	13.2	86.95
Spa-5n	2	45.38 (±0.29)	1.59 (±0.03)	15.99 (±0.44)	7.51 (±0.63)	0.12 (±0.09)	7.30 (±0.83)	13.36 (±0.37)	4.53 (±0.09)	1.28 (±0.10)	n.d.	n.d.	0.53 (±0.09)	97.59	63.41	0.84	9.8	86.21
Spa-6	1	44.00	1.62	16.64	6.86	0.08	5.99	13.83	4.29	1.47	0.03	0.01	0.8	95.61	60.88	0.83	10.4	85.70
Spa-7	3	50.19 (±0.17)	1.89 (±0.18)	17.91 (±0.05)	6.23 (±0.32)	0.14 (±0.04)	5.26 (±0.20)	10.96 (±0.37)	4.29 (±0.16)	1.89 (±0.06)	n.d.	n.d.	0.65 (±0.10)	99.41	60.08	0.61	8.8	85.29
Spa-7n	2	51.33 (±0.17)	1.33 (±0.12)	16.92 (±0.02)	5.13 (±0.24)	0.08 (±0.03)	5.24 (±0.03)	9.95 (±0.05)	5.54 (±0.06)	2.17 (±0.24)	n.d.	n.d.	0.36 (±0.16)	98.05	64.55	0.59	7.9	87.48
Spa-9	2	44.04 (±0.49)	1.75 (±0.04)	16.64 (±0.37)	7.14 (±0.36)	0.09 (±0.02)	6.03 (±0.09)	13.50 (±0.42)	4.08 (±0.17)	1.49 (±0.03)	0.058 (±0.03)	b.d.l.	0.69 (±0.02)	95.51	60.09	0.81	10.8	85.67
Spa-11	1	44.57	1.76	17.07	7.17	0.13	5.93	12.6	4.2	1.62	n.d.	n.d.	0.95	96.00	59.58	0.74	9.8	85.00
Spa- D	1	46.22	1.72	13.51	7.76	0.19	7.41	7.74	5.85	3.10	n.d.	n.d.	0.79	94.29	62.99	0.57	10.8	86.77
Spa- L	1	44.05	1.57	19.07	6.72	0.23	6.27	6.41	5.38	2.91	n.d.	n.d.	1.51	94.12	62.45	0.34	23.4	86.50
Spa- O1	1	46.49	1.89	13.79	9.54	0.11	7.37	8.70	5.31	2.20	n.d.	n.d.	0.67	96.07	57.93	0.63	14.6	84.12
Spa-R	1	46.40	1.47	15.47	7.13	0	7.76	11.00	5.37	1.45	n.d.	n.d.	0.62	96.67	65.99	0.71	12.7	71.17
Spa-T1	2	43.34 (±0.20)	1.51 (±0.07)	14.22 (±0.37)	7.98 (±0.07)	0.21 (±0.05)	8.09 (±0.07)	14.20 (±0.07)	3.97 (±0.06)	0.87 (±0.13)	n.d.	n.d.	0.58 (±0.03)	94.97	64.38	1.00	12.1	87.42
Spa-T2	1	45.07	1.55	14.42	7.37	0.01	7.50	14.84	4.70	1.01	n.d.	n.d.	0.62	97.09	64.46	1.03	10.5	87.42
Spa-T3	1	44.63	1.41	14.21	7.55	0.18	7.65	15.08	4.34	1.04	n.d.	n.d.	0.61	96.70	64.36	1.06	11.0	87.42
Spa-T4	2	44.78 (±0.95)	1.69 (±0.13)	14.63 (±0.06)	8.65 (±0.46)	b.d.l.	8.77 (±0.22)	13.04 (±0.43)	4.29 (±0.29)	1.20 (±0.05)	n.d.	n.d.	0.33 (±0.21)	97.43	64.38	0.89	13.5	87.42

Spa-U1	2	48.02 (±0.38)	2.13 (±0.14)	15.57 (±0.52)	6.55 (±0.40)	b.d.l.	7.14 (±0.13)	5.93 (±1.05)	5.65 (±0.59)	2.51 (±0.09)	n.d.	n.d.	0.75 (±0.02)	94.37	66.02	0.38	13.5	88.21
Spa-U2	1	47.93	2.18	15.65	6.55	0.12	7.14	5.93	5.65	2.51	n.d.	n.d.	0.75	94.41	66.02	0.38	19.7	88.21
Spa-U3	3	47.65 (±0.45)	2.10 (±0.17)	14.47 (±0.33)	7.58 (±0.34)	b.d.l.	8.26 (±0.02)	7.34 (±0.13)	4.91 (±0.78)	3.06 (±0.03)	n.d.	n.d.	0.73 (±0.02)	96.24	66.01	0.51	16.0	88.21
Spa-U4	1	47.92	1.90	14.94	7.23	0.16	7.89	8.30	5.45	2.35	n.d.	n.d.	0.71	96.85	66.05	0.56	14.5	88.21
FS-00	6	48.99 (±0.32)	0.85 (±0.17)	10.23 (±0.10)	8.62 (±0.43)	0.09 (±0.05)	10.76 (±0.12)	13.16 (±0.19)	1.89 (±0.09)	0.82 (±0.07)	0.09 (±0.01)	0.05 (±0.01)	n.d.	95.55	68.99	1.29	3.5	89.54
FS-01	9	47.29 (±0.37)	0.99 (±0.11)	9.89 (±0.47)	8.59 (±0.36)	0.21 (±0.07)	10.66 (±0.84)	13.13 (±0.28)	1.50 (±0.07)	0.91 (±0.11)	0.06 (±0.01)	0.04 (±0.01)	n.d.	93.27	68.87	1.33	11.7	89.49
FS-03b	5	46.69 (±0.38)	1.08 (±0.07)	9.16 (±0.18)	8.46 (±0.20	0.19 (±0.11)	10.37 (±0.35)	13.66 (±0.21)	1.58 (±0.06)	0.71 (±0.07)	0.09 (±0.01)	0.02 (±0.01)	n.d.	92.01	68.60	1.49	11.3	89.37
FS-03c	6	47.19 (±0.32)	1.16 (±0.07)	9.54 (±0.33)	8.55 (±0.23)	0.16 (±0.07)	10.48 (±0.51)	13.40 (±0.37)	1.70 (±0.04)	0.75 (±0.06)	0.07 (±0.01)	0.05 (±0.01)	n.d.	93.05	68.60	1.40	7.4	89.48
FS-05	5	46.58 (±0.37)	1.19 (±0.18)	8.91 (±0.30)	9.17 (±0.38)	b.d.l.	10.99 (±0.84)	12.64 (±0.21)	1.55 (±0.03)	1.17 (±0.07)	0.06 (±0.01)	0.05 (±0.01)	n.d.	92.31	68.12	1.42	13.3	89.15
FS-06b	7	47.10 (±0.26)	0.93 (±0.14)	9.59 (±0.08)	8.61 (±0.38)	0.14 (±0.08)	11.45 (±0.53)	13.14 (±0.37)	1.63 (±0.07)	0.87 (±0.06)	0.06 (±0.01)	0.03 (±0.01)	n.d.	93.55	70.33	1.37	6.5	90.12
FS-06c	2	46.35 (±0.12)	0.86 (±0.04)	9.19 (±0.05)	8.62 (±0.39)	0.17 (±0.09)	11.47 (±0.60)	13.68 (±0.34)	1.61 (±0.09)	0.74 (±0.06)	b.d.l.	b.d.l.	n.d.	92.74	70.34	1.49	12.9	90.11
FS-06n	1	46.02	0.83	9.77	8.85	0.22	12.38	12.21	1.43	0.83	0.047 (±0.01)	0.302 (±0.01)	0.22 (±0.10)	93.11	71.38	1.25	10.3	90.11
FS-07	5	47.85 (±0.19)	0.94 (±0.06)	9.31 (±0.06)	8.54 (±0.48)	0.13 (±0.07)	10.32 (±0.18)	13.71 (±0.26)	1.44 (±0.08)	0.89 (±0.08)	0.07 (±0.01)	0.02 (±0.01)	n.d.	93.22	68.30	1.47	9.2	89.72
FS-08b	9	47.30 (±0.26)	1.18 (±0.06)	9.96 (±0.21)	8.70 (±0.25)	0.12 (±0.07)	10.29 (±0.53)	12.38 (±0.32)	1.88 (±0.07)	1.04 (±0.05)	0.07 (±0.01)	0.02 (±0.01)	n.d.	92.94	67.83	1.24	8.0	89.03
FS-08c	4	46.49 (±0.37)	1.09 (±0.04)	9.30 (±0.11)	8.64 (±0.22)	0.16 (±0.11)	10.44 (±0.19)	12.92 (±0.38)	1.71 (±0.09)	1.01 (±0.08)	0.08 (±0.01)	0.02 (±0.01)	n.d.	91.86	68.29	1.39	12.2	89.23
FS-09 n	4	46.07 (±0.26)	1.02 (±0.07)	9.93 (±0.05)	7.82 (±0.15)	0.15 (±0.08)	11.16 (±0.31)	13.36 (±0.48)	1.61 (±0.08)	0.88 (±0.03)	b.d.l.	b.d.l.	0.30 (±0.20)	92.3	71.78	1.35	5.1	90.73
FS-09	2	47.61 (±0.01)	1.10 (±0.03)	9.77 (±0.25)	8.02 (±0.12)	0.21 (±0.05)	10.53 (±0.24)	14.74 (±0.44)	1.71 (±0.05)	0.90 (±0.03)	0.09 (±0.01)	0.05 (±0.01)	n.d.	94.73	70.06	1.51	12.6	90.00
FS-10b	11	46.28 (±0.42)	0.89 (±0.06)	9.65 (±0.21)	8.75 (±0.21)	0.17 (±0.11)	11.81 (±0.67)	12.97 (±0.33)	1.54 (±0.05)	0.78 (±0.09)	0.07 (±0.01)	0.04	n.d.	92.95	70.64	1.34	9.3	90.26
FS-10c	6	44.93 (±0.30)	1.20 (±0.10)	9.88 (±0.51)	8.23 (±0.25)	0.13 (±0.09)	11.42 (±0.78)	13.23 (±0.19)	1.63 (±0.12)	0.58 (±0.08)	0.08 (±0.01)	0.02 (±0.01)	n.d.	91.33	71.21	1.34	15.9	90.5
FS-11	11	47.30 (±0.25)	1.02 (±0.12)	10.20 (±0.15)	8.79 (±0.39)	0.16 (±0.08)	11.50 (±0.26)	11.45 (±0.19)	1.89 (±0.07)	1.13 (±0.06)	b.d.l.	b.d.l.	n.d.	93.44	69.99	1.12	8.9	89.97
FS-12a	3	44.87 (±0.40)	0.95 (±0.07)	10.39 (±0.24)	10.26 (±0.24)	0.21 (±0.06)	12.36 (±0.03)	13.34 (±0.11)	1.96 (±0.04)	0.79 (±0.05)	n.d.	n.d.	0.25 (±0.03)	95.38	68.23	1.28	12.2	89.21
FS-12b	2	46.39 (±0.83)	0.87 (±0.07)	10.25 (±0.43)	8.90 (±0.13)	0.23 (±0.10)	10.72 (±0.22)	12.80 (±0.08)	1.49 (±0.17)	0.86 (±0.02)	n.d.	n.d.	0.23 (±0.05)	92.74	68.22	1.25	10.4	89.21

FS-13b	5	46.46 (±0.43)	1.00 (±0.12)	9.39 (±0.48)	8.69 (±0.30)	0.19 (±0.08)	10.95 (±0.81)	13.74 (±0.21)	1.56 (±0.13)	0.72 (±0.13)	b.d.l.	0.04 (±0.01)	n.d.	92.74	69.19	1.46	13.3	89.63
FS-13c	3	46.38 (±0.33)	0.93 (±0.06)	9.29 (±0.32)	8.77 (±0.43)	0.16 (±0.10)	11.04 (±0.30)	13.85 (±0.13)	1.57 (±0.05)	0.63 (±0.05)	0.08 (±0.01)	0.05 (±0.01)	n.d.	92.75	69.17	1.49	12.5	89.63
FS-14	5	46.6 (±0.15)	1.05 (±0.08)	9.16 (±0.20)	8.93 (±0.23)	b.d.l.	10.89 (±0.34)	12.96 (±0.15)	1.65 (±0.08)	1.03 (±0.05)	n.d.	0.05 (±0.01)	n.d.	92.32	68.49	1.41	8.8	89.32
FS-21	3	44.06 (±0.33)	0.92 (±0.11)	9.82 (±0.27)	8.33 (±0.65)	0.17 (±0.02)	11.14 (±0.69)	13.72 (±0.56)	1.39 (±0.06)	1.02 (±0.03)	0.075 (±0.01)	b.d.l.	0.31 (±0.18)	90.96	70.45	1.40	6.4	90.17
FS-24	1	44.70	1.51	9.44	9.26	0.19	10.52	12.27	1.74	0.81	n.d.	n.d.	0.08	90.52	66.94	1.30	8.6	88.64
FS-25	2	45.27 (±0.01)	0.78 (±0.06)	9.07 (±0.07)	8.74 (±0.57)	0.23 (±0.12)	12.21 (±0.19)	13.01 (±0.17)	1.58 (±0.02)	0.63 (±0.06)	n.d.	b.d.l.	0.38 (±0.13)	91.90	71.35	1.43	10.0	90.56
FS-26	5	46.26 (±0.60)	0.95 (±0.09)	9.99 (±0.60)	7.82 (±0.47)	b.d.l.	10.38 (±0.70)	13.14 (±0.16)	1.90 (±0.16)	0.80 (±0.60)	n.d.	0.114 (±0.01)	0.33 (±0.02)	91.83	70.29	1.32	4.1	89.96
FS-28a	2	44.31 (±0.54)	0.88 (±0.14)	9.32 (±0.17)	8.42 (±0.09)	b.d.l.	11.49 (±0.22)	13.36 (±0.22)	1.56 (±0.05)	0.65 (±0.01)	0.047 (±0.01)	b.d.l.	0.49 (±0.17)	90.63	70.87	1.43	6.5	90.35
FS-28b	2	45.96 (±0.19)	0.86 (±0.03)	9.46 (±0.05)	8.12 (±0.20)	b.d.l.	11.07 (±0.01)	14.01 (±0.16)	1.58 (±0.07)	0.78 (±0.02)	0.102 (±0.05)	b.d.l.	0.16 (±0.03)	92.22	70.85	1.48	7.1	90.35
FS-B	2	43.97 (±0.39)	0.86 (±0.01)	9.20 (±0.08)	8.08 (±0.10)	0.10 (±0.01)	11.27 (±0.36)	13.28 (±0.30)	1.43 (±0.33)	0.87 (±0.01)	0.06 (±0.04)	b.d.l.	0.16 (±0.10)	89.43	71.32	1.44	5.6	90.53
FS-D	2	44.66 (±0.25)	1.08 (±0.08)	10.26 (±0.22)	7.91 (±0.21)	0.13 (±0.06)	11.12 (±0.07)	12.55 (±0.01)	1.86 (±0.02)	0.84 (±0.01)	0.12 (±0.08)	b.d.l.	0.41 (±0.03)	90.94	71.48	1.22	3.8	90.60
FS-E	3	49.14 (±2.11)	0.88 (±0.04)	10.60 (±0.25)	6.18 (±0.35)	0.10 (±0.08)	9.99 (±0.20)	13.62 (±0.98)	2.39 (±0.43)	1.39 (±0.40)	n.d.	n.d.	0.11 (±0.11)	94.40	74.24	1.28	0	90.56
FS-Xa	2	44.09 (±0.56)	0.99 (±0.11)	10.28 (±0.27)	7.76 (±0.17)	0.17 (±0.04)	10.10 (±0.67)	13.80 (±0.25)	1.74 (±0.11)	1.09 (±0.11)	0.028 (±0.01)	b.d.l.	0.25 (±0.07)	90.30	69.88	1.34	4.2	89.92
FS-Z	2	43.7 (±0.39)	1.11 (±0.06)	8.80 (±0.11)	8.21 (±0.58)	0.10 (±0.01)	12.15 (±0.05)	12.47 (±0.01)	1.75 (±0.07)	0.87 (±0.02)	0.04 (±0.06)	b.d.l.	0.35 (±0.12)	89.55	72.51	1.42	7.3	91.02
ET2002/3S-1	3	46.95 (±0.87)	1.25 (±0.14)	16.90 (±0.23)	10.67 (±0.35)	0.35 (±0.12)	4.72 (±0.08)	7.08 (±0.10)	4.34 (±0.17)	1.96 (±0.10)	b.d.l.	b.d.l.	0.8	95.02	44.09	0.42	1.6	75.21
ET2002/3S-3	5	45.53 (±0.20)	1.50 (±0.07)	16.30 (±0.08)	10.29 (±0.51)	0.19 (±0.13)	4.95 (±0.10)	10.69 (±0.27)	3.18 (±0.07)	2.03 (±0.10)	n.d.	n.d.	0.44	95.1	46.16	0.66		75.69
ET2002/3S-5	2	42.83 (±0.95)	1.97 (±0.02)	15.10 (±0.16)	10.24 (±0.09)	0.12 (±0.01)	6.71 (±0.02)	12.27 (±0.01)	2.69 (±0.21)	1.68 (±0.06)	n.d.	n.d.	0.34 (±0.03)	93.95	53.88	0.81	9.3	81.79
ET2002/3S-6	3	48.68 (±0.17)	1.59 (±0.07)	15.55 (±0.34)	9.32 (±0.47)	0.23 (±0.16)	4.75 (±0.16)	6.49 (±0.07)	4.02 (±0.17)	2.12 (±0.11)	n.d.	n.d.	0.69	93.44	47.6	0.42	1.4	77.76
ET2002/3S-7	3	44.87 (±0.38)	1.84 (±0.05)	15.88 (±0.09)	11.12 (±0.13)	0.22 (±0.12)	4.85 (±0.12)	6.71 (±0.03)	4.06 (±0.12)	4.74 (±0.03)	n.d.	n.d.	0.78	95.07	43.74	0.42	6.4	74.96
ET2002/3S-9	2	50.49 (±1.79)	1.93 (±0.28)	17.39 (±0.76)	8.15 (±1.14)	0.09 (±0.07)	3.65 (±0.59)	7.59 (±0.68)	4.01 (±0.24)	2.82 (±0.27)	n.d.	n.d.	0.98	97.1	44.39	0.44	0.5	75.43
ET2002/3S-10	4	50.09 (±0.69)	1.56 (±0.06)	15.79 (±0.13)	10.21 (±0.24)	0.20 (±0.13)	4.22 (±0.15)	6.06 (±0.10)	4.32 (±0.07)	2.35 (±0.11)	n.d.	n.d.	0.70	95.5	42.42	0.38	1.3	73.94
ET2002/3S-11b	1	42.94	2.11	17.15	8.56	0.25	6.06	13.17	3.32	2.27	n.d.	n.d.	0.50	96.33	55.79	0.77	7.7	82.90

ET2002/3S-13	2	42.92 (±0.80)	1.74 (±0.01)	15.53 (±0.09)	9.69	0.16 (±0.07)	6.74 (±0.08)	11.65	2.86 (±0.07)	1.98 (±0.09)	n.d.	n.d.	0.37	93.64	55.35	0.75	6.0	82.68
ET2002/3S-16a	2	46.48 (±1.39)	1.56 (±0.11)	15.26 (±0.50)	11.54 (±0.57)	b.d.l.	4.38 (±0.01)	7.82 (±0.21)	5.39 (±0.22)	1.69 (±0.06)	n.d.	n.d.	1.04 (±0.18)	95.19	40.35	0.51	1.6	73.65
ET2002/3S-16b	1	45.46	1.61	14.45	11.72	0.22	4.85	6.43	6.56	2.03	n.d.	n.d.	0.72	94.04	42.44	0.44	0	73.65
ET2002/3S-23	2	43.92 (±0.60)	1.57 (±0.15)	15.50 (±0.20)	9.79 (±0.38)	0.10 (±0.14)	6.78 (±0.04)	10.70 (±0.03)	3.57 (±0.03)	1.96 (±0.02)	n.d.	n.d.	0.35 (±0.18)	94.24	55.25	0.69	3.5	82.61
ET2002/3S-24	2	44.72 (±0.23)	1.62 (±0.14)	15.00 (±0.03)	11.83 (±0.25)	0.19 (±0.03)	7.01 (±0.11)	8.09 (±0.11)	4.12 (±0.11)	2.74 (±0.04)	n.d.	n.d.	0.54 (±0.03)	95.86	51.37	0.54	8.9	80.26
ET2002/3S-26	2	48.34 (±0.86)	1.91 (±0.02)	15.28 (±0.44)	9.37 (±0.128)	b.d.l.	3.61 (±0.06)	6.24 (±0.20)	4.91 (±0.22)	3.51 (±0.19)	b.d.l.	n.d.	0.83 (±0.10)	94.13	40.72	0.41	4.5	72.57
ET2002/3S-29a	1	51.92	1.01	14.5	10.20	0.25	3.87	5.88	4.93	2.94	n.d.	n.d.	0.80	96.3	40.35	0.41	2.4	69.64
ET2002/3S-29b	2	50.47 (±0.10)	1.20 (±0.01)	13.56 (±0.03)	11.64 (±0.05)	b.d.l.	4.13 (±0.11)	5.40 (±0.07)	5.39 (±0.19)	3.21 (±0.01)	n.d.	n.d.	0.79 (±0.01)	95.91	38.74	0.40	2.7	69.64
ET2002/3S-31	1	49.43	1.09	17.05	8.40	0.18	2.83	9.44	5.4	2.01	n.d.	n.d.	0.70	96.53	37.52	0.55	5.3	69.77
ET2002/3S-32	4	46.31 (±1.52)	1.88 (±0.18)	14.07 (±0.25)	9.21 (±0.53)	b.d.l.	3.75 (±0.08)	6.37 (±0.20)	4.24 (±0.30)	2.83 (±0.05)	b.d.l.	0.22 (±0.03)	0.82 (±0.11)	89.59	42.06	0.45	0	72.90
ET2002/3S-33a	3	43.00 (±0.20)	1.71 (±0.10)	15.69 (±0.11)	9.15 (±0.45)	0.21 (±0.06)	5.58 (±0.11)	11.11 (±0.18)	3.47 (±0.08)	2.08 (±0.07)	n.d.	n.d.	0.59 (±0.07)	92.59	52.09	0.71	0	80.68
ET2002/3S-33b	3	42.71 (±0.27)	1.56 (±0.07)	15.45 (±0.33)	10.30 (±0.46)	b.d.l.	6.27 (±0.16)	11.22 (±0.19)	3.27 (±0.11)	1.97 (±0.06)	n.d.	n.d.	0.55 (±0.14)	93.3	52.04	0.73	4.4	80.68
ET2002/3S-14 secondary MI	1	49.07	0.82	13.03	13.23	0.31	3.96	8.39	3.72	1.38	n.d.	n.d.	0.21	94.12	34.8	0.64	0	67.96
ET2002/3S-24 embayments	2	46.68 (±0.50)	2.19 (±0.15)	14.91 (±0.60)	10.84 (±0.30)	0.22 (±0.03)	3.45 (±0.20)	7.90 (±0.07)	4.72 (±0.11)	3.46 (±0.19)	n.d.	n.d.	0.63 (±0.15)	95	36.2	0.53		80.26
ET2002/3S-6 gm	3	43.40 (±2.68)	1.96 (±0.11)	13.84 (±0.32)	10.47 (±0.41)	b.d.l.	3.17 (±0.24)	6.98 (±0.43)	3.85 (±0.30)	3.31 (±0.08)	n.d.	n.d.	0.78 (±0.24)	87.86	35.05	0.50		
ET2002/3S-10 gm	3	48.51 (±0.80)	1.99 (±0.02)	16.14 (±0.29)	10.33 (±0.59)	0.27 (±0.11)	3.28 (±0.10)	7.79 (±0.10)	3.78 (±0.05)	3.48 (±0.18)	n.d.	n.d.	0.95 (±0.05)	96.52	36.14	0.48		
ET2002/3S-13 gm	3	50.88 (±0.57)	2.00 (±0.08)	16.29 (±0.11)	10.77 (±0.11)	0.13 (±0.12)	3.21 (±0.15)	7.78 (±0.05)	3.72 (±0.12)	3.62 (±0.15)	n.d.	n.d.	0.81 (±0.14)	99.21	34.7	0.48		
ET2002/3S-23 gm	1	49.49	2.12	14.61	11.78	0.21	2.92	7.02	4.96	3.70	n.d.	n.d.	0.91	97.73	30.66	0.48		
ET2002/3S-32 gm	1	48.75	1.73	15.69	10.39	0.33	3.54	8.04	4.62	3.21	n.d.	n.d.	0.71	92.72	37.79	0.51		
ET2006-1 a	4	49.57 (±0.17)	1.37 (±0.21)	16.00 (±0.13)	11.07 (±0.24)	0.23 (±0.10)	3.70 (±0.04)	6.81 (±0.09)	3.84 (±0.73)	2.61 (±0.14)	n.d.	n.d.	0.70 (±0.12)	95.90	37.34	0.43	0.8	69.64
ET2006-1 b	2	49.03 (±0.46)	1.54 (±0.08)	15.73 (±0.23)	11.14 (±0.05)	0.21 (±0.04)	3.85 (±0.02)	6.95 (±0.11)	3.73 (±0.84)	2.55 (±0.11)	n.d.	n.d.	0.66 (±0.07)	95.39	38.12	0.44	1.1	70.35
ET2006-4	2	49.42 (±0.01)	1.60 (±0.08)	15.66 (±0.06)	10.20 (±0.04)	b.d.l.	3.67 (±0.03)	7.75 (±0.08)	4.66	2.26 (±0.01)	n.d.	n.d.	0.83 (±0.28)	96.98	39.08	0.49	0	70.48

ET2006-7	2	42.25 (±0.31)	1.33 (±0.26)	15.71 (±0.08)	10.53 (±0.11)	0.09 (±0.08)	6.58 (±0.01)	11.10 (±0.14)	2.93 (±0.07)	1.73 (±0.10)	n.d.	n.d.	0.37 (±0.10)	92.62	52.69	0.71	3.4	81.08
ET2006-12	3	45.02 (±0.08)	1.76 (±0.15)	16.79 (±0.02)	10.11 (±0.22)	0.16 (±0.03)	5.13 (±0.02)	10.70 (±0.30)	3.24 (±0.10)	2.07 (±0.12)	n.d.	n.d.	0.57 (±0.11)	95.55	47.49	0.64	0.5	78.75
ET2006-B3a	4	46.75 (±0.21)	1.52 (±0.06)	16.03 (±0.10)	10.44 (±0.24)	0.07 (±0.05)	5.14 (±0.15)	8.52 (±0.18)	4.08 (±0.72)	1.66 (±0.03)	n.d.	n.d.	0.57 (±0.09)	94.78	46.74	0.53	1.5	77.15
ET2006-B3b	5	46.86 (±0.29)	1.70 (±0.17)	15.78 (±0.18)	9.93 (±0.30)	0.24 (±0.13)	4.89 (±0.18)	8.45 (±0.06)	3.61 (±0.94)	1.62 (±0.05)	n.d.	n.d.	0.52 (±0.11)	93.60	46.75	0.54	0.5	77.15
ET2006-B5a	3	44.46 (±0.44)	1.52 (±0.04)	15.61 (±0.29)	10.64 (±0.22)	0.09 (±0.04)	6.30 (±0.09)	10.43 (±0.08)	3.73 (±0.07)	2.09	0.52	n.d.	0.52 (±0.06)	95.39	51.35	0.67	4.0	80.24
ET2006-B5c	2	49.40 (±0.32)	1.78 (±0.15)	14.44 (±0.11)	10.21 (±0.16)	0.26 (±0.16)	6.05 (±0.07)	7.37 (±0.14)	3.98 (±1.16)	3.27 (±0.15)	n.d.	n.d.	0.66	97.42	51.37	0.51	7.4	80.24
ET2006-B5d	3	45.01 (±0.40)	1.67 (±0.22)	15.19 (±0.18)	11.70 (±0.46)	0.31 (±0.07)	6.93 (±0.02)	8.59 (±0.07)	4.54 (±0.30)	2.62 (±0.06)	0.07 (±0.05)	n.d.	0.55 (±0.10)	97.11	51.36	0.57	8.4	80.24
ET2006-B5n	1	43.60	1.58	17.03	10.26	0.05	6.08	11.22	3.83	2.23	n.d.	n.d.	0.55	96.43	51.37	0.66	3.9	80.24
ET2006-B6	3	46.71 (±0.41)	1.48 (±0.18)	17.15 (±0.18)	9.56 (±0.24)	0.10 (±0.04)	4.46 (±0.05)	8.93 (±0.10)	5.11 (±0.18)	2.98 (±0.11)	n.d.	n.d.	0.52 (±0.10)	97.00	45.4	0.52	1.0	76.20
ET2006-B8a	3	49.40 (±0.08)	1.71 (±0.08)	15.81 (±0.17)	9.82 (±0.34)	0.18 (±0.06)	4.39 (±0.32)	6.01 (±0.11)	4.15 (±0.11)	2.81 (±0.10)	n.d.	n.d.	0.58 (±0.05)	94.86	44.35	0.38	0.7	75.42
ET2006-B8b	2	48.83 (±0.34)	1.56 (±0.06)	14.64 (±0.52)	9.82 (±0.13)	0.21 (±0.01)	4.37 (±0.01)	8.45 (±0.11)	3.88 (±0.10)	2.07	n.d.	n.d.	0.86 (±0.19)	94.70	44.23	0.58	0	75.42
ET2006-C7a	3	51.15 (±0.10)	1.51 (±0.15)	15.01 (±0.21)	9.96 (±0.34)	b.d.l.	3.71 (±0.07)	6.83 (±0.07)	4.9 (±0.15)	2.48 (±0.05)	n.d.	n.d.	0.60 (±0.11)	96.22	39.89	0.46	0	70.20
ET2006-C7b	2	49.73 (±0.51)	1.92 (±0.17)	14.54 (±0.10)	9.80 (±0.35)	0.26 (±0.15)	3.75 (±0.08)	7.37 (±0.17)	4.66 (±0.09)	2.26 (±0.03)	n.d.	n.d.	0.75 (±0.05)	95.04	40.54	0.51	0	70.20
ET2006-C8	3	48.68 (±0.32)	1.96 (±0.07)	16.24 (±0.27)	10.97 (±0.04)	0.14 (±0.11)	4.46 (±0.13)	6.24 (±0.02)	4.96 (±0.71)	2.63 (±0.06)	n.d.	n.d.	0.87 (±0.13)	97.15	42.02	0.38	3.3	73.62
ET2006-C11	2	49.65 (±0.37)	1.77 (±0.16)	15.12 (±0.29)	10.04 (±0.56)	b.d.l.	3.96 (±0.04)	7.33 (±0.19)	4.47 (±1.14)	2.52 (±0.05)	n.d.	n.d.	0.67 (±0.07)	95.73	41.3	0.49	0	71.96
ET2006-D9	2	49.66 (±0.37)	2.01 (±0.02)	14.48 (±0.12)	9.75 (±0.37)	0.24 (±0.07)	3.52 (±0.10)	7.17 (±0.17)	4.12 (±0.93)	3.26 (±0.19)	n.d.	n.d.	1.06 (±0.09)	95.27	39.11	0.49	0	70.06
ET2006-E2a	3	50.13 (±0.37)	1.85 (±0.09)	15.55 (±0.08)	10.48 (±0.18)	0.23 (±0.15)	3.53 (±0.11)	7.32 (±0.06)	2.72 (±1.23)	2.65 (±0.12)	n.d.	n.d.	0.57 (±0.06)	95.03	37.52	0.47	0	70.19
ET2006-E2b	2	48.41 (±0.19)	1.91 (±0.06)	14.50 (±0.21)	11.77 (±0.21)	0.32 (±0.12)	4.04 (±0.15)	7.33 (±0.13)	4.06 (±0.16)	2.43 (±0.04)	n.d.	n.d.	0.49 (±0.11)	95.26	37.96	0.51	3.3	70.19
ET2006-F5a	3	46.22 (±0.38)	1.65 (±0.13)	14.94 (±0.08)	10.70 (±0.54)	0.13 (±0.08)	5.50 (±0.05)	8.96 (±0.02)	4.64 (±0.06)	2.65 (±0.10)	n.d.	n.d.	0.54	95.93	47.82	0.60	4.4	77.95
ET2006-F5b	1	47.59	1.67	14.38	10.71	0.21	5.52	7.49	4.82	3.21	n.d.	n.d.	0.95	96.55	47.88	0.52	5.9	77.95
ET2006-F5c	3	42.95 (±0.05)	1.63 (±0.13)	16.31 (±0.08)	11.10 (±0.21)	0.24 (±0.06)	5.71 (±0.06)	9.85 (±0.13)	3.85 (±0.10)	1.89 (±0.10)	n.d.	n.d.	0.53	94.06	47.83	0.60	1.0	77.95
ET2006-F5d	3	45.67 (±0.25)	1.75 (±0.17)	15.47 (±0.04)	10.90 (±0.21)	0.23 (±0.05)	5.62 (±0.06)	8.86 (±0.13)	4.30 (±0.01)	2.17 (±0.05)	n.d.	n.d.	0.52	95.49	47.89	0.57	2.4	77.95
ET2006-F5e	3	46.28 (±0.17)	1.17 (±0.10)	16.08 (±0.27)	9.87 (±0.29)	0.18 (±0.02)	5.08 (±0.09)	8.04 (±0.11)	4.67 (±0.10)	2.12 (±0.19)	n.d.	n.d.	0.83	94.32	47.85	0.50	1.8	77.95

ET2006-F5n	1	51.63	1.09	14.66	10.07	0.11	5.19	4.27	4.16	3.47	n.d.	n.d.	1.16	95.81	47.88	0.29	7.5	71.28
ET2006-H2	3	49.29 (±0.52)	1.36 (±0.18)	14.64 (±0.33)	10.04 (±0.58)	0.13 (±0.08)	4.08 (±0.08)	6.96 (±0.13)	5.13 (±0.21)	2.60 (±0.14)	n.d.	n.d.	0.53	94.77	42.01	0.48	0	71.18
ET2006-H4a	3	48.71 (±0.12)	1.74 (±0.04)	14.41 (±0.14)	11.37 (±0.09)	0.22 (±0.17)	4.10 (±0.06)	7.58 (±0.15)	4.23 (±0.72)	2.68 (±0.12)	n.d.	n.d.	0.76	95.8	39.13	0.53	1.5	71.21
ET2006-H4b	3	47.99 (±0.20)	1.79 (±0.13)	14.39 (±0.17)	11.45 (±0.14)	0.30 (±0.16)	4.13 (±0.01)	8.68 (±0.03)	3.53 (±0.63)	2.33 (±0.07)	n.d.	n.d.	1.02	95.61	39.13	0.60	1.1	71.21
ET2006-H4c	2	48.46 (±0.30)	1.79 (±0.22)	14.52 (±0.04)	11.92 (±0.05)	0.25 (±0.14)	4.30 (±0.07)	7.89 (±0.03)	3.58 (±0.16)	2.64 (±0.13)	n.d.	n.d.	0.93	96.28	39.14	0.54	3.1	71.21
ET2006-H7a	3	49.65 (±0.61)	1.27 (±0.04)	16.45 (±0.44)	9.15 (±0.87)	0.24 (±0.07)	3.53 (±0.19)	8.30 (±0.30)	4.27 (±0.77)	3.36 (±0.25)	n.d.	n.d.	0.87	97.08	40.78	0.50	0	69.06
ET2006-H7b	2	49.44 (±0.43)	1.86	15.79 (±0.74)	9.55 (±0.34)	0.18 (±0.09)	3.72 (±0.09)	7.43 (±0.01)	3.70 (±1.40)	3.29 (±0.10)	n.d.	n.d.	0.93 (±0.27)	95.89	41.01	0.47	0	69.06
ET2006-H7c	3	48.33 (±0.35)	1.47 (±0.15)	15.40 (±0.23)	10.59 (±0.39)	0.25 (±0.11)	3.83 (±0.04)	9.11 (±0.12)	4.24 (±0.74)	2.91 (±0.06)	n.d.	n.d.	0.90 (±0.09)	97.04	39.22	0.59	0	69.06
ET2006-18a	1	48.71	1.63	14.86	12.41	0.32	4.38	7.72	4.23	2.50	n.d.	n.d.	1.19	97.95	38.62	0.52	2.9	70.76
ET2006-18b	1	49.07	1.52	14.71	12.62	0.48	4.45	7.73	4.23	2.29	n.d.	n.d.	1.13	98.23	38.6	0.53	3.9	70.76
ET2006-7 embayments	2	47.77 (±0.01)	1.87 (±0.07)	16.25 (±0.28)	10.61 (±0.36)	0.25 (±0.02)	3.40 (±0.08)	8.54 (±0.01)	4.35 (±0.17)	3.30 (±0.01)	n.d.	n.d.	0.88 (±0.17)	97.22	36.36	0.50		81.08
ET2006-E2 embayments	1	49.90	1.97	15.86	10.41	0.19	4.05	7.88	3.26	3.05	n.d.	n.d.	0.85	97.42	40.95	0.50		70.19
ET2008/9-1	9	48.64 (±0.27)	2.02 (±0.11)	16.60 (±0.20)	9.16 (±0.40)	0.20 (±0.10)	4.06 (±0.05)	8.56 (±0.20)	4.61 (±0.13)	2.76 (±0.17)	n.d.	n.d.	0.93 (±0.19)	97.54	44.14	0.52	4.5	75.24
ET2008/9-10a	1	48.30	1.71	14.65	9.32	0.19	2.99	9.56	5.15	2.46	n.d.	n.d.	0.79	95.12	36.38	0.65	5.4	68.72
ET2008/9-10b	1	49.77	1.54	14.67	9.81	0.18	3.26	8.17	5.64	3.04	n.d.	n.d.	1.1	97.18	37.2	0.56	6.5	69.49
ET2008/9-5	7	48.47 (±0.77)	1.83 (±0.17)	16.18 (±0.27)	9.34 (±0.64)	0.17 (±0.10)	4.43 (±0.13)	8.74 (±0.48)	4.74 (±0.30)	3.34 (±0.22)	n.d.	n.d.	0.84 (±0.14)	98.08	45.81	0.54	6.2	76.52
ET2008/9-6a	3	55.33 (±0.30)	0.95 (±0.13)	17.98 (±0.26)	7.51 (±0.72)	0.18 (±0.07)	2.53 (±0.02)	7.67 (±0.33)	4.39 (±0.06)	3.45 (±0.13)	n.d.	n.d.	1.15 (±0.20)	101.14	37.52	0.43	4.4	69.77
ET2008/9-6b	7	45.12 (±0.32)	1.74 (±0.08)	16.06 (±0.23)	10.01 (±0.47)	0.17 (±0.12)	3.37 (±0.12)	9.97 (±0.19)	4.95 (±0.06)	3.14 (±0.10)	n.d.	n.d.	0.83 (±0.16)	95.36	37.5	0.62	4.0	69.77
ET2008/9-7a	1	52.49	1.32	17.28	7.50	0.08	2.47	7.73	5.12	3.42	0.03	0.09	1.21	98.62	36.99	0.45	4.7	69.34
ET2008/9-7b	2	48.90 (±0.11)	2.27 (±0.07)	16.14 (±0.44)	7.99 (±0.03)	0.21 (±0.11)	2.64 (±0.04)	9.62 (±0.54)	5.41 (±0.22)	4.05 (±0.27)	n.d.	n.d.	1.13	98.36	37.07	0.60	4.3	69.34
ET2008/9-8	2	46.12 (±0.10)	1.43 (±0.21)	14.80 (±0.49)	4.89 (±0.58)	0.14 (±0.13)	2.37 (±0.05)	5.36 (±0.37)	5.34 (±0.09)	4.71 (±0.29)	n.d.	n.d.	0.74 (±0.20)	85.90	46.35	0.36	3.1	76.85
ET2008/9-9b	7	44.57 (±0.40)	1.64 (±0.17)	14.58 (±0.40)	11.91 (±0.52)	0.22 (±0.09)	7.60 (±0.86)	8.41 (±0.37)	4.41 (±0.12)	2.88 (±0.11)	n.d.	n.d.	0.60 (±0.10)	96.82	53.22	0.58	10.3	81.38

ET2008/9-11	1	52.17	1.30	17.36	8.45	0.35	2.79	8.75	4.44	2.69	0.06	0.02	1.07	99.37	37.05	0.50	5.6	69.37
ET2008/9-12a	1	56.03	1.27	17.95	5.06	0.11	2.42	5.36	5.07	3.03	0.03	n.d.	n.d.	96.3	45.97	0.30	0	68.90
ET2008/9-12b	1	54.77	0.94	17.25	6.71	0.18	2.12	6.71	5.32	2.93	n.d.	n.d.	1.13	98.06	36.03	0.39	3.3	68.90
ET2008/9-16	1	52.76	0.90	15.77	9.44	0.24	3.36	7.02	4.65	3.43	n.d.	n.d.	0.84	98.41	38.82	0.45	6.0	70.91
ET2008/9-18	1	47.49	1.15	15.13	9.92	0.07	5.41	8.96	5.21	3.30	n.d.	n.d.	0.72	97.36	49.29	0.59	7.9	78.89
ET2008/9-23	1	50.47	1.31	14	12.26	0.24	4.05	8.69	3.99	2.70	n.d.	n.d.	0.69	98.4	37.06	0.62	6.6	69.36
ET2013-1	5	49.54 (±0.58)	1.27 (±0.14)	19.31 (±0.32)	6.84 (±0.29)	0.09 (±0.07)	2.77 (±0.05)	7.23 (±0.18)	6.14 (±0.16)	3.65 (±0.13)	n.d.	n.d.	1.26 (±0.26)	98.1	41.92	0.37	3.2	73.46
ET2013-2a	2	46.95 (±0.70)	1.94 (±0.05)	17.65 (±0.15)	7.66 (±0.02)	0.12 (±0.02)	3.81	10.23 (±0.04)	5.38 (±0.25)	2.57 (±0.15)	n.d.	n.d.	1.10 (±0.24)	97.41	47	0.58	4.3	77.28
ET2013-2b	1	46.74	1.2	19.21	5.99	0.03	2.97	4.95	6.95	4.08	n.d.	n.d.	1.29	93.41	46.92	0.26	4.5	77.28
ET2013-3a	3	50.47 (±0.49)	1.35 (±0.11)	17.25 (±0.27)	8.04 (±0.20)	0.17 (±0.13)	2.77 (±0.03)	7.67 (±0.08)	5.35 (±0.18)	3.48 (±0.11)	n.d.	n.d.	0.97 (±0.29)	97.52	38.05	0.44	3.1	70.26
ET2013-3b	5	51.06 (±0.46)	1.41 (±0.12)	17.34 (±0.13)	7.74 (±0.46)	0.12 (±0.10)	2.67 (±0.07)	6.66 (±0.10)	5.85 (±0.06)	3.12 (±0.10)	n.d.	n.d.	1.22 (±0.22)	97.19	38.08	0.38	2.4	70.26
ET2013-3c	1	52.09	1.12	18.27	6.51	0.20	2.24	7.20	5.37	3.85	n.d.	n.d.	1.20	98.05	38.02	0.39	2.4	70.26
ET2013-4	5	52.14 (±0.40)	1.72 (±0.08)	17.74 (±0.10)	6.48 (±0.22)	0.09 (±0.05)	2.61 (±0.06)	6.84 (±0.11)	5.64 (±0.09)	3.83 (±0.16)	n.d.	n.d.	0.58 (±0.12)	97.67	41.79	0.39	1.9	73.47
ET2013-6a	5	49.16 (±0.30)	1.26 (±0.13)	17.15 (±0.01)	8.64 (±0.34)	0.13 (±0.09)	2.96 (±0.01)	9.28 (±0.07)	5.50 (±0.03)	2.36 (±0.02)	n.d.	n.d.	0.82 (±0.08)	97.26	37.91	0.54	2.0	70.14
ET2013-6b	5	49.52 (±0.18)	1.12 (±0.07)	17.28 (±0.24)	8.60 (±0.20)	0.16 (±0.06)	2.94 (±0.04)	8.70 (±0.13)	5.65 (±0.07)	2.26 (±0.08)	n.d.	n.d.	0.89 (±0.22)	97.12	37.86	0.50	2.4	70.14
ET2013-7a	3	53.99 (±0.36)	1.19 (±0.04)	19.40 (±0.22)	5.98 (±0.33)	0.10 (±0.09)	1.98 (±0.04)	3.42 (±0.08)	6.02 (±0.13)	4.26 (±0.18)	n.d.	n.d.	0.38 (±0.20)	96.72	37.12	0.18	3.0	68.17
ET2013-7b	2	51.93 (±0.44)	2.01 (±0.10)	17.47 (±0.03)	7.13 (±0.22)	b.d.l.	2.23 (±0.06)	7.56 (±0.02)	5.41 (±0.09)	3.33 (±0.07)	n.d.	n.d.	1.24 (±0.18)	98.58	35.8	0.43	1.0	68.17
ET2013-7c	2	51.90 (±0.29)	0.83 (±0.16)	17.83 (±0.06)	7.09 (±0.27)	0.09 (±0.07)	2.21 (±0.09)	7.17 (±0.16)	6.49 (±0.13)	3.30 (±0.16)	n.d.	n.d.	1.07 (±0.34)	97.98	35.72	0.40	1.4	68.17
ET2013-7n	2	54.46 (±0.18)	1.21 (±0.08)	19.79 (±0.18)	5.76 (±0.27)	0.10 (±0.01)	1.92 (±0.02)	3.25 (±0.02)	7.59 (±0.03)	3.85 (±0.01)	n.d.	n.d.	0.36 (±0.02)	98.29	37.27	0.16	2.5	69.62
ET2013-11	5	51.72 (±0.21)	1.12 (±0.14)	20.40 (±0.19)	4.30 (±0.23)	0.10 (±0.05)	2.55 (±0.05)	4.21 (±0.07)	6.85 (±0.10)	4.95 (±0.11)	n.d.	n.d.	1.06 (±0.15)	97.26	51.39	0.21	2.1	80.30
ET2013-12	1	49.91	1.18	17.43	8.26	0.27	2.96	7.96	5.47	3.20	n.d.	n.d.	1.04	97.68	38.98	0.46	4.4	71.10
ET2013-12	1	46.72	1.01	16.8	6.53	0.08	2.34	7.57	5.40	3.31	n.d.	n.d.	0.65	90.41	38.98	0.45	4.1	71.10
ET2013-12	3	52.84 (±0.61)	0.702 (±0.09)	18.53 (±0.17)	5.89 (±0.12)	b.d.l.	2.11 (±0.06)	3.92 (±0.08)	6.08 (±0.13)	5.63 (±0.10)	n.d.	n.d.	1.05 (±0.14)	96.84	38.97	0.21	2.8	71.10

ET2013-12	1	50.15	1.13	17.8	6.66	0.12	2.39	7.89	5.73	3.26	n.d.	n.d.	1.06	96.19	39.01	0.44	2.6	71.10
ET2013-14	7	52.78 (±0.61)	2.07 (±0.09)	18.21 (±0.18)	5.86 (±0.39)	0.12 (±0.09)	2.45 (±0.02)	7.60 (±0.06)	4.73 (±0.08)	3.96 (±0.16)	n.d.	n.d.	1.07 (±0.12)	98.85	42.7	0.42	2.2	74.18
ET2013-14	5	47.26 (±0.55)	1.96 (±0.06)	17.88 (±0.18)	5.87 (±0.25)	0.14 (±0.09)	2.46 (±0.05)	9.63 (±0.10)	4.27 (±0.06)	3.67 (±0.14)	n.d.	n.d.	0.95 (±0.16)	94.09	42.76	0.54	1.6	74.18
ET2013-16	5	52.34 (±0.24)	2.51 (±0.08)	16.95 (±0.12)	6.35 (±0.19)	b.d.l.	3.05 (±0.02)	5.78 (±0.16)	5.30 (±0.04)	4.79 (±0.16)	n.d.	n.d.	1.03 (±0.14)	98.19	46.13	0.34	3.2	76.69
ET2013-17a	5	50.14 (±0.42)	1.54 (±0.10)	17.69 (±0.17)	7.81 (±0.52)	0.21 (±0.17)	2.58 (±0.04)	7.28 (±0.07)	5.92 (±0.08)	3.09 (±0.16)	n.d.	n.d.	1.14 (±0.21)	97.4	37.06	0.41	0.6	69.40
ET2013-17b	5	48.84 (±0.46)	1.94 (±0.11)	16.91 (±0.20)	7.78 (±0.27)	0.16 (±0.12)	2.57 (±0.05)	7.44 (±0.07)	5.15 (±0.11)	3.27 (±0.07)	n.d.	n.d.	1.29 (±0.13)	95.35	37.06	0.44	1.2	69.40
ET2013-17c	1	51.65	1.88	17.42	7.28	0.06	2.41	6.82	5.15	3.90	n.d.	n.d.	1.11	97.68	37.11	0.39	3.2	69.40
ET2013-17d	1	50.39	1.37	19.04	7.04	0.24	2.33	8.19	5.45	2.89	n.d.	n.d.	0.71	97.65	37.11	0.43	2.2	69.40
ET2013-19a	5	50.55 (±0.33)	2.23 (±0.13)	17.15 (±0.25)	5.99 (±0.41)	0.17 (±0.05)	2.41 (±0.05)	7.84 (±0.16)	5.24 (±0.11)	3.99 (±0.12)	n.d.	n.d.	1.13 (±0.09)	96.7	41.77	0.46	1.8	73.39
ET2013-27	1	51.98	1.1	20.78	5.05	0.12	2.52	4.26	8.15	4.15			0.84	98.95	47.08	0.21	1.9	77.42
ET2013-30	2	45.61 (±2.25)	1.44	18.24 (±0.01)	7.13 (±0.04)	0.15 (±0.11)	2.66 (±0.07)	7.96	5.82 (±0.26)	3.00 (±0.09)	b.d.l.	b.d.l.	0.83 (±0.14)	92.84	39.94	0.44	3.3	71.87
ET2013-32	2	48.16 (±0.39)	1.69 (±0.14)	16.53 (±0.34)	7.44 (±0.30)	0.18 (±0.09)	2.71 (±0.03)	7.28 (±0.03)	5.75 (±0.02)	3.45 (±0.03)	b.d.l.	b.d.l.	1.11 (±0.23)	94.3	39.37	0.44	1.9	71.51
ET2013-34	1	51.47	1.49	19.16	6.23	0.17	2.21	4.98	6.06	3.67	n.d.	n.d.	0.96	96.4	38.74	0.26	2.8	70.97
ET2013-36	2	52.09 (±1.43)	1.10 (±0.62)	20.08 (±0.63)	5.93 (±1.13)	b.d.l.	2.18 (±0.20)	4.72	7.21 (±0.14)	4.34 (±0.01)	n.d.	n.d.	0.94 (±0.01)	98.64	39.59	0.24	1.8	71.58
ET2013-37	1	50.51	1.75	17.85	6.44	0.23	2.66	7.30	6.80	4.37	n.d.	n.d.	0.73	98.64	42.41	0.41	1.3	73.93
ET2013-41	2	51.37 (±0.03)	0.87 (±0.05)	20.67 (±0.10)	4.30 (±0.01)	b.d.l.	2.18 (±0.12)	4.00 (±0.06)	7.24 (±0.14)	5.47 (±0.29)	b.d.l.	b.d.l.	0.83 (±0.10)	97.02	47.47	0.19	1.8	77.70

b.d.l. = below detection limit; n.d. = not determined

Table A3.8 - Oxide inclusions in olivine (ol) and/or melt inclusions (MI).

sample name	Inside	SiO_2	TiO_2	Al_2O_3	FeO	MnO	MgO	CaO	Na_2O	K_2O	Cr_2O_3	NiO	tot	Cr#[a]	Usp%[b]	Fo mol.% [c]
Spa-4n	ol	0.10	2.06	14.13	36.09	0.04	11.36	b.d.l.	b.d.l.	b.d.l.	36.13	0.04	99.95	63.17		86.85
Spa-4n	ol	0.13	1.91	14.26	37.10	0.37	11.67	b.d.l.	b.d.l.	b.d.l.	34.52	b.d.l.	99.96	61.89		86.85
Spa-T	ol	0.07	0.90	12.95	27.00	0.17	12.43	0.10	b.d.l.	b.d.l.	46.23	b.d.l.	99.85	70.54		87.42
FS-06c	MI	16.46	0.41	4.61	18.66	0.30	29.29	0.52	0.05	0.09	29.29	0.34	100.02	81.00		90.11
FS-26 (2)	MI	12.44	0.78	7.77	22.75	0.36	14.26	2.63	0.11	0.11	38.64	b.d.l.	99.84	77.79		89.96
FS-21 (2)	MI	0.37	0.65	9.74	24.52	0.34	13.2	0.20	0.02	b.d.l.	50.86	0.01	99.90	78.23		90.17
FS-D	MI	5.62	0.61	7.50	22.03	0.09	17.45	0.20	b.d.l.	b.d.l.	46.38	b.d.l.	99.88	80.58		90.60
FS-D	ol	0.10	0.70	10.74	22.50	0.19	13.33	0.05	0.02	0.02	52.26	0.09	100.0	76.55		90.60
ET2002/3S-26 (2)	ol	0.12	13.13	6.01	73.50	0.54	6.54	0.03	b.d.l.	b.d.l.	0.11	b.d.l.	99.97		35.83	72.57
ET2002/3S-29b	ol	0.67	7.54	5.09	81.42	0.58	4.35	0.09	0.1	b.d.l.	0.02	b.d.l.	99.86		20.87	69.64
ET2002/3S-31	ol	0.11	13.01	8.41	73.26	0.41	4.44	b.d.l.	b.d.l.	b.d.l.	0.30	b.d.l.	99.94		42.93	69.77
ET2002/3S-32	ol	0.12	10.75	7.04	75.11	0.45	6.29	0.06	b.d.l.	b.d.l.	0.06	0.07	99.95		29.99	72.90
ET2006-4	ol	0.13	11.59	7.06	75.43	0.59	5.05	0.04	b.d.l.	b.d.l.	0.12	b.d.l.	100.01		34.49	70.48
ET2006-B5 (3)	ol	0.14	9.15	8.42	73.54	0.35	6.92	0.02	0.02	b.d.l.	1.23	0.09	99.87		26.81	80.24
ET2008/9-16	ol	0.12	4.97	5.32	84.92	0.58	3.55	0.09	b.d.l.	0.08	b.d.l.	b.d.l.	99.63		13.74	70.91
ET2008/9-18	ol	0.05	13.72	5.63	74.55	0.53	5.25	b.d.l.	b.d.l.	b.d.l.	b.d.l.	b.d.l.	99.73		38.95	78.89
ET2008/9-23	ol	0.18	7.78	5.52	81.12	0.38	4.32	0.04	b.d.l.	b.d.l.	b.d.l.	b.d.l.	99.34		21.73	69.36
ET2013-1	MI	0.08	19.10	8.22	65.9	0.45	5.86	b.d.l.	b.d.l.	b.d.l.	0.30	b.d.l.	99.91		62.62	73.46
ET2013-3a	MI	0.11	14.76	6.72	72.42	0.66	4.99	0.08	b.d.l.	b.d.l.	0.17	b.d.l.	99.91		44.83	70.26

ET2013-6a	MI	0.10	11.10	8.61	73.45	0.52	4.89	0.10	b.d.l.	b.d.l.	0.90	0.16	99.83		36.32	70.14
ET2013-30	ol	0.18	20.12	3.51	69.49	0.48	5.67	0.06	0.02	b.d.l.	0.21	0.25	99.99		55.68	71.87
ET2013-32	ol	0.38	11.48	5.69	76.76	0.40	5.18	b.d.l.	b.d.l.	b.d.l.	0.11	b.d.l.	100.0		32.58	71.51
ET2013-34	ol	0.05	22.36	4.30	66.98	0.62	5.43	0.11	b.d.l.	b.d.l.	0.06	b.d.l.	99.91		64.55	70.97

[a]Cr# = Cr number, calculated as Cr_2O_3/Al_2O_3 molar ratio.

[b]Usp % = Composition of solid solution between magnetite [$Fe^{3+}(Fe^{2+}Fe^{3+}O_4)$] and ulvospinel [$Fe^{2+}(Fe^{2+}TiO_4)$], calculated using Stormer (1983)

[c]Fo mol = Fo content of the host olivine.

b.d.l. = below the detection limit

Table A3.9 - Chemical composition of some sulfide globules inside the 2013 melt inclusions and 2008 olivine phenocryst.

sample name	Inside	Si	S	Fe	Co	Ni	Cu	Total	Fo mol.% [a]
ET2013-1	MI	0.13	33.57	50.10	b.d.l.	0.59	15.61	100.0	73.46
ET2013-3b	MI	0.04	30.95	34.83	b.d.l.	0.37	33.82	100.0	70.26
ET2013-14	ol	0.13	32.85	45.68	b.d.l.	2.82	18.52	100.0	74.18
ET2008/9-12	ol	0.03	30.39	69.56	n.d.	n.d.	n.d.	99.9	68.90

All data as reported as atomic weight %, for each elements.

[a]Fo mol = Fo content of the host olivine

b.d.l. = below the detection limit; n.d. = not determined

A4. Melt inclusions: correction for Post entrapment crystallization (PEC)

Silicate melt inclusions are small drops of silicate melt entrapped in different minerals during their growth at different depth inside the magmatic system. For this reason, they provide a unique possibility of reconstructing the chemical composition of the magma at specific stages of its evolution, from its formation at mantle depth through ts ascent toward the surface. This depends on the assumption that inclusions behave as closed and isolated systems after their formation (Frezzotti, 2001).

After trapping, the cooling of an inclusion produces the crystallization of an olivine rim on the walls of the inclusion, and this consequently depletes the residual melt in MgO and FeO. The crystallizing olivine rim is progressively enriched in FeO and depleted in MgO, due to the evolution of the melt, resulting in a compositional gradient within the rim. The existence of this compositional gradient causes the reequilibration of the inclusion with its host, by diffusion of Fe out of, and Mg into the initial volume of the inclusion. This leads to a rapid decrease in the Fe content of the residual melt inside the inclusion, a process referred to as "Fe loss" by Danyushevsky et al. (2000). During a fast cooling there is not enough time for a complete reequilibration, and diffusion profiles can be preserved in the melt inclusion and its olivine rim.

For reconstructing the initially trapped melt composition, Danyushevsky and Plechov (2011) created the "PETROLOG3" software. This algorithm simulates the exchanges of Fe and Mg between the entrapped melt and the olivine, which occur during the reequilibration process. For the calculation, this software requires the composition of the entrapped melt, of the host olivine (Fo mol %) and FeO* content of the trapped melt.
The optimal FeO* content to use has to be calculated, through modelling diffusive reequilibration during "Fe loss" using the same PETROLOG3 software. Redox conditions have to be know because fO_2 needs to be fixed in Petrolog3.

A simpler method for reconstructing the initially trapped melt composition, largely used in other studies (Métrich et al., 2004; Spilliaert et al., 2006a), is to assume the equilibrium between the host olivine and the melt inclusion: this consists in adding olivine to the melt (entrapped as inclusion) until reaching the equilibrium composition dictated by the Mg-Fe exchange coefficient:

$$K_D = [(FeO/MgO)_{ol}/(FeO/MgO)_{melt}]$$

where Fe can be Fe^{2+} or total Fe, and the K_D will therefore be 0.30-0.29 (Métrich and Clocchiatti, 1996) or 0.26 (Di Carlo et al., 2006).
In the first case, constraints on the redox conditions are required because the Fe_2O_3/FeO ratio in the melt is needed, but not in the second case. We corrected 17 melt inclusions of the FS eruption using the three methods (fixing for two of them fO_2 at NNO+0.5), and we compare the results in figure A4.1.
The reconstructed melt inclusion compositions are similar between the three methods, and are also very close to the FS inclusions previously studied by Kamenetsky et al. (2007), corrected using the PETROLOG software (Danyushevsky, 2001). In particular, MgO contents corrected using PETROLOG3 and the K_D=0.26 method are very similar for all

inclusions (either slightly or importantly recrystallized), we therefore preferred to use the latter to correct the composition of all melt inclusions for post entrapment crystallization, due to its significantly easier application.
The post entrapment crystallization (PEC) % is calculated as $[1-(K_2O_{corr}/ K_2O_{uncorr})]*100$.

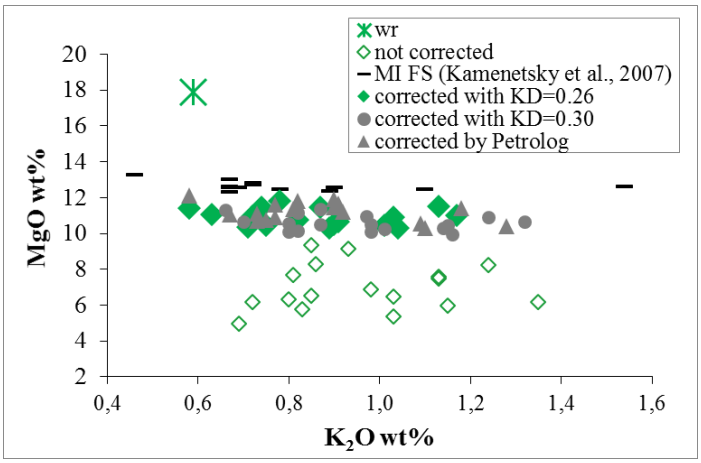

Fig. A4.1 - MgO and K_2O content in some melt inclusions from FS eruption. In the graph the originally measured (by EMP) contents, and the corrected (by PETROLOG3 and olivine-liquid equilibrium calculations. as described in the text) values are shown. (All data are normalized to 100%).

A5. Volatiles (H_2O. CO_2. S. Cl) content: methods comparison

In order to determine volatile contents in etnean melt inclusions with the highest precision, several methods were tested. The experimental glasses have been very useful to discriminate and evaluate the reliability of the different analytical techniques.

S contents were determined both in the experimental glasses and in the melt inclusions by electron microprobe (EMP) at the ISTO-CNRS and by secondary ion mass spectrometry (SIMS) at the CRPG of Nancy. The comparison between the values measured with the two techniques is shown in figure A5.1, for the experimental samples (fig. A5.1a), and for the melt inclusions (fig. A5.1b). Data for melt inclusions are significantly more scattered than those for experimental glasses, and show no systematic variations between EMP and SIMS analyses (fig. A5.1b). On the contrary, experimental data show a systematic overestimation of SIMS data, respect to EMP data, for S contents > 2000 ppm, and a good agreement for lower S contents (fig. 5A.1a).
We checked that no sulfur was lost during EMP analyses, by measuring S counts/second as function of time (fig. A5.2a) in the S-richest experimental glass (SPA1902#2), using a beam energy higher than that normally used for S acquisition (20 keV versus 15 keV, see paragraph 3.4 for EMP analytical conditions). This test confirms that no sulfur loss occurred during electron microprobe analysis. We conclude that the overestimation by SIMS of S contents >2000 ppm, if any, could be due to the low S contents (130-1406 ppm, see paragraph 3.5) of the reference glasses used for SIMS acquisitions. MORB standard (see

paragraph 3.4) were also used to estimate the S contents in some melt inclusions by EMP (fig. A5.2 b-c). These data (S = 0-4000 ppm) are in agreement with the common EMP contents and with SIMS S contents <1000 ppm. In our study we therefore prefer to consider S abundances determined by EMP that, although less precise (standard deviation: 87-410 ppm for experimental glasses) than SIMS data (standard deviation: 7-93 ppm), are more easily obtained. For S contents lower than 450 ppm (that is the major detection limits of EMP measurements), when available, SIMS data are preferred.

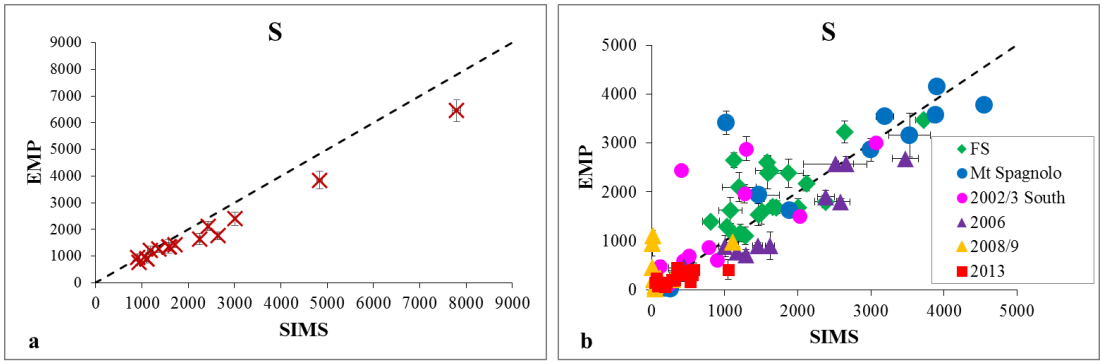

Fig. A5.1 - a) S contents (in ppm) of the experimental glasses determined by EMP and SIMS. b) S contents (in ppm) of the studied melt inclusions determined by EMP and SIMS. The dashed line indicates the 1:1 line; error bars indicate the standard deviation.

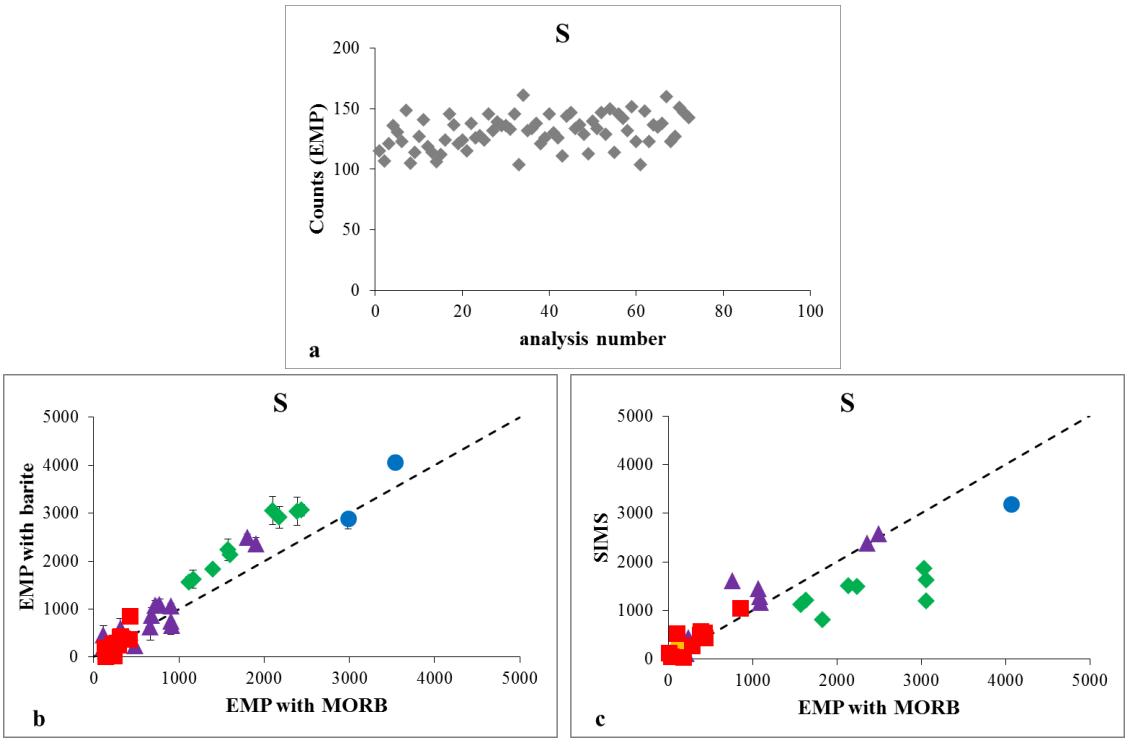

Fig. A5.2 - a) EMP sulfur loss test carried out in the SPA 1902#2 experimental glasses, using a beam energy of 20 keV. b-c) EMP S contents determined with MORB standard compared with the common EMP data (barite standard) and with SIMS S contents. (For the symbols, see the legend of fig A5.1). The dashed line indicates the 1:1 line; error bars indicate the standard deviation.

Chlorine contents in melt inclusions were also measured by both EMP and SIMS and show a similar behavior to S: a large scatter and no systematic variations between SIMS and EMP data (fig. A5.3).

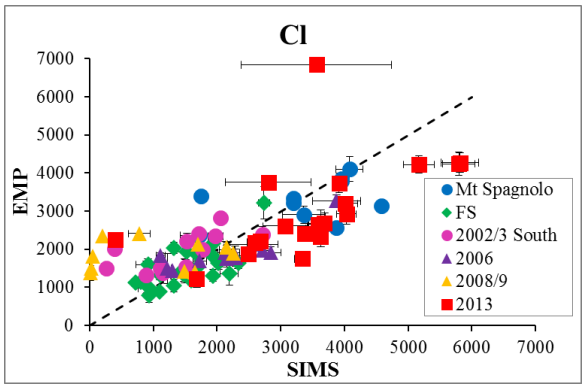

Fig. A5.3 - Cl contents of the studied melt inclusions determined by EMP and SIMS analyses. The dashed line indicates 1:1 line; error bars indicate the standard deviation.

H_2O contents in melt inclusions and experimental glasses were determined by both SIMS and Infrared spectroscopy (FTIR). H_2O contents in experimental glasses, estimated by both methods, are reported figure A.5.4a. Both datasets have similar standard deviations (SIMS: 0-0.22 wt.%, n. analysis: 5; FTIR: 0-0.27 wt.% n. analysis: 3-7), but the measured H_2O content are sometimes substantially different.

We therefore performed two tests on few experimental glasses, using Raman spectroscopy at the University of Nantes and EMP at ISTO-CNRS, in order to verify which are the more reliable estimations.

Micro-Raman spectra were acquired on a Jobin-Yvon Labram HR800 equipped with a solid-state diode laser operating at 532 nm. The Labram HR800 spectrometer is equipped with an 1800 grooves/mm grating allowing a spectral resolution on the order of 0.4 cm^{-1}. Analyses were performed in confocal mode, using x50 Olympus objectives. The spectral range covered was between 2500 and 3900 cm-1. The spectral frequency position was calibrated using the emission lines of Ne- and Hg-lamps. The output power was set to 60 mW. For each spectrum, we performed X scans on a given sample with an acquisition time of X to X s each. H_2O contents were calculated using the calibration of Mercier et al., 2009. H_2O abundances were also estimated by EMP using the "by difference method - WBD" from the totals of the microprobe analyses (Devine et al., 1995), using 4 standards of similar composition and H_2O contents (Stromboli glasses with 0, 3.2, 4.6, 5.1 wt.% H_2O). The results from these tests are reported in figure A5.4. There are no clear systematic relations between the data obtained with the different methods (fig. A5.4), a generally good agreement is however observed between SIMS and Raman data (fig. A5.4b). EMP data are similar to both SIMS (fig. A5.4c) and FTIR data, within the standard deviation.

CO_2 contents in the experimental glasses were estimated also by SIMS and FTIR (fig. A5.5a). Data SIMS are characterized by lower standard deviation (8-27 ppm) than those by FTIR (85-146 ppm). CO_2 SIMS measurement are also characterized by a low instrumental error (about 15 ppm), even if this can to be higher. In fact, SIMS acquisition for CO_2 - free experimental glasses show a minimum of CO_2 contents (around 141 ± 55 ppm). The two data set are not in good agree. Unfortunately, only 4 melt inclusions are analyzed by FTIR and SIMS (fig. A5.5b), and as for the experimental glasses, CO_2 contents are not in agree. For the experimental products, we have any explication for these discrepancies, while for melt inclusions, we suggest that the highest SIMS CO_2 contents are possibly contaminated by the not perfect cleaning of carbon used for the previous EMP analyses.

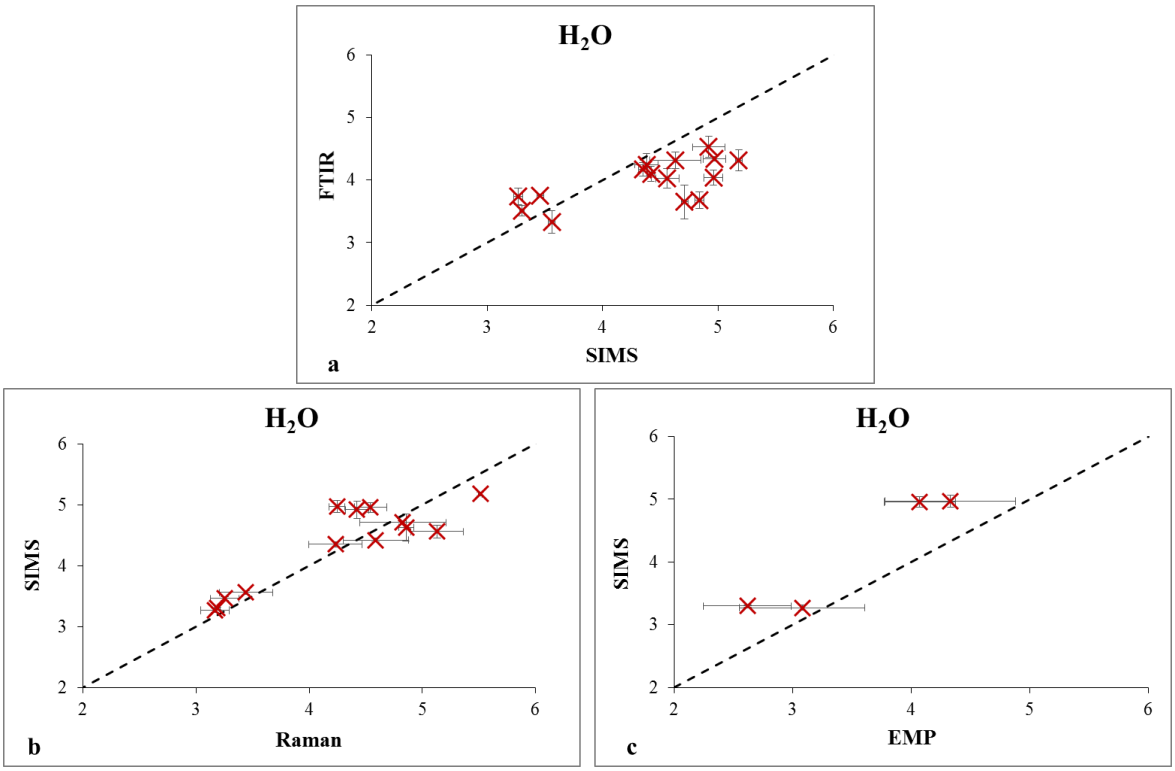

Fig A5.4 - H_2O contents (reported in wt.%) in the experimental glasses determined by several methods: a) FTIR versus SIMS; b) SIMS versus Raman; c) SIMS) versus EMP.
Dashed lines indicate the 1:1 line; error bars indicate the standard deviation.

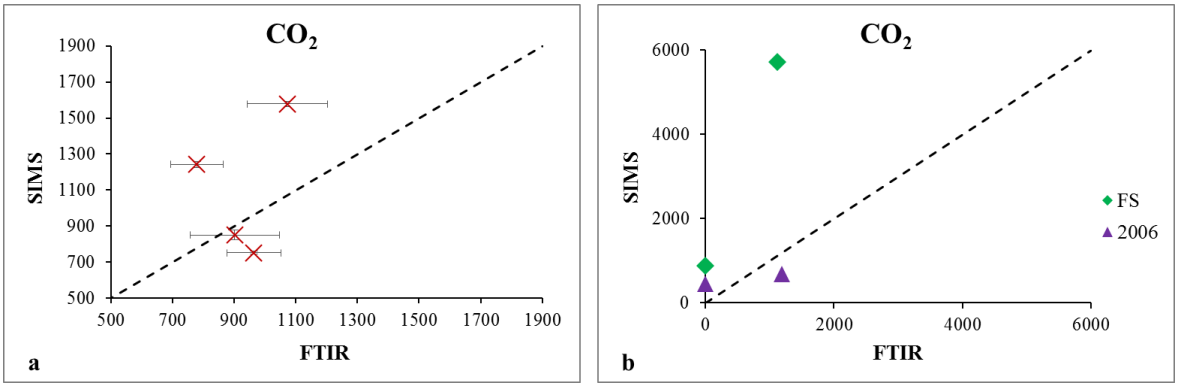

Fig. A5.5 - CO_2 content (reported in ppm) in the 4 experimental glasses containing CO_2 (a), and in some melt inclusions (b) determined by infrared spectroscopy (FTIR) and by secondary ionic mass spectrometer (SIMS).
Dashed line indicates 1:1 correspondence; error bars indicate the standard deviation.

Anyway, we think that SIMS data are affected by a lower uncertainty respect to the FTIR method, which depends on several parameters hard to define (thickness, density, and absorption coefficient, see paragraph 3.6). We therefore prefer SIMS data, when available (e.g. for the experimental glasses). The melt inclusions have been analyzed by both methods (depending on the different preparation procedures), consequently we used both datasets in the discussions (from SIMS and FTIR measurements).

A6. MELTS calculation

In order to explain the whole range of FeO* content (4.3-12.6 wt.%) measured in Etnean melt inclusions and to check the effect of pressure, oxygen fugacity and water on the iron content, we performed MELTS calculations in different P-T-fO_2 conditions and initial H_2O content, using the same FS composition. The major effect is shown by the used oxygen fugacity values (fig. A5.6a): the test with an initial lowest fO_2 condition (NNO+1) goes toward the highest FeO* content of 2002/3, 2006 and 2008/9 MIs, while the test performed at the highest fO_2 condition (NNO+2) approaches to the 2013 MIs with the minor FeO* content. The effect of the initial H_2O content and pressure on the residual liquid produced by MELTS fractional crystallization simulations is minor (figs. A5.6 b-c). Anyway, these simulations not reproduce the whole FeO* content range, above all the lowest ones. The figure A5.6d shows the relevant effect of the crystallization of the spinel phase on the FeO* content, independently of the oxygen fugacity.

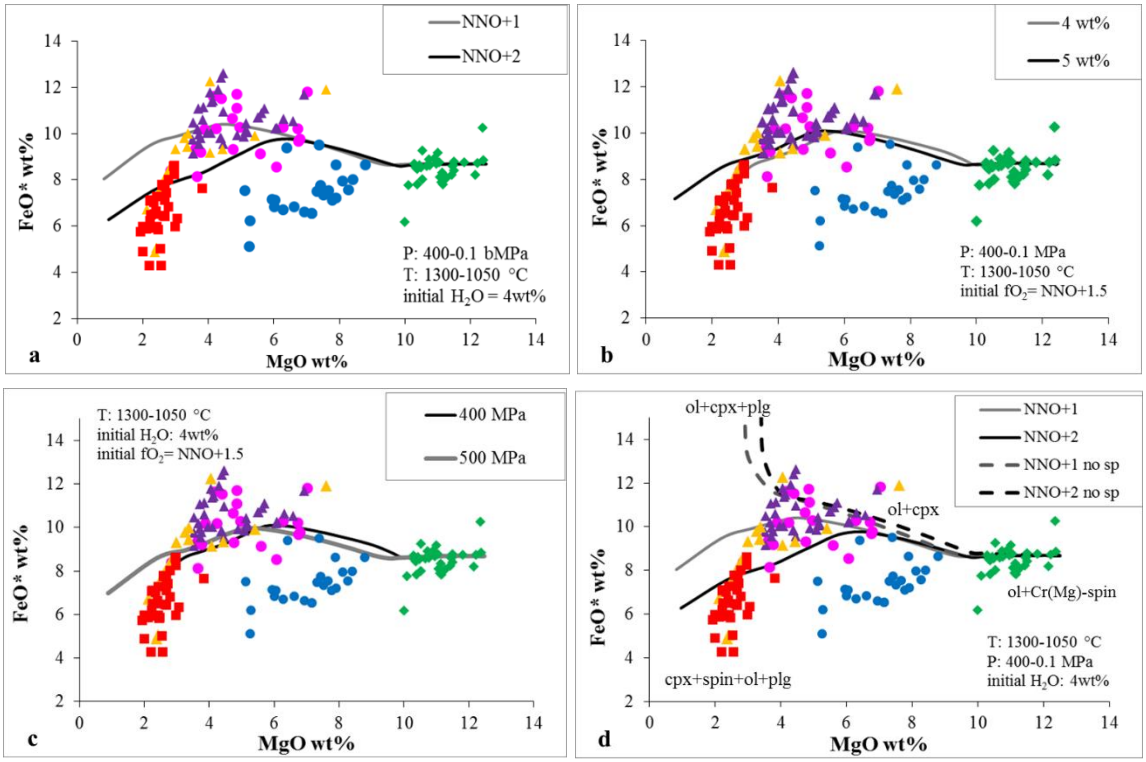

Fig. A5.6 - FeO* (= FeO total) versus MgO of the investigated melt inclusions and those calculated by MELTS code, varying the initial oxygen fugacity (a); the initial water content (b); the initial pressure (c). In the plot d, MELTS calculation at NNO+1 and NNO+2 with and without the spinel crystallization.

Table A.6.1: MELTS simulations performed with an initial fO_2 = NNO+2 and an initial H_2O content of 4 wt.%

High T-P geothermal																						
P (bar)	T (°C)	**Liquid composition**												**liquid %**	**Solid phase percentage (%)**					**water %**	**log fO_2**	**ΔNNO**
		SiO_2	**TiO_2**	**Al_2O_3**	**Fe_2O_3**	**Cr_2O_3**	**FeO**	**MgO**	**CaO**	**Na_2O**	**K_2O**	**P_2O_5**	**H_2O**	**$Fe^{3+}/\Sigma Fe$**	**ol**	**cpx**	**feld**	**sp**	**whitlockite**			
5000	**1300**	46.7	1.1	9.6	3.7	0.1	5.4	12.5	13.7	1.7	0.9	0.3	4.3	0.4	100.0	0.00			0.00		0.00	-4.2	2.1
4900	**1290**	46.7	1.1	9.6	3.7	0.1	5.4	12.5	13.7	1.7	0.9	0.3	4.3	0.4	100.0	0.00			0.00		0.00	-4.4	2.1
4800	**1280**	46.7	1.1	9.6	3.7	0.1	5.4	12.5	13.7	1.7	0.9	0.3	4.3	0.4	100.0	0.00			0.00		0.00	-4.5	2.1
4700	**1270**	46.7	1.1	9.6	3.7	0.1	5.4	12.5	13.7	1.7	0.9	0.3	4.3	0.4	100.0	0.00			0.00		0.00	-4.6	2.1
4600	**1260**	46.7	1.1	9.6	3.7	0.1	5.4	12.5	13.7	1.7	0.9	0.3	4.3	0.4	100.0	0.00			0.00		0.00	-4.7	2.1
4500	**1250**	46.7	1.1	9.7	3.7	0.1	5.4	12.2	13.8	1.7	0.9	0.3	4.3	0.4	99.1	0.82			0.00		0.00	-4.8	2.0
4400	**1240**	46.8	1.1	9.8	3.7	0.1	5.3	11.8	14.0	1.7	0.9	0.3	4.3	0.4	98.2	1.77			0.00		0.00	-4.9	2.0
4300	**1230**	46.9	1.1	9.8	3.7	0.1	5.3	11.4	14.1	1.7	1.0	0.3	4.4	0.4	97.3	2.68			0.05		0.00	-5.0	2.0
4200	**1220**	47.0	1.1	9.9	3.7	0.1	5.3	11.1	14.2	1.8	1.0	0.3	4.4	0.4	96.4	3.56			0.05		0.00	-5.2	2.0
4100	**1210**	47.1	1.1	10.0	3.8	0.1	5.2	10.7	14.4	1.8	1.0	0.3	4.5	0.4	95.5	4.42			0.06		0.00	-5.3	2.0
4000	**1200**	47.1	1.1	10.1	3.8	0.1	5.2	10.4	14.5	1.8	1.0	0.3	4.5	0.4	94.7	5.25			0.06		0.00	-5.4	2.0
Isothermal (almost adiabatic)																						
P (bar)	T (°C)	**Liquid composition**												**liquid %**	**Solid phase percentage (%)**					**water %**	**log fO_2**	**ΔNNO**
		SiO_2	**TiO_2**	**Al_2O_3**	**Fe_2O_3**	**Cr_2O_3**	**FeO**	**MgO**	**CaO**	**Na_2O**	**K_2O**	**P_2O_5**	**H_2O**	**$Fe^{3+}/\Sigma Fe$**	**ol**	**cpx**	**feld**	**sp**	**whitlockite**			
4000	**1200**	47.2	1.1	10.1	3.8	0.1	5.2	10.4	14.5	1.8	1.0	0.3	4.5	0.4	100.0	0.01	0.00		0.00		0.00	-5.4	2.0
3900	**1200**	47.2	1.1	10.1	3.8	0.1	5.2	10.4	14.5	1.8	1.0	0.3	4.5	0.4	100.0	0.00	0.00		0.00		0.00	-5.4	2.0
3800	**1200**	47.2	1.1	10.1	3.8	0.1	5.2	10.4	14.5	1.8	1.0	0.3	4.5	0.4	100.0	0.00	0.00		0.00		0.00	-5.4	2.0
3700	**1200**	47.2	1.1	10.1	3.8	0.1	5.2	10.4	14.5	1.8	1.0	0.3	4.5	0.4	100.0	0.00	0.00		0.00		0.00	-5.4	2.0
3600	**1200**	47.2	1.1	10.1	3.8	0.1	5.2	10.4	14.5	1.8	1.0	0.3	4.5	0.4	100.0	0.00	0.00		0.00		0.00	-5.4	2.0
3500	**1200**	47.2	1.1	10.1	3.8	0.1	5.2	10.4	14.5	1.8	1.0	0.3	4.5	0.4	100.0	0.00	0.00		0.00		0.00	-5.4	2.0
3400	**1200**	47.2	1.1	10.1	3.8	0.1	5.2	10.4	14.5	1.8	1.0	0.3	4.5	0.4	100.0	0.00	0.00		0.00		0.00	-5.5	2.0
3300	**1200**	47.2	1.1	10.1	3.8	0.1	5.2	10.4	14.5	1.8	1.0	0.3	4.5	0.4	100.0	0.00	0.00		0.00		0.00	-5.5	2.0
3200	**1200**	47.2	1.1	10.1	3.8	0.1	5.2	10.4	14.5	1.8	1.0	0.3	4.5	0.4	100.0	0.00	0.00		0.00		0.00	-5.5	2.0
3100	**1200**	47.2	1.1	10.1	3.8	0.1	5.2	10.4	14.5	1.8	1.0	0.3	4.5	0.4	100.0	0.00	0.00		0.00		0.00	-5.5	2.0
3000	**1200**	47.2	1.1	10.1	3.8	0.1	5.2	10.4	14.5	1.8	1.0	0.3	4.5	0.4	100.0	0.00	0.00		0.00		0.00	-5.5	2.0

2900	**1200**	47.2	1.1	10.1	3.8	0.1	5.2	10.4	14.5	1.8	1.0	0.3	4.5	0.4	100.0	0.00	0.00		0.00		0.00	-5.5	2.0
2800	**1200**	47.2	1.1	10.1	3.8	0.1	5.2	10.4	14.5	1.8	1.0	0.3	4.5	0.4	100.0	0.00	0.00		0.00		0.05	-5.5	2.0
2700	**1200**	47.2	1.1	10.1	3.8	0.1	5.2	10.4	14.5	1.8	1.0	0.3	4.4	0.4	99.9	0.00	0.00		0.00		0.13	-5.5	1.9
2600	**1200**	47.3	1.1	10.1	3.8	0.1	5.2	10.4	14.5	1.8	1.0	0.3	4.3	0.4	99.8	0.00	0.00		0.00		0.22	-5.5	1.9
2500	**1200**	47.3	1.1	10.2	3.8	0.1	5.2	10.4	14.5	1.8	1.0	0.3	4.2	0.4	99.7	0.00	0.00		0.00		0.31	-5.6	1.9
2400	**1200**	47.3	1.1	10.2	3.8	0.1	5.2	10.4	14.6	1.8	1.0	0.3	4.1	0.4	99.6	0.00	0.00		0.00		0.41	-5.6	1.9
2300	**1200**	47.4	1.1	10.2	3.8	0.1	5.2	10.4	14.6	1.8	1.0	0.3	4.0	0.4	99.5	0.00	0.00		0.00		0.50	-5.6	1.9
2200	**1200**	47.4	1.1	10.2	3.8	0.1	5.2	10.4	14.6	1.8	1.0	0.3	3.9	0.4	99.4	0.00	0.00		0.00		0.60	-5.6	1.9
2100	**1200**	47.5	1.1	10.2	3.8	0.1	5.2	10.5	14.6	1.8	1.0	0.3	3.8	0.4	99.4	0.00	0.00		0.00		0.60	-5.6	1.9
2000	**1200**	47.5	1.1	10.2	3.8	0.1	5.2	10.5	14.6	1.8	1.0	0.3	3.7	0.4	99.4	0.00	0.00		0.00		0.60	-5.6	1.9
1900	**1200**	47.6	1.1	10.2	3.8	0.1	5.2	10.5	14.6	1.8	1.0	0.3	3.6	0.4	99.4	0.00	0.00		0.00		0.61	-5.6	1.9
1800	**1200**	47.6	1.1	10.2	3.8	0.1	5.2	10.5	14.6	1.8	1.0	0.3	3.5	0.4	99.4	0.00	0.00		0.00		0.61	-5.6	1.9
1700	**1200**	47.7	1.1	10.2	3.8	0.1	5.2	10.5	14.7	1.8	1.0	0.3	3.4	0.4	99.4	0.00	0.00		0.00		0.61	-5.7	1.9
1600	**1200**	47.7	1.1	10.2	3.8	0.1	5.3	10.5	14.7	1.8	1.0	0.3	3.3	0.4	99.4	0.00	0.00		0.00		0.62	-5.7	1.8
1500	**1200**	47.8	1.1	10.3	3.8	0.1	5.3	10.5	14.7	1.8	1.0	0.3	3.2	0.4	99.4	0.00	0.00		0.00		0.62	-5.7	1.8
1400	**1200**	47.9	1.1	10.3	3.8	0.1	5.3	10.5	14.7	1.8	1.0	0.3	3.1	0.4	99.4	0.00	0.00		0.00		0.62	-5.7	1.8
1300	**1200**	47.9	1.1	10.3	3.8	0.1	5.3	10.6	14.7	1.8	1.0	0.3	2.9	0.4	99.4	0.00	0.00		0.00		0.63	-5.7	1.8
1200	**1200**	48.0	1.1	10.3	3.8	0.1	5.3	10.6	14.8	1.8	1.0	0.3	2.8	0.4	99.4	0.00	0.00		0.00		0.63	-5.7	1.8
1100	**1200**	48.1	1.1	10.3	3.8	0.1	5.3	10.6	14.8	1.8	1.0	0.3	2.7	0.4	99.4	0.00	0.00		0.01		0.64	-5.7	1.8
1000	**1200**	48.1	1.1	10.3	3.8	0.1	5.3	10.6	14.8	1.8	1.0	0.3	2.5	0.4	99.3	0.00	0.00		0.01		0.65	-5.7	1.8
900	**1200**	48.2	1.1	10.3	3.8	0.1	5.3	10.6	14.8	1.8	1.0	0.3	2.4	0.4	99.3	0.00	0.00		0.02		0.65	-5.8	1.8
800	**1200**	48.3	1.1	10.4	3.8	0.1	5.3	10.6	14.8	1.8	1.0	0.3	2.2	0.4	99.3	0.00	0.00		0.03		0.66	-5.8	1.8
700	**1200**	48.4	1.1	10.4	3.8	0.1	5.3	10.7	14.9	1.8	1.0	0.3	2.1	0.4	99.3	0.00	0.00		0.04		0.67	-5.8	1.7
600	**1200**	48.5	1.2	10.4	3.8	0.0	5.3	10.7	14.9	1.8	1.0	0.3	1.9	0.4	99.3	0.00	0.00		0.05		0.68	-5.8	1.7
500	**1200**	48.6	1.2	10.4	3.8	0.0	5.3	10.7	14.9	1.8	1.0	0.3	1.7	0.4	99.2	0.00	0.00		0.07		0.69	-5.8	1.7
400	**1200**	48.7	1.2	10.4	3.9	0.0	5.3	10.7	15.0	1.8	1.0	0.3	1.5	0.4	99.2	0.00	0.00		0.08		0.71	-5.8	1.7
300	**1200**	48.8	1.2	10.6	3.9	0.0	5.4	10.6	14.9	1.9	1.0	0.3	1.3	0.4	97.6	0.00	1.53		0.10		0.75	-5.9	1.7
200	**1200**	48.8	1.2	11.1	3.9	0.0	5.6	10.3	14.4	2.0	1.1	0.3	1.0	0.4	92.6	0.00	6.46		0.14		0.82	-5.9	1.7
100	**1200**	48.8	1.3	11.9	4.0	0.0	5.9	9.7	13.7	2.2	1.2	0.4	0.7	0.4	90.7	0.00	8.18		0.21		0.87	-5.9	1.6

1	**1200**	48.9	1.5	13.4	4.1	0.0	6.4	8.6	12.2	2.6	1.5	0.4	0.1	0.4	82.3	0.00	16.18		0.37		1.15	-6.0	1.6

Geothermal dP/dT = 3 MPa °C^{-1}

P (bar)	T (°C)	liquid composition													liquid %	Solid phase percentage (%)					water %	log fO_2	ΔNNO
		SiO_2	TiO_2	Al_2O_3	Fe_2O_3	Cr_2O_3	FeO	MgO	CaO	Na_2O	K_2O	P_2O_5	H_2O	$Fe^{3+}/\Sigma Fe$		ol	cpx	feld	sp	whitlockite			
4000	**1200**	47.2	1.1	10.1	3.8	0.1	5.2	10.4	14.5	1.8	1.0	0.3	4.5	0.4	100.0	0.01	0.00	0.00	0.00	0.00	0.00	-5.4	2.0
3940	**1198**	47.2	1.1	10.1	3.8	0.1	5.2	10.3	14.5	1.8	1.0	0.3	4.5	0.4	99.9	0.14	0.00	0.00	0.00	0.00	0.00	-5.4	2.0
3880	**1196**	47.2	1.1	10.2	3.8	0.1	5.2	10.3	14.5	1.8	1.0	0.3	4.5	0.4	99.9	0.14	0.00	0.00	0.00	0.00	0.00	-5.5	2.0
3820	**1194**	47.2	1.1	10.2	3.8	0.1	5.2	10.2	14.6	1.8	1.0	0.3	4.5	0.4	99.8	0.14	0.00	0.00	0.01	0.00	0.00	-5.5	2.0
3760	**1192**	47.2	1.1	10.2	3.8	0.1	5.2	10.2	14.6	1.8	1.0	0.3	4.5	0.4	99.8	0.14	0.00	0.00	0.02	0.00	0.00	-5.5	2.0
3700	**1190**	47.2	1.1	10.2	3.8	0.1	5.2	10.1	14.6	1.8	1.0	0.3	4.5	0.4	99.8	0.14	0.00	0.00	0.03	0.00	0.00	-5.5	2.0
3640	**1188**	47.2	1.1	10.2	3.8	0.1	5.2	10.0	14.6	1.8	1.0	0.3	4.5	0.4	99.8	0.14	0.00	0.00	0.04	0.00	0.00	-5.6	2.0
3580	**1186**	47.2	1.1	10.2	3.8	0.1	5.2	10.0	14.6	1.8	1.0	0.3	4.5	0.4	99.8	0.14	0.00	0.00	0.05	0.00	0.00	-5.6	2.0
3520	**1184**	47.3	1.1	10.2	3.8	0.1	5.1	9.9	14.7	1.8	1.0	0.3	4.6	0.4	99.8	0.14	0.00	0.00	0.06	0.00	0.00	-5.6	2.0
3460	**1182**	47.3	1.1	10.3	3.8	0.0	5.1	9.9	14.7	1.8	1.0	0.3	4.6	0.4	99.8	0.14	0.00	0.00	0.07	0.00	0.00	-5.7	2.0
3400	**1180**	47.3	1.1	10.3	3.8	0.0	5.1	9.8	14.7	1.8	1.0	0.3	4.6	0.4	99.8	0.14	0.00	0.00	0.09	0.00	0.00	-5.7	2.0
3340	**1178**	47.3	1.1	10.3	3.8	0.0	5.1	9.8	14.7	1.8	1.0	0.3	4.6	0.4	99.8	0.14	0.00	0.00	0.10	0.00	0.00	-5.7	2.0
3280	**1176**	47.3	1.1	10.3	3.8	0.0	5.1	9.7	14.8	1.8	1.0	0.3	4.6	0.4	99.7	0.14	0.00	0.00	0.11	0.00	0.00	-5.8	2.0
3220	**1174**	47.3	1.1	10.3	3.8	0.0	5.1	9.7	14.8	1.8	1.0	0.3	4.6	0.4	99.7	0.14	0.00	0.00	0.13	0.00	0.00	-5.8	2.0
3160	**1172**	47.3	1.1	10.3	3.8	0.0	5.1	9.6	14.8	1.8	1.0	0.3	4.6	0.4	99.7	0.14	0.00	0.00	0.14	0.00	0.00	-5.8	2.0
3100	**1170**	47.4	1.1	10.4	3.8	0.0	5.1	9.5	14.8	1.8	1.0	0.3	4.6	0.4	99.6	0.12	0.16	0.00	0.16	0.00	0.00	-5.8	2.0
3040	**1168**	47.3	1.1	10.4	3.8	0.0	5.1	9.5	14.8	1.8	1.0	0.3	4.6	0.4	99.1	0.08	0.64	0.00	0.17	0.00	0.00	-5.9	2.0
2980	**1166**	47.3	1.1	10.5	3.8	0.0	5.1	9.4	14.7	1.9	1.0	0.3	4.7	0.4	99.1	0.08	0.64	0.00	0.20	0.00	0.00	-5.9	1.9
2920	**1164**	47.3	1.2	10.5	3.8	0.0	5.1	9.3	14.7	1.9	1.0	0.3	4.7	0.4	99.1	0.08	0.63	0.00	0.22	0.00	0.00	-6.0	1.9
2860	**1162**	47.3	1.2	10.6	3.8	0.0	5.2	9.2	14.6	1.9	1.0	0.3	4.7	0.4	98.3	0.03	1.34	0.00	0.25	0.00	0.07	-6.0	1.9
2800	**1160**	47.3	1.2	10.8	3.8	0.0	5.2	9.1	14.4	1.9	1.1	0.3	4.7	0.4	97.6	0.00	1.94	0.00	0.29	0.00	0.19	-6.0	1.9
2740	**1158**	47.3	1.2	11.0	3.8	0.0	5.3	8.9	14.3	2.0	1.1	0.3	4.7	0.4	97.4	0.00	1.90	0.00	0.34	0.00	0.32	-6.1	1.9
2680	**1156**	47.3	1.2	11.1	3.8	0.0	5.4	8.8	14.2	2.0	1.1	0.3	4.6	0.4	97.3	0.00	1.87	0.00	0.39	0.00	0.44	-6.1	1.9
2620	**1154**	47.3	1.2	11.3	3.8	0.0	5.4	8.6	14.0	2.1	1.1	0.3	4.6	0.4	97.1	0.00	1.84	0.00	0.45	0.00	0.57	-6.2	1.8

2560	**1152**	47.4	1.2	11.5	3.7	0.0	5.5	8.5	13.9	2.1	1.2	0.3	4.6	0.4	97.1	0.00	1.81	0.00	0.50	0.00	0.62	-6.2	1.8
2500	**1150**	47.4	1.2	11.6	3.7	0.0	5.5	8.4	13.7	2.1	1.2	0.3	4.6	0.4	97.0	0.00	1.79	0.00	0.57	0.00	0.62	-6.3	1.8
2440	**1148**	47.4	1.2	11.8	3.7	0.0	5.6	8.2	13.6	2.2	1.2	0.4	4.5	0.4	97.0	0.00	1.76	0.00	0.63	0.00	0.62	-6.3	1.8
2380	**1146**	47.4	1.2	12.0	3.7	0.0	5.6	8.1	13.4	2.2	1.2	0.4	4.5	0.4	96.9	0.00	1.74	0.00	0.70	0.00	0.62	-6.4	1.7
2320	**1144**	47.5	1.2	12.1	3.7	0.0	5.7	8.0	13.3	2.3	1.3	0.4	4.5	0.4	96.9	0.00	1.72	0.00	0.78	0.00	0.62	-6.5	1.7
2260	**1142**	47.5	1.2	12.3	3.7	0.0	5.7	7.8	13.2	2.3	1.3	0.4	4.4	0.4	96.8	0.00	1.70	0.00	0.86	0.00	0.62	-6.5	1.7
2200	**1140**	47.5	1.3	12.5	3.6	0.0	5.7	7.7	13.0	2.4	1.3	0.4	4.4	0.4	96.8	0.00	1.68	0.00	0.94	0.00	0.62	-6.6	1.6
2140	**1138**	47.6	1.3	12.6	3.6	0.0	5.8	7.6	12.9	2.4	1.3	0.4	4.3	0.4	96.7	0.00	1.66	0.00	1.04	0.00	0.62	-6.6	1.6
2080	**1136**	47.6	1.3	12.8	3.6	0.0	5.8	7.4	12.7	2.4	1.3	0.4	4.3	0.4	96.6	0.00	1.64	0.00	1.14	0.00	0.62	-6.7	1.6
2020	**1134**	47.7	1.3	13.0	3.6	0.0	5.9	7.3	12.6	2.5	1.4	0.4	4.3	0.4	96.5	0.00	1.62	0.00	1.24	0.00	0.62	-6.8	1.5
1960	**1132**	47.8	1.3	13.1	3.5	0.0	5.9	7.2	12.5	2.5	1.4	0.4	4.2	0.3	96.4	0.00	1.61	0.00	1.35	0.00	0.62	-6.8	1.5
1900	**1130**	47.8	1.3	13.3	3.5	0.0	5.9	7.0	12.3	2.6	1.4	0.4	4.2	0.3	96.3	0.00	1.59	0.00	1.47	0.00	0.62	-6.9	1.5
1840	**1128**	47.9	1.3	13.5	3.4	0.0	6.0	6.9	12.2	2.6	1.5	0.4	4.1	0.3	96.2	0.00	1.58	0.00	1.60	0.00	0.62	-7.0	1.4
1780	**1126**	48.0	1.3	13.7	3.4	0.0	6.0	6.8	12.0	2.7	1.5	0.4	4.1	0.3	96.1	0.00	1.56	0.00	1.73	0.00	0.62	-7.0	1.4
1720	**1124**	48.1	1.3	13.8	3.4	0.0	6.0	6.6	11.9	2.7	1.5	0.4	4.0	0.3	96.0	0.00	1.55	0.00	1.87	0.00	0.62	-7.1	1.3
1660	**1122**	48.2	1.3	14.0	3.3	0.0	6.1	6.5	11.7	2.8	1.5	0.5	4.0	0.3	95.8	0.00	1.54	0.00	2.01	0.00	0.62	-7.2	1.3
1600	**1120**	48.3	1.3	14.2	3.2	0.0	6.1	6.4	11.6	2.8	1.6	0.5	3.9	0.3	95.7	0.00	1.53	0.00	2.17	0.00	0.62	-7.2	1.2
1540	**1118**	48.4	1.3	14.4	3.2	0.0	6.1	6.2	11.4	2.9	1.6	0.5	3.9	0.3	95.5	0.00	1.52	0.00	2.33	0.00	0.62	-7.3	1.2
1480	**1116**	48.5	1.2	14.6	3.1	0.0	6.1	6.1	11.3	2.9	1.6	0.5	3.8	0.3	95.4	0.00	1.51	0.00	2.49	0.00	0.63	-7.4	1.1
1420	**1114**	48.6	1.2	14.8	3.1	0.0	6.2	6.0	11.2	3.0	1.7	0.5	3.7	0.3	95.2	0.00	1.50	0.00	2.66	0.00	0.63	-7.5	1.1
1360	**1112**	48.7	1.2	14.9	3.0	0.0	6.2	5.8	11.0	3.0	1.7	0.5	3.7	0.3	95.0	0.00	1.49	0.00	2.84	0.00	0.63	-7.6	1.0
1300	**1110**	48.8	1.2	15.1	2.9	0.0	6.2	5.7	10.9	3.1	1.7	0.5	3.6	0.3	94.9	0.00	1.48	0.00	3.03	0.00	0.63	-7.6	1.0
1240	**1108**	49.0	1.2	15.3	2.9	0.0	6.2	5.6	10.7	3.1	1.7	0.5	3.5	0.3	94.7	0.00	1.48	0.00	3.21	0.00	0.63	-7.7	0.9
1180	**1106**	49.1	1.2	15.5	2.8	0.0	6.2	5.4	10.6	3.2	1.8	0.5	3.5	0.3	94.5	0.00	1.47	0.00	3.41	0.00	0.63	-7.8	0.9
1120	**1104**	49.3	1.2	15.7	2.8	0.0	6.2	5.3	10.4	3.2	1.8	0.5	3.4	0.3	94.3	0.00	1.46	0.00	3.61	0.00	0.64	-7.9	0.8
1060	**1102**	49.4	1.2	15.9	2.7	0.0	6.2	5.1	10.2	3.3	1.8	0.5	3.3	0.3	94.1	0.00	1.46	0.00	3.81	0.00	0.64	-8.0	0.7
1000	**1100**	49.6	1.2	16.1	2.6	0.0	6.2	5.0	10.1	3.4	1.9	0.6	3.2	0.3	93.9	0.00	1.46	0.00	4.02	0.00	0.64	-8.1	0.7
940	**1098**	49.7	1.2	16.3	2.5	0.0	6.2	4.9	9.9	3.4	1.9	0.6	3.1	0.3	93.7	0.00	1.46	0.00	4.24	0.00	0.64	-8.2	0.6
880	**1096**	49.9	1.2	16.5	2.5	0.0	6.2	4.7	9.8	3.5	1.9	0.6	3.0	0.3	93.4	0.00	1.46	0.00	4.45	0.00	0.65	-8.3	0.6

820	**1094**	50.1	1.1	16.7	2.4	0.0	6.2	4.6	9.6	3.5	2.0	0.6	2.9	0.3	93.2	0.00	1.46	0.00	4.68	0.00	0.65	-8.4	0.5
760	**1092**	50.3	1.1	16.9	2.3	0.0	6.2	4.4	9.4	3.6	2.0	0.6	2.8	0.3	93.0	0.00	1.46	0.00	4.91	0.00	0.65	-8.5	0.4
700	**1090**	50.5	1.1	17.1	2.3	0.0	6.2	4.3	9.3	3.7	2.1	0.6	2.7	0.2	92.7	0.00	1.47	0.00	5.14	0.00	0.66	-8.6	0.4
640	**1088**	50.7	1.1	17.3	2.2	0.0	6.1	4.2	9.1	3.7	2.1	0.6	2.6	0.2	92.5	0.00	1.48	0.00	5.39	0.00	0.66	-8.7	0.3
580	**1086**	50.9	1.1	17.6	2.1	0.0	6.1	4.0	8.9	3.8	2.1	0.6	2.4	0.2	92.2	0.00	1.49	0.00	5.64	0.00	0.67	-8.8	0.2
520	**1084**	51.1	1.1	17.8	2.0	0.0	6.1	3.9	8.7	3.9	2.2	0.6	2.3	0.2	91.9	0.00	1.51	0.00	5.89	0.00	0.67	-8.9	0.1
460	**1082**	51.4	1.1	18.0	2.0	0.0	6.1	3.7	8.5	4.0	2.2	0.7	2.2	0.2	91.6	0.00	1.53	0.00	6.16	0.00	0.68	-9.0	0.1
400	**1080**	51.6	1.0	18.2	1.9	0.0	6.0	3.6	8.3	4.0	2.3	0.7	2.0	0.2	91.2	0.00	1.56	0.09	6.44	0.00	0.69	-9.1	0.0
340	**1078**	52.2	1.0	17.9	1.8	0.0	6.1	3.4	7.9	4.2	2.4	0.7	1.8	0.2	86.7	0.45	0.97	4.21	6.91	0.00	0.77	-9.2	-0.2
280	**1076**	53.1	1.0	17.4	1.8	0.0	6.1	3.2	7.6	4.4	2.6	0.8	1.6	0.2	80.6	1.07	0.37	9.65	7.47	0.00	0.79	-9.4	-0.3
220	**1074**	53.9	1.0	17.0	1.7	0.0	6.1	3.0	7.3	4.5	2.9	0.9	1.4	0.2	74.1	1.07	0.41	15.59	8.08	0.00	0.79	-9.6	-0.4
160	**1072**	54.8	1.0	16.4	1.6	0.0	6.1	2.7	7.0	4.7	3.2	1.0	1.2	0.2	66.6	1.08	0.54	22.28	8.75	0.00	0.78	-9.8	-0.6
100	**1070**	55.7	1.0	15.8	1.4	0.0	6.0	2.4	6.8	4.7	3.7	1.2	0.9	0.2	57.7	1.09	0.82	30.15	9.50	0.00	0.78	-10.1	-0.9
40	**1068**	57.0	1.0	15.2	1.2	0.0	5.9	2.0	6.5	4.7	4.5	1.3	0.6	0.1	45.3	0.01	0.00	0.00	0.00	0.00	0.00	-10.6	-1.4

Geothermal dP/dT = 5 MPa °C^{-1}

P (bar)	T (°C)	liquid composition													liquid %		Solid phase percentage (%)				water %	log fO_2	ΔNNO
		SiO_2	TiO_2	Al_2O_3	Fe_2O_3	Cr_2O_3	FeO	MgO	CaO	Na_2O	K_2O	P_2O_5	H_2O	$Fe^{3+}/\Sigma Fe$		ol	cpx	feld	sp	whitlockite			
4000	**1200**	47.2	1.1	10.1	3.8	0.1	5.2	10.4	14.5	1.8	1.0	0.3	4.5	0.4	100.0	0.01	0.00	0.00	0.00		0.00	-5.4	2.0
3900	**1198**	47.2	1.1	10.1	3.8	0.1	5.2	10.3	14.5	1.8	1.0	0.3	4.5	0.4	99.9	0.12	0.00	0.00	0.00		0.00	-5.4	2.0
3800	**1196**	47.2	1.1	10.1	3.8	0.1	5.2	10.3	14.5	1.8	1.0	0.3	4.5	0.4	99.9	0.12	0.00	0.00	0.00		0.00	-5.5	2.0
3700	**1194**	47.2	1.1	10.2	3.8	0.1	5.2	10.2	14.5	1.8	1.0	0.3	4.5	0.4	99.9	0.12	0.00	0.00	0.00		0.00	-5.5	2.0
3600	**1192**	47.2	1.1	10.2	3.8	0.1	5.2	10.2	14.6	1.8	1.0	0.3	4.5	0.4	99.9	0.12	0.00	0.00	0.01		0.00	-5.5	2.0
3500	**1190**	47.2	1.1	10.2	3.8	0.1	5.2	10.1	14.6	1.8	1.0	0.3	4.5	0.4	99.9	0.12	0.00	0.00	0.02		0.00	-5.6	2.0
3400	**1188**	47.2	1.1	10.2	3.8	0.1	5.2	10.1	14.6	1.8	1.0	0.3	4.5	0.4	99.9	0.12	0.00	0.00	0.02		0.00	-5.6	2.0
3300	**1186**	47.2	1.1	10.2	3.8	0.1	5.2	10.1	14.6	1.8	1.0	0.3	4.5	0.4	99.8	0.12	0.00	0.00	0.03		0.00	-5.6	2.0
3200	**1184**	47.2	1.1	10.2	3.8	0.1	5.2	10.0	14.6	1.8	1.0	0.3	4.5	0.4	99.8	0.12	0.00	0.00	0.04		0.00	-5.7	2.0
3100	**1182**	47.2	1.1	10.2	3.8	0.1	5.2	10.0	14.7	1.8	1.0	0.3	4.6	0.4	99.8	0.12	0.00	0.00	0.05		0.00	-5.7	2.0
3000	**1180**	47.3	1.1	10.2	3.8	0.1	5.1	9.9	14.7	1.8	1.0	0.3	4.6	0.4	99.8	0.12	0.00	0.00	0.06		0.00	-5.7	2.0

2900	**1178**	47.3	1.1	10.3	3.8	0.1	5.1	9.9	14.7	1.8	1.0	0.3	4.6	0.4	99.8	0.12	0.00	0.00	0.07		0.00	-5.8	2.0
2800	**1176**	47.3	1.1	10.3	3.8	0.0	5.1	9.8	14.7	1.8	1.0	0.3	4.6	0.4	99.8	0.12	0.00	0.00	0.08		0.01	-5.8	2.0
2700	**1174**	47.3	1.1	10.3	3.8	0.0	5.1	9.8	14.7	1.8	1.0	0.3	4.5	0.4	99.7	0.14	0.00	0.00	0.09		0.10	-5.8	1.9
2600	**1172**	47.4	1.1	10.3	3.8	0.0	5.1	9.7	14.8	1.8	1.0	0.3	4.4	0.4	99.6	0.14	0.00	0.00	0.11		0.19	-5.9	1.9
2500	**1170**	47.5	1.1	10.3	3.8	0.0	5.1	9.7	14.8	1.8	1.0	0.3	4.3	0.4	99.4	0.14	0.00	0.00	0.13		0.28	-5.9	1.9
2400	**1168**	47.5	1.1	10.4	3.8	0.0	5.1	9.6	14.9	1.8	1.0	0.3	4.2	0.4	99.3	0.14	0.00	0.00	0.15		0.38	-6.0	1.9
2300	**1166**	47.6	1.1	10.4	3.8	0.0	5.1	9.6	14.9	1.8	1.0	0.3	4.1	0.4	99.2	0.14	0.00	0.00	0.16		0.48	-6.0	1.9
2200	**1164**	47.6	1.2	10.6	3.8	0.0	5.2	9.4	14.8	1.9	1.0	0.3	4.1	0.4	97.2	0.00	1.97	0.00	0.20		0.64	-6.0	1.9
2100	**1162**	47.6	1.2	10.8	3.8	0.0	5.3	9.3	14.6	1.9	1.1	0.3	4.0	0.4	96.8	0.00	2.31	0.00	0.24		0.68	-6.1	1.8
2000	**1160**	47.7	1.2	11.0	3.8	0.0	5.3	9.1	14.4	2.0	1.1	0.3	3.9	0.4	96.7	0.00	2.31	0.00	0.28		0.68	-6.1	1.8
1900	**1158**	47.7	1.2	11.2	3.8	0.0	5.4	9.0	14.3	2.0	1.1	0.3	3.8	0.4	96.7	0.00	2.32	0.00	0.33		0.68	-6.2	1.8
1800	**1156**	47.7	1.2	11.4	3.8	0.0	5.5	8.8	14.1	2.1	1.1	0.3	3.7	0.4	96.6	0.00	2.34	0.00	0.39		0.68	-6.3	1.8
1700	**1154**	47.7	1.2	11.6	3.8	0.0	5.6	8.6	13.9	2.1	1.2	0.3	3.7	0.4	96.5	0.00	2.36	0.00	0.44		0.69	-6.3	1.7
1600	**1152**	47.8	1.3	11.8	3.8	0.0	5.6	8.5	13.7	2.2	1.2	0.4	3.6	0.4	96.4	0.00	2.38	0.00	0.51		0.69	-6.4	1.7
1500	**1150**	47.8	1.3	12.1	3.8	0.0	5.7	8.3	13.5	2.2	1.2	0.4	3.5	0.4	96.3	0.00	2.41	0.00	0.57		0.69	-6.4	1.7
1400	**1148**	47.9	1.3	12.3	3.8	0.0	5.8	8.1	13.3	2.3	1.3	0.4	3.4	0.4	96.2	0.00	2.45	0.00	0.65		0.70	-6.5	1.6
1300	**1146**	48.0	1.3	12.6	3.8	0.0	5.9	7.9	13.1	2.4	1.3	0.4	3.2	0.4	96.1	0.00	2.49	0.00	0.73		0.70	-6.6	1.6
1200	**1144**	48.0	1.3	12.8	3.8	0.0	5.9	7.7	12.9	2.4	1.3	0.4	3.1	0.4	95.9	0.00	2.53	0.00	0.83		0.71	-6.6	1.6
1100	**1142**	48.1	1.3	13.1	3.8	0.0	6.0	7.5	12.6	2.5	1.4	0.4	3.0	0.4	95.8	0.00	2.59	0.00	0.93		0.71	-6.7	1.5
1000	**1140**	48.2	1.3	13.4	3.7	0.0	6.1	7.3	12.4	2.6	1.4	0.4	2.9	0.4	95.6	0.00	2.65	0.00	1.05		0.72	-6.8	1.5
900	**1138**	48.3	1.4	13.7	3.7	0.0	6.2	7.1	12.2	2.7	1.5	0.4	2.7	0.3	95.4	0.00	2.73	0.00	1.18		0.73	-6.8	1.4
800	**1136**	48.5	1.4	14.0	3.6	0.0	6.2	6.9	11.9	2.7	1.5	0.5	2.6	0.3	95.1	0.00	2.82	0.00	1.33		0.74	-6.9	1.4
700	**1134**	48.6	1.4	14.3	3.6	0.0	6.3	6.6	11.6	2.8	1.6	0.5	2.4	0.3	94.8	0.00	2.92	0.00	1.51		0.75	-7.0	1.3
600	**1132**	48.8	1.4	14.7	3.5	0.0	6.4	6.4	11.3	2.9	1.6	0.5	2.2	0.3	94.5	0.00	3.05	0.00	1.72		0.76	-7.1	1.3
500	**1130**	49.1	1.4	15.0	3.4	0.0	6.5	6.1	11.0	3.0	1.7	0.5	2.0	0.3	94.1	0.00	3.20	0.00	1.97		0.77	-7.2	1.2
400	**1128**	49.3	1.4	15.5	3.3	0.0	6.5	5.8	10.6	3.2	1.8	0.5	1.8	0.3	93.5	0.00	3.41	0.00	2.26		0.79	-7.3	1.1
300	**1126**	49.7	1.4	15.9	3.2	0.0	6.6	5.5	10.2	3.3	1.9	0.5	1.5	0.3	92.9	0.00	3.69	0.00	2.62		0.81	-7.4	1.0
200	**1124**	50.1	1.4	16.4	3.1	0.0	6.6	5.1	9.8	3.5	2.0	0.6	1.2	0.3	92.0	0.00	4.12	0.00	3.08		0.85	-7.6	0.9
100	**1122**	50.8	1.4	16.7	2.9	0.0	6.8	4.8	9.1	3.7	2.1	0.6	0.8	0.3	87.8	0.00	4.95	2.53	3.74		0.94	-7.8	0.7

1	**1120**	53.5	1.6	15.0	2.4	0.0	7.1	3.6	7.7	4.3	3.2	1.0	0.1	0.2	57.7	3.61	6.52	24.52	6.42		1.24	-8.5	0.1
Low pressure geothermal																							
P (bar)	**T (°C)**	**liquid composition**														**Solid phase percentage (%)**					**water %**	**log fO_2**	**ΔNNO**
		SiO_2	**TiO_2**	**Al_2O_3**	**Fe_2O_3**	**Cr_2O_3**	**FeO**	**MgO**	**CaO**	**Na_2O**	**K_2O**	**P_2O_5**	**H_2O**	**$Fe^{3+}/\Sigma Fe$**	**liquid %**	**ol**	**cpx**	**feld**	**sp**	**whitlockite**			
100	**1200**	48.8	1.3	11.9	4.0	0.0	5.9	9.7	13.7	2.2	1.2	0.4	0.7	0.4	100.0	0.00	0.00	0.00	0.01	0.00	0.00	-5.9	1.6
90	**1185**	48.6	1.4	13.0	4.1	0.0	6.3	8.8	12.5	2.5	1.4	0.4	0.7	0.4	87.3	0.00	12.53	0.00	0.09	0.00	0.11	-6.2	1.6
80	**1170**	48.6	1.5	14.1	4.1	0.0	6.6	7.8	11.5	2.8	1.6	0.5	0.7	0.4	88.4	0.41	10.69	0.00	0.24	0.00	0.22	-6.4	1.5
70	**1155**	48.8	1.6	15.1	4.0	0.0	6.8	6.8	10.5	3.1	1.7	0.5	0.6	0.3	89.3	0.55	9.26	0.00	0.55	0.00	0.34	-6.6	1.5
60	**1140**	49.3	1.7	16.1	3.7	0.0	6.9	5.9	9.7	3.4	1.9	0.6	0.6	0.3	89.3	0.57	8.29	0.00	1.36	0.00	0.47	-7.0	1.3
50	**1125**	50.7	1.7	16.3	3.1	0.0	6.9	4.8	8.7	3.8	2.3	0.7	0.6	0.3	81.3	1.83	6.60	6.37	3.24	0.00	0.63	-7.6	0.8
40	**1110**	52.7	1.6	16.0	2.4	0.0	6.6	3.8	7.9	4.3	2.9	0.9	0.5	0.2	70.1	2.12	4.81	16.51	5.81	0.00	0.64	-8.4	0.2
30	**1095**	54.6	1.5	15.7	1.8	0.0	6.0	3.0	7.2	4.6	3.6	1.1	0.5	0.2	58.6	1.65	3.55	27.46	8.12	0.00	0.63	-9.3	-0.4
20	**1080**	56.3	1.4	15.4	1.3	0.0	5.4	2.3	6.7	4.7	4.5	1.3	0.4	0.2	46.5	1.22	2.89	38.67	9.93	0.17	0.61	-10.1	-1.1
10	**1065**	57.9	1.3	15.2	0.8	0.0	4.8	1.6	6.0	4.5	5.7	1.3	0.3	0.1	33.3	0.87	2.75	50.53	11.31	0.64	0.60	-11.1	-1.8
1	**1050**	58.6	1.4	15.1	0.5	0.0	4.1	1.0	5.8	4.0	7.1	1.4	0.1	0.1	15.1	0.62	3.19	66.85	12.43	1.20	0.58	-12.0	-2.6

Table A.6.2: MELTS simulations performed with an initial fO_2 = NNO+1.5 and an initial H_2O content of 5 wt.%

High T-P sgeothermal																							
P (bar)	**T (°C)**	**liquid composition**													**liquid %**	**Solid phase percentage (%)**					**water %**	**log fO_2**	**ΔNNO**
		SiO_2	**TiO_2**	**Al_2O_3**	**Fe_2O_3**	**Cr_2O_3**	**FeO**	**MgO**	**CaO**	**Na_2O**	**K_2O**	**P_2O_5**	**H_2O**	**$Fe^{3+}/\Sigma Fe$**		**ol**	**cpx**	**feld**	**sp**	**whitlockite**			
5000	**1300**	46.2	1.1	9.5	3.1	0.1	5.8	12.3	13.6	1.7	0.9	0.3	5.3	0.32	100.0	0.00			0.00		0.00	-4.79	1.55
4900	**1290**	46.2	1.1	9.5	3.1	0.1	5.8	12.3	13.6	1.7	0.9	0.3	5.3	0.32	100.0	0.00			0.00		0.00	-4.91	1.54
4800	**1280**	46.2	1.1	9.5	3.1	0.1	5.8	12.3	13.6	1.7	0.9	0.3	5.3	0.32	100.0	0.00			0.00		0.00	-5.02	1.53

4700	**1270**	46.2	1.1	9.5	3.1	0.1	5.8	12.3	13.6	1.7	0.9	0.3	5.3	0.32	100.0	0.00			0.00		0.00	-5.14	1.52
4600	**1260**	46.2	1.1	9.5	3.1	0.1	5.8	12.3	13.6	1.7	0.9	0.3	5.3	0.32	100.0	0.00			0.00		0.00	-5.26	1.51
4500	**1250**	46.3	1.1	9.6	3.1	0.1	5.8	12.0	13.7	1.7	0.9	0.3	5.3	0.32	99.21	0.79			0.00		0.00	-5.36	1.51
4400	**1240**	46.3	1.1	9.7	3.1	0.1	5.8	11.7	13.8	1.7	0.9	0.3	5.3	0.33	98.98	0.99			0.00		0.03	-5.47	1.52
4300	**1230**	46.4	1.1	9.8	3.2	0.1	5.8	11.3	14.0	1.7	0.9	0.3	5.3	0.33	98.96	0.96			0.00		0.08	-5.57	1.52
4200	**1220**	46.5	1.1	9.9	3.2	0.1	5.7	10.9	14.1	1.7	1.0	0.3	5.3	0.33	98.94	0.93			0.00		0.13	-5.68	1.53
4100	**1210**	46.6	1.1	10.0	3.2	0.1	5.7	10.6	14.2	1.8	1.0	0.3	5.4	0.33	98.86	0.91			0.05		0.18	-5.80	1.52
4000	**1200**	46.7	1.1	10.1	3.2	0.1	5.7	10.2	14.4	1.8	1.0	0.3	5.4	0.34	98.81	0.89			0.07		0.23	-5.93	1.51

Isothermal (almost adiabatic)

P (bar)	T (°C)	liquid composition													liquid %	Solid phase percentage (%)					water %	log f_{O_2}	ΔNNO
		SiO_2	TiO_2	Al_2O_3	Fe_2O_3	Cr_2O_3	FeO	MgO	CaO	Na_2O	K_2O	P_2O_5	H_2O	$Fe^{3+}/\Sigma Fe$		ol	cpx	feld	sp	whitlockite			
4000	**1200**	46.7	1.1	10.0	3.2	0.1	5.7	10.2	14.4	1.8	1.0	0.3	5.3	0.34	99.94	0.04	0.00		0.02		0.00	-5.94	1.50
3900	**1200**	46.8	1.1	10.0	3.2	0.1	5.7	10.2	14.4	1.8	1.0	0.3	5.3	0.34	99.98	0.00	0.00		0.00		0.02	-5.95	1.50
3800	**1200**	46.8	1.1	10.0	3.2	0.1	5.7	10.2	14.4	1.8	1.0	0.3	5.2	0.34	99.91	0.00	0.00		0.00		0.09	-5.96	1.49
3700	**1200**	46.8	1.1	10.0	3.2	0.1	5.7	10.3	14.4	1.8	1.0	0.3	5.1	0.34	99.83	0.00	0.00		0.00		0.17	-5.97	1.48
3600	**1200**	46.9	1.1	10.0	3.2	0.1	5.7	10.3	14.4	1.8	1.0	0.3	5.1	0.34	99.76	0.00	0.00		0.00		0.24	-5.98	1.47
3500	**1200**	46.9	1.1	10.0	3.2	0.1	5.7	10.3	14.4	1.8	1.0	0.3	5.0	0.34	99.68	0.00	0.00		0.00		0.32	-5.99	1.46
3400	**1200**	46.9	1.1	10.1	3.2	0.1	5.7	10.3	14.5	1.8	1.0	0.3	4.9	0.34	99.60	0.00	0.00		0.00		0.40	-6.00	1.45
3300	**1200**	47.0	1.1	10.1	3.2	0.1	5.7	10.3	14.5	1.8	1.0	0.3	4.9	0.34	99.52	0.00	0.00		0.00		0.48	-6.02	1.44
3200	**1200**	47.0	1.1	10.1	3.2	0.1	5.7	10.3	14.5	1.8	1.0	0.3	4.8	0.34	99.44	0.00	0.00		0.00		0.56	-6.03	1.44
3100	**1200**	47.0	1.1	10.1	3.2	0.1	5.7	10.3	14.5	1.8	1.0	0.3	4.7	0.34	99.42	0.00	0.00		0.00		0.58	-6.04	1.43
3000	**1200**	47.1	1.1	10.1	3.2	0.1	5.7	10.3	14.5	1.8	1.0	0.3	4.6	0.34	99.41	0.00	0.00		0.00		0.58	-6.05	1.42
2900	**1200**	47.1	1.1	10.1	3.2	0.1	5.7	10.3	14.5	1.8	1.0	0.3	4.5	0.34	99.41	0.00	0.00		0.00		0.58	-6.06	1.41
2800	**1200**	47.2	1.1	10.1	3.2	0.1	5.7	10.3	14.5	1.8	1.0	0.3	4.5	0.34	99.41	0.00	0.00		0.00		0.59	-6.08	1.40
2700	**1200**	47.2	1.1	10.1	3.2	0.1	5.7	10.3	14.5	1.8	1.0	0.3	4.4	0.34	99.41	0.00	0.00		0.00		0.59	-6.09	1.39
2600	**1200**	47.3	1.1	10.1	3.2	0.1	5.7	10.3	14.6	1.8	1.0	0.3	4.3	0.34	99.41	0.00	0.00		0.00		0.59	-6.10	1.38
2500	**1200**	47.3	1.1	10.1	3.2	0.1	5.7	10.4	14.6	1.8	1.0	0.3	4.2	0.34	99.40	0.00	0.00		0.00		0.59	-6.11	1.37
2400	**1200**	47.3	1.1	10.1	3.2	0.1	5.8	10.4	14.6	1.8	1.0	0.3	4.1	0.34	99.40	0.00	0.00		0.01		0.59	-6.13	1.36

2300	**1200**	47.4	1.1	10.2	3.2	0.1	5.8	10.4	14.6	1.8	1.0	0.3	4.0	0.34	99.40	0.00	0.00		0.01		0.60	-6.14	1.35
2200	**1200**	47.4	1.1	10.2	3.2	0.1	5.8	10.4	14.6	1.8	1.0	0.3	3.9	0.33	99.40	0.00	0.00		0.01		0.60	-6.15	1.34
2100	**1200**	47.5	1.1	10.2	3.2	0.1	5.8	10.4	14.6	1.8	1.0	0.3	3.8	0.33	99.39	0.00	0.00		0.01		0.60	-6.17	1.33
2000	**1200**	47.5	1.1	10.2	3.2	0.1	5.8	10.4	14.6	1.8	1.0	0.3	3.7	0.33	99.39	0.00	0.00		0.01		0.60	-6.18	1.32
1900	**1200**	47.6	1.1	10.2	3.2	0.1	5.8	10.4	14.7	1.8	1.0	0.3	3.6	0.33	99.39	0.00	0.00		0.01		0.61	-6.19	1.31
1800	**1200**	47.7	1.1	10.2	3.2	0.1	5.8	10.4	14.7	1.8	1.0	0.3	3.5	0.33	99.38	0.00	0.00		0.01		0.61	-6.21	1.30
1700	**1200**	47.7	1.1	10.2	3.2	0.1	5.8	10.4	14.7	1.8	1.0	0.3	3.4	0.33	99.38	0.00	0.00		0.01		0.61	-6.22	1.29
1600	**1200**	47.8	1.1	10.2	3.2	0.1	5.8	10.4	14.7	1.8	1.0	0.3	3.3	0.33	99.38	0.00	0.00		0.01		0.62	-6.24	1.28
1500	**1200**	47.8	1.1	10.2	3.3	0.1	5.8	10.5	14.7	1.8	1.0	0.3	3.2	0.33	99.37	0.00	0.00		0.01		0.62	-6.25	1.27
1400	**1200**	47.9	1.1	10.3	3.3	0.1	5.8	10.5	14.7	1.8	1.0	0.3	3.1	0.33	99.37	0.00	0.00		0.01		0.62	-6.27	1.25
1300	**1200**	48.0	1.1	10.3	3.3	0.1	5.8	10.5	14.8	1.8	1.0	0.3	2.9	0.33	99.36	0.00	0.00		0.01		0.63	-6.28	1.24
1200	**1200**	48.0	1.1	10.3	3.3	0.1	5.8	10.5	14.8	1.8	1.0	0.3	2.8	0.33	99.36	0.00	0.00		0.01		0.63	-6.30	1.23
1100	**1200**	48.1	1.1	10.3	3.3	0.1	5.8	10.5	14.8	1.8	1.0	0.3	2.7	0.33	99.35	0.00	0.00		0.01		0.64	-6.31	1.22
1000	**1200**	48.2	1.1	10.3	3.3	0.1	5.8	10.5	14.8	1.8	1.0	0.3	2.5	0.33	99.34	0.00	0.00		0.01		0.65	-6.33	1.20
900	**1200**	48.3	1.1	10.3	3.3	0.1	5.8	10.5	14.9	1.8	1.0	0.3	2.4	0.33	99.34	0.00	0.00		0.01		0.65	-6.34	1.19
800	**1200**	48.3	1.1	10.3	3.3	0.1	5.9	10.6	14.9	1.8	1.0	0.3	2.2	0.33	99.33	0.00	0.00		0.01		0.66	-6.36	1.18
700	**1200**	48.4	1.1	10.4	3.3	0.1	5.9	10.6	14.9	1.8	1.0	0.3	2.1	0.33	99.32	0.00	0.00		0.01		0.67	-6.38	1.16
600	**1200**	48.5	1.1	10.4	3.3	0.1	5.9	10.6	14.9	1.9	1.0	0.3	1.9	0.33	99.31	0.00	0.00		0.01		0.68	-6.39	1.15
500	**1200**	48.6	1.2	10.4	3.3	0.1	5.9	10.6	15.0	1.9	1.0	0.3	1.7	0.33	99.29	0.00	0.00		0.01		0.69	-6.41	1.14
400	**1200**	48.7	1.2	10.4	3.3	0.1	5.9	10.6	15.0	1.9	1.0	0.3	1.5	0.33	99.28	0.00	0.00		0.02		0.71	-6.43	1.12
300	**1200**	48.8	1.2	10.5	3.3	0.1	5.9	10.6	15.0	1.9	1.0	0.3	1.3	0.33	98.94	0.00	0.31		0.02		0.73	-6.45	1.10
200	**1200**	48.8	1.2	11.0	3.3	0.0	6.2	10.2	14.6	2.0	1.1	0.3	1.0	0.33	92.76	0.00	6.38		0.04		0.82	-6.49	1.07
100	**1200**	48.8	1.3	11.7	3.4	0.0	6.5	9.7	13.9	2.2	1.2	0.4	0.7	0.32	90.97	0.00	8.10		0.05		0.87	-6.53	1.03
1	**1200**	48.9	1.5	13.3	3.5	0.0	7.1	8.6	12.5	2.6	1.4	0.4	0.1	0.30	82.68	0.00	16.08		0.09		1.15	-6.60	0.96

Geothermal dP/dT = 3 MPa °C^{-1}

P (bar)	T (°C)	liquid composition													liquid %	Solid phase percentage (%)					water %	log f_{O_2}	ΔNNO
		SiO_2	TiO_2	Al_2O_3	Fe_2O_3	Cr_2O_3	FeO	MgO	CaO	Na_2O	K_2O	P_2O_5	H_2O	$Fe^{3+}/\Sigma Fe$		ol	cpx	feld	sp	whitlockite			
4000	**1200**	46.9	1.1	10.1	3.2	0.1	5.7	10.2	14.5	1.8	1.0	0.3	5.0	0.34	99.81	0.14	0.00	0.00	0.05	0.00	0.00	-5.95	1.49

3970	**1199**	46.9	1.1	10.1	3.2	0.1	5.7	10.2	14.5	1.8	1.0	0.3	5.0	0.34	99.92	0.08	0.00	0.00	0.01	0.00	0.00	-5.96	1.49
3940	**1198**	46.9	1.1	10.1	3.2	0.1	5.7	10.2	14.5	1.8	1.0	0.3	5.0	0.34	99.92	0.07	0.00	0.00	0.01	0.00	0.00	-5.98	1.49
3910	**1197**	46.9	1.1	10.1	3.2	0.1	5.7	10.1	14.5	1.8	1.0	0.3	5.0	0.34	99.92	0.07	0.00	0.00	0.01	0.00	0.00	-5.99	1.49
3880	**1196**	46.9	1.1	10.1	3.2	0.1	5.7	10.1	14.5	1.8	1.0	0.3	5.0	0.34	99.92	0.07	0.00	0.00	0.01	0.00	0.00	-6.01	1.48
3850	**1195**	46.9	1.1	10.1	3.2	0.1	5.7	10.1	14.5	1.8	1.0	0.3	5.1	0.34	99.92	0.07	0.00	0.00	0.01	0.00	0.00	-6.02	1.48
3820	**1194**	46.9	1.1	10.1	3.2	0.1	5.7	10.0	14.5	1.8	1.0	0.3	5.1	0.34	99.92	0.07	0.00	0.00	0.01	0.00	0.00	-6.03	1.48
3790	**1193**	47.0	1.1	10.1	3.2	0.1	5.7	10.0	14.5	1.8	1.0	0.3	5.1	0.34	99.92	0.07	0.00	0.00	0.01	0.00	0.00	-6.05	1.48
3760	**1192**	47.0	1.1	10.1	3.2	0.1	5.7	10.0	14.5	1.8	1.0	0.3	5.1	0.34	99.92	0.07	0.00	0.00	0.01	0.00	0.00	-6.06	1.47
3730	**1191**	47.0	1.1	10.1	3.2	0.1	5.7	10.0	14.6	1.8	1.0	0.3	5.1	0.34	99.92	0.07	0.00	0.00	0.01	0.00	0.00	-6.08	1.47
3700	**1190**	47.0	1.1	10.1	3.2	0.1	5.7	9.9	14.6	1.8	1.0	0.3	5.1	0.34	99.92	0.07	0.00	0.00	0.01	0.00	0.00	-6.09	1.47
3670	**1189**	47.0	1.1	10.1	3.2	0.1	5.7	9.9	14.6	1.8	1.0	0.3	5.1	0.34	99.92	0.07	0.00	0.00	0.01	0.00	0.00	-6.11	1.47
3640	**1188**	47.0	1.1	10.1	3.2	0.1	5.7	9.9	14.6	1.8	1.0	0.3	5.1	0.34	99.92	0.07	0.00	0.00	0.01	0.00	0.00	-6.12	1.46
3610	**1187**	47.0	1.1	10.2	3.2	0.1	5.7	9.8	14.6	1.8	1.0	0.3	5.1	0.34	99.92	0.07	0.00	0.00	0.01	0.00	0.00	-6.14	1.46
3580	**1186**	47.0	1.1	10.2	3.2	0.1	5.7	9.8	14.6	1.8	1.0	0.3	5.1	0.34	99.92	0.07	0.00	0.00	0.01	0.00	0.00	-6.15	1.46
3550	**1185**	47.0	1.1	10.2	3.2	0.1	5.7	9.8	14.6	1.8	1.0	0.3	5.1	0.34	99.92	0.07	0.00	0.00	0.01	0.00	0.00	-6.17	1.46
3520	**1184**	47.0	1.1	10.2	3.2	0.1	5.6	9.8	14.6	1.8	1.0	0.3	5.1	0.34	99.92	0.07	0.00	0.00	0.01	0.00	0.00	-6.18	1.45
3490	**1183**	47.0	1.1	10.2	3.2	0.1	5.6	9.7	14.6	1.8	1.0	0.3	5.1	0.34	99.92	0.07	0.00	0.00	0.01	0.00	0.00	-6.20	1.45
3460	**1182**	47.0	1.1	10.2	3.2	0.1	5.6	9.7	14.7	1.8	1.0	0.3	5.1	0.34	99.89	0.08	0.00	0.00	0.01	0.00	0.02	-6.21	1.45
3430	**1181**	47.1	1.1	10.2	3.2	0.1	5.6	9.7	14.7	1.8	1.0	0.3	5.1	0.34	99.87	0.08	0.00	0.00	0.01	0.00	0.04	-6.23	1.45
3400	**1180**	47.1	1.1	10.2	3.2	0.1	5.6	9.6	14.7	1.8	1.0	0.3	5.0	0.34	99.85	0.08	0.00	0.00	0.01	0.00	0.07	-6.25	1.44
3370	**1179**	47.1	1.1	10.2	3.2	0.1	5.6	9.6	14.7	1.8	1.0	0.3	5.0	0.34	99.83	0.08	0.00	0.00	0.01	0.00	0.09	-6.26	1.44
3340	**1178**	47.1	1.1	10.2	3.2	0.1	5.6	9.6	14.7	1.8	1.0	0.3	5.0	0.34	99.80	0.08	0.00	0.00	0.01	0.00	0.11	-6.28	1.44
3310	**1177**	47.1	1.1	10.2	3.2	0.1	5.6	9.6	14.7	1.8	1.0	0.3	5.0	0.34	99.78	0.08	0.00	0.00	0.01	0.00	0.13	-6.29	1.43
3280	**1176**	47.1	1.1	10.3	3.2	0.1	5.6	9.5	14.7	1.8	1.0	0.3	5.0	0.34	99.76	0.08	0.00	0.00	0.01	0.00	0.16	-6.31	1.43
3250	**1175**	47.2	1.1	10.3	3.2	0.1	5.6	9.5	14.8	1.8	1.0	0.3	5.0	0.34	99.73	0.08	0.00	0.00	0.01	0.00	0.18	-6.33	1.42
3220	**1174**	47.2	1.1	10.3	3.2	0.1	5.6	9.5	14.8	1.8	1.0	0.3	4.9	0.34	99.71	0.08	0.00	0.00	0.01	0.00	0.21	-6.34	1.42
3190	**1173**	47.2	1.1	10.3	3.2	0.1	5.6	9.4	14.8	1.8	1.0	0.3	4.9	0.34	99.69	0.08	0.00	0.00	0.01	0.00	0.23	-6.36	1.42
3160	**1172**	47.2	1.1	10.3	3.2	0.1	5.6	9.4	14.8	1.8	1.0	0.3	4.9	0.34	99.66	0.08	0.00	0.00	0.01	0.00	0.25	-6.38	1.41
3130	**1171**	47.2	1.1	10.3	3.2	0.1	5.6	9.4	14.8	1.8	1.0	0.3	4.9	0.34	99.64	0.08	0.00	0.00	0.01	0.00	0.28	-6.39	1.41

3100	**1170**	47.3	1.1	10.3	3.2	0.1	5.6	9.4	14.8	1.8	1.0	0.3	4.9	0.34	99.61	0.08	0.00	0.00	0.01	0.00	0.30	-6.41	1.41
3070	**1169**	47.3	1.1	10.3	3.2	0.1	5.6	9.3	14.9	1.8	1.0	0.3	4.8	0.34	99.59	0.08	0.00	0.00	0.01	0.00	0.33	-6.43	1.40
3040	**1168**	47.3	1.1	10.3	3.2	0.1	5.6	9.3	14.9	1.8	1.0	0.3	4.8	0.34	99.56	0.08	0.00	0.00	0.01	0.00	0.35	-6.44	1.40
3010	**1167**	47.3	1.1	10.4	3.2	0.1	5.6	9.3	14.9	1.8	1.0	0.3	4.8	0.34	99.54	0.08	0.00	0.00	0.01	0.00	0.38	-6.46	1.40
2980	**1166**	47.3	1.1	10.4	3.2	0.1	5.6	9.3	14.9	1.8	1.0	0.3	4.8	0.34	99.51	0.08	0.00	0.00	0.01	0.00	0.40	-6.47	1.39
2950	**1165**	47.4	1.1	10.4	3.2	0.1	5.6	9.2	14.9	1.8	1.0	0.3	4.8	0.34	99.49	0.08	0.00	0.00	0.01	0.00	0.43	-6.49	1.39
2920	**1164**	47.4	1.1	10.4	3.2	0.1	5.6	9.2	14.9	1.9	1.0	0.3	4.7	0.34	99.46	0.08	0.00	0.00	0.01	0.00	0.45	-6.51	1.39
2890	**1163**	47.4	1.2	10.5	3.2	0.1	5.6	9.1	14.9	1.9	1.0	0.3	4.7	0.34	98.58	0.00	0.89	0.00	0.01	0.00	0.51	-6.53	1.38
2860	**1162**	47.4	1.2	10.5	3.2	0.1	5.7	9.1	14.8	1.9	1.0	0.3	4.7	0.34	98.45	0.00	0.97	0.00	0.02	0.00	0.56	-6.55	1.37
2830	**1161**	47.4	1.2	10.6	3.2	0.1	5.7	9.0	14.7	1.9	1.0	0.3	4.7	0.34	98.46	0.00	0.96	0.00	0.02	0.00	0.56	-6.58	1.36
2800	**1160**	47.4	1.2	10.7	3.2	0.1	5.7	8.9	14.7	1.9	1.1	0.3	4.7	0.34	98.47	0.00	0.95	0.00	0.02	0.00	0.56	-6.60	1.34
2770	**1159**	47.4	1.2	10.8	3.2	0.1	5.8	8.9	14.6	1.9	1.1	0.3	4.7	0.33	98.48	0.00	0.95	0.00	0.02	0.00	0.56	-6.62	1.33
2740	**1158**	47.4	1.2	10.9	3.2	0.1	5.8	8.8	14.5	2.0	1.1	0.3	4.7	0.33	98.49	0.00	0.94	0.00	0.02	0.00	0.56	-6.65	1.32
2710	**1157**	47.4	1.2	10.9	3.2	0.0	5.8	8.7	14.5	2.0	1.1	0.3	4.7	0.33	98.49	0.00	0.93	0.00	0.02	0.00	0.56	-6.67	1.31
2680	**1156**	47.4	1.2	11.0	3.2	0.0	5.9	8.7	14.4	2.0	1.1	0.3	4.6	0.33	98.50	0.00	0.92	0.00	0.02	0.00	0.56	-6.70	1.30
2650	**1155**	47.4	1.2	11.1	3.2	0.0	5.9	8.6	14.3	2.0	1.1	0.3	4.6	0.33	98.51	0.00	0.92	0.00	0.02	0.00	0.56	-6.72	1.29
2620	**1154**	47.4	1.2	11.2	3.2	0.0	5.9	8.5	14.2	2.0	1.1	0.3	4.6	0.33	98.52	0.00	0.91	0.00	0.02	0.00	0.56	-6.74	1.28
2590	**1153**	47.4	1.2	11.3	3.2	0.0	6.0	8.5	14.2	2.1	1.1	0.3	4.6	0.33	98.52	0.00	0.90	0.00	0.02	0.00	0.56	-6.77	1.27
2560	**1152**	47.4	1.2	11.4	3.2	0.0	6.0	8.4	14.1	2.1	1.1	0.3	4.6	0.33	98.53	0.00	0.90	0.00	0.02	0.00	0.56	-6.79	1.26
2530	**1151**	47.4	1.2	11.4	3.2	0.0	6.0	8.3	14.0	2.1	1.2	0.3	4.6	0.33	98.54	0.00	0.89	0.00	0.02	0.00	0.56	-6.81	1.25
2500	**1150**	47.4	1.2	11.5	3.2	0.0	6.1	8.2	14.0	2.1	1.2	0.3	4.5	0.32	98.54	0.00	0.88	0.00	0.02	0.00	0.56	-6.84	1.24
2470	**1149**	47.4	1.2	11.6	3.2	0.0	6.1	8.2	13.9	2.1	1.2	0.4	4.5	0.32	98.55	0.00	0.88	0.00	0.02	0.00	0.56	-6.86	1.23
2440	**1148**	47.4	1.2	11.7	3.2	0.0	6.1	8.1	13.8	2.2	1.2	0.4	4.5	0.32	98.55	0.00	0.87	0.00	0.02	0.00	0.56	-6.89	1.22
2410	**1147**	47.4	1.2	11.8	3.2	0.0	6.1	8.0	13.8	2.2	1.2	0.4	4.5	0.32	98.56	0.00	0.86	0.00	0.02	0.00	0.56	-6.91	1.21
2380	**1146**	47.4	1.2	11.8	3.2	0.0	6.2	8.0	13.7	2.2	1.2	0.4	4.5	0.32	98.57	0.00	0.86	0.00	0.02	0.00	0.56	-6.93	1.20
2350	**1145**	47.4	1.2	11.9	3.2	0.0	6.2	7.9	13.6	2.2	1.2	0.4	4.5	0.32	98.57	0.00	0.85	0.00	0.02	0.00	0.56	-6.96	1.19
2320	**1144**	47.4	1.3	12.0	3.2	0.0	6.2	7.8	13.6	2.2	1.2	0.4	4.4	0.32	98.58	0.00	0.85	0.00	0.02	0.00	0.56	-6.98	1.17
2290	**1143**	47.4	1.3	12.1	3.2	0.0	6.3	7.8	13.5	2.3	1.2	0.4	4.4	0.32	98.58	0.00	0.84	0.00	0.02	0.00	0.56	-7.01	1.16
2260	**1142**	47.4	1.3	12.2	3.2	0.0	6.3	7.7	13.4	2.3	1.3	0.4	4.4	0.31	98.59	0.00	0.84	0.00	0.02	0.00	0.56	-7.03	1.15

2230	**1141**	47.4	1.3	12.2	3.2	0.0	6.3	7.7	13.3	2.3	1.3	0.4	4.4	0.31	98.59	0.00	0.83	0.00	0.02	0.00	0.56	-7.06	1.14
2200	**1140**	47.4	1.3	12.3	3.2	0.0	6.4	7.6	13.3	2.3	1.3	0.4	4.4	0.31	98.60	0.00	0.83	0.00	0.02	0.00	0.56	-7.08	1.13
2170	**1139**	47.4	1.3	12.4	3.2	0.0	6.4	7.5	13.2	2.3	1.3	0.4	4.3	0.31	98.60	0.00	0.82	0.00	0.02	0.00	0.56	-7.11	1.12
2140	**1138**	47.4	1.3	12.5	3.2	0.0	6.4	7.5	13.1	2.4	1.3	0.4	4.3	0.31	98.61	0.00	0.82	0.00	0.02	0.00	0.56	-7.13	1.11
2110	**1137**	47.4	1.3	12.6	3.2	0.0	6.4	7.4	13.1	2.4	1.3	0.4	4.3	0.31	98.61	0.00	0.81	0.00	0.02	0.00	0.56	-7.15	1.10
2080	**1136**	47.5	1.3	12.6	3.2	0.0	6.5	7.3	13.0	2.4	1.3	0.4	4.3	0.31	98.62	0.00	0.81	0.00	0.02	0.00	0.56	-7.18	1.08
2050	**1135**	47.5	1.3	12.7	3.2	0.0	6.5	7.3	12.9	2.4	1.3	0.4	4.3	0.31	98.62	0.00	0.81	0.00	0.02	0.00	0.56	-7.20	1.07
2020	**1134**	47.5	1.3	12.8	3.2	0.0	6.5	7.2	12.8	2.4	1.3	0.4	4.2	0.31	98.62	0.00	0.80	0.00	0.02	0.00	0.56	-7.23	1.06
1990	**1133**	47.5	1.3	12.9	3.2	0.0	6.6	7.1	12.8	2.5	1.4	0.4	4.2	0.30	98.63	0.00	0.80	0.00	0.02	0.00	0.56	-7.25	1.05
1960	**1132**	47.5	1.3	13.0	3.2	0.0	6.6	7.1	12.7	2.5	1.4	0.4	4.2	0.30	98.63	0.00	0.79	0.00	0.02	0.00	0.56	-7.28	1.04
1930	**1131**	47.5	1.3	13.0	3.2	0.0	6.6	7.0	12.6	2.5	1.4	0.4	4.2	0.30	98.64	0.00	0.79	0.00	0.02	0.00	0.56	-7.30	1.03
1900	**1130**	47.5	1.3	13.1	3.2	0.0	6.6	6.9	12.6	2.5	1.4	0.4	4.1	0.30	98.64	0.00	0.79	0.00	0.02	0.00	0.56	-7.33	1.02
1870	**1129**	47.6	1.3	13.2	3.2	0.0	6.7	6.9	12.5	2.5	1.4	0.4	4.1	0.30	98.64	0.00	0.78	0.00	0.02	0.00	0.56	-7.35	1.00
1840	**1128**	47.6	1.3	13.3	3.2	0.0	6.7	6.8	12.4	2.6	1.4	0.4	4.1	0.30	98.65	0.00	0.78	0.00	0.02	0.00	0.56	-7.38	0.99
1810	**1127**	47.6	1.3	13.4	3.2	0.0	6.7	6.7	12.3	2.6	1.4	0.4	4.1	0.30	98.65	0.00	0.78	0.00	0.02	0.00	0.56	-7.41	0.98
1780	**1126**	47.6	1.3	13.4	3.2	0.0	6.8	6.7	12.3	2.6	1.4	0.4	4.0	0.30	98.65	0.00	0.77	0.00	0.02	0.00	0.56	-7.43	0.97
1750	**1125**	47.6	1.3	13.5	3.2	0.0	6.8	6.6	12.2	2.6	1.5	0.4	4.0	0.30	98.65	0.00	0.77	0.00	0.02	0.00	0.56	-7.46	0.96
1720	**1124**	47.6	1.3	13.6	3.2	0.0	6.8	6.5	12.1	2.7	1.5	0.4	4.0	0.29	98.66	0.00	0.77	0.00	0.02	0.00	0.56	-7.48	0.94
1690	**1123**	47.7	1.3	13.7	3.2	0.0	6.8	6.5	12.1	2.7	1.5	0.4	4.0	0.29	98.66	0.00	0.76	0.00	0.02	0.00	0.56	-7.51	0.93
1660	**1122**	47.7	1.3	13.8	3.2	0.0	6.9	6.4	12.0	2.7	1.5	0.4	3.9	0.29	98.66	0.00	0.76	0.00	0.02	0.00	0.56	-7.53	0.92
1630	**1121**	47.7	1.3	13.9	3.2	0.0	6.9	6.4	11.9	2.7	1.5	0.4	3.9	0.29	98.66	0.00	0.76	0.00	0.02	0.00	0.56	-7.56	0.91
1600	**1120**	47.7	1.3	13.9	3.1	0.0	6.9	6.3	11.8	2.7	1.5	0.5	3.9	0.29	98.67	0.00	0.76	0.00	0.02	0.00	0.56	-7.59	0.90
1570	**1119**	47.7	1.3	14.0	3.1	0.0	7.0	6.2	11.8	2.8	1.5	0.5	3.8	0.29	98.67	0.00	0.75	0.00	0.02	0.00	0.56	-7.61	0.88
1540	**1118**	47.8	1.3	14.1	3.1	0.0	7.0	6.2	11.7	2.8	1.5	0.5	3.8	0.29	98.67	0.00	0.75	0.00	0.02	0.00	0.56	-7.64	0.87
1510	**1117**	47.8	1.3	14.2	3.1	0.0	7.0	6.1	11.6	2.8	1.6	0.5	3.8	0.29	98.67	0.00	0.75	0.00	0.02	0.00	0.56	-7.66	0.86
1480	**1116**	47.8	1.3	14.3	3.1	0.0	7.0	6.0	11.5	2.8	1.6	0.5	3.7	0.28	98.67	0.00	0.75	0.00	0.02	0.00	0.56	-7.69	0.85
1450	**1115**	47.8	1.3	14.3	3.1	0.0	7.1	6.0	11.5	2.9	1.6	0.5	3.7	0.28	98.67	0.00	0.75	0.00	0.02	0.00	0.56	-7.72	0.83
1420	**1114**	47.9	1.3	14.4	3.1	0.0	7.1	5.9	11.4	2.9	1.6	0.5	3.7	0.28	98.67	0.00	0.75	0.00	0.02	0.00	0.56	-7.74	0.82
1390	**1113**	47.9	1.3	14.5	3.1	0.0	7.1	5.8	11.3	2.9	1.6	0.5	3.6	0.28	98.67	0.00	0.74	0.00	0.02	0.00	0.56	-7.77	0.81

1360	**1112**	47.9	1.3	14.6	3.1	0.0	7.1	5.8	11.2	2.9	1.6	0.5	3.6	0.28	98.68	0.00	0.74	0.00	0.02	0.00	0.56	-7.80	0.79
1330	**1111**	48.0	1.3	14.7	3.1	0.0	7.2	5.7	11.2	2.9	1.6	0.5	3.6	0.28	98.68	0.00	0.74	0.00	0.02	0.00	0.57	-7.83	0.78
1300	**1110**	48.0	1.3	14.8	3.1	0.0	7.2	5.7	11.1	3.0	1.6	0.5	3.5	0.28	98.68	0.00	0.74	0.00	0.02	0.00	0.57	-7.85	0.77
1270	**1109**	48.0	1.3	14.8	3.1	0.0	7.2	5.6	11.0	3.0	1.7	0.5	3.5	0.28	98.68	0.00	0.74	0.00	0.02	0.00	0.57	-7.88	0.76
1240	**1108**	48.1	1.3	14.9	3.1	0.0	7.2	5.5	10.9	3.0	1.7	0.5	3.5	0.27	98.68	0.00	0.74	0.00	0.02	0.00	0.57	-7.91	0.74
1210	**1107**	48.1	1.3	15.0	3.1	0.0	7.3	5.5	10.8	3.0	1.7	0.5	3.4	0.27	98.68	0.00	0.74	0.00	0.02	0.00	0.57	-7.93	0.73
1180	**1106**	48.1	1.3	15.1	3.1	0.0	7.3	5.4	10.8	3.1	1.7	0.5	3.4	0.27	98.68	0.00	0.74	0.00	0.02	0.00	0.57	-7.96	0.72
1150	**1105**	48.2	1.3	15.2	3.0	0.0	7.3	5.3	10.7	3.1	1.7	0.5	3.3	0.27	98.68	0.00	0.74	0.00	0.02	0.00	0.57	-7.99	0.70
1120	**1104**	48.2	1.3	15.3	3.0	0.0	7.4	5.3	10.6	3.1	1.7	0.5	3.3	0.27	98.67	0.00	0.74	0.00	0.02	0.00	0.57	-8.02	0.69
1090	**1103**	48.2	1.3	15.4	3.0	0.0	7.4	5.2	10.5	3.1	1.7	0.5	3.3	0.27	98.67	0.00	0.74	0.00	0.02	0.00	0.57	-8.05	0.67
1060	**1102**	48.3	1.3	15.5	3.0	0.0	7.4	5.1	10.4	3.2	1.8	0.5	3.2	0.27	98.67	0.00	0.74	0.00	0.02	0.00	0.57	-8.07	0.66
1030	**1101**	48.3	1.3	15.5	3.0	0.0	7.4	5.1	10.4	3.2	1.8	0.5	3.2	0.27	98.67	0.00	0.74	0.00	0.02	0.00	0.57	-8.10	0.64
1000	**1100**	48.4	1.3	15.6	3.0	0.0	7.5	5.0	10.3	3.2	1.8	0.5	3.1	0.26	98.67	0.00	0.74	0.00	0.02	0.00	0.57	-8.13	0.63
970	**1099**	48.4	1.3	15.7	3.0	0.0	7.5	4.9	10.2	3.2	1.8	0.5	3.1	0.26	98.66	0.00	0.75	0.00	0.02	0.00	0.57	-8.16	0.61
940	**1098**	48.5	1.3	15.8	3.0	0.0	7.5	4.9	10.1	3.3	1.8	0.5	3.0	0.26	98.65	0.00	0.75	0.00	0.03	0.00	0.57	-8.20	0.60
910	**1097**	48.5	1.3	15.9	2.9	0.0	7.5	4.8	10.0	3.3	1.8	0.5	3.0	0.26	98.60	0.00	0.76	0.00	0.06	0.00	0.57	-8.24	0.57
880	**1096**	48.6	1.3	16.0	2.9	0.0	7.5	4.7	10.0	3.3	1.9	0.6	2.9	0.26	98.55	0.00	0.78	0.00	0.10	0.00	0.58	-8.29	0.52
850	**1095**	48.7	1.3	16.1	2.8	0.0	7.5	4.7	9.9	3.4	1.9	0.6	2.9	0.25	98.55	0.00	0.78	0.00	0.10	0.00	0.58	-8.35	0.48
820	**1094**	48.8	1.3	16.2	2.8	0.0	7.5	4.6	9.8	3.4	1.9	0.6	2.8	0.25	98.54	0.00	0.78	0.00	0.10	0.00	0.58	-8.41	0.44
790	**1093**	48.9	1.3	16.3	2.7	0.0	7.6	4.5	9.7	3.4	1.9	0.6	2.8	0.25	98.54	0.00	0.78	0.00	0.10	0.00	0.58	-8.47	0.40
760	**1092**	49.0	1.3	16.4	2.7	0.0	7.6	4.4	9.6	3.5	1.9	0.6	2.7	0.24	98.54	0.00	0.78	0.00	0.10	0.00	0.58	-8.52	0.35
730	**1091**	49.1	1.3	16.5	2.6	0.0	7.6	4.4	9.5	3.5	1.9	0.6	2.7	0.24	98.54	0.00	0.78	0.00	0.10	0.00	0.58	-8.58	0.31
700	**1090**	49.2	1.3	16.6	2.6	0.0	7.6	4.3	9.5	3.5	2.0	0.6	2.6	0.24	98.54	0.00	0.79	0.00	0.10	0.00	0.58	-8.64	0.26
670	**1089**	49.3	1.3	16.7	2.6	0.0	7.6	4.2	9.4	3.5	2.0	0.6	2.6	0.23	98.53	0.00	0.79	0.00	0.10	0.00	0.58	-8.70	0.22
640	**1088**	49.4	1.3	16.8	2.5	0.0	7.6	4.2	9.3	3.6	2.0	0.6	2.5	0.23	98.53	0.00	0.79	0.00	0.10	0.00	0.58	-8.76	0.17
610	**1087**	49.5	1.2	16.9	2.5	0.0	7.6	4.1	9.2	3.6	2.0	0.6	2.4	0.22	98.52	0.00	0.80	0.00	0.09	0.00	0.59	-8.82	0.13
580	**1086**	49.6	1.2	17.1	2.4	0.0	7.6	4.0	9.1	3.6	2.0	0.6	2.4	0.22	98.52	0.00	0.80	0.00	0.09	0.00	0.59	-8.88	0.08
550	**1085**	49.7	1.2	17.2	2.4	0.0	7.6	3.9	9.0	3.7	2.1	0.6	2.3	0.22	98.51	0.00	0.81	0.00	0.09	0.00	0.59	-8.95	0.03
520	**1084**	49.8	1.2	17.3	2.3	0.0	7.6	3.9	8.9	3.7	2.1	0.6	2.3	0.21	98.50	0.00	0.81	0.00	0.09	0.00	0.59	-9.01	-0.02

490	**1083**	49.9	1.2	17.4	2.3	0.0	7.6	3.8	8.8	3.8	2.1	0.6	2.2	0.21	98.50	0.00	0.82	0.00	0.09	0.00	0.59	-9.07	-0.07
460	**1082**	50.0	1.2	17.5	2.2	0.0	7.6	3.7	8.7	3.8	2.1	0.6	2.1	0.21	98.49	0.00	0.83	0.00	0.09	0.00	0.59	-9.14	-0.12
430	**1081**	50.1	1.2	17.6	2.2	0.0	7.6	3.6	8.6	3.8	2.2	0.6	2.0	0.20	98.48	0.00	0.83	0.00	0.09	0.00	0.60	-9.21	-0.17
400	**1080**	50.3	1.2	17.8	2.1	0.0	7.6	3.5	8.6	3.9	2.2	0.6	2.0	0.20	98.46	0.00	0.85	0.00	0.09	0.00	0.60	-9.28	-0.22
370	**1079**	50.4	1.2	17.7	2.1	0.0	7.7	3.5	8.4	3.9	2.2	0.7	1.9	0.19	97.60	0.00	0.80	0.86	0.13	0.00	0.62	-9.36	-0.29
340	**1078**	50.6	1.2	17.6	2.0	0.0	7.8	3.5	8.2	4.0	2.3	0.7	1.8	0.19	95.88	0.00	0.74	2.57	0.17	0.00	0.64	-9.46	-0.38
310	**1077**	51.0	1.2	17.4	2.0	0.0	7.9	3.4	8.0	4.1	2.4	0.7	1.7	0.18	93.16	0.52	0.28	5.12	0.27	0.00	0.65	-9.56	-0.47
280	**1076**	51.4	1.2	17.1	1.9	0.0	7.9	3.2	7.9	4.2	2.5	0.7	1.6	0.18	90.44	0.55	0.25	7.81	0.29	0.00	0.65	-9.68	-0.57
250	**1075**	51.7	1.2	16.9	1.9	0.0	8.0	3.1	7.7	4.3	2.6	0.8	1.5	0.17	87.59	0.56	0.26	10.65	0.30	0.00	0.65	-9.80	-0.68
220	**1074**	52.1	1.2	16.7	1.8	0.0	8.1	3.0	7.6	4.3	2.7	0.8	1.4	0.17	84.55	0.57	0.27	13.65	0.31	0.00	0.65	-9.94	-0.80
190	**1073**	52.5	1.2	16.4	1.7	0.0	8.1	2.8	7.5	4.4	2.8	0.9	1.3	0.16	81.30	0.58	0.29	16.85	0.33	0.00	0.65	-10.09	-0.94
160	**1072**	52.9	1.2	16.1	1.6	0.0	8.2	2.7	7.3	4.5	2.9	0.9	1.2	0.15	77.78	0.59	0.33	20.30	0.35	0.00	0.65	-10.26	-1.09
130	**1071**	53.4	1.2	15.8	1.6	0.0	8.3	2.5	7.2	4.5	3.1	1.0	1.0	0.14	73.91	0.61	0.38	24.08	0.37	0.00	0.65	-10.45	-1.27
100	**1070**	53.8	1.3	15.4	1.5	0.0	8.4	2.3	7.1	4.6	3.3	1.0	0.9	0.13	69.60	0.63	0.46	28.26	0.39	0.00	0.66	-10.67	-1.47
70	**1069**	54.2	1.3	15.1	1.3	0.0	8.5	2.1	7.0	4.6	3.6	1.1	0.7	0.12	64.64	0.67	0.58	33.03	0.42	0.00	0.66	-10.93	-1.72
40	**1068**	54.7	1.3	14.6	1.2	0.0	8.7	1.9	7.0	4.6	3.9	1.3	0.5	0.11	58.55	0.75	0.79	38.77	0.47	0.01	0.67	-11.26	-2.03
10	**1067**	55.7	1.3	14.1	1.0	0.0	8.9	1.5	6.7	4.5	4.5	1.2	0.3	0.09	48.28	1.05	1.55	47.33	0.66	0.43	0.70	-11.83	-2.59

Geothermal dP/dT = 5 MPa °C^{-1}

P (bar)	T (°C)	liquid composition													liquid %	Solid phase percentage (%)					water %	log f_{O_2}	ΔNNO
		SiO_2	TiO_2	Al_2O_3	Fe_2O_3	Cr_2O_3	FeO	MgO	CaO	Na_2O	K_2O	P_2O_5	H_2O	$Fe^{3+}/\Sigma Fe$		ol	cpx	feld	sp	whitlockite			
4000	**1200**	46.9	1.1	10.1	3.2	0.1	5.7	10.2	14.5	1.8	1.0	0.3	5.0	0.34	99.81	0.14	0.00	0.00	0.05		0.00	-5.95	1.49
3900	**1198**	46.9	1.1	10.1	3.2	0.1	5.7	10.2	14.5	1.8	1.0	0.3	5.0	0.34	99.87	0.13	0.00	0.00	0.01		0.00	-5.98	1.49
3800	**1196**	46.9	1.1	10.1	3.2	0.1	5.7	10.1	14.5	1.8	1.0	0.3	5.0	0.34	99.87	0.13	0.00	0.00	0.01		0.00	-6.01	1.48
3700	**1194**	46.9	1.1	10.1	3.2	0.1	5.7	10.1	14.5	1.8	1.0	0.3	5.1	0.34	99.87	0.12	0.00	0.00	0.01		0.00	-6.05	1.47
3600	**1192**	46.9	1.1	10.1	3.2	0.1	5.7	10.0	14.5	1.8	1.0	0.3	5.1	0.34	99.87	0.12	0.00	0.00	0.01		0.00	-6.08	1.46
3500	**1190**	47.0	1.1	10.1	3.2	0.1	5.7	10.0	14.5	1.8	1.0	0.3	5.1	0.34	99.87	0.12	0.00	0.00	0.01		0.00	-6.11	1.46
3400	**1188**	47.0	1.1	10.1	3.2	0.1	5.7	9.9	14.6	1.8	1.0	0.3	5.0	0.34	99.76	0.15	0.00	0.00	0.02		0.08	-6.15	1.45
3300	**1186**	47.1	1.1	10.2	3.2	0.1	5.7	9.9	14.6	1.8	1.0	0.3	4.9	0.34	99.68	0.15	0.00	0.00	0.02		0.16	-6.19	1.44

3200	**1184**	47.1	1.1	10.2	3.2	0.1	5.7	9.8	14.7	1.8	1.0	0.3	4.9	0.34	99.60	0.15	0.00	0.00	0.02		0.23	-6.22	1.43
3100	**1182**	47.2	1.1	10.2	3.2	0.1	5.7	9.8	14.7	1.8	1.0	0.3	4.8	0.34	99.52	0.15	0.00	0.00	0.02		0.32	-6.26	1.42
3000	**1180**	47.2	1.1	10.2	3.2	0.1	5.7	9.7	14.7	1.8	1.0	0.3	4.7	0.34	99.44	0.14	0.00	0.00	0.02		0.40	-6.30	1.40
2900	**1178**	47.3	1.1	10.3	3.2	0.1	5.7	9.7	14.8	1.8	1.0	0.3	4.7	0.34	99.36	0.14	0.00	0.00	0.02		0.48	-6.33	1.39
2800	**1176**	47.3	1.1	10.3	3.2	0.1	5.7	9.6	14.8	1.8	1.0	0.3	4.6	0.34	99.27	0.14	0.00	0.00	0.02		0.57	-6.37	1.38
2700	**1174**	47.4	1.1	10.3	3.2	0.1	5.7	9.6	14.8	1.8	1.0	0.3	4.5	0.34	99.25	0.14	0.00	0.00	0.02		0.59	-6.41	1.37
2600	**1172**	47.5	1.1	10.3	3.2	0.1	5.7	9.5	14.9	1.8	1.0	0.3	4.4	0.34	99.25	0.14	0.00	0.00	0.02		0.59	-6.45	1.36
2500	**1170**	47.5	1.1	10.4	3.2	0.1	5.7	9.5	14.9	1.8	1.0	0.3	4.3	0.34	99.25	0.14	0.00	0.00	0.02		0.59	-6.49	1.35
2400	**1168**	47.6	1.1	10.4	3.2	0.1	5.7	9.4	14.9	1.9	1.0	0.3	4.3	0.34	99.24	0.14	0.00	0.00	0.02		0.60	-6.52	1.34
2300	**1166**	47.6	1.1	10.4	3.2	0.1	5.7	9.4	15.0	1.9	1.0	0.3	4.2	0.34	99.24	0.15	0.00	0.00	0.02		0.60	-6.56	1.33
2200	**1164**	47.7	1.2	10.5	3.2	0.1	5.7	9.3	15.0	1.9	1.0	0.3	4.1	0.34	98.78	0.11	0.48	0.00	0.02		0.62	-6.61	1.31
2100	**1162**	47.7	1.2	10.7	3.2	0.1	5.7	9.2	14.8	1.9	1.0	0.3	4.0	0.34	97.01	0.00	2.28	0.00	0.03		0.68	-6.66	1.29
2000	**1160**	47.7	1.2	10.9	3.3	0.1	5.8	9.0	14.6	2.0	1.1	0.3	3.9	0.33	97.00	0.00	2.29	0.00	0.03		0.68	-6.71	1.26
1900	**1158**	47.7	1.2	11.1	3.3	0.0	5.9	8.8	14.5	2.0	1.1	0.3	3.8	0.33	96.99	0.00	2.30	0.00	0.03		0.68	-6.77	1.23
1800	**1156**	47.8	1.2	11.3	3.3	0.0	6.0	8.7	14.3	2.1	1.1	0.3	3.7	0.33	96.97	0.00	2.32	0.00	0.03		0.68	-6.82	1.21
1700	**1154**	47.8	1.2	11.5	3.3	0.0	6.1	8.5	14.1	2.1	1.2	0.3	3.7	0.33	96.95	0.00	2.34	0.00	0.03		0.69	-6.87	1.18
1600	**1152**	47.8	1.3	11.7	3.3	0.0	6.2	8.3	13.9	2.2	1.2	0.4	3.6	0.32	96.92	0.00	2.36	0.00	0.03		0.69	-6.93	1.15
1500	**1150**	47.8	1.3	12.0	3.3	0.0	6.3	8.2	13.8	2.2	1.2	0.4	3.5	0.32	96.89	0.00	2.39	0.00	0.03		0.69	-6.98	1.13
1400	**1148**	47.9	1.3	12.2	3.3	0.0	6.4	8.0	13.6	2.3	1.3	0.4	3.3	0.32	96.85	0.00	2.42	0.00	0.03		0.70	-7.04	1.10
1300	**1146**	47.9	1.3	12.4	3.3	0.0	6.4	7.8	13.4	2.3	1.3	0.4	3.2	0.31	96.81	0.00	2.46	0.00	0.03		0.70	-7.10	1.07
1200	**1144**	48.0	1.3	12.7	3.3	0.0	6.5	7.6	13.1	2.4	1.3	0.4	3.1	0.31	96.75	0.00	2.51	0.00	0.03		0.71	-7.16	1.04
1100	**1142**	48.0	1.3	12.9	3.3	0.0	6.6	7.4	12.9	2.5	1.4	0.4	3.0	0.31	96.69	0.00	2.56	0.00	0.03		0.71	-7.22	1.01
1000	**1140**	48.1	1.4	13.2	3.3	0.0	6.7	7.2	12.7	2.5	1.4	0.4	2.8	0.30	96.62	0.00	2.62	0.00	0.03		0.72	-7.28	0.97
900	**1138**	48.2	1.4	13.5	3.3	0.0	6.8	7.0	12.4	2.6	1.4	0.4	2.7	0.30	96.54	0.00	2.70	0.00	0.03		0.73	-7.34	0.94
800	**1136**	48.2	1.4	13.8	3.3	0.0	6.9	6.8	12.2	2.7	1.5	0.4	2.5	0.30	96.45	0.00	2.78	0.00	0.03		0.74	-7.40	0.91
700	**1134**	48.3	1.4	14.1	3.3	0.0	7.1	6.5	11.9	2.8	1.5	0.5	2.4	0.29	96.33	0.00	2.89	0.00	0.03		0.75	-7.46	0.87
600	**1132**	48.4	1.4	14.4	3.3	0.0	7.2	6.3	11.6	2.9	1.6	0.5	2.2	0.29	96.20	0.00	3.01	0.00	0.03		0.76	-7.53	0.83
500	**1130**	48.6	1.4	14.8	3.2	0.0	7.3	6.0	11.3	3.0	1.7	0.5	2.0	0.28	96.03	0.00	3.17	0.00	0.04		0.77	-7.60	0.79
400	**1128**	48.7	1.5	15.2	3.2	0.0	7.4	5.7	10.9	3.1	1.7	0.5	1.8	0.28	95.80	0.00	3.37	0.00	0.04		0.79	-7.67	0.75

300	**1126**	48.9	1.5	15.6	3.2	0.0	7.6	5.4	10.5	3.2	1.8	0.5	1.5	0.28	95.49	0.00	3.65	0.00	0.04		0.81	-7.74	0.71
200	**1124**	49.1	1.5	16.1	3.2	0.0	7.7	5.1	10.1	3.3	1.9	0.6	1.2	0.27	95.02	0.00	4.09	0.00	0.04		0.85	-7.83	0.65
100	**1122**	49.5	1.6	16.3	3.2	0.0	8.1	4.8	9.4	3.6	2.0	0.6	0.8	0.26	91.79	0.00	4.88	2.33	0.05		0.94	-7.91	0.59
1	**1120**	50.6	1.9	14.4	3.4	0.0	9.5	4.0	8.0	4.0	2.8	0.9	0.1	0.24	66.26	2.63	6.70	21.73	1.42		1.26	-8.22	0.32
Low pressure geothermal																							
P (bar)	**T (°C)**	**liquid composition**													**liquid %**	**Solid phase percentage (%)**					**water %**	**log fO_2**	**ΔNNO**
		SiO_2	**TiO_2**	**Al_2O_3**	**Fe_2O_3**	**Cr_2O_3**	**FeO**	**MgO**	**CaO**	**Na_2O**	**K_2O**	**P_2O_5**	**H_2O**	**$Fe^{3+}/\Sigma Fe$**		**ol**	**cpx**	**feld**	**sp**	**whitlockite**			
100	**1200**	48.8	1.3	11.7	3.4	0.0	6.5	9.7	13.9	2.2	1.2	0.4	0.7	0.32	99.94	0.00	0.05	0.00	0.00	0.00	0.00	-6.52	1.04
90	**1185**	48.6	1.4	12.9	3.5	0.0	6.9	8.8	12.8	2.5	1.4	0.4	0.7	0.31	87.24	0.10	12.48	0.00	0.08	0.00	0.10	-6.75	0.99
80	**1170**	48.5	1.5	14.0	3.5	0.0	7.3	7.7	11.7	2.8	1.6	0.5	0.7	0.30	88.57	0.50	10.64	0.00	0.08	0.00	0.21	-6.96	0.95
70	**1155**	48.6	1.6	15.0	3.5	0.0	7.6	6.8	10.8	3.0	1.7	0.5	0.6	0.29	89.84	0.48	9.27	0.00	0.09	0.00	0.33	-7.19	0.90
60	**1140**	48.7	1.7	15.9	3.5	0.0	7.8	5.9	9.9	3.3	1.9	0.6	0.6	0.28	90.83	0.46	8.14	0.00	0.11	0.00	0.45	-7.44	0.84
50	**1125**	49.1	1.8	15.9	3.6	0.0	8.2	5.1	8.9	3.7	2.2	0.7	0.6	0.28	85.87	1.51	6.32	5.36	0.31	0.00	0.62	-7.68	0.79
40	**1110**	51.0	1.8	15.8	2.7	0.0	8.1	4.0	8.1	4.1	2.7	0.8	0.5	0.23	74.38	2.30	5.36	14.67	2.64	0.00	0.64	-8.56	0.10
30	**1095**	53.0	1.7	15.5	1.8	0.0	7.8	3.0	7.5	4.5	3.3	1.1	0.5	0.17	65.25	1.91	4.05	25.73	2.44	0.00	0.63	-9.66	-0.79
20	**1080**	54.5	1.6	15.1	1.2	0.0	7.5	2.2	7.0	4.7	4.1	1.3	0.4	0.13	55.56	1.47	3.08	37.50	1.70	0.07	0.62	-10.84	-1.78
10	**1065**	56.1	1.5	14.8	0.7	0.0	7.3	1.5	6.4	4.7	5.0	1.2	0.3	0.08	43.80	1.21	2.79	49.80	1.22	0.58	0.61	-12.24	-2.97
1	**1050**	57.1	1.5	14.3	0.4	0.0	7.3	0.8	6.1	4.5	6.1	1.2	0.1	0.04	30.51	1.01	2.62	63.42	0.80	1.05	0.60	-14.04	-4.56

Acknowledgements

I wish to thank my Italian tutor: prof. *Silvio Rotolo* for his precious suggestions and the continuos support during this PhD research and during my complete academic education.

A particular thank to my French tutor ("*directeur de these*") *Caroline Martel*, without whom the constructive doctoral experience at the CNRS-ISTO would not have been possible.
Many thanks to my co-tutor *Andrea Rizzo* for his useful teaching and advices.

Thanks to *Michel Pichavant* that introduced me to the "fabulous world" of the experimental petrology, and for his important teaching.
Thanks to *Antonio Paonita* and *Marcello Liotta* for their precious help, for all the time they spent to teach me the approach for the elaboration of scientific data, and for their moral support.

Many thanks to all the people of the **ISTO** (France): first of all, the laboratory director *Bruno Scaillet* that welcomed me to ISTO. Thanks to *Ida Di Carlo*, for her support and help in the SEM observation and EMP analysis, as well as for the personal support and *encouragement*!
Thanks to all people that helped me in the experimental work, sample preparation and analysis (*Giada, Clément, Michel, Remi Champallier, Patricia, Esteban, Remi, Juan, Nolwenn, Nicolas, Leila,...*). Sorry, if I forget somebody.

I am grateful to *Yves Moussallam* for the great opportunity to enter to Diamond Light Source and for the "strong" synchrotron experience, together with *Nial Peters*, and for his precious help for the data elaboration and interpretation.

Collaborations with *Yann Morizet* has been noteworthy for enriching this research and my scientific background with the Raman spectroscopy.

Thanks to the people of the CRPG of Nancy (France) for their advices for the SIMS acquisition and suggestions for data elaboration (*Etienne Deloule, Micheal Champenois, Johann Villeneuve, Audrey Gurenko, Emily Thomassot,...*)
Thanks to *Fabrice Gaillard* for the constructive discussion about the "world of the oxygen fugacity and volatiles".

Thanks to all those that have helped me in somehow for this PhD as: *Pierre Cartigny* for the important discussion about sulfur isotope; *Alessandra Correale* for the informative material about Mt. Etna, as well as *Michela Costa* and *Alberto Rosciglione*.
Thanks to the referees of the manuscript: *Rosa Anna Corsaro* and *Joan Martí.*

Finally, but the most important… I wish to thank my parents and my sister for their continuous encouragement in achieving my goals. *GRAZIE famiglia*.

A great THANK at the person that has bent over backwards for me. Thanks *Giada* for all, for your encouragement, for your friendship, for trasmitting me the passion for the petrological research, for your precious teaching. Thanks for have given me the possibility to live a wonderful french adventure. *Grazie.*

Thanks to the others people of the ISTO (PhD students, post-doc, technicians,…) and the others friends of the *"Ecole Doctorale d'Orleans"* that have enriched my personal life experience. *MERCI*! I prefer do not write the names because I do not want to forget anybody. Only one: *Merci Clément.*